Analysis and design of metamaterial-inspired microwave structures and antenna applications

Analysis and Design of Metamaterial-Inspired Microwave Structures and Antenna Applications

by

Titos Kokkinos

A doctoral thesis submitted in conformity with the requirements
for the degree of Doctorate of Philosophy
Department of Electronic and Electrical Engineering
Loughborough University

Abstract

Analysis and Design of Metamaterial-Inspired Microwave Structures and Antenna Applications

Titos Kokkinos
Doctorate of Philosophy
Department of Electronic and Electrical Engineering
Loughborough University
2010

Novel metamaterial and metamaterial-inspired structures and microwave/antenna applications thereof are proposed and studied in this thesis. Motivated by the challenge of extending the applicability of metamaterial structures into practical microwave solutions, the underlying objective of this thesis has been the design of low-cost, easily fabricated and deployable metamaterial-related devices, and the development of computational tools for the analysis of those. For this purpose, metamaterials composed of tightly coupled resonators are chosen for the synthesis of artificial transmission lines and enabling antenna applications. Specifically, fully-printed double spiral resonators are employed as modular elements for the design of tightly coupled resonators arrays. After thoroughly investigating the properties of such resonators, they are used for the synthesis of artificial lines in either grounded or non-grounded configurations. In the first case, the supported backward waves are exploited for the design of microstrip-based filtering/diplexing devices and series-fed antenna arrays. In the second case, the effective properties of such structures are employed for the design of a novel class of self-resonant, low-profile folded monopoles, exhibiting low mutual coupling and robust radiating properties. Such monopoles are, in turn, used for the synthesis of different sub-wavelength antenna arrays, such as superdirective arrays. Finally, an in-house periodic FDTD-based computational tool is developed and optimized for the efficient and rigorous analysis of planar, metamaterial-based, high-gain antennas.

To my wife, Eirini.

Acknowledgements

Although doctorate research tends to be a quite lonely process, it becomes much more fruitful, efficient and enjoyable through the interaction with people that share the same research interests. During my doctorate studies in Loughborough University I had the chance to collaborate with researchers and academics that possess solid technical backgrounds and high research qualities. Now, that this endeavor reaches its end, I feel the moral obligation to thank all of them by heart and wish them all the best in their personal and professional lives.

First of all, I gratefully thank my supervisor Dr Alexandros P. Feresidis for his guidance, patience, understanding and encouragement during this research endeavor. Throughout my doctoral studies Alex has been extremely supportive and always available to help towards overcoming the encountered technical difficulties and suggest new research directions.

Together with Alex, I would also like to thank all the faculty members of the WiCR and CMCR groups, namely Prof. Yiannis Vardaxoglou, Dr Rob Edwards, Dr James Flint and Rob Seager, and the post-doctoral researchers Dr James Kelly, Dr Alford Chauraya, Dr Panagiotis Kosmas and Dr George Goussetis, for all the interaction we had during the last four years.

I would like also to thank the technicians of the Department of Electronic and Electrical Engineering Terry West, Peter Godfrey and Peter Harrison, whose help with the fabrication of some of the prototypes has been invaluable.

Special thanks go to the fellow graduate students of WiCR Stratos Doumanis, George Palikaras, Marta Padilla-Pardo and Nikos Christopoulos, the MSc students Eirini Liakou, Tomas Rufete and Anestis Katsounaros that I had the chance to work with, and all the other members of WiCR and CMCR.

Given that part of the writing up of this thesis was carried out while being with Bell Laboratories Ireland, Alcatel-Lucent, I would also like to thank my colleagues Dr Andrei Grebennikov and Dr Florian Pivit for all the stimulating discussions during the last ten months, and my manager Dr Francis Mullany for providing me the working hours flexibility required for the conclusion of the writing up and the submission of the thesis.

Also, I would like to acknowledge the financial support, through a scholarship for graduate studies and multiple travel grants, of EPSRC, the Department of Electronic and Electrical Engineering, the Faculty of Engineering, Loughborough University, and

the European Antennas Virtual Center of Excellence.

Last but definitely not least, I would like to express my deepest gratitude to my life partner and wife Eirini, who, throughout these years, has been consistently supportive, patient and willing to undergo several personal sacrifices in order for this research endeavor to be concluded. Eirini, thank you for being at my side, thank you for being yourself.

Publications from the Research

Aspects of the work of this thesis have been published or accepted for publication in the following papers.

Referred Journal Papers

- T. Kokkinos, and A. P. Feresidis,"Low-Profile Folded Monopoles with Embedded Planar Metamaterial Phase-Shifting Lines", IEEE Transactions on Antennas and Propagation, to appear, Oct. 2009.

- T. Kokkinos, E. Liakou and A. P. Feresidis,"Decoupling antenna elements of PIFA arrays on handheld devices", Electronics Letters, vol. 44, no. 25, pp. 1442-1444, Dec. 2008.

- J. R. Kelly, T. Kokkinos, and A. P. Feresidis,"Analysis and Design of Subwavelength Resonant Cavity Type 2-D Leaky-Wave Antennas", IEEE Transactions on Antennas and Propagation, vol. 56, no. 9, pp. 2817-2825, Sept. 2008.

Referred Conference Papers

- A.P. Feresidis, T. Kokkinos and Q. Li, "Isolation Enhancement of Monopole Antennas and PIFAs on a Compact Ground Planes", to be presented in Proc. IEEE LAPC 2009, Loughborough, UK.

- T. Kokkinos and A.P. Feresidis, "An Electrically Small Monopole-Like Antenna with Embedded Metamaterial High-μ Matching Network", Proc. Metamaterials 2008, Pamplona, Spain, Sept. 2008 *(oral presenantion) (Best Student Paper Award Finalist).*

- T. Kokkinos, T. Rufete-Martinez and A.P. Feresidis, "lectrically Small Superdirective Endfire Arrays of Low-Profile Folded Monopoles", Proc. Metamaterials 2008, Pamplona, Spain, Sept. 2008 *(oral presentation).*

- T. Kokkinos, A. Katsounaros and A.P. Feresidis, "Series-Fed Microstrip Patch Arrays Employing Metamaterial Transmission Lines: A Comparative Study" Proc. IET EuCAP 2007, Edinburgh UK, Nov. 2007 *(poster presentation).*

- T. Kokkinos, A.P. Feresidis and J.C. Vardaxoglou, "A Low-profile Monopolelike Small Antenna with Embedded Metamaterial Spiral-based Matching Network", Proc. IET EuCAP 2007, Edinburgh UK, Nov. 2007 *(poster presentation).*

- J. R. Kelly, T. Kokkinos, and A. P. Feresidis, "Modeling and Design of a Subwavelength Resonant Cavity Antenna" Proc. Metamaterials 2007, Rome, Oct. 2007 *(oral presentation).*

- T. Kokkinos, A.P. Feresidis and J.C. Vardaxoglou, "Equivalent Circuit of Double Spiral Resonators Supporting Backward Waves", Proc. IEEE LAPC 2007, Loughborough, UK *(poster presentation).*

- T. Kokkinos, A.P. Feresidis and J.C. Vardaxoglou, "Analysis and Application of Metamaterial Spiral-Based Transmission Lines" Proc. IWAT 2007, Cambridge, UK (oral presentation).

- T. Kokkinos, A.P. Feresidis and J.C. Vardaxoglou, "On the Use of Spiral Resonators for the Design of Uniplanar Microstrip-Based Left-Handed Metamaterials", Proc. 2006 IEEE European Conference on Antennas and Propagation, Nice, France *(poster presentation).*

Other aspects of the work of this thesis have been recently submitted for publication or remain under submission.

Contents

List of Tables

List of Figures

Chapter 1

Introduction

This chapter offers a general introduction to the thesis. Initially, a brief but inclusive introduction to electromagnetic metamaterials is attempted. In the second section of the chapter, the major classes of metamaterial applications are described. The reasons that motivated this research endeavor are discussed in the third section of the chapter, while an overview of the thesis is offered in the last section of the chapter.

1.1 Electromagnetic Metamaterials

Electromagnetic metamaterials constitute an extended class of electromagnetic structures that has attracted significant interest among electromagnetic engineers, microwave engineers and physicists during the last decade. Deriving its name from the Greek prefix $\mu\epsilon\tau\alpha-$, meaning beyond, the term "metamaterial" had been originally employed to describe any artificial (engineered) structure possessing effective electromagnetic properties not encountered among natural materials.

The first theoretical study of the properties of a hypothetical medium possessing unnatural electromagnetic parameters was pursued in 1967 by V.G. Veselago who examined the electromagnetic properties of an ideal medium that possesses simultaneously negative values of its electric permittivity ϵ and its magnetic permeability μ [7]. In this study, Veselago showed that when both ϵ and μ are negative, the phase constant $\beta = \omega\sqrt{\epsilon\mu}$ of a wave that propagates in that medium remains real allowing the electromagnetic waves to propagate without any attenuation, losses or internal reflections. By means of Maxwell's equations, he proved that in such a medium the electric field $\overline{E}$, the magnetic field $\overline{H}$ and the wave vector $\overline{k}$ form a left-handed triplet, in contrast to the ordinary media where they

form a right-handed triplet. Therefore, media with simultaneously negative values of ϵ and μ are nowadays called Left-Handed Media (LHM). Also, by comparing the direction of the wave vector $\overline{k}$ to the Pointing vector $\overline{S}$, defined as $\overline{S} = \overline{E} \times \overline{H^*}$ and always forming a right-handed triplet with the electric and magnetic field components, he concluded that in media that simultaneously exhibit negative ϵ and μ the wave vector $\overline{k}$ and the Poynting vector $\overline{S}$ are contra-directional, as opposed to common right-handed media where they are co-directed. This suggests that in LHM the power flows in the opposite direction of phase progression or, equivalently, that the group velocity $\overline{u}_g$ and the phase velocity $\overline{u}_\varphi$ are antiparallel. The electromagnetic waves which are characterized by antiparallel group and phase velocities are called backward-waves [1] and such waves can be supported in LHM. Extending his study, Veselago examined the reflection of a wave at an interface between a right-handed and a left-handed medium. By properly applying the boundary conditions at this interface, he proved that the angle of refraction of this wave is negative, regardless of its polarization. This finding suggests that the index of refraction of LHM is negative and can be mathematically formulated by recalling the definition of the index of refraction, which is $n = \pm\sqrt{\epsilon\mu}$. When ϵ and μ are of the same sign, the index of refraction remains real and therefore lossless propagation in the medium is allowed. For the case of a right-handed medium, the "+" sign is chosen for n (Positive-Refractive-Index (PRI) medium), while for the case of the left-handed medium, Veselago proved that the "-" sign should be chosen, resulting in a negative, relative to the vacuum, index of refraction (Negative-Refractive-Index (NRI) medium).

Veselago's seminal work on media possessing simultaneously negative values of ϵ and μ was purely theoretical given that at that time no media with such properties had been engineered. Even though it was known that electromagnetic plasma exhibits negative ϵ values below its cut-off and W. Rotman had proposed an artificial dielectric, composed of periodic arrays of wires, that simulated plasma operation [2] [9], no medium with a

[1] Backward-waves had been known for years before Veselago's study and have been extensively used in numerous electromagnetic applications such as backward-wave oscillators and backward-wave amplifiers. Nevertheless, in the aforementioned applications backward-waves are supported by periodic structures that exhibit periodic effective refractive indexes, and they correspond to higher-order spatial harmonics (*i.e.* n=-1 spatial harmonic) [8], as compared to Veselago's backward-waves that are attributed to negative values of the fundamental spatial mode (*i.e.* n=0) of the refractive index.

[2] Plasma is any gas that contains certain quantities of charged (ionized) particles. From an electromagnetic point of view, in the absence DC magnetic fields, plasma can be considered as an isotropic lossy dielectric with magnetic permeability of unity and dispersive electric permittivity $\epsilon_p = 1 - \frac{\omega_p^2}{\nu^2+\omega^2} + j\frac{\omega_p^2 \nu/\omega}{\nu^2+\omega^2}$, where ω_p is the so-called plasma frequency and ν is the collision frequency.

negative μ property was available.

The interest for artificial media possessing electromagnetic properties not encountered among natural materials was renewed in the $90's$ mostly by physicists and engineers working on photonic crystals (PC) [10], [11], [12], electromagnetic/photonic bandgap structures (EBG/PGB) [13], [14], [15], frequency selective surfaces (FSS) [16], [17], hard/soft electromagnetic surfaces [18], chiral media [19], [20], [21] and other periodic artificial structures.

Since 1996 Sir J. Pendry had been studying plasmons supported by arrays of wires [22] while in his seminal work published in 1999 he reported the magnetic activity of conducting resonators interacting with electromagnetic waves [3]. Specifically, in this work Sir J. Pendry showed that arrays of metallic resonators, each of those being of sub-wavelength dimensions, when properly excited with plane waves, form an effective medium exhibiting negative μ property for a certain frequency band after the self-resonance of the resonators. This work constituted the most significant step towards the experimental verification of negative refraction from LHM, since it provided all the theoretical background for the synthesis of media exhibiting an effective negative μ property, even though composed of non-magnetic modular elements. Shortly afterwards, D.R Smith *et al.* experimentally demonstrated negative refraction using artificial LHM [23], [24], by synthesising a medium composed of arrays of properly tuned sub-wavelength metallic resonators, similar with those proposed by Sir J. Pendry in [3], and metallic wires, similar with those studied by W. Rotman in [9].

Simultaneously with the efforts for the development of LHM, other engineers and scientists had been working on the synthesis and development of artificial dielectrics (either 3-D structures or 2-D surfaces) possessing properties resembling those of what would be magnetic conductors in the existence of magnetic charges. Published results of these studies suggested that such properties can be obtained from arrays of properly excited resonators and for frequency bands centered at the resonance of these resonators [25], [26], [27]. As a result, a new type of artificial structures/surfaces, emulating the inexistent magnetic conductor and called either Artificial Magnetic Conductors (AMC) or High Impedance Surfaces (HIS), was added to the class of metamaterials, attracting significant interest among researchers. At this point, it is worth mentioning that both the synthesis of LHM, reported in [24], and AMC or HIS, reported in [27] and [25], relied on the synthesis of specific effective permeability profiles using arrays of resonating metallic modular elements of sub-wavelength dimensions. Therefore, in both types of

metamaterial structures the results of [3] have been exploited.

Another type of metamaterial structures that are directly derived from the work of [3] are the so-called artificial magneto-dielectrics, that are composed of arrays of non-magnetic, metallic resonators and are employed to provide unusual magnetic permeability values, such as $\mu >> 1$ or $\mu \rightarrow 0$, or certain spatial permeability profiles (tensors), such as magnetically anisotropic media. Similar artificial dielectrics can be employed for the extraction of the corresponding cases for the effective electric permittivity.

The last major type of metamaterial structures, that were proposed shortly after the experimental verification of LHM negative refraction by D.R Smith *et al.*, were the, so-called, *LC*-loaded transmission lines and were introduced independently G.V. Eleftheriades *et al.* [28], [29], and C. Caloz *et al.* [30]. In this approach, LHM are synthesised by periodically loading, in the sub-wavelength scale, conventional transmission lines (supporting TEM or quasi-TEM modes) with series capacitance and shunt inductance. The origin of this idea for the implementation of LHM can be traced back to the equivalent circuit representations of media supporting conventional (right-handed) plane/TEM waves. The propagation properties in such cases can be modeled through series inductances and a shunt capacitances representing the magnetic permeability and the electric permittivity, respectively, of these media. Therefore, it is reasonable to suggest that the dual equivalent circuit representation (series capacitors and shunt inductors) would correspond to the propagation of a left-handed waves. Even though such dual 1-D transmission lines had been used in the past for the representation of backward waves [31] or the implementation of high-pass filter configurations [32], they had never been treated in the context of LHM, considering effective negative indexes of refraction for the fundamental spatial harmonic and all the emerging microwave applications (these applications will be presented in the following section of the thesis). Furthermore, the 2-D [33] and 3-D [34], [35] versions of these structures and the properties of those had never been investigated. Given that the *LC*-loaded transmission lines metamaterials are usually implemented by loading conventional (right-handed) transmission lines with series capacitors and shunt inductors, the final structures are composed of series and shunt branches that can be both capacitive and inductive. Therefore, a single structure may support simultaneously forward (right-handed), backward (left-handed) and standing (phase-matched) waves. This feature together with the compatibility of this type of metamaterials with standard microwave technologies (such as microstip and CPW lines) enabled the use of *LC*-loaded transmission lines in numerous microwave and antenna applications that require phase

manipulation of the involved waves.

The term "metamaterials" was originally used exclusively in order to refer to any of the aforementioned periodic structures that possess effective electromagnetic parameters that are not encountered among natural substances/materials. Because of the unusual but promising properties of these structures, the interest for metamaterials expanded rapidly among physicists and engineers, and more and more researchers were initiating new research projects on metamaterials and other periodic or dispersive structures that could possibly lead to further interesting applications or unusual phenomena. As a result, nowadays, approximately 10 years after the first metamaterial electromagnetic structure, the term "metamaterials" has gained a much broader context, including almost any periodic structure that is employed as a substrate or superstrate to enhance the performance or the properties of conventional microwave and antenna structures, and even non-periodic structures that rely their operation on some kind of phase manipulation technique, similar with those of the LC-loaded transmission lines.

Finally, it is worth mentioning that metamaterials, since ever their formulation as a research field, apart from intense interest have also attracted severe critique. Originally, that critique was focused on the physics of LHM [36], [37], [38], [39], while later on that critique was maintained by engineers working in other well-established areas of electromagnetism and microwave engineering such as microwave filters [40] and FSS [41]. The latter critique was mostly focused on the novelty of some metamaterial structures and their applications, given that all metamaterials, microwave filters and FSS rely their operation predominantly on very well known and extensively studied electromagnetic/microwave resonators. Furthermore, during the recent years, the critique against metamaterials also refers to their applicability only to a limited number of microwave and antenna applications, the inherent imperfections associated with their operation (*i.e.* ohmic losses, narrow bandwidth of operation) and the inexistence of rigorous proof of the superior performance of metamaterial-based applications through their systematic comparison with their conventional counterparts.

1.2 Metamaterial and Metamaterial-Inspired Applications

The rapid spread of the interest for metamaterial structures must be attributed to the several promising applications that have been proposed in the literature and that involve both interesting/unusual physical aspects and device designs with enhanced characteristics/performance as compared to their conventional counterparts.

The first and possibly the most significant application of LHM and negative refraction is the, so-called, perfect lens. Veselago had already in the 60's envisioned the possibility of designing a new type of flat lens composed of a NRI slab bounded by two conventional PRI slabs. In such configuration, any cylindrical wave traveling in the first PRI slab and impinging on the first PRI/NRI interface would be negatively refracted and, hence, focused within the NRI slab. Consequently, waves emanating from the NRI focal point would be again negatively refracted at the second NRI/PRI interface, creating a second focal point withing the second PRI slab. Many decades after the proposal of the flat NRI lens by Veselago, Sir J. Pendry not only confirmed the feasibility of such a scheme, but also showed that such lens, if properly designed, could function as "perfect"lens, being able to focus the whole spectrum of the source (*i.e.* both the propagating and the evanescent spectrum) [42]. This is achieved by the evanescent part of the source spectrum being amplified within the NRI slab and, hence, recovered at its original magnitude at the two focal points. This property of the Veselago-Pendry flat lens offers the possibility of imaging beyond the diffraction limit (sub-wavelength imaging). Up to date, even though there have been several attempts, the only successfully experimental verification of the Veselago-Pendry flat lens has been presented by G.V. Eleftheriades *et al.* and A. Grbic *et al.*, initially using a planar 2-D lens [43] and thereafter full 3-D structures [44], [45], [46]. All these structures, that have been implemented employing either directly or indirectly the *LC*-loaded transmission lines metamaterials, have been used to reconstruct point source images of sub-wavelength dimensions.

Another large class of metamaterial applications are those involving artificial dielectrics and magneto-dielectrics exhibiting tailored values and forms of their effective dielectric constants. An extremely popular example of these applications is the controlling of electromagnetic waves using engineered dielectric/magneto-dielectric tensors (anisotropic artificial material profiles) [47] and the synthesis of coatings (cloaks) [48],

[49] that offer electromagnetic invisibility to coated scatterers. Another example of metamaterial applications involving artificial dielectrics with permittivities near to zero are those referring to the tunneling of electromagnetic energy through waveguides of arbitrary shapes filled with such artificial dielectrics [50], [51]. Finally, the most popular application of metamaterial magneto-dielectrics, composed of several non-magnetic resonant modular elements such as those of [3], [52], [53], is their use to provide increased miniaturization factors, potentially without significantly reducing the operating bandwidth [3], in several antenna, mostly microstrip-based, applications [59], [60], [61], [62], [63]. In such antenna applications, artificial magneto-dielectrics exhibiting high-μ values could provide similar miniaturization factors with those of conventional dielectrics ($\lambda_g = \lambda/\sqrt{\epsilon_r \mu_r}$) while when used together with conventional dielectrics may be exploited to maintain the impedance level close to that of free space ($Z = \sqrt{\mu_r/\epsilon_r}$).

A third class of metamaterial applications are those involving the use of AMC/HIS and other periodic meta-surfaces or EBG structures for the size-reduction and the radiating properties enhancement of highly-directive antennas and antenna arrays [27], [6], [64], [65], [66], [67], [68], [69],[70], [71], [72].

Finally, the most extended class of metamaterial applications are those employing the LC-loaded transmission line structures for the design of microwave devices and antennas with enhanced performance as compared with their conventional counterparts. Given the compatibility of this type of metamaterial with standard microwave technologies (*i.e.* microstrip, CPW, CPS), its use for the development of such applications had been a straightforward procedure. A big portion of these applications are based on the phase-shifting lines of [73] that exploit the backward and forward waves that can be supported simultaneously by 1-D LC-loaded transmission lines to design phase-shifters that can insert any required phase-shift (positive or negative) independently of their physical dimensions (usually being of sub-wavelength dimensions). The possibility of controlling the phase of microwaves using devices of sub-wavelength dimensions can be employed for the miniaturization of the vast majority of microwave devices that involve phase-shifting lines (*e.g.* power dividers, baluns, couplers etc) [74], [75], [76], [77]. Other applications of

[3] It is pointed out that the performance of all radiating structures is governed by fundamental physical limits that relate the antennas operating bandwidth with their volume and their radiating efficiency (Chu and Chu-Harrington limits [54], [55], [56], [57], [58]). Operation of any antenna beyond these limits is not possible by any means. Nevertheless, smart design approaches could enable the design of antennas operating closer to the these limits than others. Metamaterial magneto-dielectrics have been proposed as one of these design approaches.

the LC-loaded transmission lines include spatial filtering applications [78], [79], miniaturized filters [80], [81], zeroth-order resonators (inspired by the work of N. Engheta [82]), leaky-wave antennas able of scanning their beams with frequency from the backward to the forward direction [83], [84], [85] and other antenna designs that employ negative- and zeroth-order resonances of LC-loaded structures to achieve miniaturization [86], [87].

Apart from microwave devices and antenna designs that involve directly metamaterial structures, in recent years there have have been several other designs that even though they do not employ any of the well-known metamaterial structures, they can be considered to be metamaterial-inspired. An example of such design is the small antenna design of [88] that has been inspired by the ideal metamaterial-based structures that had been proposed and theoretically studied in [89] (the term metamaterial-inspired has been attributed to Prof. R. Ziolkowski). Another example of metamaterial-inspired designs are the near-field plates of [90], [91] that can be employed to focus an impinging plane wave to a focal point of sub-wavelength dimensions (subdiffraction focusing). This design has been directly inspired by Veselago-Pendry perfect lens given that the flat-plates operation is based on the reconstruction of the impedance profile along the second NRI/PRI interface of the Veselago-Pendry perfect lens.

1.3 Motivation

Electromagnetic metamaterials are definitely an interesting and challenging area of study and research. The richness of the electromagnetic phenomena associated with their operation, the great variety of their unconventional properties and their potential applicability in the design of novel applications or alternative implementations of conventional applications with enhanced performance have motivated several engineers to perform research in that area.

When this research endeavor started, back in 2005, most of the conceptual aspects related to the operation of electromagnetic metamaterials had been well studied and understood, and the research interest was moving towards the development of metamaterials structures operating in higher frequencies ($i.e$ millimeter waves, THz and optical frequencies) and the development of metamaterial-based devices that could be employed in practical applications. In the latter front, there are three major challenges that have to be faced in order to allow metamaterial enabled devices to penetrate into real world applications. First, being inherently resonant structures, metamaterials usually exhibit

narrowband and lossy operation. Secondly, the LC-loaded transmission lines, the only broadband implementation of metamaterials, in most of the cases incorporate large numbers of lumped-elements that would increase the fabrication cost and the required fabrication effort of applications employing them. Finally, being periodic structures, metamaterials and metamaterial-based applications usually require large computational resources and time to be analysed or synthesised, unless dedicated periodic tools are employed.

The three aforementioned constraint factors are those that motivated this research project. The main target of this project has been set to be the proposal of metamaterial or metamaterial-inspired structures and devices that would be easily fabricated and could be used to tackle major challenges in modern microwave and antenna design, such as size miniaturization, fabrication cost reduction and performance enhancement. Also, on the front of modeling, the evolution of pre-existing periodic tools, such as the periodic FDTD tool of [92], to allow for the fast and computationally efficient analysis and synthesis of useful antenna applications, such as the high-gain antenna designs presented in this thesis, has been considered of great importance, as well.

1.4 Aim and Overview of the Thesis

The main objective of this thesis has been the enhancement of the applicability of metamaterial and metamaterial-inspired structures and devices into practical microwave and antenna solutions. For this purpose, novel, low-cost, compatible with standard microwave technologies, 1-D artificial lines are synthesised using compact, fully-printed, tightly coupled resonators. Such artificial lines are initially employed in grounded configurations for the synthesis of innovative series-fed microstrip patch arrays and compact filtering/diplexing devices. In turn, similar artificial lines are employed in non-grounded configurations for the design of a novel class of self-resonant, low-profile folded monopoles with enhanced, as compared to their conventional counterparts, performance. The unique features of these radiators are exploited for the synthesis of different compact (sub-wavelength) antenna arrays that could be employed in several emerging wireless applications. Finally, novel and computationally efficient approaches are proposed for the rigorous modeling of periodic, metamaterial-based leaky-wave structures, enabling the fast, accurate and optimized design of flat-plate, metamaterial-based, high-gain antennas.

The thesis has been divided into seven chapters. In chapter 2, that follows this in-

troductory chapter, all the theoretical aspects that are employed within the thesis are presented. In the first part of this chapter, an inclusive derivation of any metamaterial properties through the equivalent circuit analysis of random resonators is presented. This analysis shows that metamaterial properties can be derived not only in the well-known case of free standing resonators interacting with impinging plane waves but also in the much less investigated case of tightly coupled resonators. The results of the latter case have been employed in the following chapters for the synthesis of fully-printed, microstrip-based metamaterial lines. In the second part of the same chapter the theoretical background of the periodic FDTD tool that has been developed in [93] is briefly presented. This tool has been furthered developed and optimized as part of this research endeavor while it has been extensively used for the analysis of some of the proposed structures of this thesis. Finally, in the last part of chapter 2 the commercial electromagnetic solvers that have been employed throughout the thesis are briefly presented.

In chapter 3, fully-printed, microstrip-based resonators are studied and employed together with the theory of chapter 2 for the synthesis of novel metamaterial 1-D lines supporting backward waves. The proposed lines are fabricated and tested and their metamaterial properties are experimentally validated. Finally, these lines are employed for the synthesis of series-fed microstrip patch arrays.

In chapter 4, fully-printed, metamaterial-inspired phase-shifting lines composed of tightly coupled resonators are employed for the synthesis of a novel class of low-profile folded monopoles. The operation of these monopoles are explicitly explained through the phase-shifting properties of the employed lines, while an equivalent circuit for the proposed antennas is presented. Several versions of the proposed antenna design are examined, and the impact of the ground plane against which it is fed and its profile on its radiating properties are thoroughly investigated. Finally, two different versions of the proposed antennas are built and measured. Finally, the electromagnetic coupling between any pair of the proposed antennas is modeled.

Chapter 5 is dedicated to the design of different types of sub-wavelength antenna arrays. Initially, two sub-wavelength phased arrays, one composed of conventional monopoles and one composed of the low-profile folded monopoles of chapter 4, are built, measured and compared, exhibiting the importance of using low-coupling radiating elements when designing sub-wavelength antenna arrays. Subsequently, the low-coupling monopoles of chapter 4 are employed for the design of single-port, off-the-shelf, superdirective arrays and the limits of such arrays are explored. Finally, in the last part of chapter 5, a novel,

metamaterial-inspired scheme for the decoupling of PIFAs on handhelds is presented and experimentally validated.

In chapter 6, the periodic FDTD tool originally developed in [93] is furthered developed, optimized and employed for the analysis of novel leaky-wave sub-wavelength resonant cavity type high-gain antennas. Specifically the computational performance of the FDTD tool, when employed for the modeling of leaky-wave structures, is significantly improved by introducing rigorous post-processing techniques that are based on solid electromagnetic arguments. In turn, this tool is employed for the analysis of the computationally demanding, novel class of sub-wavelength resonant cavity type leaky-wave antennas comprising of an AMC and a PRS. Finally, a second post-processing algorithm, that is also derived from electromagnetic arguments, is developed, enabling the approximate calculation of the radiation patterns of the aforementioned antennas employing only the periodic FDTD tool and the developed post-processing algorithm.

In chapter 7, the conclusions of the thesis are summarized.

Chapter 2

Theoretical Background

In this chapter, the theoretical aspects, the analytical and numerical methodologies and the commercial electromagnetic tools that have been developed and employed throughout this thesis are being reported. The majority of the reported material has been extracted from the general literature. In the first section of the chapter, an inclusive theory for the analysis or synthesis of any metamaterial structure through its equivalent circuit is presented. This theory has been inspired from the study of numerous metamaterial-related references and has been formulated in accordance with the standard approaches for the analysis of periodic structures [2], [94]. Following this theory, a periodic FDTD-based computational tool that has been developed and optimized for the analysis and modeling of periodic metamaterial structures is reported. The reported FDTD background has been mostly extracted from [1], while the presented FDTD-based tool was originally reported in [93], [95]. Finally, in the last section of this chapter, a short description of the commercial electromagnetic solvers employed for the needs of the thesis is also provided.

2.1 Synthesis and Analysis of Metamaterial Structures Considering Arbitrary Resonators and Their Equivalent Circuits

2.1.1 General

A simplified theory for the analysis of any metamaterial structure already proposed in the literature and the synthesis of novel metamaterial structures is reported in this section.

According to this theory, any metamaterial-like properties can be obtained by considering two discrete cases. The first of them refers to the interaction of arbitrary chosen resonators with plane waves, and the second to the electromagnetic behavior of arrays of tightly coupled resonators. Even though the first case (synthesis of metamaterial structures considering interaction of resonators with plane waves) has been well-known for years, it is hereby suggested that this case is only one of the eigen-solutions of the problem of metamaterial synthesis and that the consideration of tightly coupled resonators provides the second eigen-solution of the same problem. This second eigen-solution has been employed extensively in this thesis for the synthesis of novel metamaterial structures and corresponding microwave applications.

2.1.2 Free-Standing Resonators Interacting with Plane Waves

In this section, it is shown how it is possible to obtain several metamaterial-like properties by considering arbitrary chosen resonators interacting with impinging plane waves. This is achieved through the analysis of the equivalent circuits of resonators excited either by the magnetic or the electric component of the impinging plane wave. In practice, it is hard to imagine any resonator that interacts with impinging plane waves purely electrically or purely magnetically, but for the sake of the presentation of the proposed theory, the assumption of the existence of purely electrically or purely magnetically excited resonators is made. Specifically, it is shown that a medium loaded with resonators magnetically interacting with plane waves behaves like an artificial magneto-dielectric, exhibiting either high-μ or negative-μ values. Similarly, it is shown that a medium loaded with resonators electrically interacting with plane waves behaves like an artificial dielectric, exhibiting either high-ϵ or negative-ϵ values. Therefore, by properly combining or configuring these artificial media, all the well-known metamaterial structures can be designed.

Resonators Magnetically Coupled to Plane Waves

Let us consider a free-standing LC resonator and an incident plane wave that magnetically excites the resonator (*i.e.* the magnetic component of the plane wave is aligned with the magnetic moment of the resonator), as in Fig. 2.1. The propagation of the plane wave through the resonator can be modeled using the lumped-element circuit representation of Fig. 2.2(a). Specifically, the propagation characteristics of the plane wave along a distance d of free space are modeled through the distributed inductance

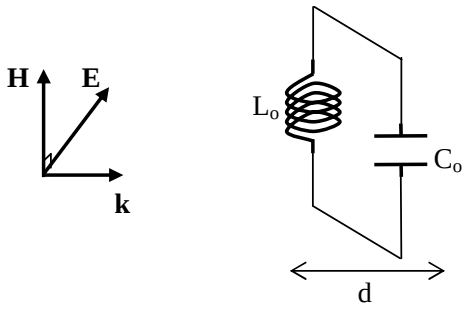

Figure 2.1: Schematic representation of an LC resonator inductively coupled to an impinging plane wave.

$L_d = \mu_o = 4\pi \times 10^{-7}\, H/m$ and the distributed capacitance $C_d = \epsilon_o = 8.854 \times 10^{-12}\, F/m$, resulting in a wave impedance $Z_o = L_d d/C_d d = 120\pi\Omega$ (free space impedance). The presence of the magnetically excited resonator is taken into account through an LC circuit, that is composed of an inductance L_o and capacitance C_o, exhibiting a self-resonance $\omega_o = 1/\sqrt{L_o C_o}$. No losses are assumed at this stage of the analysis. Given that magnetic interaction between the plane wave and the resonator has been considered, the inductor of the resonator L_o is shown to be coupled to the distributed inductance of the hosting medium L_d, exhibiting a coupling coefficient k_M.

The Kirchoff's voltage law applied to the lumped-element circuit of Fig. 2.2(a) reads

$$V_1 - j\omega L_d d I_1 + j\omega L_m I_o - V_2 = 0 \tag{2.1}$$

or, equivalently,

$$V_1 - V_2 = j\omega \left(L_d d I_1 - L_m I_o \right), \tag{2.2}$$

where $L_m = k_M \sqrt{L_d d L_o}$ is the mutual inductance supported between the resonator and the hosting medium. Besides, the Kirchoff's voltage law applied to the resonator of Fig. 2.2(a) gives

$$j\omega L_o I_o - j\omega L_m I_1 + \frac{I_o}{j\omega C_o} = 0 \tag{2.3}$$

Equation (2.2) can be rewritten, using equation (2.3), as

$$V_1 - V_2 = j\omega I_1 \left[L_d d + L_d d \frac{\omega^2 k_M^2 L_o C_o}{1 - \omega^2 L_o C_o} \right]. \tag{2.4}$$

Equation (2.4) suggests that the lumped-element circuit of Fig. 2.2(a) is equivalent with the lumped-element circuit of Fig. 2.2(b), in which the series equivalent inductance

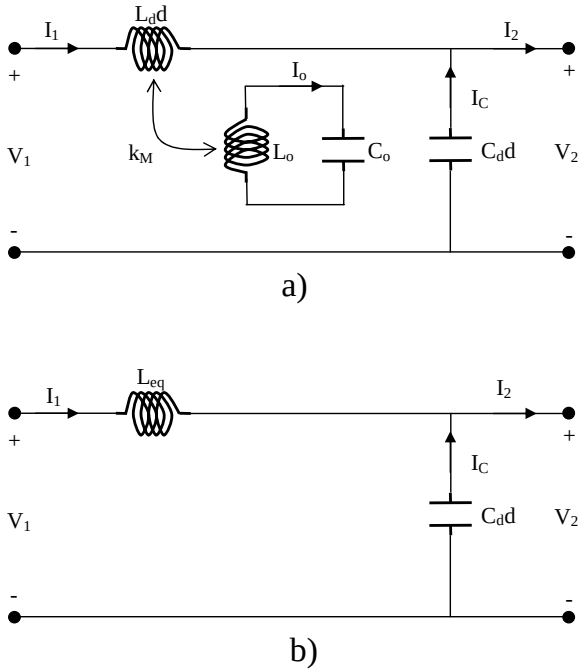

Figure 2.2: a) Lumped-element circuit model for a plane wave magnetically coupled to a free-standing LC resonator. b) Equivalent circuit of the model a).

L_{eq} is given by equation

$$L_{eq} = L_d d \left(1 + k_M^2 \frac{\omega^2 L_o C_o}{1 - \omega^2 L_o C_o}\right) \tag{2.5}$$

The equivalent inductance of equation (2.4) expresses the effective distributed inductance encountered by a plane wave traveling in a medium loaded with resonators that are being excited magnetically. Therefore, the equivalent circuit of Fig. 2.2(b) can be employed for the analysis of this type of loaded medium and the extraction of its effective constitutive parameters or the dispersion diagram of a periodic structure that is composed of unit cells similar with that of Fig. 2.1.

It is well-known that the equivalent circuit of Fig. 2.2(b) models a medium with the effective constitutive parameters:

$$\mu_{eff} = \frac{Z(\omega)/d}{j\omega} \tag{2.6}$$

$$\epsilon_{eff} = \frac{Y(\omega)/d}{j\omega} \tag{2.7}$$

where $Z(\omega)$ and $Y(\omega)$ are the series impedance and the shunt admittance of the equivalent circuit [28]. Hence, equations (2.6) and (2.7), together with equation (2.5), result

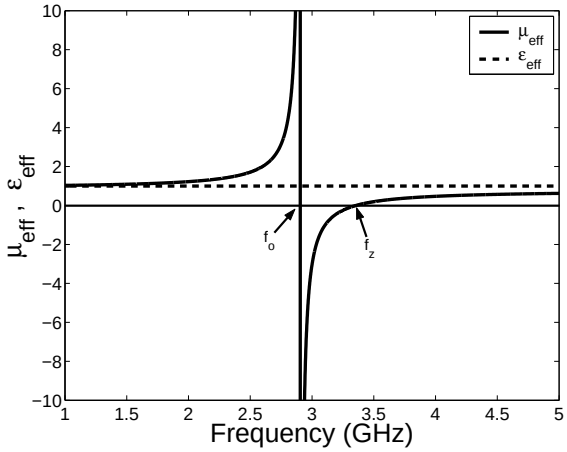

Figure 2.3: Relative effective constitutive parameters when free-space is loaded with inductively excited resonators. The parameters of the resonators are $L_o = 3.0\,nH$, $C_o = 1.0\,pF$, $f_o = 2.906\,GHz$, $k_M = 0.5$ and $d = 3\,mm$

in the following constitutive parameters for a medium loaded with inductively excited resonators

$$\mu_{eff} = \frac{j\omega L_d \left(1 + k_M^2 \frac{\omega^2 L_o C_o}{1-\omega^2 L_o C_o}\right)}{j\omega} \tag{2.8}$$

$$\epsilon_{eff} = \frac{j\omega C_d}{j\omega} \tag{2.9}$$

In the case that the hosting medium is free space,

$$\mu_{eff} = \mu_o \left(1 - k_M^2 \frac{1}{1 - \frac{\omega_o^2}{\omega^2}}\right) \tag{2.10}$$

$$\epsilon_{eff} = \epsilon_o \tag{2.11}$$

Assuming that the parameters of the loading resonators are $L_o = 3.0nH$, $C_o = 1.0pF$ and $f_o = 2.906\,GHz$, and that the coupling between the resonators and the impinging wave is $k_M = 0.5$, the relative effective parameters of equations (2.10) and (2.11) are shown in Fig. 2.3.

As equations (2.10) and (2.11), and Fig. 2.3 suggest the effective electric permittivity of the loaded medium remains constant, as frequency increases, and equal to that of the free space. Therefore, it is concluded that the loading of a medium with inductively excited resonators does not affect its effective electric permittivity. On the other hand, the effective magnetic permeability is significantly affected by the presence of the inductively coupled resonators. Specifically, Fig. 2.3 suggests that the effective permeability

of the loaded medium is increased from the original value of the permeability of the hosting medium, in this case that of free-space ($\mu_{eff} = \mu_o$), to infinity. This maximum value occurs at frequency f_o, which is the self-resonance of the loading resonators. In this bandwidth the structure behaves as a magneto-dielectric or ferromagnetic material, although composed exclusively of non-magnetic structures. From frequency f_o to frequency f_z, given by equation (2.12), the effective permeability of the loaded medium assumes negative values. Given that in this bandwidth the effective electric permittivity of the loaded medium remains positive, the effective refractive index $n_{eff} = \pm\sqrt{\mu_{eff}\epsilon_{eff}}$ becomes imaginary suggesting that the examined medium can not support any propagating wave. Finally, above the frequency f_z the effective permeability of the loaded medium grows from 0 to the the permittivity values of the hosting medium.

$$\omega_z = \frac{\omega_o}{1 - k_M^2} \tag{2.12}$$

All the aforementioned suggestions are also validated through the dispersion analysis of the equivalent circuit of Fig. 2.2(b) that can be performed using the analysis of [2]. The extracted dispersion diagram of the unit cell of Fig. 2.2(b) is presented in Fig. 2.4. This dispersion diagram has been plotted for both positive and negative values of the wavenumber k and suggests that the examined medium exhibits two passbands, with right-handed modes supported in both these passbands (for any mode on any of the curves of the dispersion diagram the corresponding group velocity, calculated as $u_g = \frac{\partial\omega}{\partial k}$, and the phase velocity, calculated as $u_{ph} = \frac{\omega}{k}$, are of the same sign). Specifically, the first right-handed mode extends from dc to the frequency f_o and corresponds to the variation of μ_{eff} from unity to ∞, and the second mode is supported from the frequency f_z and upwards and corresponds to the variation of μ_{eff} from zero to unity. A stopband is being developed within the bandwidth $f_z - f_o$ that is attributed to the effective negative values of the magnetic permeability of the proposed medium.

Resonators Electrically Coupled to Plane Waves

The second major class of artificial materials that are examined are composed of resonators electrically excited by impinging plane waves, resulting in artificial dielectrics. Such a configuration is shown in Fig. 2.5. Similar to the case of the magnetically excited resonators, the effective parameters can be extracted from the analysis of the equivalent circuit of Fig. 2.6(a). In that case the capacitance C_o of the resonator is shown to be coupled to the distributed capacitance of the free space under a coupling coefficient k_E.

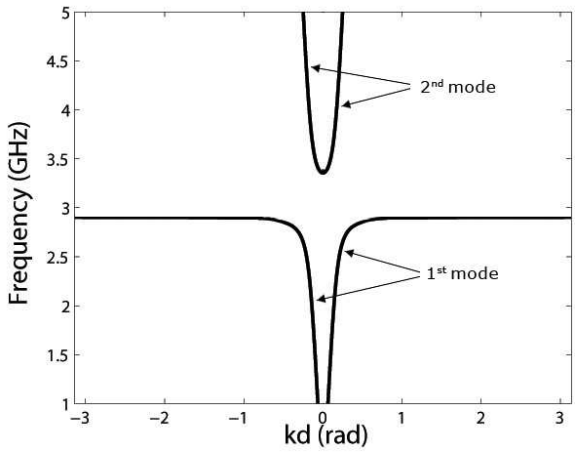

Figure 2.4: Dispersion analysis of the unit cell of Fig. 2.2(b) extracted through the periodic analysis of [2].

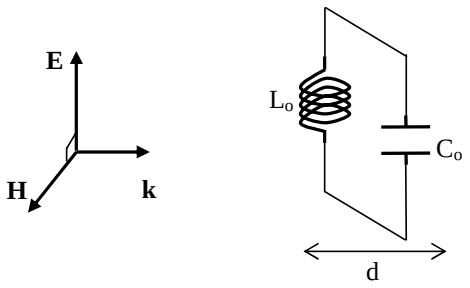

Figure 2.5: Schematic representation of an LC resonator electrically coupled to an impinging plane wave.

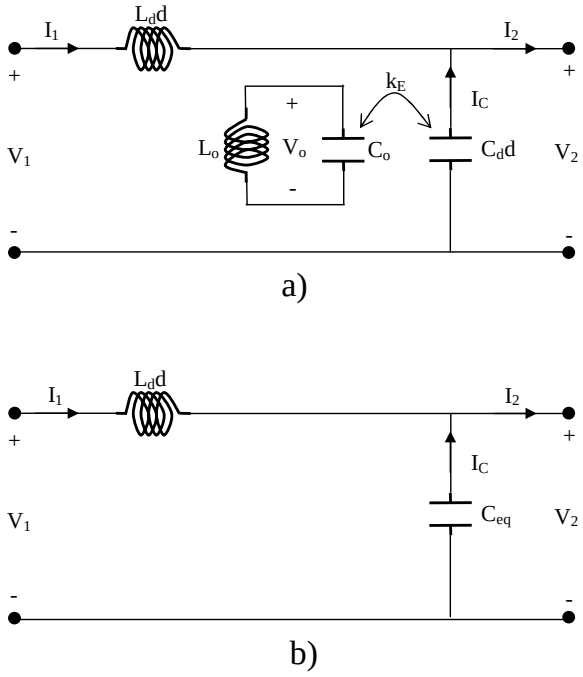

Figure 2.6: a) Lumped-element circuit model for a plane wave electrically coupled to a free-standing LC resonator. b) Equivalent circuit of the model a).

Kirchoff's current law on the hosting transmission line equivalent circuit reads

$$I_1 - I_2 = V_o j\omega C_m - V_2 j\omega C_d d, \tag{2.13}$$

where $C_m = k_E\sqrt{C_d d C_o}$ is the mutual capacitance supported between the resonator and the hosting medium.

Also, Kirchoff's current law on the resonator reads

$$j\omega C_o V_o - j\omega C_m V_2 + \frac{V_o}{j\omega L_o} = 0. \tag{2.14}$$

Equation (2.13) can be rewritten, using equation (2.14), as

$$I_2 - I_1 = j\omega V_2 \left[C_d d + C_d d \frac{\omega^2 k_E^2 L_o C_o}{1 - \omega^2 L_o C_o} \right], \tag{2.15}$$

suggesting that the lumped-element circuit of Fig. 2.6(a) is equivalent with that of Fig. 2.6(b), where the shunt capacitance C_{eq} is given by equation

$$C_{eq} = C_d d \left(1 + k_E^2 \frac{\omega^2 L_o C_o}{1 - \omega^2 L_o C_o} \right). \tag{2.16}$$

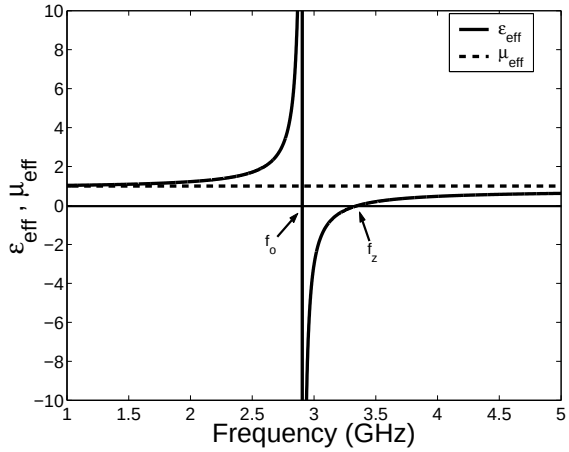

Figure 2.7: Relative effective constitutive parameters when free-space is loaded with capacitively excited resonators. The parameters of the resonators are $L_o = 3.0\,nH$, $C_o = 1.0\,pF$, $f_o = 2.906\,GHz$, $k_E = 0.5$ and $d = 3\,mm$

Similar as before, the effective constitutive parameter of the resulting medium are

$$\mu_{eff} = \frac{j\omega L_d}{j\omega} \tag{2.17}$$

and

$$\epsilon_{eff} = \frac{j\omega C_d \left(1 + k_E^2 \frac{\omega^2 L_o C_o}{1-\omega^2 L_o C_o}\right)}{j\omega} \tag{2.18}$$

In the case that the hosting medium is free space,

$$\mu_{eff} = \mu_o \tag{2.19}$$

$$\epsilon_{eff} = \epsilon_o \left(1 - k_E^2 \frac{1}{1 - \frac{\omega_o^2}{\omega^2}}\right) \tag{2.20}$$

Equations (2.19) and (2.20) have been plotted in Fig. 2.7. The frequency dependence of the effective electric permittivity in that case is identical with that of the magnetic permeability in the case of the magnetically excited resonators. Therefore, it is reasonable to expect that the dispersion analysis of the unit cell of Fig. 2.6 results in the dispersion diagram of Fig. 2.4.

Examples of Resonators

Up to this point, all the considered resonators have been represented through their equivalent circuits and no mention has be made to any specific type of resonators. Nevertheless,

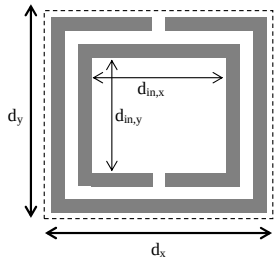

Figure 2.8: The well-known split-ring resonator [3] has been extensively used in the literature for the synthesis of artificial magnetodielectrics.

in practice, not all resonators can be employed to synthesise such artificial media. For example, in the case of magnetically excited resonators, the employed resonators should possess a discrete magnetic moment, so that they can couple effectively to the magnetic component of an impinging wave. Such a resonator is the well known split-ring resonator [3] (shown in Fig. 2.8). The major advantage of this resonator is its compact size that is attributed to the capacitance supported between the two rings. The shape of the resonator also defines the coupling coefficient between itself and the impinging wave. For example, for the split-ring resonator of Fig. 2.8 the coupling coefficient k_M can be approximated as $k_M \approx (d_{in,x} d_{in,y}) \,/\, (d_x d_x)$. Other examples of resonators that can be employed for the synthesis of artificial magneto-dielectrics are several slightly altered versions of the original spit-ring resonator, the swiss-roll resonator, the omega particle, the spiral resonator [52] and others.

In order for a resonator to be electrically excited by impinging plane waves, it should possess a discrete electric moment. Such an example is the dipole resonator of Fig. 2.9. Its use for the synthesis of artificial dielectrics was originally proposed in [9] and in [22] thereafter. For this resonator the coupling coefficient k_E can be approximated as $k_E \approx (d_{met,x} d_{met,x}) \,/\, (d_x d_x)$. Other examples of electrically excited resonators include tripole resonators, square patches and others.

Metamaterial Applications

As shown above, the analysis a medium loaded either with magnetically or electrically excited resonators can provide all the well-known metamaterial-like properties and electromagnetic parameters. For example, given that it has been shown that by loading a medium separately with magnetically and electrically excited resonators it is possible to

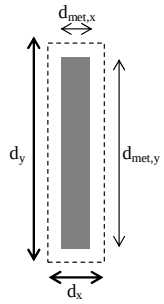

Figure 2.9: The well-known dipole resonator. Arrays of such resonators can be used for the synthesis of artificial dielectrics.

obtain negative values for the effective magnetic permeability and electric permittivity, respectively, for a bandwidth just after the self-resonance of the resonators, it is reasonable to suggest that by loading a medium simultaneously with both electrically and magnetically excited resonators of similar self-resonances, it is possible to achieve a bandwidth at which both the effective magnetic permeability and electric permittivity assume negative values and therefore obtain a left-handed behavior. The equivalent circuit of such a scenario is depicted in Fig. 2.10.

Besides, in both cases of resonators-loaded media, a stopband is created that is attributed to the negative effective μ or ϵ, obtaining an FSS behavior. Also, in the case of the magnetically excited resonators, the exhibited effective permeability values before the self-resonance assume large values even though the loaded medium consists exclusively of non-magnetic materials. Therefore, such a medium can be employed as an artificial magneto-dielectric. Finally, given that the effective impedance of any medium is defined as $Z_{eff} = \sqrt{\mu_{eff}/\epsilon_{eff}}$, it is clear that both media can be employed for the synthesis of High-Impedance Structures or, equivalently, Artificial Magnetic Conductors. For the case of the magnetically excited resonators, this is achieved exactly at or slightly before the resonance, where the effective permeability assumes very large values. For the case of the electrically excited resonators, this is achieved exactly at or slight after the frequency f_z at which the effective permittivity becomes zero.

2.1.3 Arrays of Tightly Coupled Resonators

Up to this point, only interaction of resonators with plane waves has been considered, while any interaction between resonators has been ignored. In this section, the other

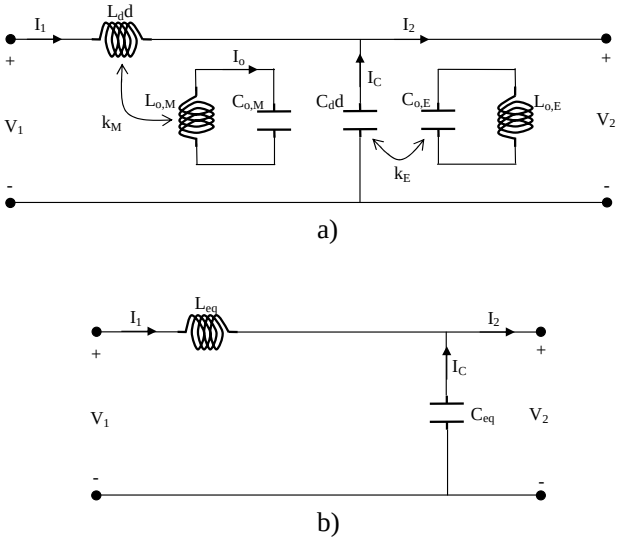

Figure 2.10: Equivalent circuit of a medium loaded with both magnetically and electrically excited resonators. By properly tuning the two resonators, left-handed modes may be supported by the loaded medium.

extreme scenario is considered. Specifically, it is assumed that the wave propagation is achieved exclusively through interacting resonators (tightly coupled resonators), in the absence of free-space propagation. It will be shown that through this approach, a second class of structures with metamaterial-like properties can be formed.

For this purpose, let us assume an infinite array of ideal, lossless $L-C$ resonators with resonant frequency $\omega_o = 1/\sqrt{L_o C_o}$. In the general case, each resonator can be assumed to be both electrically (capacitively) and magnetically (inductively) coupled with its adjacent resonators, as in Fig. 2.11, exhibiting a total coupling coefficient $k = k_E + k_M$, where k_E and k_M are the electric and magnetic coupling coefficients, given by equations (2.21) and (2.22), respectively. In the following text, the two extreme cases, in which the coupling between the resonators is considered either purely electric or purely magnetic, are examined and the traveling waves supported by such arrays are studied.

$$k_E = \frac{\int\int\int \epsilon \vec{E}_1 \cdot \vec{E}_2 dv}{\sqrt{\int\int\int \epsilon \left|\vec{E}_1\right|^2 dv \times \int\int\int \epsilon \left|\vec{E}_2\right|^2 dv}} \tag{2.21}$$

$$k_M = \frac{\int\int\int \mu \vec{H}_1 \cdot \vec{H}_2 dv}{\sqrt{\int\int\int \mu \left|\vec{H}_1\right|^2 dv \times \int\int\int \mu \left|\vec{H}_2\right|^2 dv}} \tag{2.22}$$

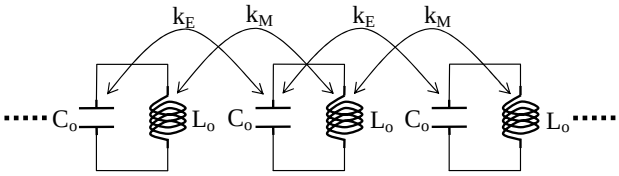

Figure 2.11: An array of tightly coupled resonators. In the general case, the resonators may be both electrically (k_E) and magnetically (k_M) coupled.

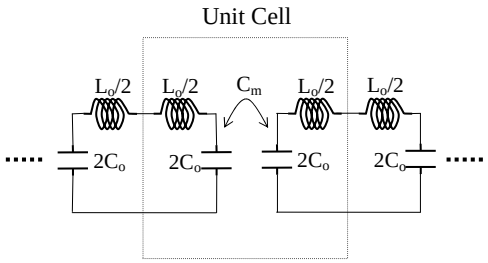

Figure 2.12: A unit cell of the array of Fig. 2.11, where the resonators are considered to be exclusively electrically coupled.

Electrically Coupled Resonators

In the first instance, each resonator of the chain of Fig. 2.11 is assumed to be purely electrically coupled with its adjacent resonators, *i.e.* $k_M = 0$, as shown in Fig. 2.12. In this figure, each resonator has been redrawn as a series connection of two $2C_o$ capacitors and two $L_o/2$ inductors, in order to allow for the better representation of the capacitive coupling between any two adjacent resonators and point out the symmetries in the resulting array. The mutual capacitance supported between the electrically coupled resonators $C_m = k_E 2C_o$ assumes negative values, since the electric coupling coefficient k_E, given by equation (2.21), also assumes negative values. In fact, the sign of k_E is defined by the dot product $\vec{E}_1 \cdot \vec{E}_2$. Due to the existence of electric charges, the aforementioned dot product assumes large negative values if the vectors $\vec{E}_1$ and $\vec{E}_2$ are contra-directional and small positive values if the vectors $\vec{E}_1$ and $\vec{E}_2$ are co-directional (uncoupled resonators).

The unit cell of Fig. 2.12 has been redrawn in Fig. 2.13, where the coupling mechanism is represented with an admittance inverter $J = \omega C_m$. Fig. 2.13 can be employed for the analysis of electrically coupled resonators and the modeling of traveling waves supported by such arrays. For example, the transmission ($ABCD$) matrix of the unit cell can be employed together with $Floquet's$ theorem, in a similar manner as in [96] and

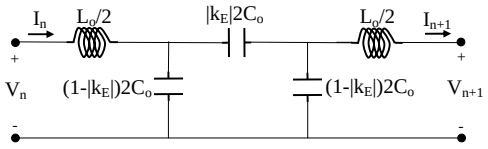

Figure 2.13: Equivalent circuit of the unit cell of Fig. 2.12. The coupling mechanism has been represented with an admittance inverter $J = \omega C_m$

[97], to solve for the complex propagation of the waves supported by infinite arrays of electrically coupled resonators. Specifically, the transmission matrix employed together with the *Floquet's* theorem, as in [96], reads

$$\begin{bmatrix} V_n \\ I_n \end{bmatrix} = \begin{bmatrix} A & B \\ C & D \end{bmatrix}_{UC} \cdot \begin{bmatrix} V_{n+1} \\ I_{n+1} \end{bmatrix} = \begin{bmatrix} V_{n+1}e^{\gamma d} \\ I_{n+1}e^{\gamma d} \end{bmatrix}. \tag{2.23}$$

where $\gamma = \alpha + j\beta$ is the complex propagation constant of the sought traveling waves. For reciprocal unit cells, equation (2.23) leads to nontrivial solutions of the form

$$cosh\,(\gamma d) = \frac{A_{UC} + D_{UC}}{2} \tag{2.24}$$

Calculating the parameters A_{UC} and D_{UC} for the unit cell of Fig. 2.13 and substituting them in equation (2.24) leads to the following dispersion relation for the supported traveling waves:

$$cosh\,(\gamma d) = -\frac{2C_o}{C_m} + \omega^2 \frac{L_o\left((2C_o)^2 - C_m^2\right)}{2C_m} \tag{2.25}$$

Given that $C_m = -\,|k_E|\,(2C_o)$ and $\omega_o = 1/\sqrt{L_o C_o}$, equation (2.25) becomes equivalent to

$$cosh\,(\gamma d) = \frac{1}{|k_E|} - \frac{\omega^2}{\omega_o^2}\frac{1 - |k_E|^2}{|k_E|} \tag{2.26}$$

The dispersion relation of equation (2.26) is exclusively depended on the parameters of each of the resonators and the electric coupling between them. When a purely imaginary propagation constant is assumed, $\gamma = j\beta$, equation (2.26) results in dispersion curves similar with those depicted in Fig. 2.14. These curves correspond to the well-known forward, slow waves, that have been extensively studied in the past in the context of filter design. These slow waves are supported within a bandwidth that is defined by the frequencies f_{lower} and f_{upper} (obtained from equation (2.26) for $\beta d = 0, \pi$ and given in equations (2.27) and (2.28), respectively) and depends on the coupling coefficient k_E, according to equation (2.29).

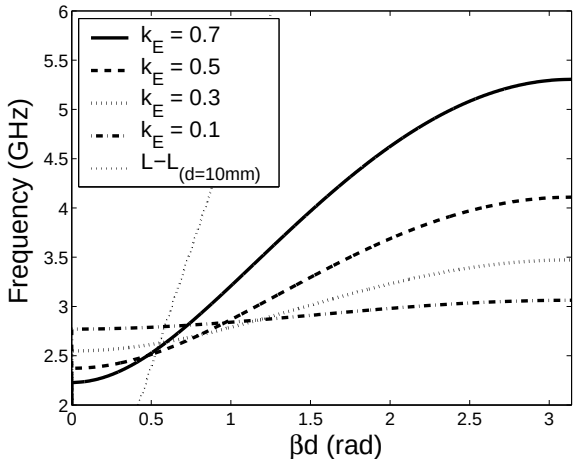

Figure 2.14: Dispersion relation (2.26) for different values of the coupling coefficient $|k_E|$.

$$f_{lower} = f_o \sqrt{\frac{1 - |k_E|}{1 - |k_E|^2}} \tag{2.27}$$

$$f_{upper} = f_o \sqrt{\frac{1 + |k_E|}{1 - |k_E|^2}} \tag{2.28}$$

$$\frac{\Delta f}{f_o} = \frac{\sqrt{1 + |k_E|} - \sqrt{1 - |k_E|}}{\sqrt{1 - |k_E|^2}} \tag{2.29}$$

For $\omega = \omega_o$, the dispersion relation of equation (2.26) is simplified to $cosh\,(\gamma d) = k_E$. Hence, the dispersion equation still depends on the electric coupling between the resonators. This is the reason why the dispersion curves of Fig. 2.14 do not intersect at a certain point. Also, in Fig. 2.14 the dotted curve $L - L$ corresponds to the light-line when periodicity of $d = 10\,mm$ is considered.

Magnetically Coupled Resonators

In this section, the resonators that form the array of Fig. 2.11 are assumed to be exclusively magnetically (inductively) coupled, as shown in Fig. 2.15. It will be shown that this case is much more interesting than the previous one and can lead to much more interesting results. In Fig. 2.15, the $L - C$ resonators have been redrawn as a series connection of two $L_o/2$ inductors and two $2C_o$ capacitors, so as to exhibit the symmetries in the array and show schematically that half of the total inductance of each resonators is coupled to each of the two adjacent resonators. In that case the mutual inductance

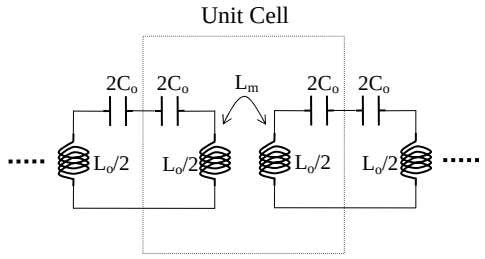

Figure 2.15: $L-C$ resonators array consisted of magnetically coupled resonators.

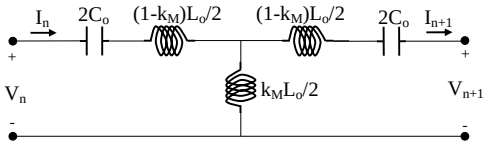

Figure 2.16: Equivalent circuit of the structural unit cell of the magnetically coupled resonators array. In this unit cell the inductive coupling mechanism is represented with an equivalent impedance inverter $K = \omega L_m$.

between any pair of adjacent resonators is $L_m = k_M L_o/2$. The magnetic coupling coefficient k_M, that is given from equation (2.22), assumes both positive and negative values, due to the non-existence of magnetic charges and because of the fact that the magnetic fields appear always with closed magnetic lines.

Careful observation of Fig. 2.15 shows that such an array can be created by the repetition of a structural unit cell that includes the two halves of two adjacent resonators and the coupling mechanism between them. The exact equivalent circuit of this unit cell is dependent by both the sign of the magnetic coupling coefficient and the relative polarity of the coupled inductors. In order, though, to strictly speak about the relative polarity of two inductors and sign of their coupling coefficient the exact topology of the inductors should be known. Therefore, a generic equivalent circuit, identical with that of [32], is employed for the purposes of this analysis. This equivalent circuit cell is shown in Fig. 2.16. In this equivalent circuit of the unit cell, the coupling mechanism is represented by an impedance inverter $K = \omega L_m$, as also suggested in [32].

Using the unit cell of Fig. 2.16 and equations (2.6) and (2.7), it possible to calculate the equivalent effective parameters of an 1-D array composed of inductively coupled resonators. It is pointed out that the extraction of such parameters for a structure that is composed of tightly coupled resonators and the electromagnetic wave propagation is exclusively achieved through these resonators (spatial resonances) is not an absolutely

rigorous way of modeling since the formed arrays do not constitute an actual medium and, therefore, can not be described through its effective parameters. Furthermore, the extraction of the effective parameters for an one-dimensional array can be more effectively substituted by simply carrying out the dispersion analysis of the periodic structure. Nevertheless, the effective parameters of the array of inductively coupled resonators are extracted here in order to point out the nature of the supported propagating waves for different values and signs of the coupling coefficient k_M.

After calculating equations (2.6) and (2.7) for the unit cell of Fig. 2.16, the effective magnetic permeability and the electric permittivity of the considered arrays of inductively coupled resonators are found to be

$$\mu_{eff}(\omega) = -\frac{1-(1-k_M)\frac{\omega^2}{\omega_o^2}}{\omega^2 C_o d} \tag{2.30}$$

$$\epsilon_{eff}(\omega) = -\frac{2}{\omega^2 k_M L_o d} \tag{2.31}$$

where L_o, C_o and ω_o are the self-inductance, self-capacitance and self-resonance of the considered resonators, k_M is the magnetic coupling coefficient, and d is the periodicity of the array. Equations (2.6) and (2.7) suggest that both $\mu_{eff}(\omega)$ and $\epsilon_{eff}(\omega)$ assume negative values when $k_M > 0$ for any frequency smaller than f_{upper}, where f_{upper} is given by equation (2.32). In that case, the supported modes by the examined arrays are expected to be left-handed or, equivalently, backward-waves .

$$f_{upper} = f_o \frac{1}{\sqrt{1-k_M}} \tag{2.32}$$

On the other hand, for negative values of the coupling coefficient ($k_M < 0$), both the effective constitutive parameters assume positive values for any frequency larger than f_{lower}, where f_{lower} is given by equation (2.33). In that case, the corresponding supported modes are right-handed and the corresponding medium can be considered as an artificial magnetodielectric.

$$f_{lower} = f_o \frac{1}{\sqrt{1+k_M}} \tag{2.33}$$

Similar conclusions can be extracted through the dispersion analysis of the unit cell of Fig. 2.16. Specifically, employing equations (2.23) and (2.24) together with the unit cell of Fig. 2.16, similar to the case of the electrically coupled resonators, the dispersion relation for the waves supported by an array of magnetically coupled resonators is found to be

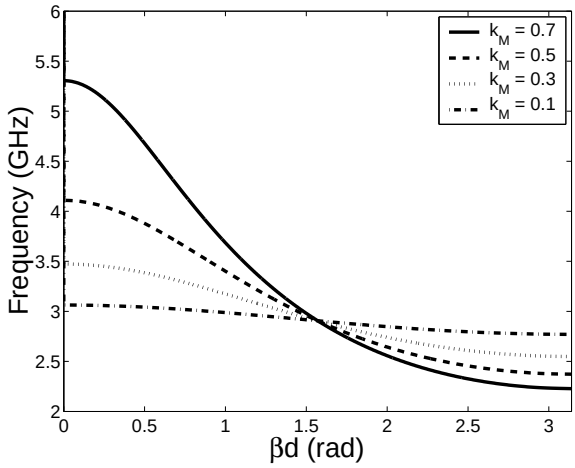

Figure 2.17: Dispersion relation (2.34) for different values of the coupling coefficient $|k_M|$.

$$cosh\,(\gamma d) = \frac{1}{k_M} - \frac{\omega_o^2}{\omega^2}\frac{1}{k_M} \tag{2.34}$$

As with the dispersion relation of the electrically coupled resonators, equation (2.34) depends only on the characteristics of the resonators that comprise the array and the coupling between them. For positive values of the coupling coefficient k_M, the dispersion equation (2.34) has been plotted in Fig. 2.17, where $\gamma = j\beta$. This figure validates that indeed the supported waves by an array of inductively coupled resonators with $k_M > 0$ are backward and the corresponding modes are left-handed.

These modes are supported between the frequencies f_{lower} and f_{upper}, as described above, over a fractional bandwidth that is given by equation (2.35). This equation suggests that the larger k_M is, the larger is the bandwidth of these left-handed modes. For $\omega = \omega_o$, the dispersion relation of equation (2.34) is simplified to $cosh\,(\gamma d) = 0$, hence the dispersion equation does not depend on the magnetic coupling between the resonators. This is the reason why the dispersion curves of Fig. 2.17 intersect at the point $(\pi/2, \omega_o)$ of the dispersion diagram.

$$\frac{\Delta f}{f_o} = \frac{\sqrt{1+k_M} - \sqrt{1-k_M}}{\sqrt{1-k_M^2}} \tag{2.35}$$

Metamaterial Applications

The synthesis of metamaterial structures using tightly coupled resonators has not been extensively described in the literature. For this reason, a portion of this thesis has been dedicated to the development of such structures and corresponding antenna applications.

Nevertheless, there are two types of already reported metamaterial structures that can be assumed to be part of this class of metamaterials. The first type of those is the well-known LC-loaded transmission lines. This type of left-handed media can be considered as arrays of inductively coupled resonators where $k_M = 1$, suggesting a perfect coupling between the resonators [98]. The second refers to the magneto-inductive waves that have been experimentally shown to be supported by arrays composed of large coupled inductive loops [99], [100].

2.1.4 Discussion

In the theory presented in the previous paragraphs, all the possible ways to synthesise any of the well-known metamaterial properties were derived through the consideration of resonators either interacting with impinging plane waves or forming tightly coupled arrays. Therefore, all the up-to-date proposed metamaterial structures should attribute their operation either to one of those cases or to a combination of both. In the framework of this thesis, novel metamaterial structures that rely their operation on the second, least investigated, case will be developed and studied.

2.2 Periodic FDTD Analysis of Metamaterial Structures

The theory presented in the previous section of this chapter offers an analytical tool for the synthesis of any type of metamaterial structure. Nevertheless, it can be employed only as a first step towards the design or the analysis of a metamaterial structure. For a more accurate analysis of these structures, a full-wave tool would be required. Given that metamaterial structures are usually periodic structures, a periodic full-wave computational tool should be employed for the rigorous and computationally efficient modeling of metamaterial structures. For this reason, the development of such a tool was considered extremely important and effort was dedicated to it. Specifically, this tool is a Finite Difference Time-Domain (FDTD) code that terminated the computational domain with periodic boundary conditions. Therefore, by simulating a single unit cell of a periodic structure, the expected response of an infinitely large structure can be obtained. Even though this tool was initially reported in [93], [95], [92], it has been furthered developed and optimized for the needs of this thesis and, also, has been extensively employed for

the analysis of the metamaterial and metamaterial-inspired structures proposed in this thesis. Therefore, the theoretical background of the tool is reported in this chapter for reasons of completeness.

2.2.1 The Finite-Difference Time-Domain Technique

In the FDTD technique, initially proposed by K.S. Yee in 1966 [101], the space for which Maxwell's equations have to be solved is properly discretized and all the related components of the electromagnetic fields are properly located within the formulated mesh. In turn, time-dependent Maxwell's equations, in their differential form, are solved by means of approximative numerical procedures (centered differences), resulting in a time-marching technique that provides with the temporal evolution of the fields within the space under consideration.

Although Yee's algorithm was proposed almost 40 years ago, it was not until the $80's$ that scientists started to further develop it and use it for the modeling of practical applications. This delay was caused by the lack of computational resources by the time that the algorithm was initially proposed; the FDTD technique is a computationally demanding technique (in terms of computational memory and power), as Maxwell's equations are solved for the whole medium under consideration on a rather dense mesh, in order for certain conditions, related with the accuracy of the technique, to be satisfied. Therefore, the development of advanced computational systems was a prerequisite for the further development and the extended use of the technique.

Maxwell's Equations in the FDTD Technique

The centered-difference approximation can be used for the solution of the three-dimensional time-dependent Maxwell's equations, resulting in a fully explicit, time-stepping, algorithm. Time-dependent Maxwell's equations, in their differential form, are those of equations (2.36)-(2.39). Out of these 4 equations, only (2.36)-(2.38) are linearly independent, while equation (2.39) can be derived using the other three.

$$\nabla \times \overline{E} = -\frac{\partial \overline{B}}{\partial t} \tag{2.36}$$

$$\nabla \times \overline{H} = \frac{\partial \overline{D}}{\partial t} + \overline{J}_C \tag{2.37}$$

$$\nabla \cdot \overline{E} = \rho \tag{2.38}$$

$$\nabla \cdot \overline{B} = 0 \tag{2.39}$$

For the needs of the FDTD technique, only equations (2.36) and (2.37) are used, while it can be shown that equation (2.38) is inherently satisfied for a charge free medium [1]. Equations (2.36) and (2.37), together with the constitutive relations $\overline{D} = \epsilon \overline{E}$ and $\overline{B} = \mu \overline{H}$, can be cast, in rectangular coordinates, for a source free and lossless medium, in the form:

$$\frac{\partial}{\partial t} \begin{pmatrix} E_x \\ E_y \\ E_z \end{pmatrix} = \frac{1}{\epsilon} \begin{pmatrix} \frac{\partial H_z}{\partial y} - \frac{\partial H_y}{\partial z} \\ \frac{\partial H_x}{\partial z} - \frac{\partial H_z}{\partial x} \\ \frac{\partial H_y}{\partial x} - \frac{\partial H_x}{\partial y} \end{pmatrix} \tag{2.40}$$

$$\frac{\partial}{\partial t} \begin{pmatrix} H_x \\ H_y \\ H_z \end{pmatrix} = \frac{1}{\mu} \begin{pmatrix} \frac{\partial E_y}{\partial z} - \frac{\partial E_z}{\partial y} \\ \frac{\partial E_z}{\partial x} - \frac{\partial E_x}{\partial z} \\ \frac{\partial E_x}{\partial y} - \frac{\partial E_y}{\partial x} \end{pmatrix} \tag{2.41}$$

Then, the problem of the proper discretization of the field components in the three-dimensional space and time is raised. The best up-to-date solution to this problem has been proposed by K.S. Yee [101]. According to this solution, the spatial discretization of the fields should be done according to Fig. 2.18, where the, so-called, Yee's cell is depicted. The first sign for the validity of this discretization scheme is that on the Yee's cell each electric/magnetic field component is encircled by all the perpendicular to it magnetic/electric, respectively, components, fact that is implied by the Maxwell's integral equations. Therefore, in order to apply the centered-differences approximation for the solution of three-dimensional problems, the space should be discretized using such cubic unit cells, with dimensions $\Delta x \times \Delta y \times \Delta z$, and the field components should be located on each cell as shown in Fig. 2.18 and extensively presented in Table 2.1. As far as the discretization in time is concerned, again it is chosen that electric field components should be sampled at time moments $n\Delta t$ and the magnetic field components at time moments $(n + \frac{1}{2})\Delta t$. Hereafter, the points is space and time at which the derivatives will be approximated have to be properly chosen. As far as the temporal derivatives are concerned, they are calculated at points $(n + \frac{1}{2})\Delta t$ and $n\Delta t$, for the electric and magnetic field components, respectively. The points at which the spatial derivatives are calculated are shown in Table 2.2. Finally, equations (2.40) and (2.41) can be approximated,

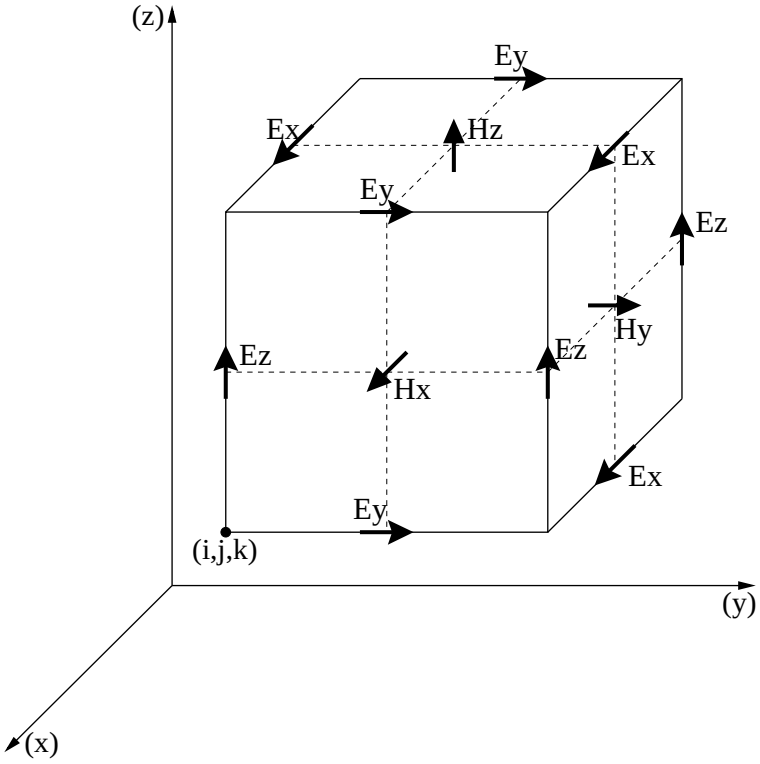

Figure 2.18: Yee's cell.

Field Component	Location on Yee's Space Lattice
E_x	$(i+\frac{1}{2})\Delta x, j\Delta y, k\Delta z$
E_y	$i\Delta x, (j+\frac{1}{2})\Delta y, k\Delta z$
E_z	$i\Delta x, j\Delta y, (k+\frac{1}{2})\Delta z$
H_x	$i\Delta x, (j+\frac{1}{2})\Delta y, (k+\frac{1}{2})\Delta z$
H_y	$(i+\frac{1}{2})\Delta x, j\Delta y, (k+\frac{1}{2})\Delta z$
H_z	$(i+\frac{1}{2})\Delta x, (j+\frac{1}{2})\Delta y, k\Delta z$

Table 2.1: Location of field components on the Yee's space lattice (according to the convention of this thesis).

	$\partial/\partial x$	$\partial/\partial y$	$\partial/\partial z$
E_x		$(i+\frac{1}{2})\Delta x, (y+\frac{1}{2})\Delta y, k\Delta z$	$(i+\frac{1}{2})\Delta x, j\Delta y, (k+\frac{1}{2})\Delta z$
E_y	$(i+\frac{1}{2})\Delta x, (j+\frac{1}{2})\Delta y, k\Delta z$		$i\Delta x, (j+\frac{1}{2})\Delta y, (k+\frac{1}{2})\Delta z$
E_z	$(i+\frac{1}{2})\Delta x, j\Delta y, (k+\frac{1}{2})\Delta z$	$(i+\frac{1}{2})\Delta x, j\Delta y, (k+\frac{1}{2})\Delta z$	
H_x		$i\Delta x, j\Delta y, (k+\frac{1}{2})\Delta z$	$i\Delta x, (j+\frac{1}{2})\Delta y, k\Delta z$
H_y	$i\Delta x, j\Delta y, (k+\frac{1}{2})\Delta z$		$(i+\frac{1}{2})\Delta x, j\Delta y, k\Delta z$
H_z	$i\Delta x, (j+\frac{1}{2})\Delta y, k\Delta z$	$(i+\frac{1}{2})\Delta x, j\Delta y, k\Delta z$	

Table 2.2: Points on the Yee's cell at which the partial spatial derivatives of the field components are calculated (according to the convention of this thesis).

resulting in the following FDTD update equations for the field components:

$$E_x\Big|_{i+\frac{1}{2},j,k}^{n+1} = E_x\Big|_{i+\frac{1}{2},j,k}^{n} + \frac{\Delta t}{\epsilon}\left(\frac{H_z\Big|_{i+\frac{1}{2},j+\frac{1}{2},k}^{n+\frac{1}{2}} - H_z\Big|_{i+\frac{1}{2},j-\frac{1}{2},k}^{n+\frac{1}{2}}}{\Delta y} - \frac{H_y\Big|_{i+\frac{1}{2},j,k+\frac{1}{2}}^{n+\frac{1}{2}} - H_y\Big|_{i+\frac{1}{2},j,k-\frac{1}{2}}^{n+\frac{1}{2}}}{\Delta z}\right) \tag{2.42}$$

$$E_y\Big|_{i,j+\frac{1}{2},k}^{n+1} = E_y\Big|_{i,j+\frac{1}{2},k}^{n} + \frac{\Delta t}{\epsilon}\left(\frac{H_x\Big|_{i,j+\frac{1}{2},k+\frac{1}{2}}^{n+\frac{1}{2}} - H_x\Big|_{i,j+\frac{1}{2},k-\frac{1}{2}}^{n+\frac{1}{2}}}{\Delta z} - \frac{H_z\Big|_{i+\frac{1}{2},j+\frac{1}{2},k}^{n+\frac{1}{2}} - H_z\Big|_{i-\frac{1}{2},j+\frac{1}{2},k}^{n+\frac{1}{2}}}{\Delta x}\right) \tag{2.43}$$

$$E_z\Big|_{i,j,k+\frac{1}{2}}^{n+1} = E_z\Big|_{i,j,k+\frac{1}{2}}^{n} + \frac{\Delta t}{\epsilon}\left(\frac{H_y\Big|_{i+\frac{1}{2},j,k+\frac{1}{2}}^{n+\frac{1}{2}} - H_y\Big|_{i-\frac{1}{2},j,k+\frac{1}{2}}^{n+\frac{1}{2}}}{\Delta x} - \frac{H_x\Big|_{i,j+\frac{1}{2},k+\frac{1}{2}}^{n+\frac{1}{2}} - H_x\Big|_{i,j-\frac{1}{2},k+\frac{1}{2}}^{n+\frac{1}{2}}}{\Delta y}\right) \tag{2.44}$$

$$H_x\Big|_{i,j+\frac{1}{2},k+\frac{1}{2}}^{n+\frac{1}{2}} = H_x\Big|_{i,j+\frac{1}{2},k+\frac{1}{2}}^{n-\frac{1}{2}} + \frac{\Delta t}{\mu}\left(\frac{E_y\Big|_{i,j+\frac{1}{2},k+1}^{n} - E_y\Big|_{i,j+\frac{1}{2},k}^{n}}{\Delta z} - \frac{E_z\Big|_{i,j+1,k+\frac{1}{2}}^{n} - E_z\Big|_{i,j,k+\frac{1}{2}}^{n}}{\Delta y}\right) \tag{2.45}$$

$$H_y\Big|_{i+\frac{1}{2},j,k+\frac{1}{2}}^{n+\frac{1}{2}} = H_y\Big|_{i+\frac{1}{2},j,k+\frac{1}{2}}^{n-\frac{1}{2}} + \frac{\Delta t}{\mu}\left(\frac{E_z\Big|_{i+1,j,k+\frac{1}{2}}^{n} - E_z\Big|_{i,j,k+\frac{1}{2}}^{n}}{\Delta x} - \frac{E_x\Big|_{i+\frac{1}{2},j,k+1}^{n} - E_x\Big|_{i+\frac{1}{2},j,k}^{n}}{\Delta z}\right) \tag{2.46}$$

$$H_z\Big|_{i+\frac{1}{2},j+\frac{1}{2},k}^{n+\frac{1}{2}} = H_z\Big|_{i+\frac{1}{2},j+\frac{1}{2},k}^{n-\frac{1}{2}} + \frac{\Delta t}{\mu}\left(\frac{E_x\Big|_{i+\frac{1}{2},j+1,k}^{n} - E_x\Big|_{i+\frac{1}{2},j,k}^{n}}{\Delta y} - \frac{E_y\Big|_{i+1,j+\frac{1}{2},k}^{n} - E_y\Big|_{i,j+\frac{1}{2},k}^{n}}{\Delta x}\right) \tag{2.47}$$

Up to this point, only isotropic, homogeneous, lossless and source/charge free media have been assumed. However, the FDTD technique is much more general and can be used

for the solution of Maxwell's equations in any kind of medium or topology, by properly adjusting equations (2.42)-(2.47). An extended analysis of how arbitrary media should be treated can be found in [1].

2.2.2 Floquet's Theorem

Floquet's Theorem in Frequency-Domain

The cornerstone of the analysis of any type of periodic structures is Floquet's theorem, named after the French mathematician G. Floquet whose work on periodic coefficients theory [102] inspired the formulation of the theorem. For the purpose of illustration of the theorem, an arbitrary periodic structure is assumed with spatial period d and the axis of periodicity to be along the z-axis. According to Floquet's theorem, if $\tilde{\overline{E}}(x,y,z)$ and $\tilde{\overline{H}}(x,y,z)$ are the phasors of the fields in the unit cell between $0 \leq z \leq d$, then the phasors of the fields in the unit cell located in the region $d \leq z \leq 2d$ should be $e^{-j\gamma d}\tilde{\overline{E}}(x,y,z)$ and $e^{-j\gamma d}\,\tilde{\overline{H}}(x,y,z)$, where γ stands for the complex propagation constant. Consequently, everywhere in the periodic structure, the fields at two different points, being one period apart, are related according to equation set (2.48).

$$\begin{aligned} \tilde{\overline{E}}(x,y,z+d) &= e^{-j\gamma d}\tilde{\overline{E}}(x,y,z) \\ \tilde{\overline{H}}(x,y,z+d) &= e^{-j\gamma d}\tilde{\overline{H}}(x,y,z) \end{aligned} \tag{2.48}$$

Equivalently, the fields everywhere in a periodic structure are given by equation set (2.49),

$$\begin{aligned} \tilde{\overline{E}}(x,y,z) &= e^{-j\gamma z}\tilde{\overline{E}}_p(x,y,z) \\ \tilde{\overline{H}}(x,y,z) &= e^{-j\gamma z}\tilde{\overline{H}}_p(x,y,z) \end{aligned} \tag{2.49}$$

where $\tilde{\overline{E}}_p(x,y,z)$ and $\tilde{\overline{H}}_p(x,y,z)$ are periodic functions of z with period d. These functions can be expanded to the infinite Fourier series of equation set (2.50).

$$\begin{aligned} \tilde{\overline{E}}_p(x,y,z) &= \sum_{n=-\infty}^{\infty} \tilde{\overline{E}}_{pn}(x,y,z)e^{-j\frac{2n\pi}{d}z} \\ \tilde{\overline{H}}_p(x,y,z) &= \sum_{n=-\infty}^{\infty} \tilde{\overline{H}}_{pn}(x,y,z)e^{-j\frac{2n\pi}{d}z} \end{aligned} \tag{2.50}$$

Using (2.49) together with (2.50), the fields anywhere in the periodic structure can

be written as:

$$\begin{aligned} \tilde{\overline{E}}(x,y,z) &= \sum_{n=-\infty}^{\infty} \tilde{\overline{E}}_{pn}(x,y,z)e^{-j\gamma z - j\frac{2n\pi}{d}z} \\ \tilde{\overline{H}}(x,y,z) &= \sum_{n=-\infty}^{\infty} \tilde{\overline{H}}_{pn}(x,y,z)e^{-j\gamma z - j\frac{2n\pi}{d}z} \end{aligned} \tag{2.51}$$

Given that the propagation constant γ can be written as $\gamma = \beta - j\alpha$, where α is the attenuation constant and β the real propagation constant, equation set (2.51) can be rewritten as:

$$\begin{aligned} \tilde{\overline{E}}(x,y,z) &= \sum_{n=-\infty}^{\infty} \tilde{\overline{E}}_{pn}(x,y,z)e^{-\alpha z - j(\beta + \frac{2n\pi}{d})z} \\ \tilde{\overline{H}}(x,y,z) &= \sum_{n=-\infty}^{\infty} \tilde{\overline{H}}_{pn}(x,y,z)e^{-\alpha z - j(\beta + \frac{2n\pi}{d})z} \end{aligned} \tag{2.52}$$

where $\beta_n = \beta + \frac{2n\pi}{d}$ defines all the possibly supported modes (spatial harmonics).

Floquet's Theorem in Time-Domain

Floquet's theorem in the form of equation set (2.48) involves the phasors of the fields (frequency-domain analysis). In order for this theorem to be applied to a time-domain analysis, it has to be properly expressed in terms of the actual time-varying fields.

In the case of a lossless medium ($\alpha = 0$), Floquet's theorem suggests that the fields at two points, that are one period apart, differ only by the phase factor $e^{-\beta d}$. This phase corresponds to the phase added to a wave after traveling distance d. The proper interpretation of this statement in time-domain implies that the actual fields, at those two points, are identical at two time moments which differ by the time interval τ_d needed for the wave to travel from the first point to the other (equation set (2.53)).

$$\begin{aligned} \overline{E}(x,y,z,t) &= \overline{E}(x,y,z+d,t+\tau_d) \\ \overline{H}(x,y,z+d,t) &= \overline{H}(x,y,z,t-\tau_d) \end{aligned} \tag{2.53}$$

According to equation set (2.53), Floquet's theorem in time-domain involves both previous as well as future snapshots of the fields. The time difference between these snapshots is dependent on the periodicity of the structure and the phase velocity of the waves in the medium under consideration, and usually is unknown. This interpretation of Floquet's theorem suggests that the theorem cannot be used directly in any kind of time-marching algorithm, as the knowledge of future snapshots of the fields is impossible.

FDTD with Periodic Boundary Conditions	
Direct Field Methods	Field Transformation Methods
Normal Incidence Method	Multi-Spatial Grid
Sine-Cosine Method	Split-Field
Multiple Unit Cell Methods	
Angled Update Method	

Table 2.3: Methods that have been proposed for the application of periodic boundary conditions in time-domain [1].

2.2.3 Periodic Boundary Conditions in the FDTD Technique

General

Floquet's theorem in the time-domain, as expressed in equation (2.53), can not be used directly within the FDTD technique, given that this would require the knowledge of future snapshots of the fields. On the other hand, the existence of several electromagnetic applications which involve periodic structures and the intense interest for the time-domain modeling of these structures have motivated researchers to develop techniques that would overcome this inherent difficulty and allow for the use of Floquet's theorem in time-domain analyses. Some of the techniques that have been developed in order to apply periodic boundary conditions in time-domain are shown in Table 2.2.3. The techniques listed on the right side of Table 2.2.3 are based on a field transformation, used to overcome the need for time-advanced data, while those listed on the left side provide ways of directly solving equations (2.42)-(2.47).

Out of these techniques, the one that seems to be more promising for the needs and the purposes of this thesis is the, so-called, sine-cosine method. This method will be extensively presented in the next section, while further details about all the other techniques can be found in [1].

Sine-Cosine Method

The sine-cosine method was initially proposed by Harms *et al.* [103]. In this method, a transformation of the Floquet's theorem is used to overcome the problem of applying the periodic boundary conditions in time-domain. For the purpose of illustrating the method, let us assume an arbitrary two-dimensional periodic structure with a direct lattice vector

$\overline{p} = d_x\hat{x} + d_y\hat{y}$ and reciprocal lattice wave vector $\overline{k} = k_x\hat{x} + k_y\hat{y}$. In that case, Floquet's theorem of equation (2.48) (expressed in frequency-domain), for a point of the structure $\overline{r}$, can be written as follows:

$$\tilde{\overline{E}}(\overline{r}) = \tilde{\overline{E}}(\overline{r} + \overline{p})e^{+j\overline{k}\cdot\overline{p}} \tag{2.54}$$

$$\tilde{\overline{H}}(\overline{r} + \overline{p}) = \tilde{\overline{H}}(\overline{r})e^{-j\overline{k}\cdot\overline{p}} \tag{2.55}$$

Assuming that the wave vector $\overline{k} = k_x\hat{x} + k_y\hat{y}$ corresponds to a wave of frequency ω, equations (2.54) and (2.55) are equivalent with (2.56) and (2.57), respectively.

$$\tilde{\overline{E}}(\overline{r})e^{j\omega t} = \tilde{\overline{E}}(\overline{r} + \overline{p})e^{+j\overline{k}\cdot\overline{p}}e^{j\omega t} \tag{2.56}$$

$$\tilde{\overline{H}}(\overline{r} + \overline{p})e^{j\omega t} = \tilde{\overline{H}}(\overline{r})e^{-j\overline{k}\cdot\overline{p}}e^{j\omega t} \tag{2.57}$$

Expanding all the exponential factors of equations (2.56) and (2.57), using Euler's relation, and carrying out some basic algebraic manipulations, equation (2.56) becomes equivalent with equation set (2.58), while equation (2.57) is equivalent to the equation set (2.59):

$$\begin{aligned} \overline{E}_{cos}(\overline{r}, t) &= \overline{E}_{cos}(\overline{r} + \overline{p}, t)cos(\overline{k}\cdot\overline{p}) - \overline{E}_{sin}(\overline{r} + \overline{p}, t)sin(\overline{k}\cdot\overline{p}) \\ \overline{E}_{sin}(\overline{r}, t) &= \overline{E}_{sin}(\overline{r} + \overline{p}, t)cos(\overline{k}\cdot\overline{p}) + \overline{E}_{cos}(\overline{r} + \overline{p}, t)sin(\overline{k}\cdot\overline{p}) \end{aligned} \tag{2.58}$$

$$\begin{aligned} \overline{H}_{cos}(\overline{r} + \overline{p}, t) &= \overline{H}_{cos}(\overline{r}, t)cos(\overline{k}\cdot\overline{p}) + \overline{H}_{sin}(\overline{r}, t)sin(\overline{k}\cdot\overline{p}) \\ \overline{H}_{sin}(\overline{r} + \overline{p}, t) &= \overline{H}_{sin}(\overline{r}, t)cos(\overline{k}\cdot\overline{p}) - \overline{H}_{cos}(\overline{r}, t)sin(\overline{k}\cdot\overline{p}) \end{aligned} \tag{2.59}$$

In equation sets (2.58) and (2.59), $\overline{E}_{cos}(\overline{r}, t)$ and $\overline{H}_{cos}(\overline{r}, t)$ stand for the actual time-varying electric and magnetic fields that possess cosinusoidal time variation[1], while $\overline{E}_{sin}(\overline{r}, t)$ and $\overline{H}_{sin}(\overline{r}, t)$ stand for time-varying electric and magnetic fields that possess sinusoidal time variation[2].

Using this transformation, equation sets (2.58) and (2.59), which are equivalent to Floquet's theorem of equation (2.48) and its expression in time-domain (equation (2.53)), are extracted. These equations involve field values which refer exclusively to the same snapshot. This fact enables the use of periodic boundary conditions, through equation sets (2.58) and (2.59), within the FDTD technique and the time-domain modeling of periodic structures.

[1] $\overline{E}_{cos}(\overline{r}, t) = \tilde{\overline{E}}(\overline{r}) \cdot cos(\omega t)$ and $\overline{H}_{cos}(\overline{r}, t) = \tilde{\overline{H}}(\overline{r}) \cdot cos(\omega t)$

[2] $\overline{E}_{sin}(\overline{r}, t) = \tilde{\overline{E}}(\overline{r}) \cdot sin(\omega t)$ and $\overline{H}_{sin}(\overline{r}, t) = \tilde{\overline{H}}(\overline{r}) \cdot sin(\omega t)$

Sine-Cosine Method in Practice

In order to illustrate how periodic boundary conditions, through the sine-cosine method, are applied in practice within the FDTD algorithm, the computational domain of Fig. 2.19 is used. This computational domain can be employed for the modeling of a two-dimensional periodic structure of a direct lattice vector $\overline{p} = d_x\hat{x} + d_y\hat{y}$. In the following, without loss of generality, only TM waves are assumed and, therefore, only the E_x, E_y and H_z field components are shown on the computational domain of Fig. 2.19. This analysis can be easily extended to full three-dimensional cases.

The computational domain of Fig. 2.19 is composed of two grids; the first for the electric field components (solid line) and the second for the magnetic field components (dashed line). The dimensions and the location of the electric grid are identical with the dimensions and the location of the actual physical structure, while the magnetic grid is half Yee's cell offset with respect to the electric grid. The location of all the field components has been chosen in accordance with Table 2.1.

When the computational domain is terminated with periodic boundary conditions, enforced through the sine-cosine method, the dimensions of the electric and the magnetic grids have to be identical. In that occasion, the exterior field components of the computational domain are always the electric field components, resulting in a electric grid which is larger, by one Yee's cell, than the magnetic grid.

As mentioned in section 2.2.1, the core of the FDTD algorithm is the update equations (2.42)-(2.47). For those equations to be solved, each electric/magnetic field component should be encircled by all the perpendicular to it magnetic/electric, respectively, field components. Going back to the computational domain of Fig. 2.19, it is easy to observe that the majority of the electric/magnetic field components are encircled by the proper magnetic/electric field components, so that they can be updated by FDTD equations. At the same time, this is not the case for certain arrays of grid points. These are the array of E_x components along the line $y = y_o$, the array of E_y components along the line $x = x_o$, the array of H_z components along the line $y = y_o + d_y + \Delta y/2$ and the array of H_z components along the line $x = x_o + d_x + \Delta x/2$, as shown in Fig. 2.19. Each of these arrays is on each of the four exterior boundaries of the rectangular computational domain. Besides, for all these four grid points arrays, there is the corresponding, parallel to each of them, array, which is exactly one spatial period (d_x or d_y) apart. The elements of the latter grid points arrays can be calculated through Maxwell's update equations, as

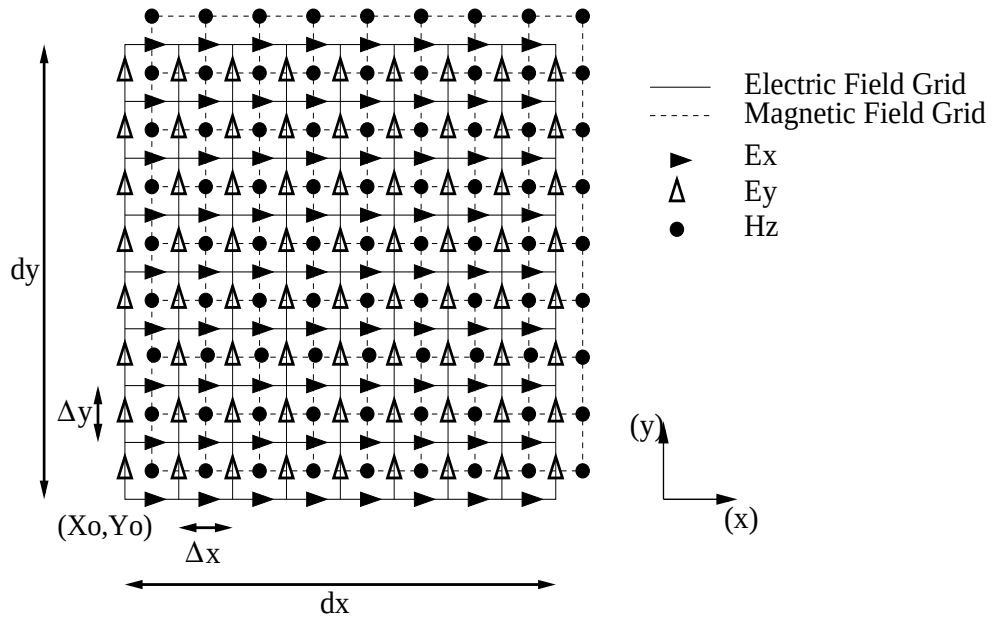

Figure 2.19: Computational domain used for the FDTD analysis of a two-dimensional periodic structure (only TM modes are assumed).

they are composed of field elements that are encircled by the proper field components. Therefore, it is reasonable to suggest that the elements of each array of the first category should be updated through the periodic boundary conditions and the use of the field elements of the arrays of the second category. The pairs of the arrays of field components, that are updated through the periodic boundary conditions, are summarized in Table 2.4.

After exhibiting how the periodic boundary conditions are applied in space, it remains to be explained how they will be applied within a time-marching technique. Equation sets (2.58) and (2.59) involve field snapshots with sinusoidal and cosinusoidal time variation. Given that a single computational domain could be either exclusively sinusoidally or cosinusoidally time-varying, it is suggested that *two* identical computational domains (e.g. this of Fig. 2.19) should be used for the simulation of a single structure. In the first one, all the field components will be characterized by a sinusoidal time variation (sine computational domain) and in the second, all the field components will be characterized by a cosinusoidal time variation (cosine computational domain). These two computational domains simulate the same structure, for the wave vector $\overline{k} = k_x\hat{x} + k_y\hat{y}$, that is involved in equation sets 2.58) and (2.59), and run in parallel. The only difference

Array of field components updated using Maxwell's Equations	Array of field components updated using Periodic Boundary Conditions
E_x at $y = y_o + d_y$	E_x at $y = y_o$
E_y at $x = x_o + d_x$	E_y at $x = x_o$
H_z at $y = y_o + \Delta y/2$	H_z at $y = y_o + d_y + \Delta y/2$
H_z at $x = x_o + \Delta x/2$	H_z at $x = x_o + d_x + \Delta x/2$

Table 2.4: Pairs of field elements arrays of the computational domain of Fig. 2.19 that are involved in the application of the periodic boundary conditions.

of these domains is that the excitation of the first is sinusoidally modulated, while the excitation of the second is cosinusoidally modulated. These two domains interact only when the periodic boundary conditions of equation sets (2.58) and (2.59) have to be calculated. It has to be pointed out that, although, these two domains run in parallel and interact only for the calculation of the periodic boundary conditions, none of them can produce correct results independently. The whole algorithm for the use of periodic boundary conditions, through sine-cosine method, in the FDTD technique is shown in the flow chart of Fig. 2.20.

At this point, the key role of the reciprocal lattice wave vector $\overline{k} = k_x\hat{x} + k_y\hat{y}$, which is involved in equation sets (2.58) and (2.59), should be explicitly discussed. As shown in the flow chart of Fig. 2.20, the first step of any simulation that involves periodic boundary conditions, through the sine-cosine method, is the enforcement of a certain value for this reciprocal lattice wave vector $\overline{k}$, both in the sine and the cosine computational domains. The knowledge of the value of this wave number is a prerequisite for the use of the algorithm. Therefore, the algorithm calculates the time-domain response of a periodic medium that corresponds to a certain lattice wave number. This fact imposes a certain limitation to this type of analysis; each time it is applied to a structure, it solves only for the waves that correspond to the enforced reciprocal lattice wave vector. Therefore, in the case that a periodic structure has to be solved for a certain range of wave vectors, the simulation has to be repeated for all the possible values of the wave vector. The impact of this limitation to the proposed methodology is reduced by L. Brillouin's work on periodic structures [104]. According to this work, for a periodic structure that is described by a lattice vector $\overline{p} = d_x\hat{x} + d_y\hat{y}$, where $d_x = d_y$ (square unit cell), all the supported modes are characterized by a wave vector $\overline{k} = k_x\hat{x} + k_y\hat{y}$ that assumes a limited

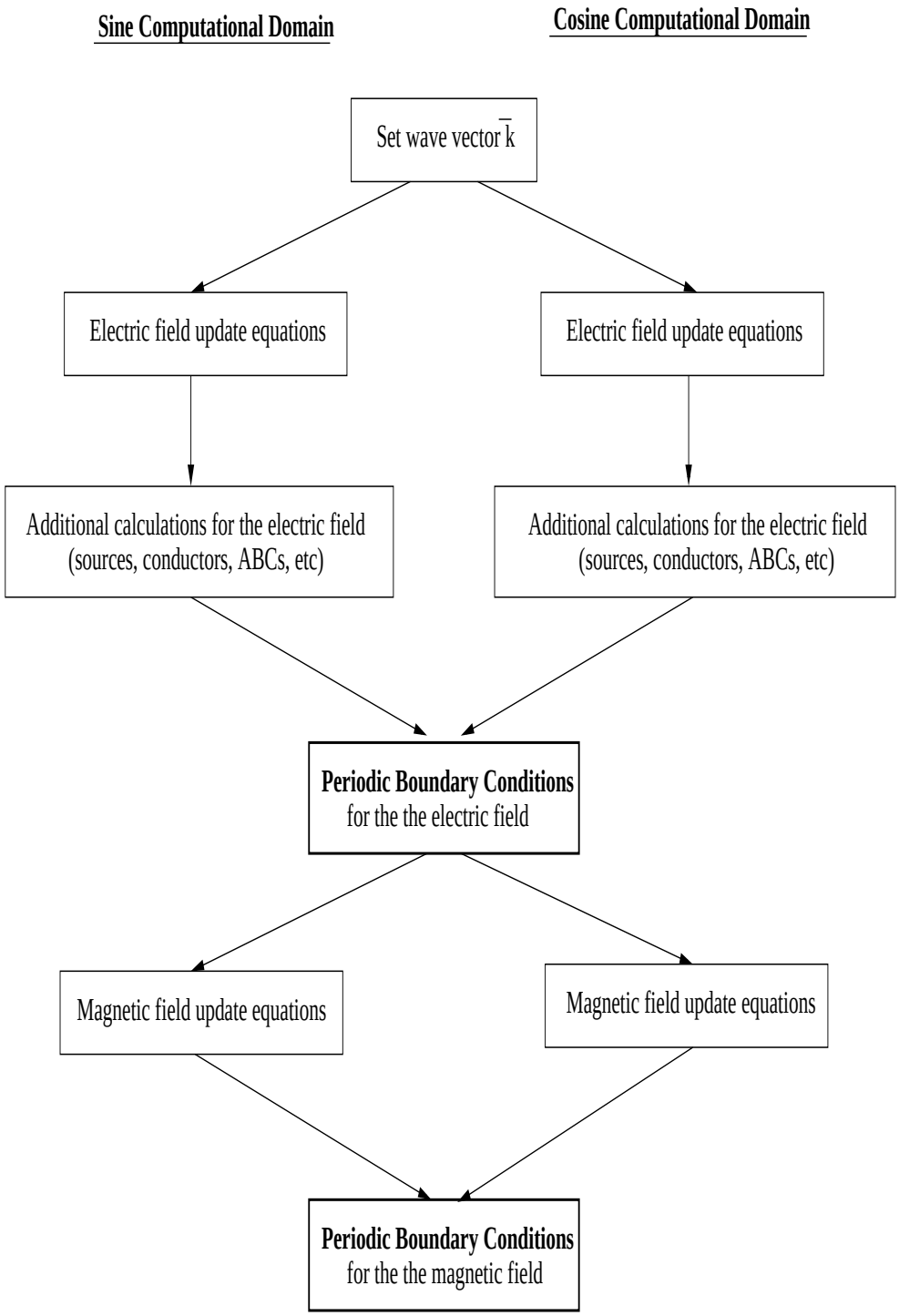

Figure 2.20: Flow chart of the algorithm that is used for the application of periodic boundary conditions, through the sine-cosine method, in the FDTD technique.

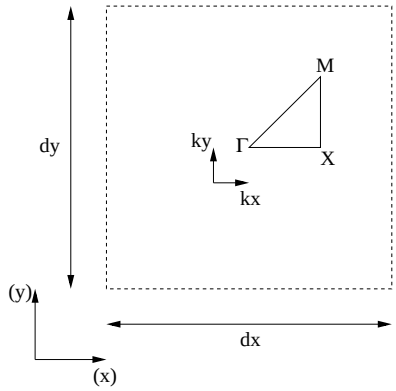

Figure 2.21: Square unit cell (dashed line) and its reciprocal irreducible Brillouin zone (solid line).

number of values. These values belong to the reciprocal irreducible Brillouin zone on the $k-$space. For the case of a two-dimensional periodic structure with square unit cell, the irreducible Brillouin zone is the triangle ΓXM on the $k-$space of Fig. 2.21, where Γ corresponds to the point $(k_x, k_y) = (0, 0)$, X corresponds to the point $(k_x, k_y) = (\pi, 0)$ and M corresponds to the point $(k_x, k_y) = (\pi, \pi)$.

To conclude this discussion about the way sine-cosine method is applied in practice, a last comment should be made about the broadband character of the FDTD technique and whether or not it is affected by the fact that equations (2.56) and (2.57) refer to monochromatic waves. It has to be pointed out that the periodic boundary conditions of (2.58) and (2.59) do not affect the broadband characteristics of FDTD. Using arguments related to Fourier analysis, it can be shown that an analysis that employs equation sets (2.58) and (2.59) can provide simultaneously with all the supported frequencies (modes) that correspond to the enforced reciprocal lattice wave vector $\overline{k} = k_x\hat{x} + k_y\hat{y}$. This statement is also supported in [105].

2.2.4 Applications of the Periodic FDTD-based Tool

Dispersion Analysis of Periodic Structures

The first type of analysis that can be performed using the proposed computational tool is the dispersion analysis of any type of periodic/metamaterial structure. In order for such an analysis to be carried out successfully, all the modes that can be supported by the

structure, for all the wave vectors $\overline{k} = k_x\hat{x} + k_y\hat{y}$ of the reciprocal irreducible Brillouin zone on the k-space of Fig. (2.21), have to be detected. This is achieved by enforcing the aforementioned wave vectors through the periodic boundary conditions and, in turn, by detecting all the supported resonances through the spectral analysis of the extracted time-domain responses of the simulated unit cell.

Modal Field Patterns Extraction

Apart from the calculation of the dispersion equations and diagrams of periodic structures, the proposed methodology can be directly applied to the extraction of the modal field patterns of the supported modes. These field patterns are calculated from the Fourier transform of the field components within the FDTD computational domain, iteratively applied on their time samples. In particular, the Fourier transform of the electric field is evaluated at a known frequency ω as in equation (2.60),

$$\widetilde{\overline{E}}\left(\overline{r}_{i,j,k},\omega\right) \approx \sum_{n=1}^{N_{tot}} \overline{E}\left(\overline{r}_{i,j,k}, n\Delta t\right) \times \exp(-j\omega n\ \Delta t) \tag{2.60}$$

where $\overline{r}_{i,j,k} = \hat{x}\, i\Delta x + \hat{y}\, j\Delta y + \hat{z}\, k\Delta z$ is the position vector of a FDTD grid point, N the number of time-steps, counted after the excitation has faded away, used for the Fourier transform, and $\overline{E}\left(\overline{r}_{i,j,k}, n\Delta t\right) = \overline{E}_{cos}\left(\overline{r}_{i,j,k}, n\Delta t\right) + j\overline{E}_{sin}\left(\overline{r}_{i,j,k}, n\Delta t\right)$.

Analysis of Leaky-Wave Structures

Finally, the proposed methodology can be employed for the analysis of leaky-wave structures and the calculation of the complex wave numbers of leaky-waves. The details of this type of analysis will be presented in details in chapter 6 of this thesis, where this methodology is developed, optimized and employed for the analysis of several leaky-wave structures.

2.3 Commercial Electromagnetic Solvers

2.3.1 General

The theory for the synthesis of metamaterial structures considering coupled resonators and the developed periodic FDTD numerical tool have been extensively used throughout this thesis, mostly during the initial stages of the analysis and design of novel periodic

structures and devices. Nevertheless, many additional commercially available numerical tools were used for the complete and inclusive characterization of the developed finite-size structures. These tools are briefly presented in the following text for reasons of completeness of this theoretical chapter.

2.3.2 Ansoft HFSS

Ansoft HFSS used to be for years the most popular, commercially available, 3-D full-wave electromagnetic solver. It employs the finite-element-method (FEM) for the solution of Maxwell's equation in frequency domain. Ansoft HFSS offers a stable, rigorous, frequency-domain electromagnetic solver that can be effectively employed for the computationally efficient analysis of complicated structures. It's comparative advantages are becoming critical when referring to highly resonant structures, such as filters or metamaterial structures, while its weak points are becoming dominant when referring to the analysis of broadband structures (frequency sweeping is required for any broadband analysis). Ansoft HFSS was one of the first commercially available full-wave tools to support periodic boundary conditions and a periodic (eigenmode) solver. For this reason, HFSS was used for the validation of the developed periodic FDTD-based tool.

2.3.3 Ansoft Designer

Ansoft Designer is a 2.5-D, method-of-moment (MOM) based electromagnetic tool, capable of solving Maxwell's equations in planar electromagnetic structures. Its use becomes efficient, in terms of the required computational resources and time, when referring to planar electromagetic structures, such as microstrip-based microwave circuits and antennas. Ansoft Designer also includes a circuit simulator that was used for the circuit simulations that were required for needs of this thesis.

2.3.4 CST Microwave Studio

CST Microwave Studio (CST MWS) is a relatively new commercial, 3-D full-wave, numerical tool. In its present form, it integrates three different electromagnetic solvers; a finite-integral time-domain solver, a finite-element frequency-domain solver and a transmission-line-matrix (TLM) time-domain solver (prior Microstripes solver). The first solver to be included in CST Microwave Studio was the finite-integral time-domain solver. This solver

employs sophisticated, non-orthogonal discretization (meshing) schemes, that allow the tool to efficiently and rigorously model complicated structures. CST Microwave Studio offers an extremely convenient and robust graphical user interface that allows for the accurate and fast insertion of complicated electromagnetic models. Being a time-domain solver, allows for the broadband analysis of the structures under investigation, while it becomes inefficient (time-consuming) for highly resonant structures. Nevertheless, for the analysis of such highly resonant structures, the available frequency-domain solver may be used. Conclusively, CST Microwave Studio constitutes a robust, rigorous and efficient computational electromagnetic tool that can be employed for the analysis of almost any type of electromagnetic problems. This feature together with its excellent graphical user interface justifies the impressive spread of its use among microwave engineers during the recent years.

Chapter 3

Spiral-based Artificial Transmission Lines and Applications

In this chapter, a novel class of uniplanar, fully-printed, microstrip-based artificial lines supporting backward waves is reported. The synthesis of these lines has been based on the theory of section 2.1.3 for the synthesis of arrays supporting left-handed modes considering exclusively inductively tightly coupled resonators. The resonators employed for the synthesis of the proposed artificial lines are compact, symmetrical, microstrip-based, fully-printed resonators that possess well-defined inductive characteristics and, therefore, tend to couple inductively to similar adjacent resonators. These resonators are explicitly described and modeled in the first section of the chapter. In turn, these resonators are properly arranged in arrays that support backward waves. Such arrays are built, measured and characterized at microwave frequencies. Finally, these artificial lines are employed in the design of series-fed microstrip patch arrays.

3.1 Review of Artificial Transmission Lines

Artificial transmission lines are any engineered transmission lines that apart from the traditional parameters of conventional transmission lines (characteristic impedance, phase velocity, time delay) also possess additional features that make them attractive for certain microwave applications. One of the most popular classes of artificial transmission lines are the so-called slow-wave transmission lines [32], that exhibit effective refractive indexes smaller than the unity. In the context of metamaterials and LHM, the first class of artificial transmission lines was proposed by G.V. Eleftheriades *et. al* [28] and C.

Caloz *et. al* [30]. These artificial transmission lines are synthesized by periodically loading conventional transmission lines with series capacitances and shunt inductances, and exhibit dispersive properties for their effective index of refraction and their characteristic impedance. Following the original implementation of these lines, several alternative implementations have been proposed in the literature (*e.g.* [86], [87], [81]).

3.2 Double Spiral Resonators

3.2.1 Description

The fundamental resonator employed in this chapter for the synthesis of the artificial, fully-printed, microstrip-based left-handed lines is the, so-called, double spiral resonator (DSR), shown in Fig. 3.1. It is composed of two single spirals that are connected in series and printed on a grounded dielectric substrate (microstrip-like configuration). This structure can be assumed to be an alteration of the well-known open-loop resonator (Fig. 3.2), or even the split-ring resonator, towards the direction of enhancing its inductive components and further minimizing its total size. In its final version, the DSR can be considered to be composed of two single spirals connected in series. The main reasons why the DSR has been chosen, in the framework of this project, are its symmetric properties and the fact that it possesses two discrete and spatially separated magnetic moments that could be separately coupled to adjacent elements. Even though DSR is not the most compact resonant element that has been proposed so far in the literature (for example, the SRR is more compact), for the purposes of this work, these two features are of much higher importance.

The structure of Fig. 3.1 is an extremely interesting element that could be exploited both for its inductive and capacitive properties. Therefore, the study of its electromagnetic properties in several different configurations (backed on several types of substrates, free standing in the air and others), in accordance with the theory of section 2.1, could potentially lead to several different metamaterial applications, such as the design of magneto-dielectrics, EBG structures, LHM, AMC and others. Nevertheless, in the framework of this thesis, the DSR will be studied exclusive for the case in which they form arrays of tightly coupled resonators. Furthermore, as far as this chapter of the thesis is concerned, DSR will be considered exclusively backed on grounded dielectric substrates (microstrip-like configuration), forming transmission lines that support backward waves.

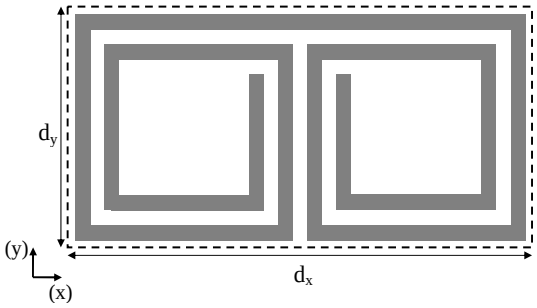

Figure 3.1: Schematic of a double spiral resonator. In our approach, the spiral is to be printed on a grounded substrate. The figure should be also assumed to be the computational domain of the full-wave periodic analysis.

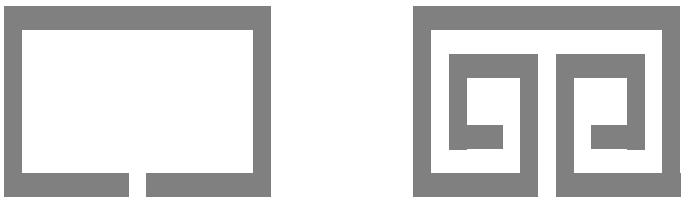

Figure 3.2: a) Open-loop resonator. b) Double spiral can be formed by wounding the open ends of the open-loop resonator.

3.2.2 Periodic Analysis

As it has been already mentioned in the introduction of the thesis, metamaterials are periodic structures whose properties are partially attributed to their periodic nature. Therefore, a periodic analysis of the structural unit cell under consideration should be always considered as the first step in their analysis. In the following, the double spiral of Fig. 3.1, backed on a grounded dielectric substrate, will be treated as the structural unit cell of two-dimensional arrays. The periodicity of these arrays is assumed to be $d_x = 6.4\,mm$ and $d_y = 3.2\,mm$, along $x-$ and $y-$axis, respectively, both the strips width and the gaps width are $s = w = 0.2\,mm$, while the arrays are built on a substrate of dielectric constant $\epsilon_r = 2.2$ and height $h = 1.15\,mm$.

Dispersion Analysis

In order to calculate the modes supported by an array of DSR, the unit cell is analysed using full-wave simulations with the computational domain being terminated with periodic boundary conditions. In turn, the frequencies of all the supported modes are estimated in terms of the phase shift per unit cell of all the Bloch wave-vectors being within the irreducible Brillouin zone. For the DSR of Fig. 3.1, the calculated dispersion diagram is shown in Fig. 3.3. These results were extracted using the periodic FDTD tool presented in section 2.2 and validated (at several points) using Ansoft HFSS.

The results of the dispersion analysis of the DSR show that the first (fundamental) mode supported by the proposed structure is a backward wave since the corresponding phase and group velocities are anti-parallel. The formulated passband in which the two-dimensional structure supports backwards waves extends from approximately $2.5\,GHz$ to $4\,GHz$. Specifically for the case that 1-D propagation along $x-$axis is assumed, the bandwidth over which backward waves are supported extends from $3.3\,GHz$ to $3.9\,GHz$, a fractional bandwidth of $FGW = 17\,\%$. At these frequencies, the total length $\ell_{DblSpiral}$ of the turns of the double spiral corresponds approximately to the half of the guided wavelength ($\ell_{DblSpiral} = \lambda_g/2$). Furthermore, the physical dimensions of the unit cell of Fig. 3.1 are equivalent to $\lambda_g/12$ and $\lambda_o/16$, where λ_g and λ_o are the guided and free-space wavelength of the frequencies within the passband. As a result the medium under consideration can be treated as an effective dielectric.

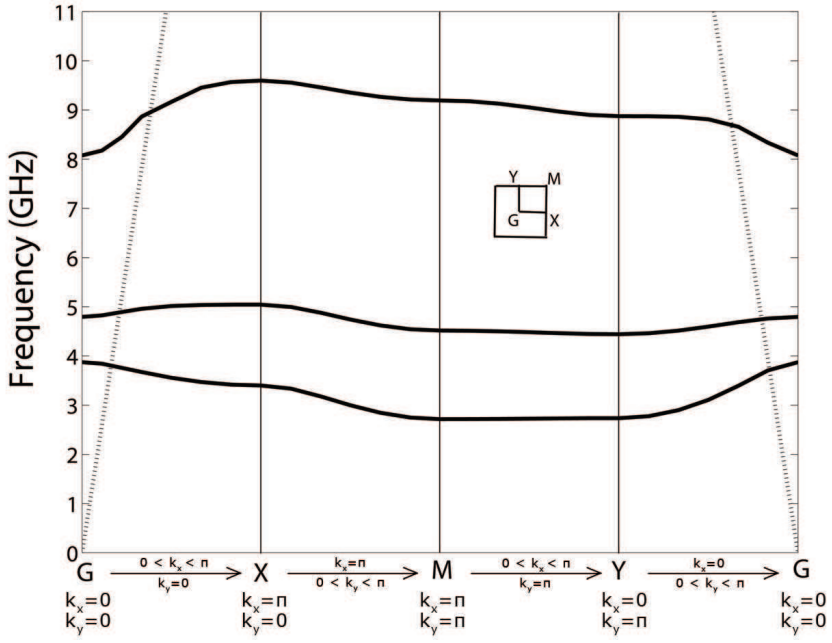

Figure 3.3: Dispersion diagram of the unit cell of Fig. 3.1. The first formulated passband (fundamental mode) is clearly a backward wave band.

Modal Field Patterns

In order to study the identifying characteristics of the left-handed modes supported by the double spirals, the in-house FDTD code is employed for the extraction of the modal field patterns of the major field components of the modes. The periodic FDTD analysis of the unit cell shows that the identifying components of the electric and magnetic field that determine the operation of this structure are the electric field components along $x-$ and $z-$ axes and the magnetic field component along $z-$ axis.

In Fig. 3.4, the modal pattern of the E_x field component is plotted for a backward wave supported at $f_o = 3.4\,GHz$ and propagating along $x-$axis ($k_x d_x = \pi/2$,$k_y d_y = 0$). This modal field pattern shows that the electric field along $x-$axis is negligible everywhere in the unit cell, but the edges of the unit cell and the very middle of the unit cell. These observations lead to three important conclusions. First, it is shown that between the adjacent $y-$oriented metal strips of the spirals the magnitude of the fringing fields are orders of magnitude below the maximum value of the E_x field component. Therefore, these strips can be assumed to be coupled under an even-mode excitation (see appendix A) and no capacitance is developed between them. The same is the situation with the

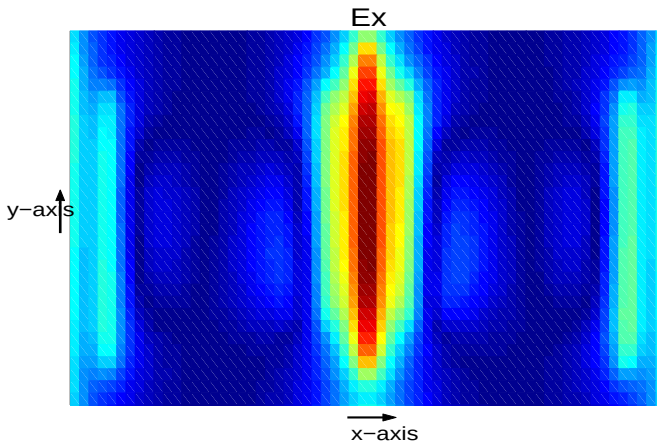

Figure 3.4: Modal field pattern of the electric field component oriented along $x-$axis for the mode that is supported at $f_o = 3.4\,GHz$ and propagating along $x-$axis ($k_x d_x = \pi/2$,$k_y d_y = 0$).

$x-$oriented strips of the spiral, conclusion that can be extracted from the observation of the modal field patterns of the E_y electric field component. The second conclusion is based on the observation of the very strong E_x component that is supported between the two adjacent $y-$oriented strips that belong to the two different single spirals in the middle of the unit cell. These two strips will be assumed as coupled under an odd-mode excitation and the supported capacitance between them should be always taken into account. Last but not least, the E_x field that is supported along $y-$axis at the edges of the unit cell (this electric field component is actually supported between two neighboring unit cells) lead to the conclusion that there is some capacitive coupling supported between adjacent double spirals.

Fig. 3.5 shows the modal field pattern of the $z-$oriented component of the electric field of the same wave as before. The reason why this pattern is presented is to show that the E_z field component is strong all along the length of the wounded spiral. Therefore, it can be concluded that all along the length of the spiral a quasi-TEM wave is supported between the spiral and the ground plane. The same conclusion is supported by observation of the H_x and H_y modal field patterns, in which the $x-$oriented component of the magnetic field assumes large values below the $y-$oriented strips of the spiral and the $y-$oriented component of the magnetic field assumes large values below the $x-$oriented strips.

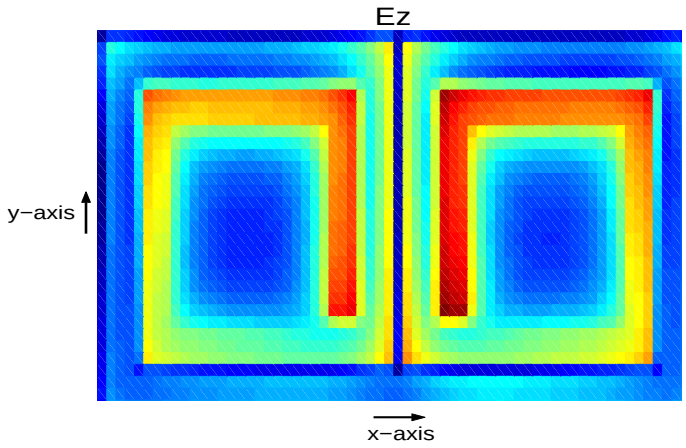

Figure 3.5: Modal field pattern of the electric field component oriented along $z-$axis for the mode that is supported at $f_o = 3.4\,GHz$ and propagating along $x-$axis ($k_x d_x = \pi/2, k_y d_y = 0$).

To conclude the analysis of the modal field patterns of the supported backward waves, the modal pattern of the $z-$oriented component of the magnetic field is shown in Fig. 3.6. This pattern suggests that the vertical magnetic field is assumes large values in the middle of each of the single spirals that compose the double spiral. This field is supported by the currents on the spirals and suggests that the DSR can support a shunt inductance that is required for the generation of backward waves, as suggested by Eleftheriades *etal*. in [28]. Observation of the phase of the two discrete magnetic components shows that these are in phase. In an array configuration, these components couple to the corresponding components of the adjacent DSR, providing the required inductive coupling for the array to support backward waves.

3.2.3 Equivalent Circuit

In this section, a simplified equivalent circuit for the DSR backed on grounded dielectric substrates is proposed. This equivalent circuit will be employed in the following text for the efficient analysis and design of DSR-based artificial transmission lines.

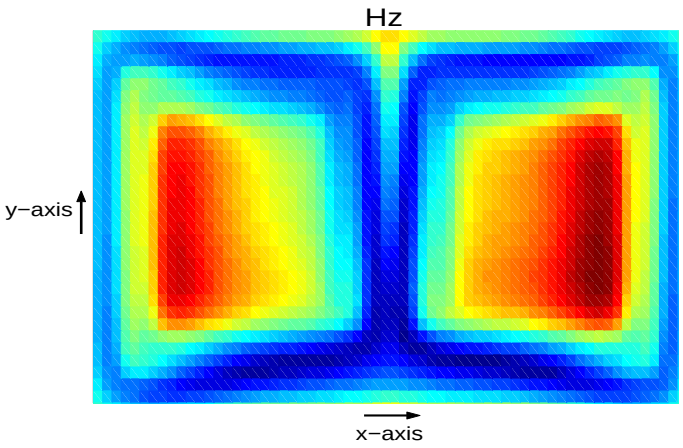

Figure 3.6: Modal field pattern of the magnetic field component oriented along $z-$axis for the mode that is supported at $f_o = 3.4\,GHz$ and propagating along $x-$axis ($k_x d_x = \pi/2$,$k_y d_y = 0$).

Lossless Approach

As it was shown though the extraction of the modal field patterns of the DSR there are two identifying field components associated with the operation of the DSR; the strong vertical magnetic field supported by the single spiral resonators and the series capacitance supported between the two different single spirals of the same DSR. Therefore in the extraction of the equivalent circuit those two characteristics should be taken into account.

The most simplified equivalent circuit that rigorously and effectively describes all the electromagnetic properties of the DSR is the one proposed in Fig. 3.7. In this equivalent circuit, each single spiral is represented with a shunt LC resonator of inductance L_{ss} and capacitance C_{ss}, connected with each other through a series capacitance C_{ser}.

The shunt inductance of each of the single spiral resonators L_{ss} can be calculated analytically using several different approaches [106], [107], [108]. Most of these models were compared with each other and were shown to be in good agreement. For the purposes of this thesis, the inductance of a spiral resonator is calculated using the modified Wheeler formula proposed in [107]. According to this model, the inductance of a printed spiral resonator is given by equation (3.1)

$$L_{spiral} = K_1 \mu_0 \frac{n^2 d_{avg}}{1 + K_2 \rho} \tag{3.1}$$

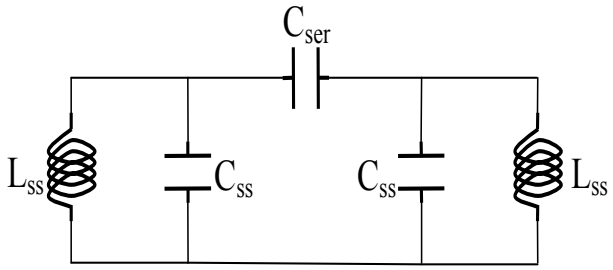

Figure 3.7: Equivalent circuit of the DSR of Fig. 3.1 (lossless case).

where n are the number of the turns of the spiral, d_{avg} is the average value of the inner and outer diameter of the spiral ($d_{avg} = (d_{in} + d_{out})/2$), ρ is the so-called fill ratio of the spiral defined as $\rho = (d_{out} - d_{in})/(d_{out} + d_{in})$, and the coefficients K_1 and K_2 are dependent on the geometry of the spiral under consideration and are reported in [107]. For the case of the square spiral, K_1 and K_2 have been found to be 2.34 and 2.75, respectively.

Equation (3.1) estimates the inductance of a printed spiral that is not in close proximity to a ground plane. According to the analysis of [32], when an inductive structure is in close proximity to a ground plane and a microstrip-like mode is supported, the inductance of the structure in the absence of the ground plane should be corrected by the factor

$$K_g = 0.57 - \left(0.145 * \ell n \frac{w}{h}\right) \tag{3.2}$$

in order to account for the presence of the ground plane. In equation (3.2) h is the distance between the spiral and the ground plane and w stands for the width of the strips that forms the spirals. Combining equations (3.1) and (3.2), the inductance L_{ss} involved in the proposed equivalent circuit is given by equation

$$L_{ss} = K_g L_{spiral}. \tag{3.3}$$

For the single spirals of the DSR of Fig. 3.1, equation (3.3) calculates its inductances L_{ss} as $L_{ss} = 13.78\, nH$.

The capacitance C_{ss} of the single spiral involved in the equivalent circuit of Fig. 3.7 is attributed to both the capacitance supported between the strips that form the spiral (minor contribution) and the capacitance supported between the strips and the ground plane (major contribution). The analytical calculation of this parameter in much more challenging than the calculation of the inductance. Even though there are references in

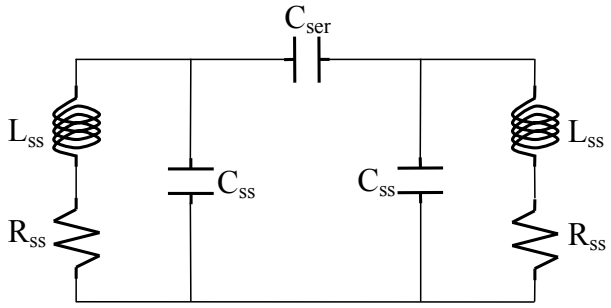

Figure 3.8: Equivalent circuit of the DSR of Fig. 3.1 (including losses).

the literature that could be employed for this calculation ([107], [108]), it has been seen that this calculation does not lead to satisfying accurate results and inserts a major error to the extracted self-resonance of any of the single spirals ω_{ss}. For this reason, in the following analysis, the estimation of the capacitance C_{ss} is performed through the full-wave estimation of the self-resonance of the single spirals. Specifically, the self-resonance f_{ss} of the single spirals is estimated through the full-wave analysis of a weakly excited single spiral. Then, the capacitance C_{ss} is calculated through equation

$$C_{ss} = \frac{1}{(2\pi f_{ss})^2 L_{ss}} \tag{3.4}$$

For the single spirals of the DSR of Fig. 3.1, full-wave simulation carried out using Ansoft Designer estimated the self-resonance of the single spiral to be $f_{ss} = 5.05\,GHz$. Then, equation (3.4) estimates the capacitance C_{ss} as $C_{ss} = 0.072\,pF$

Finally, the series capacitance C_{ser} involved in the equivalent circuit of Fig. 3.7 can be considered as the capacitance supported between two strips coupled under an odd mode. The equations for the calculation of this capacitance are provided in appendix A, and for the DSR of Fig. 3.1 the series capacitance has been calculated to be $C_{ser} = 0.053\,pF$

Impact of Losses

The equivalent circuit of Fig. 3.7 does not involve any kind of losses. In practice, however, the operation of the proposed DSR is associated with some ohmic losses that are attributed mostly to the resistance of the metallic spirals. This resistance can be represented as an ohmic resistance R_{ss} connected in series with the inductances L_{ss}, as in Fig. 3.8.

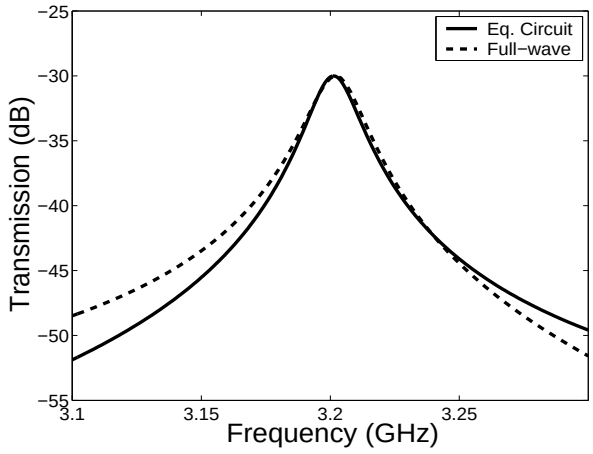

Figure 3.9: Normalized transmission through a weakly excited DSR calculated using the equivalent circuit of Fig. 3.8 and Ansoft Designer.

The value of the resistance R_{ss} can be approximated using equation (3.5) [109].

$$R_{ss} = \frac{\ell}{\sigma w \delta \left(1 - e^{-\frac{t}{\delta}}\right)} \tag{3.5}$$

In equation (3.5), ℓ is again the total length of the strips that form the single spiral resonators, w is the width of these strips, σ is the conductivity of the metal employed to print the spirals (in our case copper), δ is the skin-depth of the strips at the frequencies of interest, and t is the actual thickness of these strips. For the DSR of Fig. 3.1 and for operation around $3.2\,GHz$, R_{ss} is approximated as $R_{ss} \approx 1.4\,\Omega$

In order to validate the equivalent circuit of Fig. 3.8 and the approximated associated parameters, the transmission through a weakly excited DSR, calculated using both the equivalent circuit of Fig. 3.8 and a full-wave simulation, are compared. For the case of the results extracted through the equivalent circuit, the equivalent inductors of the DSR were considered to be weakly coupled to two auxiliary inductors that were directly connected to the ports of a circuit simulator, while for the case of the full-wave results, the DSR was excited through two microstrips that were weakly and inductively coupled to it. Given that for these two cases equivalent coupling coefficients were hard to be obtained, the magnitudes of the two extracted curves were normalized to each other. Finally, the results are depicted in Fig. 3.9.

The results of Fig. 3.9 show that the proposed equivalent circuit predicts quite ac-

curately both the self-resonance and the Q-factor of the DSR. Specifically, both the equivalent circuit and the full-wave results suggest that the self-resonance of the DSR is achieved at $f_o = 3.2GHz$, while the associated Q-factor, approximated as $Q \approx f_o/\Delta f_{3dB}$, has been calculated to be $Q = 170$. Nevertheless, this equivalent circuit is valid only over a narrow bandwidth around the resonance of the modelled structure, given that some of the values of the involved lumped elements were extracted considering resonance conditions. This is the reason why some divergence between the full-wave and the equivalent circuit results is observed away from the resonant frequency.

3.3 Analysis of Coupled DSR

Up to this point, the properties of the self-standing DSR have been studied. In the following text, the DSRs are employed for the synthesis of optimized 1-D arrays supporting backward waves. As shown in chapter 2, the properties of such arrays are much depended on both the nature and the magnitude of the coupling between the modular elements. In the case of DSR, the coupling between adjacent unit cells has been found to be dominantly inductive, supported between any pair of adjacent single spirals belonging to different DSR, without the existence of capacitance coupling to be ruled out. Nevertheless, for the purposes of this study, the capacitive coupling between the DSR will be considered unwanted as it turns out to cancel with the inductive coupling, and, as shown in section 2.1.3, larger inductive coupling values lead to more broadband backward wave passbands and more accurate phase control across these passbands. Therefore, the purpose of this analysis is to come up with DSR configurations that enhance the inductive coupling between them.

3.3.1 DSR Coupling Configurations

As it has been already mentioned, the inductive coupling coefficient k_M, given by equation (3.6), can be both positive and negative due to the inexistence of magnetic charges (always closed magnetic lines). Also, between any two coupled inductors (spirals) there are two possible relative polarities, depending on the windings of the two inductors. Inclusively, for the case of 1-D DSR arrays (periodicity along the $x-$axis of Fig. 3.1 is considered), there are four different scenarios for the coupling between adjacent spirals. These coupling scenarios, depicted in Fig. 3.10, correspond to all the possible combinations of polarities

and signs of the coupling coefficient.

$$k_M = \frac{\int\int\int \mu \vec{H}_1 \cdot \vec{H}_2 d\upsilon}{\sqrt{\int\int\int \mu \left|\vec{H}_1\right|^2 d\upsilon \times \int\int\int \mu \left|\vec{H}_2\right|^2 d\upsilon}} \tag{3.6}$$

Specifically, Fig. 3.10(a) and Fig. 3.10(c) depict the case in which the coupled spirals possess opposite polarities (the left spiral has a clockwise winding and the right spiral has an anti-clockwise winging). This configuration occurs when the spirals are aligned symmetrically with respect to the $y-$axis. Depending on the currents that flow on the spirals, this configuration may lead to two signs of the coupling coefficient; when currents are flowing as shown in Fig. 3.10(a) the supported inductive coupling coefficient is negative (considering that the magnetic lines of each spiral close through its adjacent spiral, the two magnetic components, where overlapping, are contra-directional and, hence, the dot product $\vec{H}_1 \cdot \vec{H}_2$ is negative). For the same reasons, the inductive coupling coefficient of the configuration of Fig. 3.10(c) is positive. The lumped-element representations of the two scenarios are depicted in Fig. 3.10(b) and Fig. 3.10(d), respectively.

Accordingly, the scenarios in which the coupled spirals possess same polarities are shown in Fig. 3.10(e) and Fig. 3.10(g). For the same reasons as before, the coupling coefficient in the first of these scenarios will be positive and in the second will be negative.

Artificial lines composed of coupled DSR would not necessarily result in transmission lines supporting backward waves. On the contrary, as mentioned in chapter 2, the type of the supported waves will be depending on the sign of the coupling coefficient, or, more accurately, on the combination of coupling sign and polarity. Specifically, out of the four scenarios of Fig. 3.10 only two of them will result in backward waves and two of them will result in forward, right-handed, slow-waves, attributed to an effective high-μ property (magneto-dielectric). The exact equivalent circuits of these four cases are depicted in Fig. 3.11. The dispersion analysis of all the four equivalent circuits of Fig. 3.11 shows that the two scenarios that lead to backward waves are the first and the third (Fig. 3.11(a) and Fig. 3.11(c)) (effective left-handed behaviour) , while those of Fig. 3.11(b) and Fig. 3.11(d) provide solutions only for forward waves (effective magneto-dielectric behavior). In fact, the cases that lead to backward waves are those that involve shunt inductances (in Fig. 3.11(a) the equivalent shunt inductance of the coupled spirals is $-(-|k_M| L_o)$ while in Fig. 3.11(c) is $(|k_M| L_o)$).

Given that the purpose of this chapter is the synthesis of artificial lines supporting

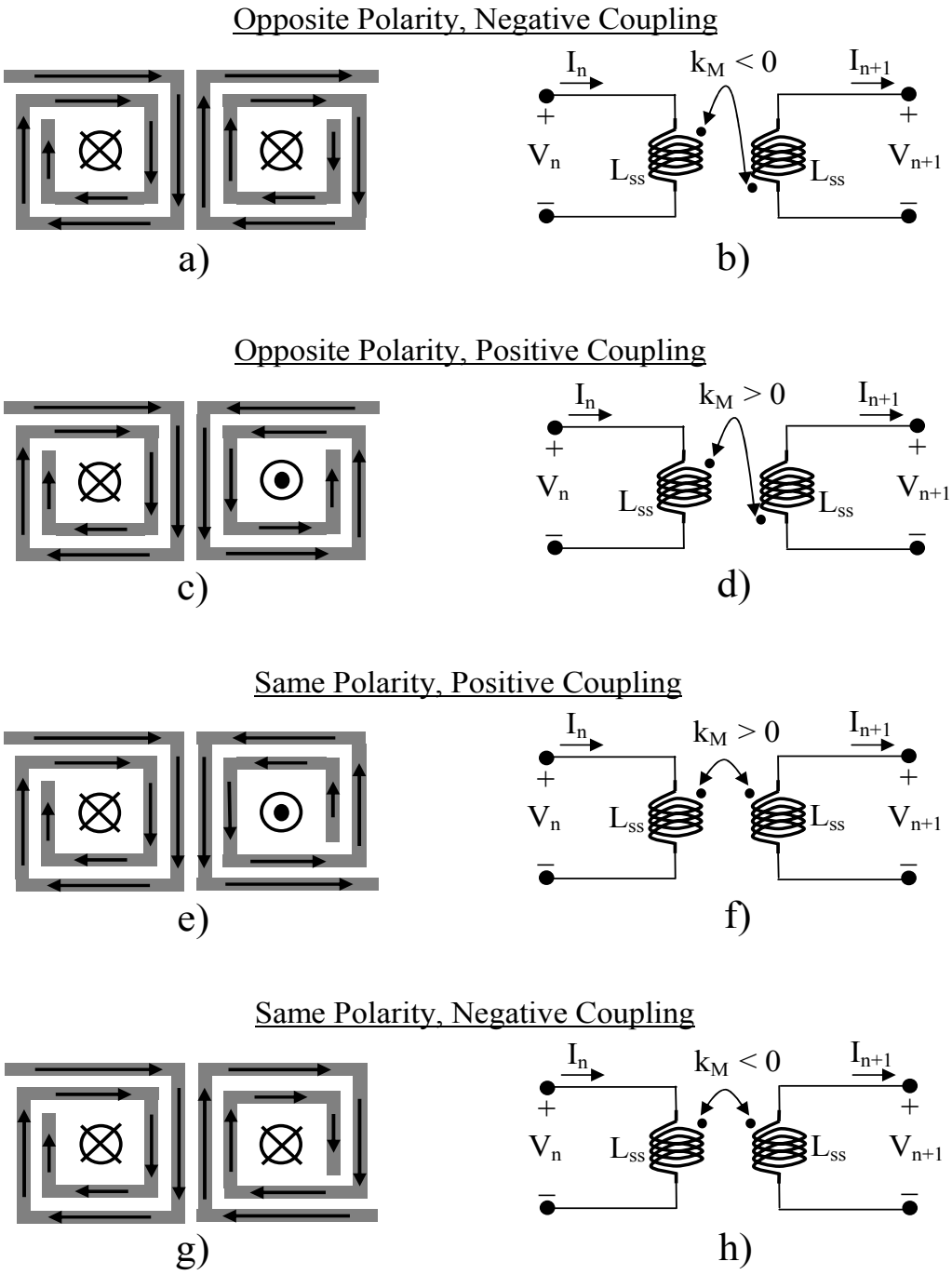

Figure 3.10: Four possible scenarios and equivalent lumped-element representation for two inductively coupled spirals, depending on their polarities (windings of the spirals) and the sign of the coupling coefficient (direction of the flowing currents and the corresponding magnetic flux).

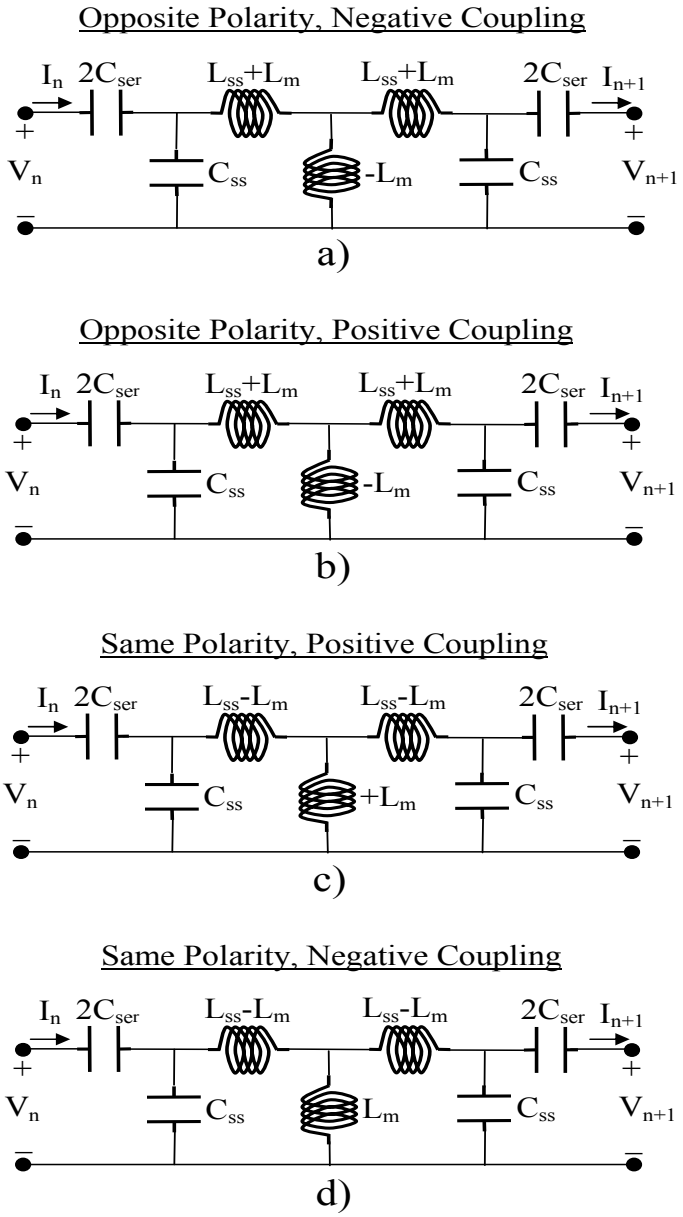

Figure 3.11: Exact equivalent circuits of the four scenarios of Fig. 3.10. For all the equivalent circuits, regardless of the sign of k_M, $L_m = k_M L_o$

backward waves, only the cases of Fig. 3.10(a) and Fig. 3.10(e) will be further investigated. On the other hand, in the following chapters of the thesis, the remaining two cases will be exploited. Finally, it is clarified that the two coupling scenarios that correspond to each of the two spirals configurations (polarities) correspond to the two eigensolutions (modes) of each configuration. Which of the two modes will be established in a certain application will be depended on the way the spirals are being excited and the surrounding electromagnetic environment (boundary conditions). Specifically for the case of the DSRs-based arrays, it has been seen that the dominant mode is determined by the number of the DSRs that constitute the array: even number of resonators enhance the modes that lead to backward waves and odd number of resonators enhance the modes that lead to forward waves. The latter observation applies exclusively to finite size arrays.

3.3.2 DSR Coupling Assessment

In order to decide which of the two configurations of Fig. 3.10 that lead to backward waves will be chosen for the synthesis of artificial lines supporting such waves, the coupling coefficient for the two cases will be calculated. In turn, the configuration that exhibits larger coupling will be chosen, given that, as shown in chapter 2, larger couplings between the resonators lead to larger useful bandwidths.

Before proceeding to the rigorous quantitative calculation of the coupling in these two cases, a comparative estimation for the coupling can be made only by the observation of Fig. 3.10 and the schematic representation of the currents on this figure. As it has been mentioned, the coupling between the resonators is mainly inductive and any capacitive coupling between the DSRs tends to cancel with the inductive coupling, reducing the total coupling coefficient. The schematic representation of the currents on Fig. 3.10(a) shows that for this configuration the adjacent strips of the two neighboring spirals are flown by contra-directional currents (coupled lines under an odd-mode excitation) and, hence, some coupling capacitance will be supported between them. This capacitance corresponds to the E_x component that is supported at the edges of the unit cell in the modal field pattern of Fig. 3.4. Such capacitance is not supported in the configuration of Fig. 3.10(e), given that the corresponding currents are co-directional. Therefore, it is expected that the total coupling will be larger for the configuration of Fig. 3.10(e).

For the numerical estimation of the coupling of the two configurations, the well-known technique of the full-wave simulation of the transmission through pairs of weakly excited

coupled resonators is employed. Ansoft Designer is used for the full-wave transmission simulation and the employed models for the two configurations are depicted in Fig. 3.12 and Fig. 3.13, respectively.

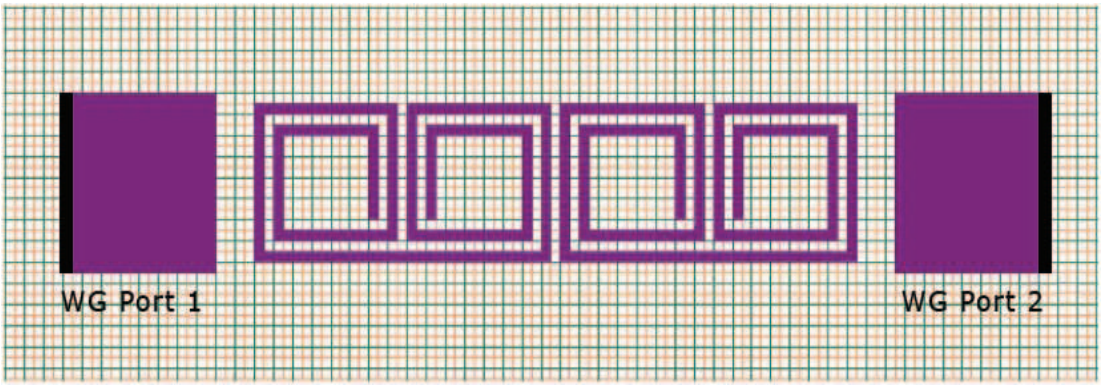

Figure 3.12: Ansoft Designer model used for the calculation of the transmission through a weakly excited pair of coupled DSRs. In this configuration, the double spirals have been arranged symmetrically along the axis of propagation (as in Fig. 3.10(a)).

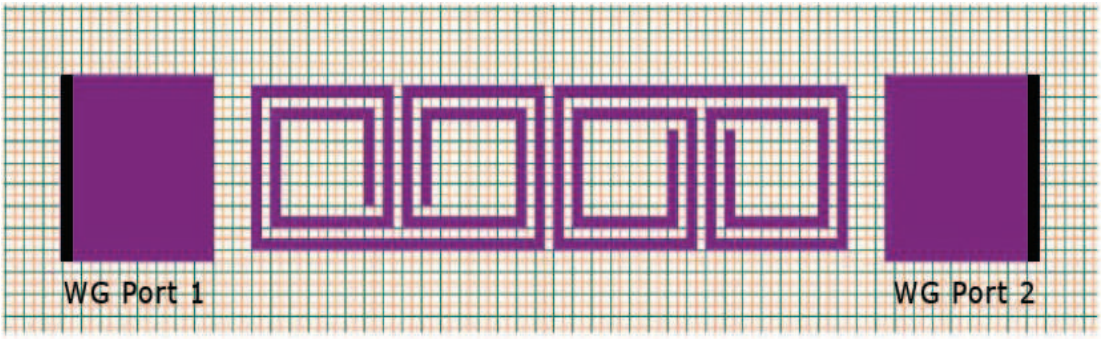

Figure 3.13: Ansoft Designer model used for the calculation of the transmission through a weakly excited pair of coupled DSRs. In this configuration, the double spirals have been arranged asymmetrically along the axis of propagation (each spiral is rotated by 180^o compared to its adjacent spirals) (as in Fig. 3.10(e)).

The transmission results obtained for the models of Fig. 3.12 and Fig. 3.13 are depicted in Fig. 3.14 and Fig. 3.15, respectively. In both cases, the transmission is maximized at the frequencies f_1 and f_2, that correspond to the two eigenmodes of each

configuration. Finally, according to the analysis of [32], the magnitude of the coupling between the DSR for each configuration is given by equation (3.7).

$$k = \frac{|f_1^2 - f_2^2|}{f_1^2 + f_2^2} \tag{3.7}$$

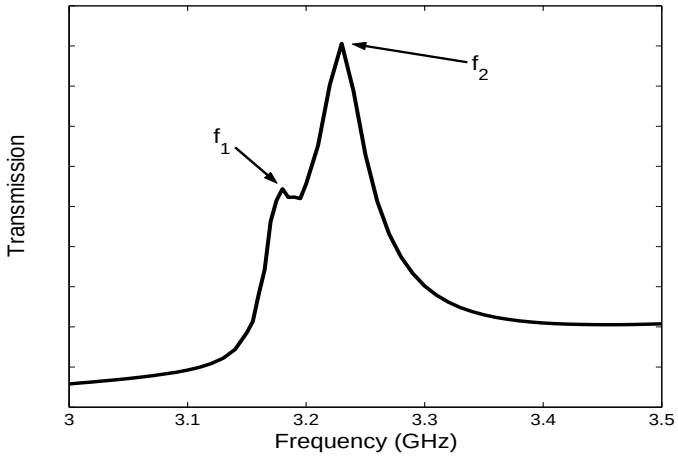

Figure 3.14: Simulated transmission through the weakly excited pair of coupled DSR of Fig. 3.12.

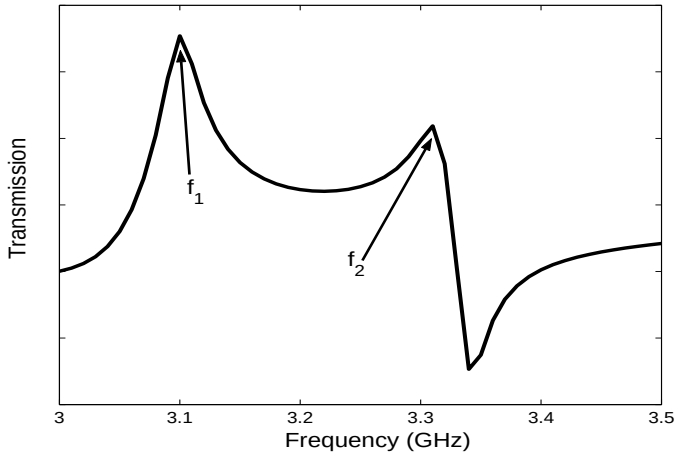

Figure 3.15: Simulated transmission through the weakly excited pair of coupled DSRs of Fig. 3.13.

Using the results of Fig. 3.14 and Fig. 3.15 together with equation (3.7), the coupling coefficient for the configuration of Fig. 3.12 is found to be $k = 0.0085$ ($f_1 = 3.175\,GHz$

and $f_2 = 3.23\,GHz$), while for the configuration of Fig. 3.13 $k = 0.035$ ($f_1 = 3.1\,GHz$ and $f_2 = 3.31\,GHz$).

As expected, the total coupling coefficient for the configuration of Fig. 3.13 and Fig. 3.10(e) is larger of that of Fig. 3.12 and Fig. 3.10(a). Therefore, the configuration of Fig. 3.13 is the one that will be used for the synthesis of 1-D artificial transmission lines supporting backward waves.

3.4 1-D DSR-based Artificial Transmission Lines

In this section, DSR are employed for the design and fabrication of microstrip-based transmission lines that support backward waves. Such transmission lines are simulated and the propagation characteristics are studied. The results of these studies are validated through the fabrication and measurement of the aforementioned lines. The advantages of such transmission lines are that these lines are compatible with standard microwave technologies (microstrip lines), will be fully-printed, and therefore easily fabricated, completely uniplanar and easily scalable to higher and lower frequencies.

3.4.1 Simulation

Up to this point, the configurations of the DSR along 1-D arrays has been optimized. What still remains to be identified is the way spiral based transmission lines will be fed and will match the standard $50\,\Omega$ impedance level. It is a common practice, in the literature, to feed left-handed media using planes waves, properly polarized to excite the structural elements of the medium. In our case, though, this technique can not be used given the topology of the medium (printed on a grounded substrate). Furthermore this technique is usually accompanied by poor transmission through the medium due to mismatching effects between of the medium with the air.

Therefore a different technique is used to feed the spirals. At the two edges of the DSR-based transmission lines, single spirals, identical with those that compose the DSR, properly oriented and perfectly coupled to the adjacent DSR are employed. These single spirals are open-ended and, therefore, they can be directly attached to a conventional transmission line. Due to the way the single spirals are located at the edges of the lines they can be assumed to be part of them. Consequently, these transmission line are fed by exciting currents directly on them. This is the first time that direct excitation of

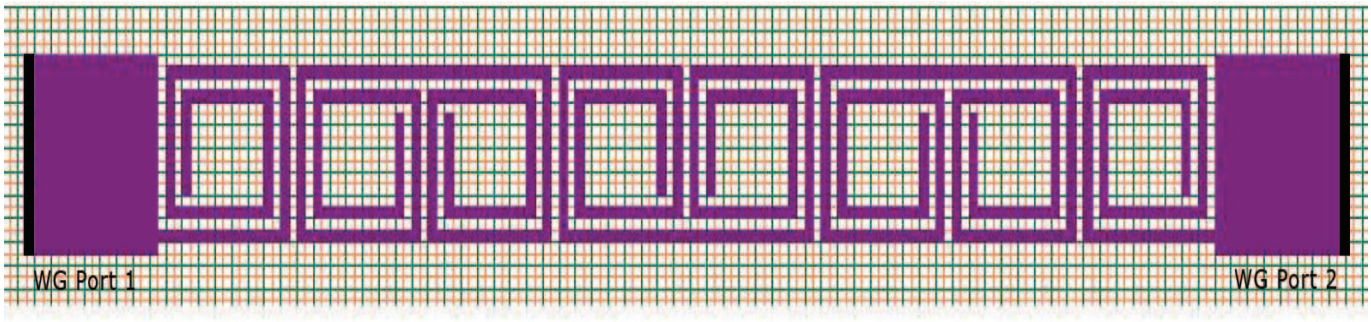

Figure 3.16: Top view of a DSR-based transmission line composed of 4 DSR and embedded within a common 50 Ω microstrip line.

currents on the left-handed medium is reported in the literature to feed such a medium. Finally, the resulting artificial transmission line is shown in Fig. 3.16.

The simulated $S-$parameters of the line of Fig. 3.16 are shown in Fig. 3.17. These results show that the proposed structure exhibit a passband from 3 GHz to 3.4 GHz ($FBW = 13\,\%$), in which the backward waves are supported.

3.4.2 Fabrication and Measurements

In this section, the fabrication and measurement of the transmission line of Fig. 3.16 is reported. The dimensions of each of the DSR that are used are $d_x = 6.4\,mm$ and $d_y = 3.2\,mm$, while the width of the metallic strips and the gabs between them are $g = s = 0.2mm$. The LHM transmission lines are built on $RT/duroid5880$ dielectric substrate of dielectric constant $\epsilon_r = 2.2$ and height $h = 1.15mm$. The fabricated prototype is shown in Fig. 3.18. In this prototype six unit cells have been used for the synthesis of the line.

In Fig. 3.19 and Fig. 3.20 the measured and simulated $S-$parameters of a fabricated prototype that is composed of four unit cells have been plotted. These figures show that the fabricated LHM transmission line supports backward waves from 2.9 GHz to 3.3 GHz, a fractional bandwidth of about $FBW = 13\,\%$. In this passband, a fairly satisfying trasmission of $-1.8\,dB$ is achieved.

In order to experimentally validate the suggestion that the supported modes in the formulated passband correspond to backward waves, the inserted phases, by two LHM transmission lines of different lengths, to a propagating wave are examined. It is well-known that the difference between these phases are given by equation (3.8), where d_1

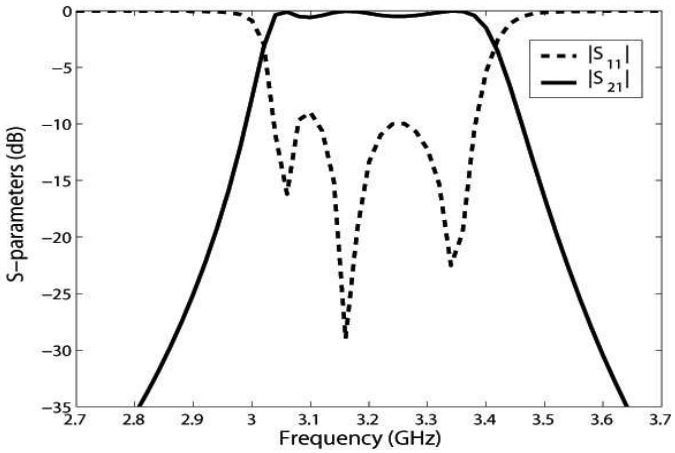

Figure 3.17: Simulated $S-$parameters of the transmission line of Fig. 3.16.

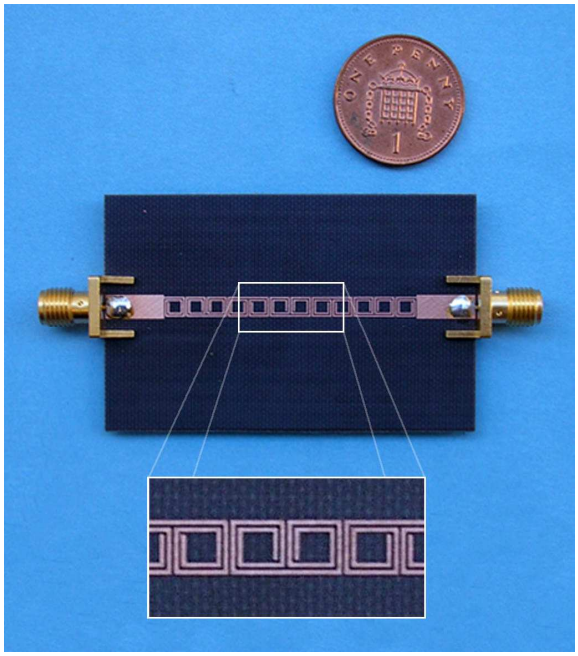

Figure 3.18: Fabricated prototype of a spiral-based transmission line that is composed of six unit cells.

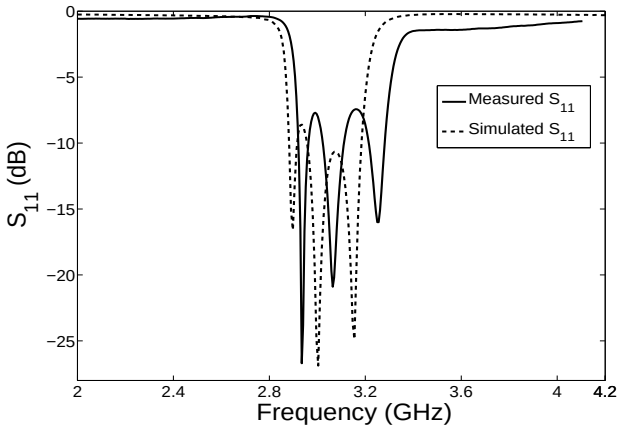

Figure 3.19: Measured and simulated S_{11} of the prototype of Fig. 3.18.

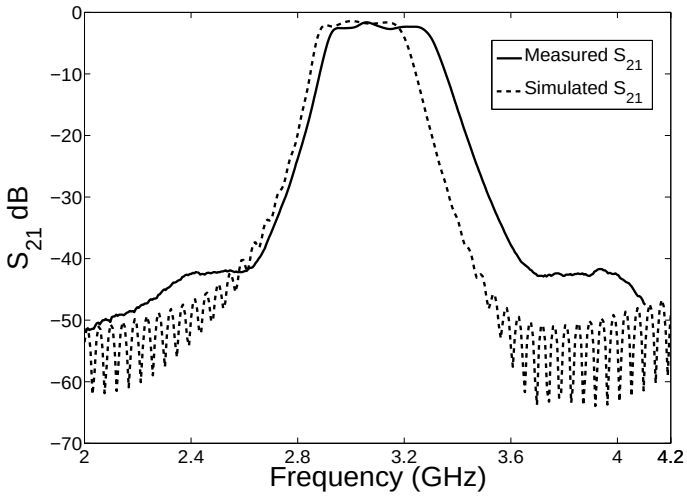

Figure 3.20: Measured and simulated $S_{21}$of the prototype of Fig. 3.18.

and d_2 are the lengths of the transmission lines under consideration [110].

$$\Delta\varphi = \varphi_2 - \varphi_1 = -\frac{\omega n(\omega)}{c}(d_2 - d_1) \tag{3.8}$$

Fig. 3.21 shows the measured unwrapped phases that are inserted to a propagating wave by two of the proposed LHM transmission lines that are composed of four and six unit cells, respectively. According to these results, the phase inserted by the six unit cells

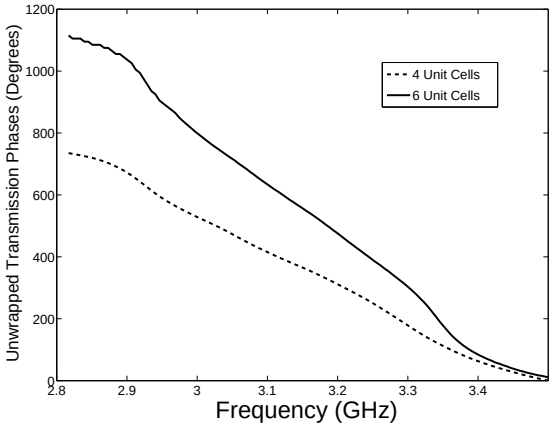

Figure 3.21: Measured unwrapped transmission phases of two DSR-based transmission lines that are composed of 4 and 6 unit cells, respectively.

line is always greater than this inserted from the four unit cells one. Assuming that d_2 is the total length of the six unit cells and that d_1 is the length of the four unit cells, then $\Delta\varphi > 0$, $d_2 - d_1 > 0$ and, hence, in order for equation (3.8) to be satisfied, $n(\omega)$ must be negative. Therefore, the effective index of refraction of the proposed transmission lines is negative.

3.4.3 Impact of Losses

One of the major constraints in the operation of LHM that are composed of highly resonant metallic particles, such as the SRR or the DSR, is the losses that are inserted to the waves within the bandwidth of interest. These losses are attributed mostly to the strong currents that are induced on the metallic elements of the aforementioned structures at their resonance (ohmic losses). In the following, the nature of these losses and their impact to the operation of DSR-based transmission lines are studied.

In Fig. 3.22 the simulated power losses across a transmission line that is composed of four unit cells are plotted for four different cases. In the three of them, the spirals are assumed to be formed by perfect conductors ($\sigma \to \infty$), being printed on a substrate with variable losses. In the fourth case, the spiral are assumed to be printed on a lossless substrate but using copper ($\sigma = 5.88 * 10^{07}\ Siemens/m$). For the cases that the losses of the dielectric substrate are varied ($tan\delta = 0, 10^{-4}, 10^{-3}$) and perfect conductor is assumed, the power losses across the transmission line are growing as the loss tangent

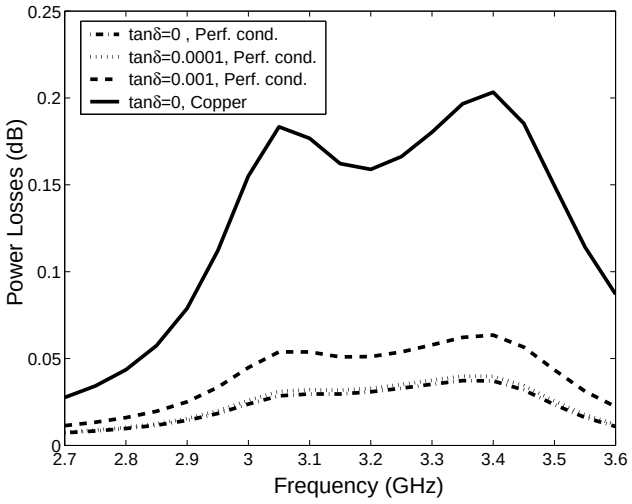

Figure 3.22: Simulated power losses across a 4-unit-cell spiral-based transmission line for several cases of ohmic and dielectric losses.

of the substrate grows, but still assume extremely small values (at the order of 0.05 dB for a four-cell long line). These values of power losses are of the same order as the losses that are encountered in the case that no dielectric and conductor losses are assumed (inherent radiation losses of the structure, at the order of 0.025 dB for a four-cell long line). Therefore it is concluded that neither the inherent radiation losses of the structure itself, nor the losses inserted by the dielectric substrate are of critical importance for the operation of the structure, allowing for the spiral based medium to be printed on cheap and relatively lossy dielectric substrates (e.g. $FR-4$).

On the other hand, the role of the ohmic losses in the operation of this structure is much more significant. As shown in Fig. 3.22, for the case that conductor losses are taken into account, the total power losses are significantly large and, specifically, four times larger than the losses inserted by a substrate of $tan\delta = 10^{-3}$ (worst case scenario for the dielectric losses). This is due to the strong currents that are developed on the spirals at their fundamental mode (backward waves modes).

A rough quantitative estimation of ohmic losses, for the structure under consideration, can be performed by means of the measured transmitted and reflected power. In Fig. 3.23 the total transmitted and reflected power at two LHM transmission lines that are composed of four and six unit cells is plotted.

Although the exact value of the ohmic losses varies with frequency within the pass-band (group delay variation), it can be seen that the four unit cells degrade the total

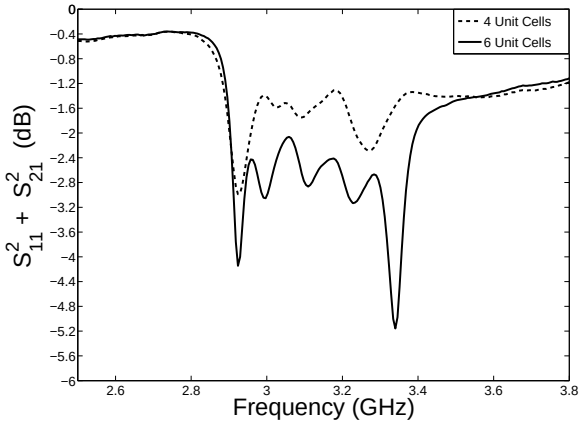

Figure 3.23: Measured power losses across a 4-unit-cell and a 6-unit-cell spiral-based transmission line.

transmitted and reflected power by 1.6 dB, on average, while the six unit cells degrade the total power by 2.4 dB. Both these observations conclude that each unit cell inserts, approximately, 0.4 dB power loss. In practice, the actual ohmic power losses per unit cell are even less since in the estimation of the total losses other sources of power loss, such as dielectric losses and losses inserted by the connectors, have been included.

3.5 DSR-based Artificial Transmission Lines Applications

In this section, an application that employs the proposed DSR-based artificial lines is presented. This application is a series-fed microstrip patch array.

3.5.1 Series-Fed Patch Arrays

General

Series-fed microstrip patch arrays are always good candidates as radiators for applications that require single-feed, low-profile, fully-printed, highly directive antennas. During the years, several different series-fed microstrip patch array topologies have been proposed in the literature. Depending on the specific topology, series-fed arrays can deliver high directivities in either their E-plane or their H-plane, while, in cases in which both series

and parallel feeding networks are employed, increased directivities in both the E-plane and H-plane can be achieved. Furthermore, several studies have been published proposing techniques for the shaping of the radiated beams. These techniques are mostly employing the beam shaping possibilities offered by the parameters involved in the array factor of the array under consideration, *i.e.* the relative magnitude and phase of the excitations of each of the elements of the phased array.

In this study, equally spaced, series-fed, microstrip patch arrays that achieve increased directivity in the E-plane and radiate at broadside are considered. In order for these arrays to be synthesised, the microstrip patches should be connected in series along their resonating dimension and be fed in phase. Given the resonant length of each patch antenna ($\lambda_{g1}/2$) and that between the radiating edges of each microstrip patch there is a phase shift of -180^o, the interconnecting transmission lines should also insert a phase shift of 180^o between neighboring patches, in order for the latter condition to be fulfilled. Therefore, conventional microstrip transmission line segments of length $\lambda_{g2}/2$ should be used to connect any pair of neighboring patches. Usually, $\lambda_{g1}/2$ and $\lambda_{g2}/2$ significantly differ in length, even though they are referring to the same operating frequency and the same hosting medium, because of the different widths of the microstrip patches and the interconnecting transmission lines that result in different effective dielectric constants.

As far as the calculation of the input impedance of such arrays is concerned, it is possible to assume that both the microstrip patches and the interconnecting transmission lines act as half-wavelength transformers of the loads that correspond to each of the radiating edges of the microstrip patches. Therefore the total input impedance of such array can be assumed, in good proximity, to be equal to the parallel combination of these loads. In order to get a decent input real impedance, the width of each patch, that defines the equivalent load of each radiating edge, should be decreased as the number of the array elements is increased

Proposed study

It is well-known that the directivity of uniformly excited, equally spaced, broadside arrays depends both on the number of array elements N and the element spacing d. In Fig. 3.24, the analytically calculated directivity of two microstrip patch arrays, composed of 3 and 4 elements, respectively, as a function of the distance between the edges of any pair of neighboring array elements, is depicted. For this calculation it has been

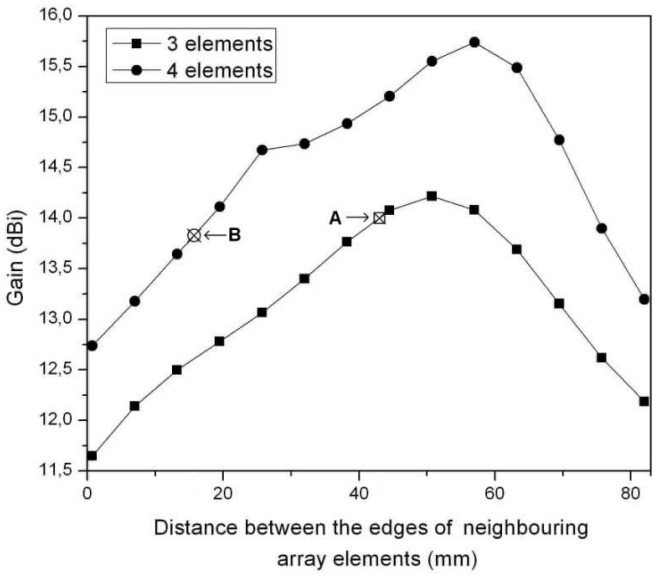

Figure 3.24: Analytically calculated directivity of a three-element and a four-element microstrip patch array, as a function of the distance between any pair of neighboring patches.

assumed that the minimum distance between the edges of any pair of neighboring array elements ($0\,mm$) corresponds to a $\lambda_{g1}/2$ distance (resonant length of the patch) between the point radiators for which the array factor has been calculated. As it is shown in Fig. 3.24, for any given element spacing, the four-element array always achieves higher directivity (larger effective radiating aperture), while any specific value of directivity can be achieved by both the three- and four-element arrays, provided that the distance between the elements is properly set.

As it has been already mentioned, the use of artificial phase-shifting lines allows for the manipulation of the phase of electromagnetic waves independently of the size of the structure that supports these waves. In the framework of the uniformly excited, equally spaced, broadside series-fed arrays, this property could be exploited for the synthesis of arrays that will be composed of different number of elements but will be able to achieve the same directivity and occupy the same volume.

Based on this idea, the properties of two different broadside, series-fed arrays, that are composed of 3 and 4 microstrip patches, respectively, occupy the same volume and have been designed so as to deliver the same directivity, are compared in this section. More specifically, the first of these two arrays, shown in Fig. 3.26(a), is composed of

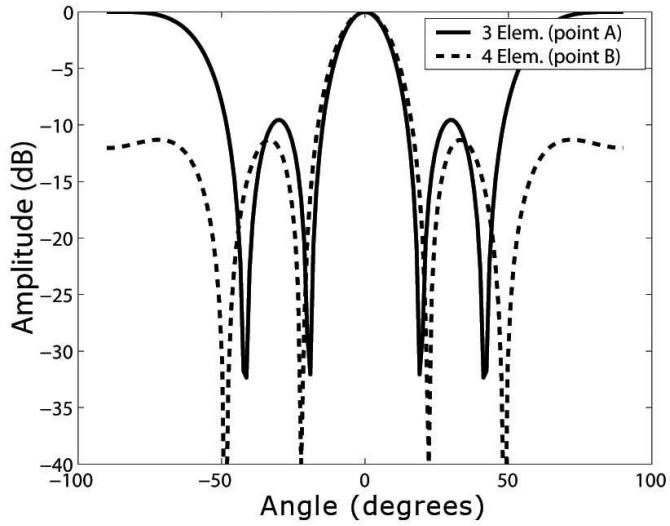

Figure 3.25: Array factors of a three-element (point A in Fig. 3.24) and a four-element array (point B in Fig. 3.24) occupying the same area.

3 microstrip patches that are connected using conventional transmission line segments that are 43 mm long (point A in Fig. 3.24). The second array, shown in Fig. 3.26(b), is composed of 4 microstrip patches that are connected in series using the proposed DSR-based artificial lines. Given that these lines can be designed to insert the phase-shift required for the patches to radiate in phase irrespectively of their physical length, the distance between these patches was chosen to be 15.75 mm, so that the two arrays occupy the same volume/area and deliver approximately the same directivities (point B in Fig. 3.24). The analytically calculated array factors for the two aforementioned cases are depicted in Fig. 3.25. These patterns suggest that indeed the two arrays deliver approximately the same directivity but the four-element one achieves a reduced by 2.5 dB sidelobe level.

In the following text, the exact dimensions of the two arrays, their fabrication, measurement and comparison are reported.

Fabrication and Measurements

The three-element series-fed array of Fig. 3.26(a) is designed and fabricated on a $TACONIC\ TLY-5$, 2.38 mm thick, dielectric substrate of dielectric constant $\epsilon_r = 2.2$. Each patch is designed to operate at $2.40\,GHz$; its resonant length is $l_1 = \lambda_{g1}/2 = 40\,mm$ and its width is $w_1 = 34mm$. The interconnecting transmission line segments are of length

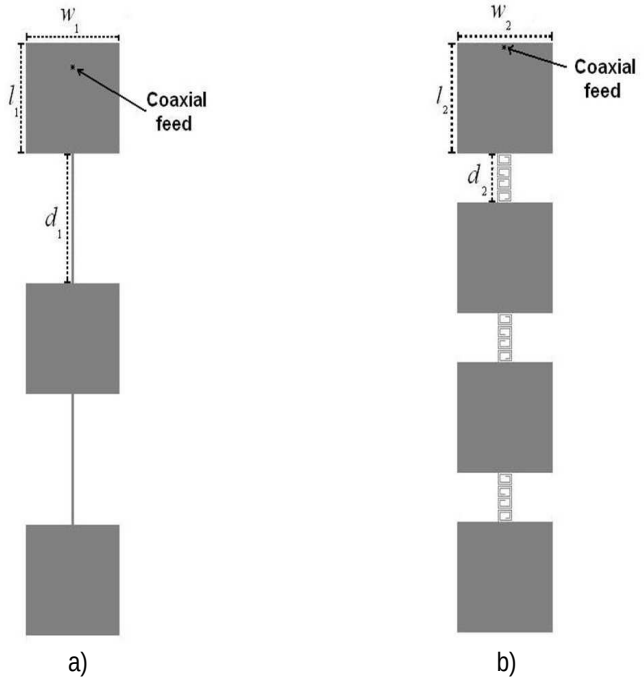

Figure 3.26: a) Three-element series-fed array, incorporating conventional interconnecting lines, that corresponds to point A of Fig. 3.24 and b) four-element series-fed array, incorporating artificial DSR-based interconnecting lines, that corresponds to point B of Fig. 3.24.

$d_1 = \lambda_{g2}/2 = 43\,mm$ (point A in Fig. 3.24) and width $2.0\,mm$. The total length of the array is $3l_1 + 2d_1 = 206.0\,mm$, while it is fed with a coaxial cable that is attached on the first element of the array.

The four-element series-fed array of Fig. 3.26(b) is designed and fabricated on the same dielectric substrate. This array is composed of 4 microstrip patches that are identical with those employed in the three-element array. The conventional interconnecting transmission lines of the three-element array have been substituted in this array with the spiral-based artificial lines. These lines are composed of two DSRs each. The total physical length of each of the spiral-based lines is $d_2 = 15.3\,mm$. Each DSR has been designed according to the unit cell of Fig. 3.1, employing $0.35\,mm$ wide strips and gaps (to reduce ohmic losses). In order for the spiral-based artificial line to enforce the elements of the array to radiate in phase at the targeted operating frequency ($2.45\,GHz$), each DSR has been designed so as this frequency point to correspond to the $+90^o$ phase-shift point on its dispersion diagram. Finally, the total length of the four-element array is $4l_1 + 3d_2 = 205.9\,mm$.A photograph of the two fabricated prototypes is depicted in Fig. 3.27. Both antennas are being fed using a coaxial cable, that is connected to the first patch through the ground plane and the dielectric substrate.

The measured return loss of the conventional three-element array is presented in Fig. 3.28. These results suggest that the three-element array achieves five different resonances from $1.9\,GHz$ to $2.9\,GHz$. The third of them, that supported at $2.40\,GHz$, is the one at which the array has be designed to operate. Indeed, this is the resonance that corresponds to the the case that all the array elements are fed in-phase and the array is radiating at the broadside direction. The measured $-10\,dB$ fractional bandwidth of the antenna at this frequency is $FBW_{-10\,dB} = 2.0\%$. All the other four resonances correspond to traveling waves that are supported by the array.

The measured return loss of the fabricated four-element array is presented in Fig. 3.29. These results show that the four-element array exhibits a $-10\,dB$ fractional bandwidth of the order of $FBW_{-10\,dB} = 15.0\%$ that extends symmetrically around $2.4\,GHz$. This bandwidth corresponds to the fractional bandwidth of the employed DSR-based artificial lines (because of the larger size of the employed DSRs and the higher dielectic substrate, the bandwidth of these DSRs is larger than those examined in the previous sections of this chapter). Across that bandwidth of the metamaterial series-fed array multiple resonances are observed. These resonances are attributed to both the discrete resonances of the 3-element array, that have been now all included in the operational bandwidth of the

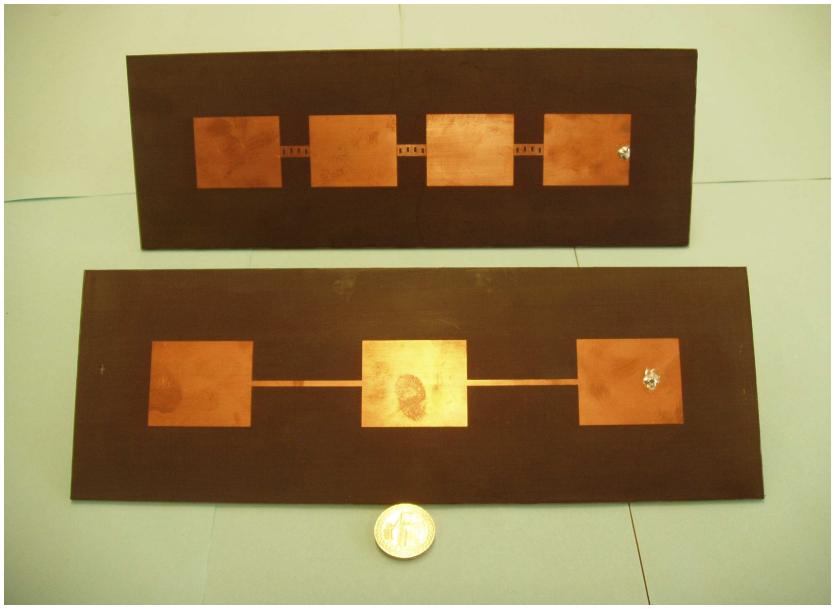

Figure 3.27: Photograph of the fabricated three- and four-element series-fed array prototypes.

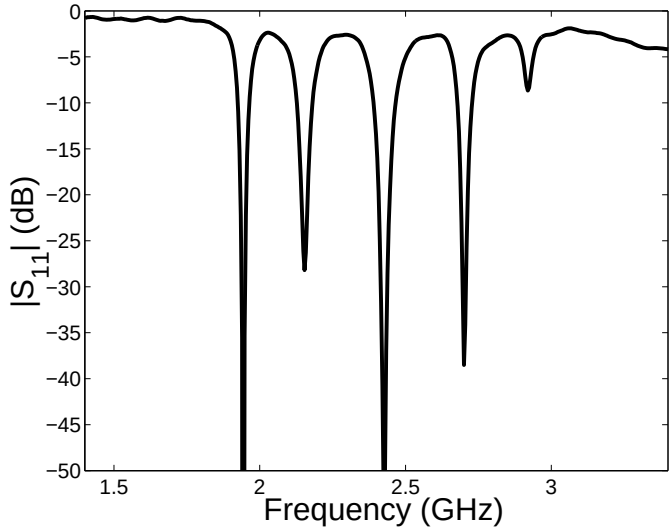

Figure 3.28: Measured return loss of the conventional three-element array.

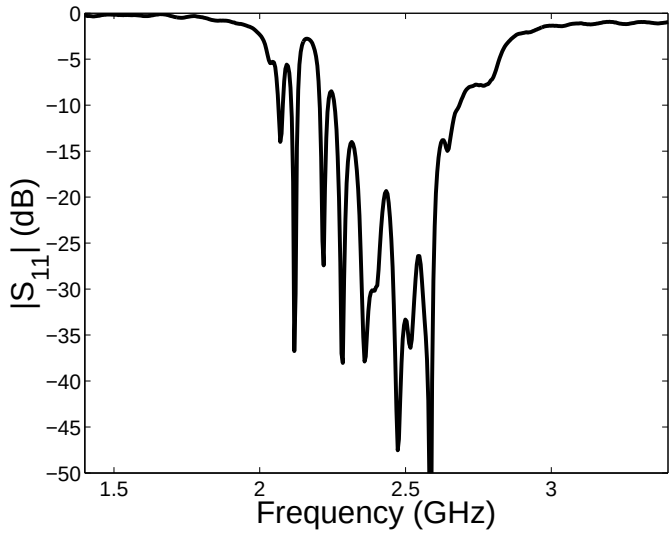

Figure 3.29: Measured return loss of the four-element array.

4-element array, and the resonances of each of the resonators (spirals) that constitute the artificial inteconnecting lines. A similar phenomenon (multiple resonances) has been also observed in [111], where a different class of series-fed arrays with artificial inteconnecting lines has been investigated.

The E-plane radiation patterns of both the three-element and four-element arrays at $2.4GHz$ are shown in Fig. 3.30. At this frequency, both arrays exhibit broadside radiation patterns. The three-element array is slightly more directional than the four-element array, delivering broadside gain of $11\,dBi$ with a radiation efficiency of approximately 75%. As far as the four-element array is concerned, it exhibits approximately $2.5\,dB$ reduced sidelobe levels, as compared to the three-element array, while the delivered gain of this antenna is $9\,dBi$ and its radiation efficiency approximately 50%. The reduced efficiency of the four-element array is attributed to the losses on the artificial transmission lines.

Finally, three different E-plane measured radiation patterns of the four-element array across its enhanced operating bandwidth are presented in Fig. 3.31. It has been found that the four-element array scans its main radiating beam with frequency from the backward direction to the forward direction. Specifically, in Fig. 3.31 the radiation patterns at frequencies $2.31\,GHz$, $2.40\,GHz$ and $2.49\,GHz$ are presented. At $2.31\,GHz$ the four-element array scans its beam at -25^o. This beam scans with frequency towards broadside, where the beam is scanned at $2.40\,GHz$, and then through broadside towards positive scanning angles (at $2.49\,GHz$ that beam is scanned at 30^o). The efficiency of

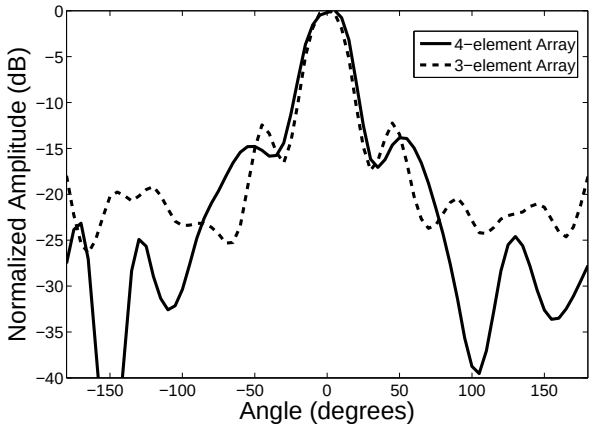

Figure 3.30: Measured E-plane radiation patterns of the three-element and four-element patch arrays at $2.4\,GHz$.

this antenna across the entire operating bandwidth and all the scanning angles remains roughly constant. Therefore, the proposed four-element array that employs the artificial interconnecting lines could be used in application that require beam scanning with frequency (such as radar applications). The major advantage of the proposed array, as compared to other metamaterial-based beam-scanning arrays [83], [84], [92], is that it scans its beam through broadside without any significant reduction of the total achieved radiation efficiency due to either mismatching effects [92] or increased ohmic losses.

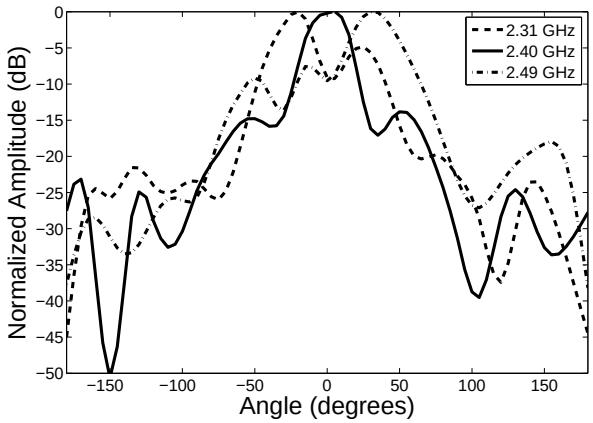

Figure 3.31: E-plane radiation patterns of the four-element array at frequencies $2.31 GHz$, $2.40\,GHz$ and $2.49\,GHz$.

Chapter 4

A Metamaterial Low-Profile Monopole-Like Antenna

The analysis, design and measurement of novel, low-profile, small-footprint folded monopoles employing planar metamaterial phase-shifting lines is presented in this chapter. These lines are composed of fully-printed spiral elements, that are inductively coupled in order to exhibit an effective high-μ property. An equivalent circuit for the proposed structure is presented, validating the operating principles of the antenna and the metamaterial line. The impact of the antenna profile and the ground plane size on the antenna performance are investigated using accurate full-wave simulations. A $\lambda/9$ antenna prototype, designed to operate at $2.36\,GHz$, is fabricated and tested on both electrically large and small ground planes, achieving on average 80% radiation efficiency, 5% ($110\,MHz$) and 2.5% ($55\,MHz$) $-10\,dB$ measured bandwidths, respectively, and fully omnidirectional, vertically polarized, monopole-type radiation patterns.

4.1 Introduction

Folded dipoles and monopoles are well-known radiators [112] that provide increased radiation resistance, as compared to the original dipoles and monopoles, while retaining the same self-resonance. A self-resonant folded monopole of N arms is formed when $N-1$ shorted $\lambda/4$ monopoles are placed in close proximity to a driven monopole, with the open ends of all the N wires being connected. At resonance the input radiation resistance of

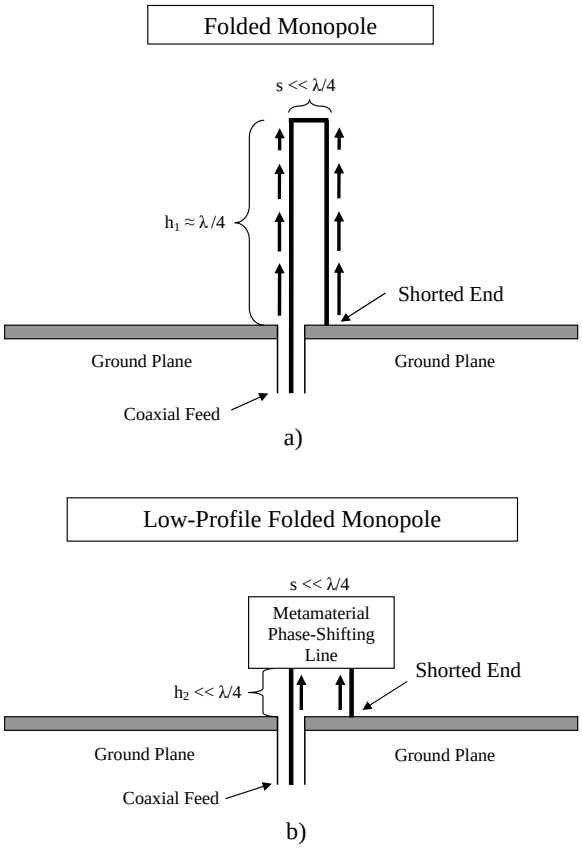

Figure 4.1: Schematic representation of a) the typical folded monopole of height $h_1 = \lambda/4$ and b) a low-profile folded monopole with an embedded metamaterial phase-shifting line.

the N-arm folded monopole is

$$R_{rad,fold-mono} \approx N^2 R_{rad,mono} \tag{4.1}$$

where $R_{rad,mono}$ is the radiation resistance of the single monopole. A coaxially fed folded monopole composed of two arms is shown in Fig. 4.1(a). The operation of a folded monopole can be assumed as a superposition of a non-radiating transmission line mode (contradirectional currents on the wires of the monopole) and an antenna mode (codirectional currents on the wires of the monopole) [112]. The resonance condition of the first mode is $\Delta\varphi_{tl} = n2\pi,\ n = 0, \pm1, \pm2...$, while the resonance condition for the antenna mode is $\Delta\varphi_{ant} = (n + 1/2)2\pi,\ n = 0, \pm1, \pm2...$, where $\Delta\varphi$ denotes the phase shift of currents flowing between the feeding and the shorting points of the wire that forms the folded monopole (effective electrical length of the wire). The total current distribution on a radiating folded monopole is schematically shown in Fig. 4.1(a), suggesting that the antenna mode becomes dominant.

The radiation resistance of a $\lambda/4$ monopole is approximately $R_{mono} = 36.5\,\Omega$. According to equation (4.1), the radiation resistance of the $\lambda/4$ folded monopole of Fig. 4.1(a) is expected to be $R_{fold-mono} = 146\,\Omega$. This feature makes the full-length $\lambda/4$ folded monopole inappropriate for applications that involve $50\,\Omega$ feeding lines. Nevertheless, the folded monopole configuration has been proved extremely useful in the design of electrically small antennas that involve low-profile arms with much smaller radiation resistances than that of the $\lambda/4$ monopole. In these cases, the self-resonance of the antenna is secured either by loading the low-profile monopoles with discrete or distributed inductance (properly meandered radiating wires) or by increasing the monopoles capacitance to the ground. An inclusive study of electrically small folded monopoles, in either loaded or meandered and multiple-arm configurations, has been presented in [113].

With the advent of metamaterial structures a novel approach for the design of self-resonant, low-profile folded monopoles has been proposed, originally in [114], [115], [116] and very recently in [117]. According to this approach, the use of sub-wavelength metamaterial phase-shifting lines is exploited in order to connect the radiating posts of the folded monopoles and satisfy a self-resonance condition, as shown in Fig. 4.1(b). Specifically, in the antenna designs of [114], [115], [116], [117] different numbers of radiating posts have been connected through zero-degree phase-shifting $L - C$ loaded transmission lines that enforce the posts to radiate in-phase, resulting in a folded-monopole-like behavior.

In the present chapter, a new approach for the design of self-resonant, low-profile folded monopoles is reported. In this approach, the use of subwavelength metamaterial phase-shifting lines is exploited in order to connect the radiating low-profile posts of two-arm folded monopoles and enforce the actual resonance condition of the supported antenna mode. In the proposed antenna design, the phase-shifting line is implemented through a single line that is composed of fully-printed, inductively coupled resonators that synthesise a medium supporting mostly slow waves and characterized by an effective high-μ property. In fact, the embedded phase-shifting lines are employed in order to insert the phase-shift required to be added to the phase of the currents flowing on the radiating, low-profile posts in order for the resonance condition of the antenna mode $\Delta\varphi_{ant} = \pi$ to be established between the feeding and shorting points, in contrast to the antenna designs of [114], [115], [116], [117] in which the metamaterial phase-shifting lines were employed to insert a zero-degree phase shift and enforce the radiating posts to radiate in-phase. As compared to the folded monopoles investigated in [113], the proposed low-profile folded monopoles do not require any loading with discrete elements (lumped inductors), do not involve any meandered radiating wires (that may impose difficulties in the fabrication procedure), and exhibit much smaller footprint than that of the capacitively loaded monopoles.

A general description of the proposed class of self-resonant, coaxially-fed low-profile folded monopoles is presented in section 4.2 of the chapter. A detailed description of the employed phase-shifting lines and their operation when embedded within the proposed folded monopoles is presented in section 4.3, while a simplified equivalent circuit for the proposed antenna is presented in section 4.4. Subsequently, an initial implementation of the proposed low-profile folded monopole, designed to operate at $2.4\,GHz$ and built on an electrically large ground plane, together with simulated and measured results are reported in section 4.5. In section 4.6, it is shown that the employed phase-shifting lines can be used to enforce the antenna mode irrespectively of the profile of the radiating posts and the radiation properties of ultra low-profile folded monopoles are investigated. In section 4.7, the impact of the ground plane against which the proposed antennas are built is examined. Based on the results of this study, the measurement of two optimal antenna designs are reported in the same section. In section 4.8 a microstrip-fed version of the proposed antenna is presented and, finally, in section 4.9 the electromagnetic coupling between pairs of the proposed antenna is assessed.

4.2 Proposed Antenna Design - General Description

A general description of the proposed antenna design that effectively implements the antenna model of Fig. 4.1(b) is reported in this section. The side view of the proposed antenna is depicted in Fig. 4.2(a). As shown in Fig. 4.2(a), the antenna is mainly composed of two vertical posts, that constitute the main radiation mechanism of the antenna. The bottom of the first post is directly connected to a feeding port that is a coaxial cable in this case (feeding post). The second post is connected directly to the ground plane against which the antenna is fed, at an electrically small distance from the first post, similarly with the folded monopoles of Fig. 4.1 (shorting post). These two posts are connected through a spiral-based, metamaterial, phase-shifting line that is presented in detail in the next section. In the space around these two posts, three layers of different materials are present. Two of them, these represented with grey color in Fig. 4.2(a), are dielectric substrates of dielectric constant ϵ_r and heights h_{sub1} and h_{sub2}, that are used in order to bear the ground plane against which the antenna is fed and the printed metamaterial phase-shifting line, respectively. The space between these two substrates is filled with air or any other material with dielectric constant close to that of the free space ϵ_0 (*e.g.* Rohacell foam) that can be employed to hold the two substrates apart at a certain distance h_{air}. The total profile of the antenna is $h = h_{sub1} + h_{air} + h_{sub2}$.

The top view of the proposed antenna is shown in Fig. 4.2(b). It mainly depicts the metalization that is printed on the top side of the upper dielectric substrate of Fig. 4.2(a). The metalization is composed of two square pads that directly load the two posts, and the employed metamaterial phase-shifting line that is composed of two inductively coupled spiral resonators directly attached to the square pads. The operation of the phase-shifting line will be explicitly explained in the following section. The total dimensions of the metalization printed on the top side of the upper dielectric substrate are $d_{x,total} \times d_{y,total}$. For the cases that will be discussed in the following text, these dimensions are always much smaller than the operating wavelength ($d_{x,total}, d_{y,total} << \lambda$), ensuring that the employed metamaterial phase-shifting line is always of subwavelength dimensions and the two vertical posts are separated by a subwavelength distance. In contrast to all the antenna designs investigated in [113], in the proposed antenna design there is no dc connection between the two vertical posts. The latter feature, apart from being a major differentiator of the proposed antenna, could be potentially exploited for the design of easily fabricated reconfigurable monopoles. Such reconfigurable folded

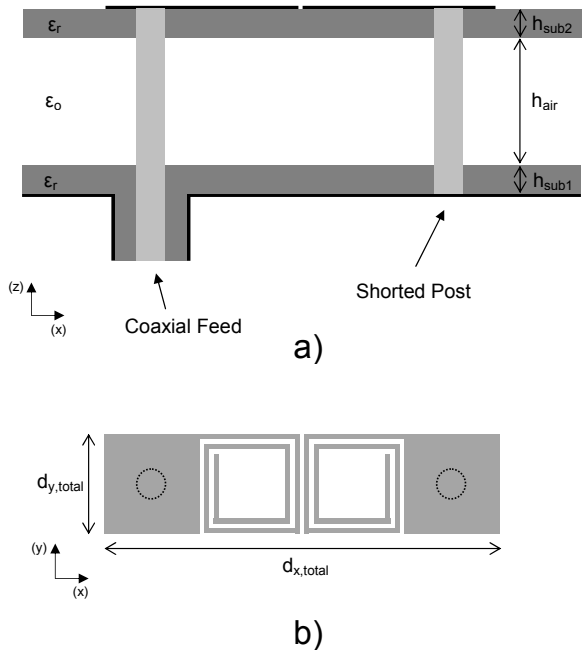

Figure 4.2: a) Side view and b) top view schematic of the proposed low-profile antenna.

monopoles could be designed if the employed phase shifting lines were loaded with any dc-controlled reactive elements (such as PIN diodes or varactors). In that case, the biasing dc signal would be multiplexed with the RF at the input port of the antenna and no additional biasing circuitry would be required.

The radiation resistance of the proposed antenna at its self-resonance can be effectively approximated under the assumption that the currents flowing through the two posts are equal in magnitude and constant across the length of the posts (this assumption is valid given the low-profile characteristics of the proposed antenna). In that case, the radiation resistance of any of the two posts is given by equation (4.2) [112]

$$R_{rad,post} = 160\pi^2 \left(\frac{h}{\lambda}\right)^2 \tag{4.2}$$

and the total radiation resistance of the proposed antenna can be approximated, using equation (4.1), as

$$R_{rad,in} \approx 640\pi^2 \left(\frac{h}{\lambda}\right)^2 . \tag{4.3}$$

Equation (4.3) suggests that the proposed antenna design, at its self-resonance, could achieve a radiation resistance of the order of 50 Ω even for a profile of $h \approx \lambda/12$.

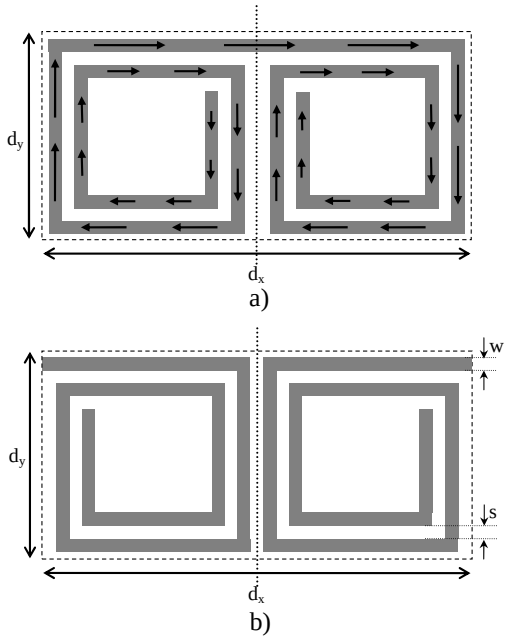

Figure 4.3: Unit cell of a) a free standing DSR and b) a DSR participating in an array.

4.3 Spiral-Based Phase-Shifting Lines

An antenna design similar to the low-profile folded monopole of Fig. 4.1(b) requires a metamaterial phase-shifting line that would be compact ($s << \lambda/4$), non-radiating, and preferably planar, fully-printed and low-loss. It is reminded at this point that the purpose of this phase-shifting line is to add the required phase in order for the flowing on the radiating posts currents to satisfy the resonance condition of the antenna mode of a typical folded monopole ($\Delta\varphi_{ant} = \pi$). For the design of such a phase-shifting line, the use of tightly coupled resonators can be considered. Nevertheless, for this application, the wanted supported mode is not the backward wave mode discussed in chapter 3, but a slow wave mode instead.

For the implementation of the required slow waves, the use of the DSR, similar with that of Fig. 4.3(a), is also proposed. Nevertheless, in this case different polarities, as compared to these considered in chapter 3, between adjacent spirals will be required to achieve the required operating mode. Specifically, the relative polarities of adjacent tightly coupled spirals in this case will be similar with that depicted in Fig. 4.3(b).

The equivalent circuit of the DSR of Fig. 4.3(a) is depicted in Fig. 4.4(a), while that of the configuration of Fig. 4.3(b) is depicted in Fig. 4.4(b). For a DSR employed

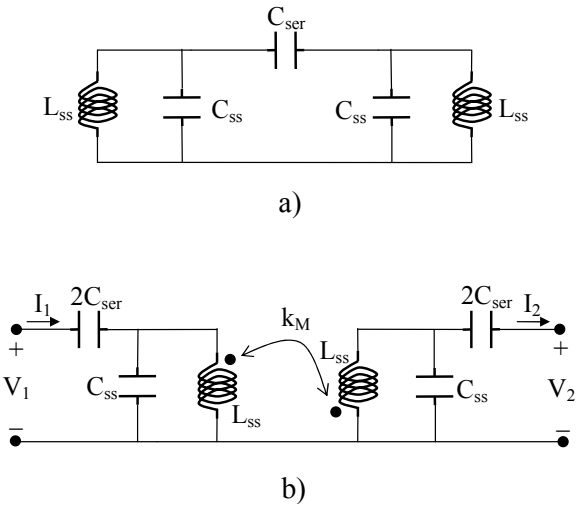

Figure 4.4: Equivalent circuit representation of the unit cells of a) Fig. 4.3(a) and b) Fig. 4.3(b).

in a non-grounded configuration, printed on a substrate of dielectric constant $\epsilon_r = 2.2$, and designed to operate at the $2.4\,GHz$ band, with $d_x = 8.2\,mm$, $d_y = 3.8\,mm$ and $w = s = 0.2\,mm$, the involved equivalent circuit parameters have been found to be $L_{ss} = 24.8\,nH$, $C_{ss} = 0.085\,pF$ and $C_{ser} = 0.06\,pF$.

For reasons of completeness, it is reminded that, in the general case, the periodic analysis of the configuration of Fig. 4.3(b) and the equivalent circuit of Fig. 4.4(b) can provide non-trivial solutions both for backward and forward slow waves, depending on the sign of the coupling coefficient k_M (as also shown in Fig. 4.5 and Fig. 4.6). Nevertheless, the specific configuration secures an optimized (maximized) positive coupling coefficient that enables the forward slow waves to become dominant.

Finally, in order to quantify the propagation characteristics along a single unit cell identical with that of Fig. 4.3(b), its transmission magnitude and phase, obtained through the analysis of the equivalent circuit of Fig. 4.4(b), are presented in Fig. 4.7. These results suggest that the single unit cell exhibit satisfying transmission for all the points of its dispersion curve. Across this bandwidth, the single unit cell could provide any phase-shift between 0^o and -180^o. Therefore, the single unit cell of Fig. 4.3(b) could be used as phase-shifting line for the proposed low-profile folded monopole of Fig. 4.1(b).

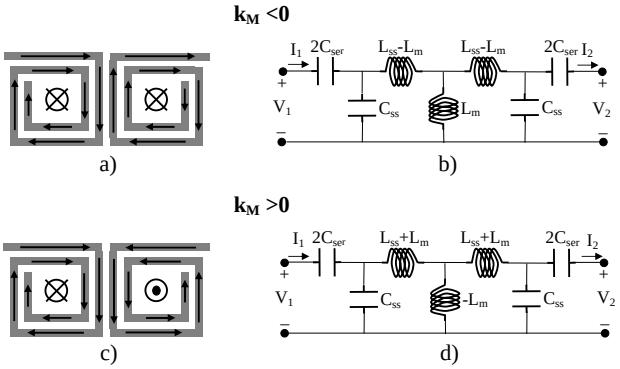

Figure 4.5: Coupling scenarios for a pair of spirals and equivalent circuit representations. L_{ss} corresponds to the self-inductance of each of the spirals and $L_m = |k_M|L_{ss}$ to the absolute value of their mutual inductance.

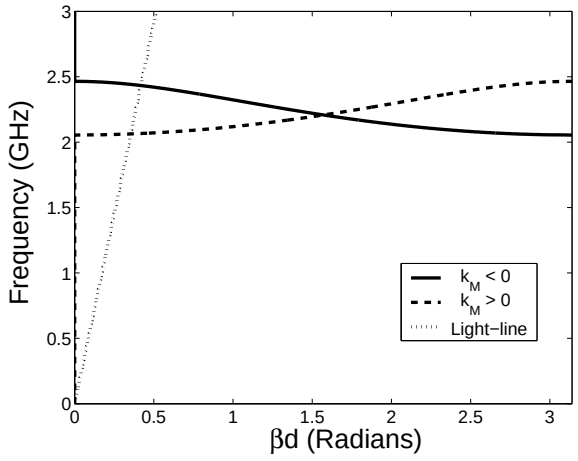

Figure 4.6: Dispersion curves of the unit cell of Fig. 4.4(b) for positive and negative values of the coupling coefficient k_M.

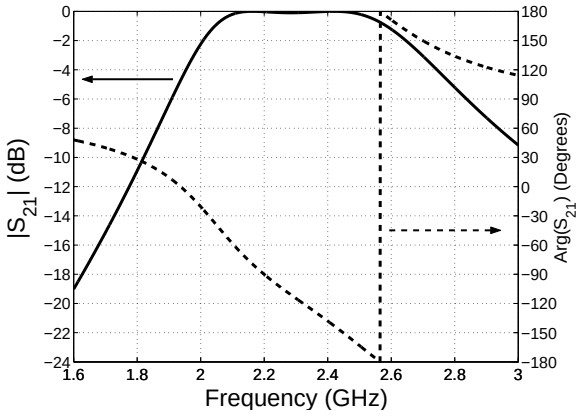

Figure 4.7: Transmission magnitude and phase through a single unit cell similar with that of Fig. 4.4(b) for a positive coupling coefficient ($k_M > 0$).

4.4 Equivalent Circuit

Given the general description of the proposed antenna and the analysis of the employed spiral-based phase-shifting lines, the extraction of the equivalent circuit of the proposed low-profile folded monopoles is possible. This equivalent circuit, that could be used as a design tool for this type of antennas, is composed of three discrete entities; the two vertical posts and the phase-shifting line. Even though the two posts slightly differ from each other (the first is coaxially fed and the second is directly connected to the ground plane), for reasons of simplicity and without significantly affecting the final results, they will be considered identical and they will be both treated as coaxially fed monopoles. Regarding the spiral-based line, it will be modeled according to the equivalent circuit of Fig. 4.4(b).

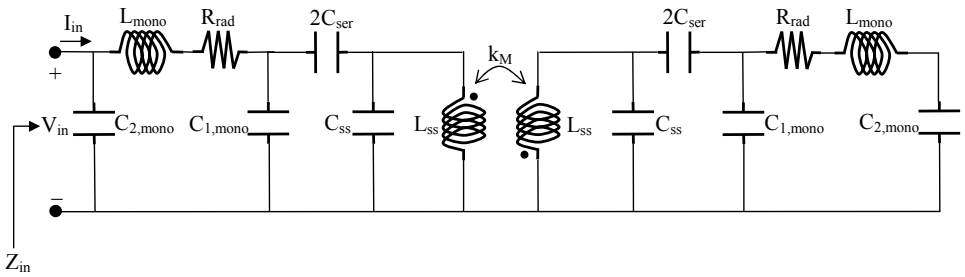

Figure 4.8: Equivalent circuit of the proposed low-profile folded monopole antenna.

The proposed equivalent circuit for the reported antenna design is depicted in Fig.

4.8. The first and the last parts of the proposed equivalent circuit correspond to the two vertical monopoles. The inductance L_{mono} of the two posts depends on their length and their radius and can be calculated, assuming the quasi-static analysis of [106], using equation (4.4).

$$L_{mono} = 0.2 \cdot h \cdot \left[\ell n \left(\frac{4h}{d_{post}} \right) - \frac{3}{4} \right] \quad [nH]\,. \tag{4.4}$$

Assuming that the vertical posts are lossless, the only resistive component involved in their equivalent circuit is their radiation resistance R_{rad}. The radiation resistance of each post can be calculated, when considering it to be short and be driven by a constant current, using equation (4.2). Finally, the capacitances $C_{1,mono}$ and $C_{2,mono}$ involved in the equivalent circuit of Fig. 4.8 represent the internal capacitance of each monopole, that defines together with L_{mono} the input impedance and the self-resonances of the monopole, and its external capacitance, that is encountered when a monopole is fed coaxially against a ground plane, respectively. These capacitances depend on the loading of each of the posts (surrounding dielectric material, loading pads etc) and the most effective way to be calculated are through the full-wave simulation of the coaxially fed short monopole and the full-wave estimation of its self-resonance ω_{res} and its anti-resonance $\omega_{anti-res}$. Specifically, given that the series branch $L_{mono} - C_{1,mono}$ defines the resonance of the monopole and the parallel combination of the branch $L_{mono} - C_{1,mono}$ with the capacitance $C_{1,mono}$ defines its anti-resonance, the capacitances $C_{1,mono}$ and $C_{2,mono}$ can be approximated, when ω_{res} and $\omega_{anti-res}$ have been estimated through a full-wave simulation, using equations (4.5) and (4.6), respectively.

$$C_{1,mono} \approx \frac{1}{\omega_{res}^2 L_{mono}} \tag{4.5}$$

$$C_{2,mono} \approx \frac{C_{1,mono}}{\omega_{anti-res}^2 L_{mono} C_{1,mono} - 1} \tag{4.6}$$

The remaining lumped elements involved in the equivalent circuit of Fig. 4.8 refer to the employed phase-shifting line. Both the impact and the way their values can be estimated have been reported in section 4.3. Therefore, the only parameter involved in the equivalent circuit that remains to be quantified is the inductive coupling coefficient k_M. According to [32], when the transmission through a weakly excited pair of coupled resonators is known, the coupling coefficient can be calculated using equation

$$k_M = \frac{f_2^2 - f_1^2}{f_2^2 + f_1^2}, \tag{4.7}$$

where f_1 and f_2 are the two resonances of the coupled configuration (frequencies at which the transmission through the coupled pair is maximized). At these frequencies the transmission phase sign is altered. Consequently, in cases that only the transmission through a strongly excited pair is known, as in Fig. 4.7, the coupling coefficient can be approximated by calculating equation (4.7) for two frequencies that correspond to transmission phases that differ by 180^o.

Considering the antenna model of section 4.2 with a profile of $\lambda/9$ and the spiral dimensions reported in section 4.3, the parameters of the presented equivalent circuit assume the following values; for the short monopoles $L_{mono} = 9.3\,nH$, $R_{rad} = 19\,\Omega$, $C_{1,mono} = 0.25\,pF$ and $C_{2,mono} = 0.29\,pF$, and for the metamaterial phase-shifting line $L_{ss} = 24.8\,nH$, $C_{ss} = 0.081\,pF$, $C_{ser} = 0.06\,pF$ and $k_M = 0.2$. It is pointed out that all the values of the parameters associated with the operation of the phase-shifting line are dependent on the distance of the line from the employed ground plane. Therefore, different antenna profiles will result in different values for these parameters.

The input impedance of the considered $\lambda/9$ antenna design, calculated using the proposed equivalent circuit and also using a full-wave Ansoft HFSS simulation, is shown in Fig. 4.9 and Fig. 4.10. The equivalent circuit results are in good agreement with the full-wave results. The major disagreement between them concerns the values of the calculated impedance around the anti-resonances of the structure. This disagreement should be attributed to the modeling of the posts and the phase-shifting line as lossless structures and also to the fact that the two posts were considered identical. However, good agreement is achieved for the resonances that are of our interest.

4.5 Low-Profile Antenna at $2.4\,GHz$

4.5.1 Antenna Parameters and Full-wave Simulations

The parameters that were considered in the previous sections for the profile of the folded monopole and the dimensions of the spirals are used in this section for the simulation and fabrication of an initial prototype of the proposed low-profile antenna that would operate at approximately $2.4\,GHz$. The profile of this initial antenna prototype has been chosen to be approximately $\lambda/9$ in order to ensure that, according to equation (4.3), the antenna prototype would exhibit a decent radiation resistance ($\approx 50\,\Omega$) and, therefore, could be easily matched to a $50\,\Omega$ feeding port (SMA connector). This $\lambda/9$

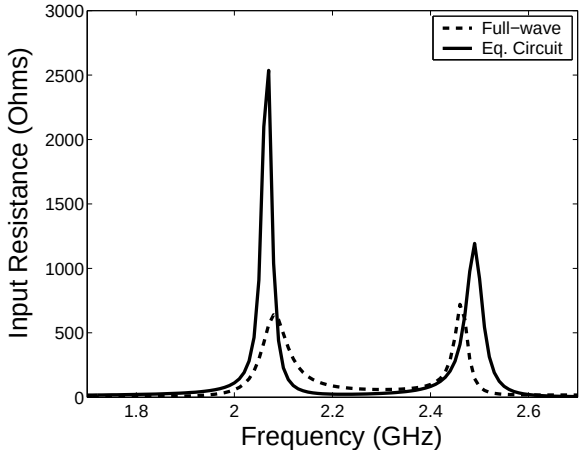

Figure 4.9: Input resistance of the antenna of section 4.2 calculated using the equivalent circuit of Fig. 4.8 and Ansoft HFSS simulations.

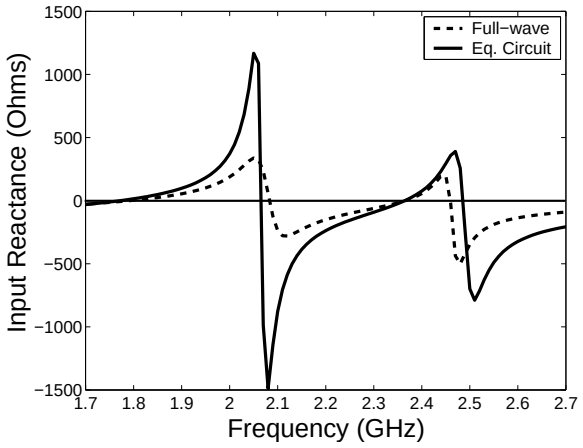

Figure 4.10: Input reactance of the antenna of section 4.2 calculated using the equivalent circuit of Fig. 4.8 and Ansoft HFSS simulations.

monopole is initially built on an electrically large ground plane (the employed ground plane dimensions are $2\lambda \times 2\lambda$). At the targeted operating frequency the wavelength is $\lambda = 125\,mm$. In order to achieve an antenna profile of $h = \lambda/9$, the length of the employed posts is set to be $h_{post} = h_{sub1} + h_{air} + h_{sub2} = 13.8\,mm$. The diameter of the posts is $d_{post} = 0.91\,mm$. This dimension is mainly enforced by fabrication restrictions (core wire of the used coaxial cable). The employed dielectric substrates are of dielectric constant $\epsilon_r = 2.2$ and height $h_{sub1} = h_{sub2} = 2.4\,mm$. Therefore, the distance between the two substrates is set to be, in this initial design, $h_{air} = 9.0\,mm$. Referring to

the top view of the reported design (Fig. 4.2(b)), the total footprint of the antenna is $d_{x,total} \times d_{y,total} = 15.8\,mm \times 3.8\,mm \approx \lambda/8 \times \lambda/33$. The square pads that directly load the posts are of dimensions $3.8\,mm \times 3.8\,mm$.

As far as the metamaterial phase-shifting line is concerned, the double spiral resonators are designed to achieve their first self-resonance (half-wavelength resonators) at $2.34\,GHz$, when placed $13.8\,mm$ above a ground plane and in the presence of all the dielectric layers of Fig. 4.2(a). Referring to Fig. 4.3, this is achieved when $d_x = 8.2\,mm$, $d_y = 3.8\,mm$ and the width of the strips and the gaps between them is set to be $w = s = 0.2\,mm$. The transmission characteristics of this specific phase-shifting line have been already presented in Fig. 4.7.

The proposed antenna was simulated using Ansoft HFSS. The simulated input impedance of the $\lambda/9$ antenna design is depicted in Fig. 4.11. This result suggests that the proposed structure achieves its first self-resonance ($X_{in}(\omega) = 0$ and $\partial X_{in}(\omega)/\partial\omega > 0$) at $1.8\,GHz$. Even though this frequency is out of the band of operation of the employed phase-shifting line (Fig. 4.7), there is some wave transmission through the spirals at this frequency, with a positive phase-shift added to the transmitted waves (assuming that negative phase is added to a forward propagating wave). In fact, what occurs at $1.8\,GHz$ is that the phase-shifting line compensates the negative phase-shift added to the currents when flowing on the radiating posts, resulting in a 0^o phase-shift between the feeding and shorting points. Therefore the resonance condition that is satisfied at $1.8\,GHz$ is that of the transmission line mode.

The second self-resonance of the proposed antenna is achieved at $2.36\,GHz$. The supported currents on the posts at this resonance are depicted in Fig. 4.12. These codirectional currents suggest that this resonance corresponds to the antenna mode of the proposed low-profile folded monopole. Therefore, the electrical length of the structure at $2.36\,GHz$ is of the order of -180^o. According to the calculated transmission phase of the phase-shifting line, shown in Fig. 4.7, the effective electrical length of the phase-shifting line at this frequency is approximately -120^o. Therefore, it is estimated that the effective total length of the radiating posts is approximately -60^o, which is close to the effective length of a line with physical length $2 \times \lambda/9$.

In order to validate the aforementioned arguments regarding the nature of the two self-resonances of the proposed antenna, the transmission of waves from the feeding point to the shorting point of the proposed structure has been simulated using Ansoft HFSS. For this purpose, coaxial ports have been attached to both posts. Similarly to the case of

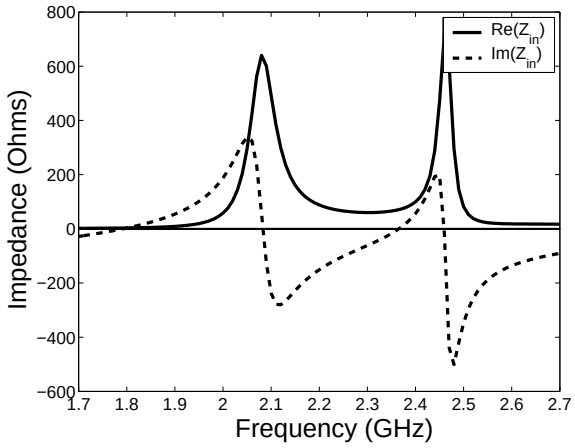

Figure 4.11: Simulated input impedance of the proposed antenna.

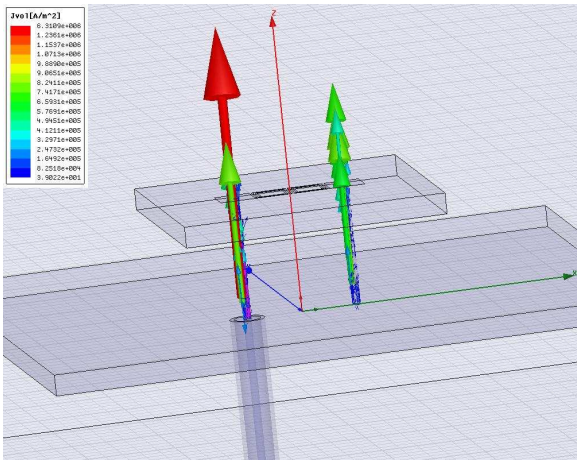

Figure 4.12: Currents on the vertical posts at 2.36 GHz.

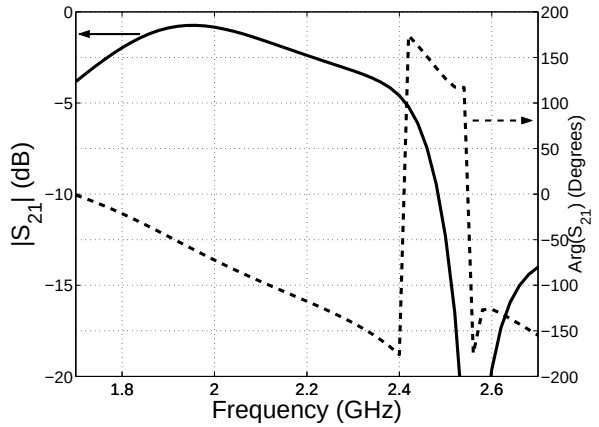

Figure 4.13: Simulated (using Ansoft HFSS) transmission magnitude and phase when both posts are terminated with coaxial ports (none of the ports is shorted in this case).

the extraction of the equivalent circuit, substituting the shorting post with a coaxially fed post does not significantly influence the electromagnetic characteristics of the structure. The results of this full-wave simulation are shown in Fig. 4.13 and certify that the currents at the feeding and shorting points of the proposed antenna are -180^o out of phase in the $2.4\,GHz$ region (antenna mode resonance) while they are in phase in the $1.8\,GHz$ region (transmission line resonance).

4.5.2 Fabrication and Measurement

The proposed antenna, operating at $2.4\,GHz$ and built on an electrically large ground plane, was in turn fabricated and measured. The dielectric material that was used for the two substrates was the $TACONIC\,TLY-5A$ ($\epsilon_r = 2.2$), while the thickness of the layer of air between the two dielectric substrates was relatively accurately maintained using *Rohacell* foam. Note that the dimensions of the lower substrate, on which the ground plane of the antenna was built, were $25cm \times 25cm$, while the dimensions of the upper substrate were slightly greater than the total dimensions the top-loading phase-shifting line. This spiral-based phase-shifting line was printed on the upper side of the top substrate using standard photolithography techniques (chemical etching). A semi-rigid coaxial cable RG 405 was employed to directly feed the antenna. In fact, the core wire of this cable was also used to implement the radiating via that was supposed to be connected directly with the feeding cable. This choice significantly simplified the

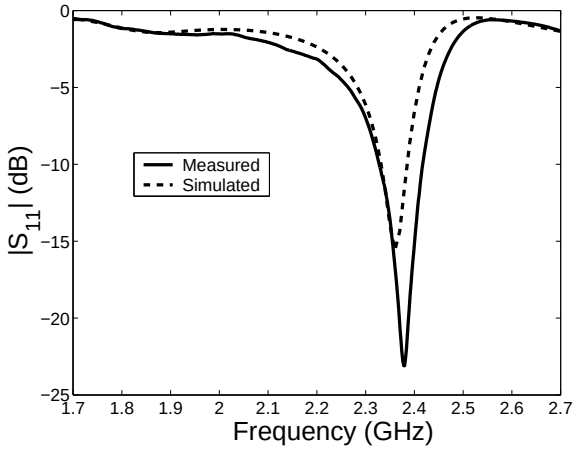

Figure 4.14: Measured and simulated return loss of the proposed antenna.

fabrication procedure. The second radiating post was implemented with a typical wire of the same diameter with that of the core of the coaxial cable.

The simulated and measured return loss (S_{11}) of the proposed antenna is shown in Fig. 4.14. These results suggest that the proposed antenna is well-matched within a fractional bandwidth of 5% ($|S_{11}| < -10\,dB$) around $2.36\,GHz$, while it is not matched at $1.8\,GHz$. This is due to the fact that for the antenna mode a decent radiation resistance, given by equation (4.3), is achieved, while for the transmission line mode resonance the effective resistance is too small for the antenna to be matched to a $50\,\Omega$ feeding line.

The simulated (Ansoft HFSS) and measured radiation efficiency of the proposed antenna together with the measured input reflection coefficient are plotted in Fig. 4.15. The measured efficiency curve has been calculated using the conventional Wheeler cap method [118] and considering constant power losses both in the presence and the absence of the cap. For the implementation of the measurement in the presence of the cap, a half-spherical cap of radius slightly larger than $\lambda/2\pi$ has been backed on the ground plane of the antenna. Even though the employed measurement technique has not been optimized and the method is conceptually an approximate one, the measured and simulated results are in good agreement and they both show that at the lower edge of the operating band ($2.32\,GHz$) rather high radiation efficiencies of the order of 90% can be achieved, while when moving towards the upper edge of the band ($2.42\,GHz$) the radiation efficiency decreases to about 60%, due to the ohmic losses on the employed spiral-based phase-shifting line. This finding is also validated by the results of Fig. 4.13,

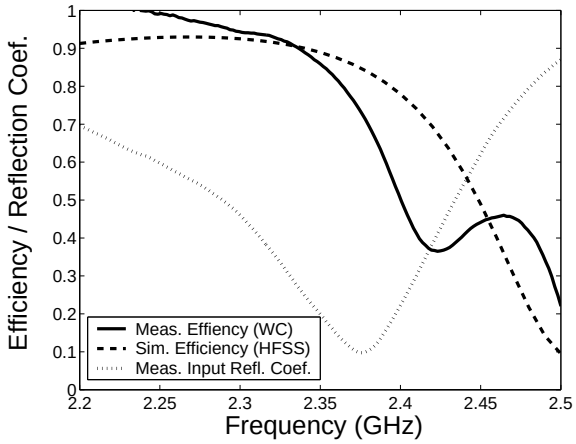

Figure 4.15: Measured (Wheeler cap method) and simulated (Ansoft HFSS) radiation efficiency of the proposed antenna.

that show a rapidly reducing transmission magnitude when moving towards the upper edge of the radiation band. This reduction must be caused by a rapid increase of the ohmic losses on the phase-shifting line, given that the radiation losses are expected to be approximately constant within the radiation bandwidth. Finally, note that the simulated and measured efficiency results are in excellent agreement (the two curves cross) at two frequency points. These two frequencies approximately coincide with the simulated resonance and the anti-resonance of the proposed antenna, as shown in Fig. 4.11. In fact, at these frequencies the measured input reflection coefficient assumes purely real values and the error in the calculation of the measured efficiency is minimized. At the resonance of the investigated antenna, the measured radiation efficiency is 90%.

Finally, the simulated $E-$ and $H-$plane radiation patterns of the proposed low-profile folded monopole are reported in Fig. 4.16 and Fig. 4.17, respectively. Both radiation patterns are affected by the square shape and the electrically large size ($2\lambda \times 2\lambda$) of the ground plane on which the antenna is built. Specifically, the electrically large ground plane tilts the $E-$plane pattern off the endfire direction ($\theta = 90^o$), resulting in a radiation pattern that achieves its maximum at approximately $\theta = 60^o$. Furthermore, its square shape enables the creation of non-negligible standing currents at all its four corners that radiate constructively in the far-field, resulting in a square-like H-plane pattern.

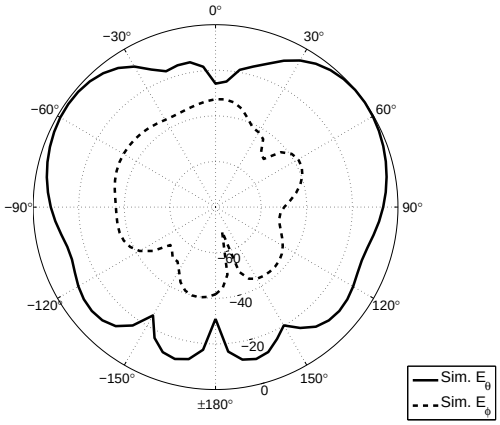

Figure 4.16: Simulated $E-$plane ($xz-$plane) of the proposed low-profile folded monopole, built on a $2\lambda \times 2\lambda$ ground plane.

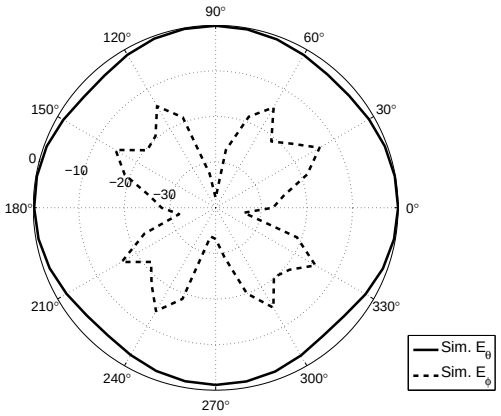

Figure 4.17: Simulated $H-$plane ($xy-$plane) of the proposed low-profile folded monopole, built on a $2\lambda \times 2\lambda$ ground plane.

4.5.3 Q-factor calculation

In this section of the thesis, the Q-factor of the proposed antenna design is reported. For the calculation of the Q-factor the lossless case is considered and equation (4.8) [113], [57] is employed. In equation (4.8), $R(\omega)$ and $X(\omega)$ stand for the resistance and reactance functions at the input of the investigated antennas, respectively, and $R'(\omega)$ and $X'(\omega)$ stand for their first derivatives with respect to frequency.

$$Q(\omega) \approx \frac{\omega}{2R(\omega)} \sqrt{R'(\omega)^2 + \left[X'(\omega) + \frac{|X(\omega)|}{\omega}\right]^2} \tag{4.8}$$

Using equation (4.8) together with full-wave simulations of a lossless antenna model, the Q-factor of the investigated $\lambda/9$ LPFM is found to be $Q \approx 15$. This value is comparable with the Q-factors of the antennas investigated in [113] (in that study, a Q-factor of $Q \approx 17.4$ had been reported for a 2-arm $\lambda/10$ folded monopole), and it is approximately 4 times larger than the Chu limit [54], [57]. In order to provide a intuitive reference for the performance of the proposed antenna, it is pointed out that the lowest Q-factor that has been ever reported in the literature was 1.5 times above the Chu limit [119].

4.6 Towards Ultra Low-Profile Folded Monopoles

The major advantage of the proposed antenna is that it can be designed to be self-resonant, within the operating bandwidth of the phase-shifting line, irrespectively of its profile. Therefore, the proposed model could be used for the design of ultra low-profile, self-resonant antennas with monopole-like radiation properties. In this section, the limits of this possibility are examined by studying different versions of the proposed antenna with decreasing profiles. Specifically, referring to the side view of the proposed antenna (Fig. 4.2(a)), four antenna designs with different values of the parameter h_{air} are considered. For these designs the parameter h_{air} assumes the values $h_{air} = 9\,mm$, $6\,mm$, $2.4\,mm$ and $0\,mm$, respectively, resulting in total antenna profiles of approximately $\lambda/9$, $\lambda/12$, $\lambda/17$ and $\lambda/26$ (at $2.4\,GHz$).

When reducing the profile of the proposed antenna by decreasing the length of the radiating posts, its antenna mode self-resonance is expected to move to a frequency that corresponds to a larger electrical length for the phase-shifting line, or, equivalently, towards the right on the transmission phase diagram of Fig. 4.7. The simulated, using Ansoft HFSS, input resistance and reactance for the aforementioned antennas are presented in Fig. 4.18 and Fig. 4.19, respectively. These results validate that, as far as the second self-resonance of the proposed structure is concerned, the resonant frequency is slightly increased with the decrease of the antenna profile. Exemption to the latter observation consists the $\lambda/26$ antenna design, that achieves its antenna mode resonance at approximately the same frequency with the $\lambda/9$ antenna design. This is due to the phase-shifting line of the $\lambda/26$ antenna design being that close to the ground plane that its transmission properties have changed, as compared to the transmission properties of the phase-shifting lines in the other investigated designs. As far as the first self-resonance is concerned, this resonance is also moving to higher frequencies as the profile of the proposed structure is decreased. Nevertheless, this shift is much more rapid, as compared to the second self-resonance shift. This rapid increment is attributed to the fact that the transmission phase curve of Fig. 4.7 is almost flat before the formulated passband (where the first resonance occurs).

Although the proposed antennas achieve an antenna mode self-resonance within the operating bandwidth of the phase-shifting line for any possible profile, their radiation properties do not remain unchanged with the reduction of their profile. First of all, their radiation resistance decreases proportionally to the ratio $(h/\lambda)^2$, as equation (4.3)

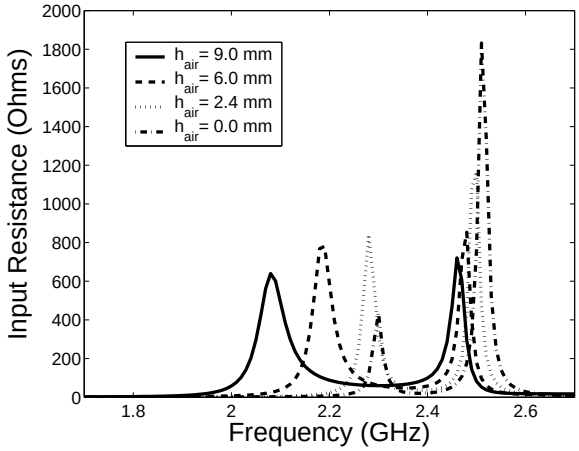

Figure 4.18: Simulated input resistance of four antennas of different profiles.

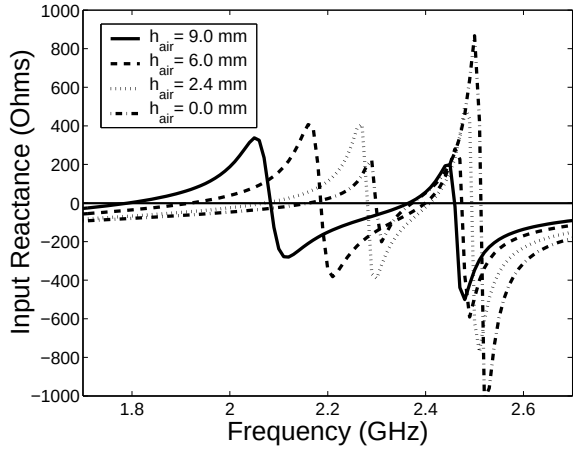

Figure 4.19: Simulated input reactance of four antennas of different profiles.

suggests and is shown in Fig. 4.18. Therefore, ultra low-profile versions of the proposed antenna exhibit too small resistances to be matched to 50 Ω feeding lines. This is shown in Fig. 4.20, where the simulated return losses of the aforementioned antenna designs are plotted. Secondly, as their radiation resistance decreases and their ohmic resistance, that is mainly attributed to the operation of the employed phase-shifting line, remains unchanged, the delivered radiation efficiency also decreases with the reduction of their profile. The simulated radiation efficiencies of the four examined antennas are shown in Fig. 4.21. A proof for the validity of these curves has been shown in section 4.5 and Fig. 4.15, where the simulated curve of the $\lambda/9$ monopole was directly compared with a measured efficiency curve. Finally, the reduction of the profile of the proposed antennas

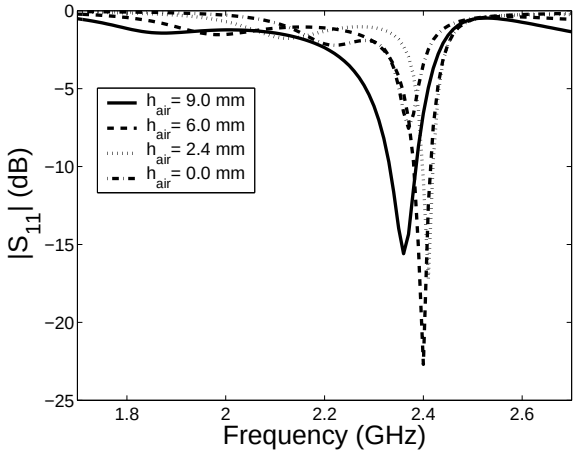

Figure 4.20: Simulated reflection coefficient of four antennas of different profiles.

results in the increase of their quality factor and the reduction of their useful bandwidth, as also shown in Fig. 4.20. An inclusive comparison of the properties of the four antennas under consideration is presented in Table 4.1 and Table 4.2.

Antenna Profile	$h_{air}\ (mm)$	$f_{res}\ (GHz)$	$FBW_{-10\,dB}$	$FBW_{-6\,dB}$
$\lambda/9$	9.0	$2.365\,GHz$	3 %	5 %
$\lambda/12$	6.0	$2.398\,GHz$	2 %	3 %
$\lambda/17$	2.4	$2.409\,GHz$	1 %	2 %
$\lambda/26$	0.0	$2.372\,GHz$	–	1 %

Table 4.1: Resonance and fractional bandwidth of the four antennas of different profiles.

Antenna Profile	$h_{air}\ (mm)$	$R_{in}\ (\Omega)$ (Full-wave)	$R_{rad}\ (\Omega)$ (Eq. (4.3))	Sim. Efficiency
$\lambda/9$	9.0	70	78	88 %
$\lambda/12$	6.0	57	44	69 %
$\lambda/17$	2.4	38	22	38 %
$\lambda/26$	0.0	19	9	15 %

Table 4.2: Input resistance, radiation resistance and simulated radiating efficiency (at resonance) of the four antennas of different profiles.

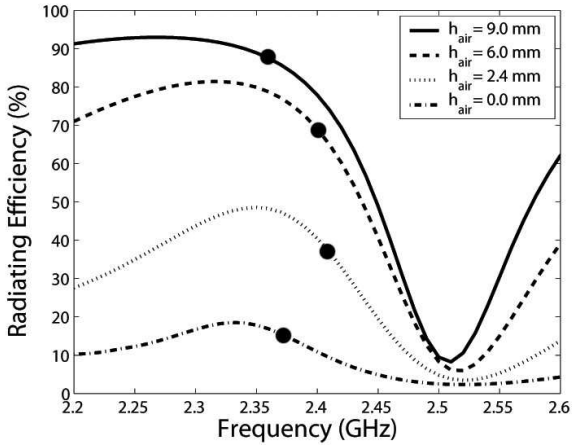

Figure 4.21: Simulated radiation efficiency of four antennas of different profiles. The dots on the traces denote the resonance of each antenna design.

4.7 Impact of the Ground Plane

4.7.1 Reducing the Ground Plane Size

The ground plane against which the proposed low-profile folded monopoles are fed has a major impact on the performance of the antennas. Up to this point, all the investigated monopoles have been considered to be on an electrically large square ground plane of size $2\lambda \times 2\lambda$. In this section, the exact impact of the employed ground plane size on the operation and the radiation properties of the proposed structure is studied by investigating several versions of the proposed antenna built on ground planes of different sizes.

In Fig. 4.22 the simulated input reactance of the $\lambda/9$ antenna built on square ground planes of five different sizes is plotted. The largest of these ground planes is $2\lambda \times 2\lambda$ and the smallest is $\lambda/8 \times \lambda/8$. These results suggest that for any ground plane larger than $\lambda/2 \times \lambda/2$ the self-resonance of the antenna is not perturbed. Nevertheless, for smaller ground planes the self-resonance of the antenna changes, while for extremely small ground planes (*i.e.* $\lambda/8 \times \lambda/8$) the resonance tends to vanish. This conclusion is also validated by the results of Fig. 4.23, where the simulated return losses of the five antennas are plotted. For this reason, it is reasonable to suggest that the proposed folded monopoles should be built on at least $\lambda/2 \times \lambda/2$ large ground planes in order for the ground plane not to significantly and destructively affect the properties of the antenna.

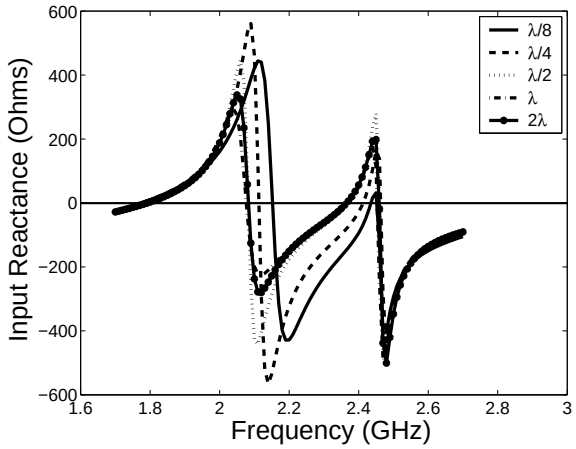

Figure 4.22: Simulated input reactance of the $\lambda/9$ folded monopole built on ground planes of different sizes.

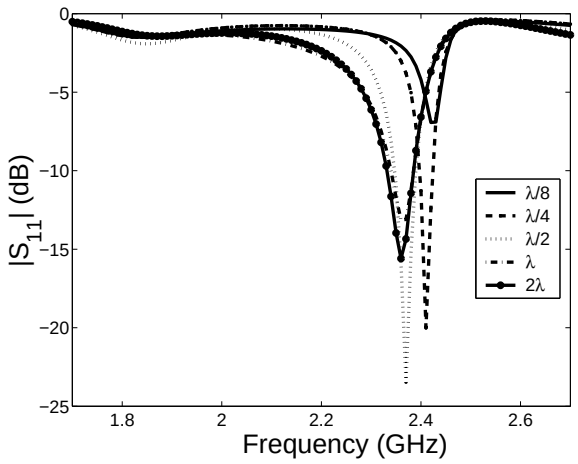

Figure 4.23: Simulated input reflection coefficient of the $\lambda/9$ folded monopole built on ground planes of different sizes.

Figure 4.24: Photograph of the proposed $\lambda/9$ folded monopole built on a $\lambda/2 \times \lambda/2$ ground plane.

4.7.2 Antenna Designs on a $\lambda/2 \times \lambda/2$ Ground Plane

Based on the conclusion of the study on the impact of the ground plane size to the input impedance of the proposed antenna, the fabrication and measurement of two antenna designs built on a $\lambda/2 \times \lambda/2$ ground plane is reported in this section.

$\lambda/9$ folded-monopole on a $\lambda/2 \times \lambda/2$ ground plane

The first of the two antennas reported in this section is a $\lambda/9$ folded-monopole built on a $\lambda/2 \times \lambda/2$ ground plane. Other than the ground plane size, the antenna parameters are identical with those of the antenna reported in section 4.5. Besides, a sleeve balun has been used to coaxially feed the antenna and ensure that the feeding cable in not radiating. A photograph of the fabricated prototype is depicted in Fig. 4.24.

The simulated and measured return losses of this antenna design are shown in Fig. 4.25. A 2.5% $-10\,dB$ and a 4% $-6\,dB$ fractional bandwidths were measured for this design. These bandwidths are smaller (approximately by a factor of 2) than those measured for the antenna fed against the $2\lambda \times 2\lambda$ large ground plane. As far as the radiation patterns are concerned, the simulated and measured $E-$ and $H-$plane patterns of an-

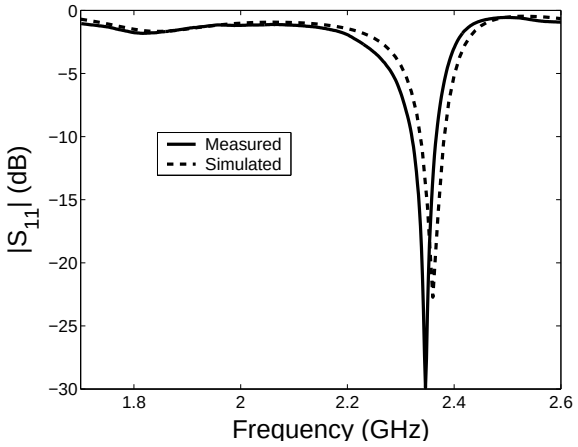

Figure 4.25: Measured and simulated return loss of the $\lambda/9$ folded monopole built on a $\lambda/2 \times \lambda/2$ ground plane.

tenna are shown in Fig. 4.26 and Fig. 4.27, respectively. It is noted that the measured $E-$plane pattern is not tilted off the $\theta = 90^o$ direction, as was for the antenna built on the large ground plane, and is similar to the doughnut-shaped radiation patterns of conventional dipoles, with the exception of the relatively high cross-polarization levels that have been measured in the $\theta = 0^o$ and $\theta = 180^o$ directions and are attributed to the radiation of the edges of ground plane. Also, the measured $H-$plane for this design is almost perfectly omnidirectional, as opposed to the antenna of section 4.5 where the standing currents on the corners of the large ground plane affected the $H-$plane pattern. Radiation efficiencies of the order of 85% were measured for this antenna using the Directivity/Gain comparison method. Specifically, by measuring the full 3-D radiation patterns with an angular step of 5^o in both the $\theta-$ and $\phi-$planes, a maximum directivity of 2.57 dBi and a maximum gain of 2 dBi were measured at the resonance of the antenna, yielding an efficiency value of 87.7%. This value is of the same order with the efficiency values measured using the Wheeler cap method for the antenna built on the $2\lambda \times 2\lambda$ large ground plane. Similarly with that antenna, the measured efficiency values decreased towards the upper edge of the operating band.

$\lambda/17$ folded-monopole on a $\lambda/2 \times \lambda/2$ ground plane

The second low-profile antenna built and measured on a $\lambda/2 \times \lambda/2$ ground plane was a $\lambda/17$ folded-monopole. For this antenna, the thickness of the air layer between the two

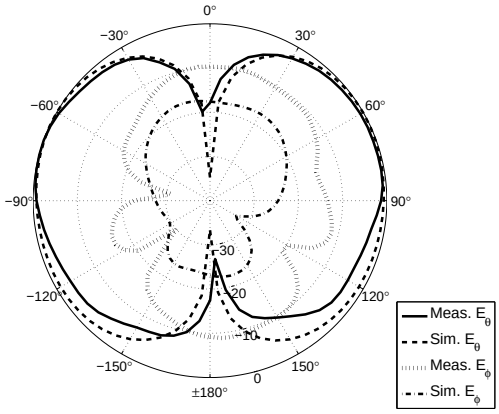

Figure 4.26: Measured and simulated $E-$plane radiation pattern of the $\lambda/9$ folded monopole built on a $\lambda/2 \times \lambda/2$ ground plane.

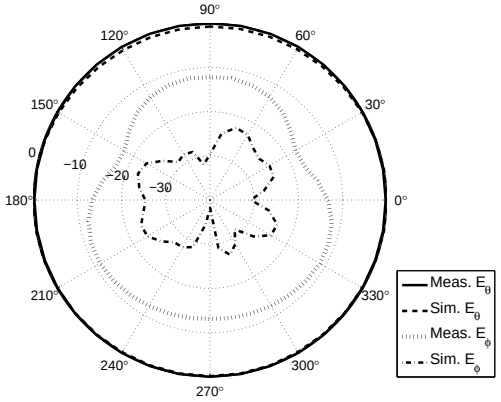

Figure 4.27: Measured and simulated $H-$plane radiation pattern of the $\lambda/9$ folded monopole built on a $\lambda/2 \times \lambda/2$ ground plane.

dielectric layers has been set to $2.4\,mm$. According to the conclusions of section 4.6, further reducing the distance of the spiral-based lines from the ground plane affects the properties of the phase-shifting lines. Therefore, the $\lambda/17$ folded-monopole is among the very ultra low-profile antenna designs that can be obtained using the proposed approach. A photograph of the fabricated prototype is shown in Fig. 4.28

The simulated and measured return losses of this antenna are shown in Fig. 4.29. These results suggest that the $\lambda/17$ antenna design does not exhibit satisfying input resistance to be well-matched to a $50\,\Omega$ feeding line. In fact, equation (4.3) suggests that the theoretically estimated radiation resistance for this profile is only $22\,\Omega$. Nevertheless, a measured $-8\,dB$ return loss is achieved at $2.45\,GHz$. For this frequency, the simulated and measured $E-$ and $H-$plane radiation patterns are shown in Fig. 4.30 and Fig. 4.31, respectively. These radiation patterns show that even for such low profiles the monopole-like radiation pattern characteristics are well-retained. Nevertheless, a total radiation efficiency of only 20% was measured (using the full 3-D radiation pattern measurements and the Directivity/Gain comparison method) for this antenna.

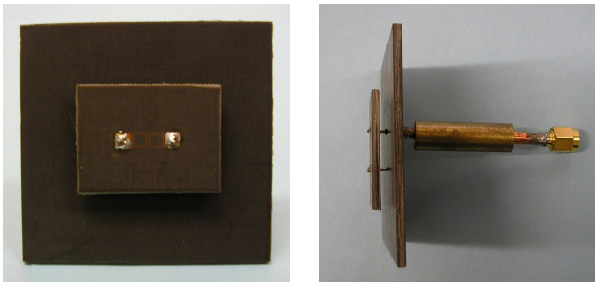

Figure 4.28: a) Top view and b) side view photograph of the $\lambda/17$ low-profile folded monopole built on a $\lambda/2 \times \lambda/2$ ground plane.

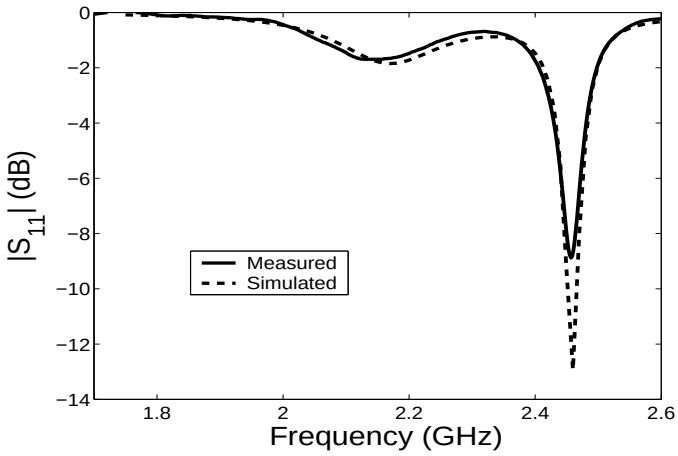

Figure 4.29: Measured and simulated return loss of the $\lambda/17$ folded monopole built on a $\lambda/2 \times \lambda/2$ ground plane.

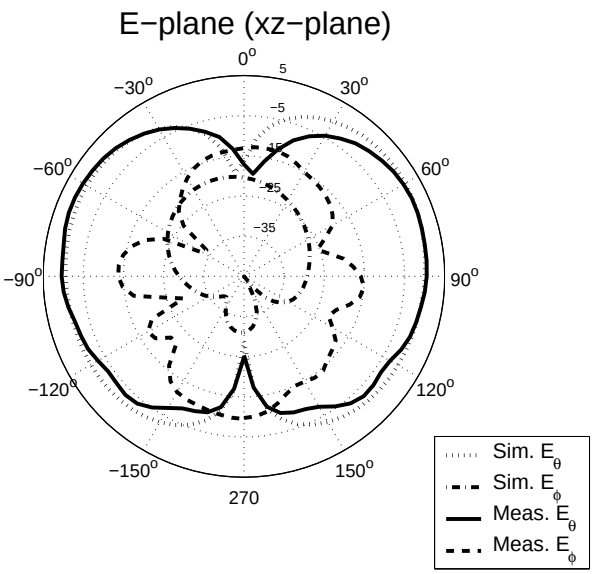

Figure 4.30: Measured and simulated $E-$plane radiation pattern of the $\lambda/17$ folded monopole built on a $\lambda/2 \times \lambda/2$ ground plane.

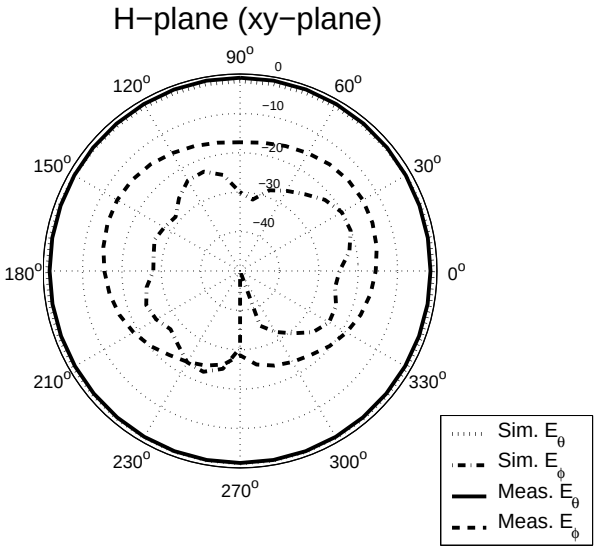

Figure 4.31: Measured and simulated $H-$plane radiation pattern of the $\lambda/17$ folded monopole built on a $\lambda/2 \times \lambda/2$ ground plane.

4.8 Microstrip-fed Low-Profile Folded Monopoles

Up to this point, all the considered low-profile monopoles were coaxially-fed. In many applications, though, the use of microstrip feeding lines may drastically simplify the design and fabrication of the RF front-end. For this reason, the proposed antenna is tested in this section when considered to be fed by a microstrip line.

The schematic of the proposed microstrip-fed low-profile folded monopole is depicted in Fig. 4.32. In fact, the only difference between this antenna and the coaxially-fed monopole is that instead of the antenna to be fed below its ground plane, it is fed from above the ground plane, using a 50Ω microstrip line. This slightly reduces the total length of the radiating posts, resulting in a slightly reduced radiation resistance, as compared to its coaxially-fed counterpart of the same profile. This feature could be inverted by designing the feeding line at the other side of the ground plane.

The microstrip-fed low-profile monopole of Fig. 4.32 was built similarly as before. The dielectric material used was again the $TACONIC\,TLY-5A$ ($\epsilon_r = 2.2$). This time the thickness of the substrates was $h_{sub1} = h_{sub2} = 1.15\,mm$, while the ground plane size

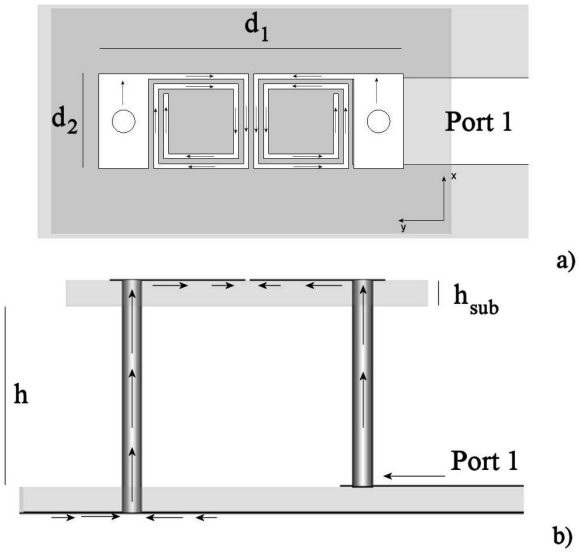

Figure 4.32: a) Top view and b) side view schematic of the microstrip-fed low-profile antenna.

is set to be $\lambda/2 \times \lambda/2$. A photograph of a $\lambda/12$ microstrip-fed low-profile monopole is shown in Fig. 4.33.

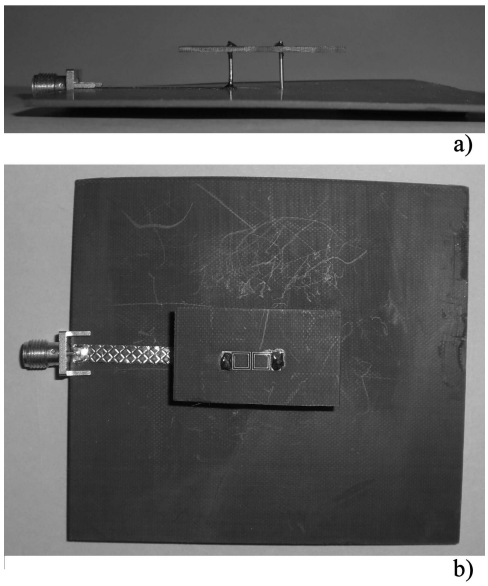

Figure 4.33: a) Side view and b)top view photograph of the microstrip-fed low-profile antenna.

The measured and simulated return losses of the antenna of the $\lambda/12$ folded monopole of Fig. 4.33 are depicted in Fig. 4.34. The simulated results were obtained using CST

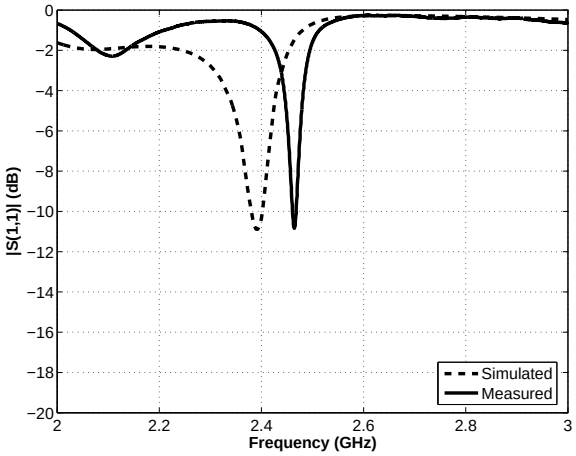

Figure 4.34: Simulated and measured return loss of the microstip-fed single element.

Microstripes. As it can be seen in Fig. 4.34, there is a discrepancy between the simulated and measured results. This can be attributed to two reasons. The first is related to the full-wave simulation of the structure. In particular, the full-wave simulation of the antenna structure together with the feeding line requires a significantly large computational domain that could be hardly solved by the available in the lab computational systems. Therefore, the meshing procedure for this structure was carried out manually, enforcing a less dense mesh. Also, the convergence criteria employed during the solution of the model were not so strict. The second reason that might have caused the observed discrepancy is the fabrication of the antenna and, specifically the microstrip-to-wire transition. It has been experimentally validated that the quantity of soldering material used to solder the radiating wire on the microstrip-line influences the inductance of the wire and, therefore, slightly detunes the final structure.

A second comment on the simulated and measured return losses of the proposed microstrip-fed low-profile monopole is that even though at resonance the antenna can be considered matched ($|S_{11}| < -10\,dB$), the return loss does not achieve very small values. This is attributed to the reduced radiation resistance of the microstrip-fed antenna (as compared to the coaxially-fed counterpart of the same profile).

The measured $E-$plane and $H-$plane radiation patterns of the microstrip-fed antenna are shown in Fig. 4.35 and Fig. 4.36, respectively. These results consist the major difference between the microstrip-fed and the coaxially-fed antenna. Specifically, given that in the microstrip-fed case the port is located within one of the two principal planes of the antenna ($H-$plane), it significantly affects its radiation patterns resulting in a

more directive $H-$plane pattern than the almost perfectly omnidirectional $H-$plane of the coaxially-fed antenna. Referring to the $H-$plane pattern of Fig. 4.36, the feeding port is located at direction $\varphi = 270^o$ and causes the two nulls at the $\varphi = 225^o$ and $\varphi = 315^o$ directions. The measured maximum directivity of the microstrip-fed antenna is $3.16\,dBi$. The efficiency value that was extracted from the Gain/Comparison method for the microstrip-fed $\lambda/12$ antenna was 43%.

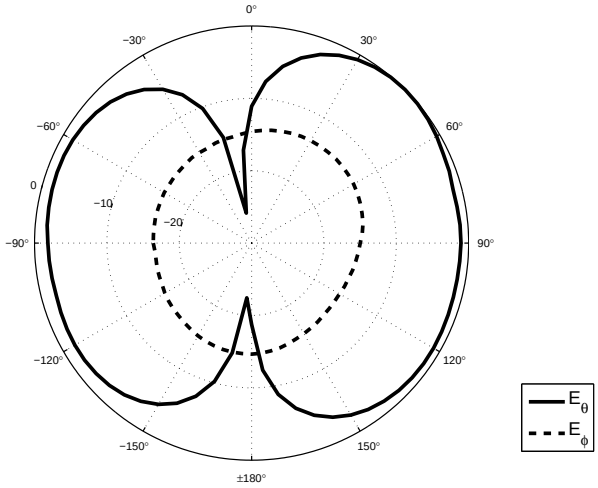

Figure 4.35: E-plane radiation pattern for a single low-profile folded monopole fed with a microstrip line.

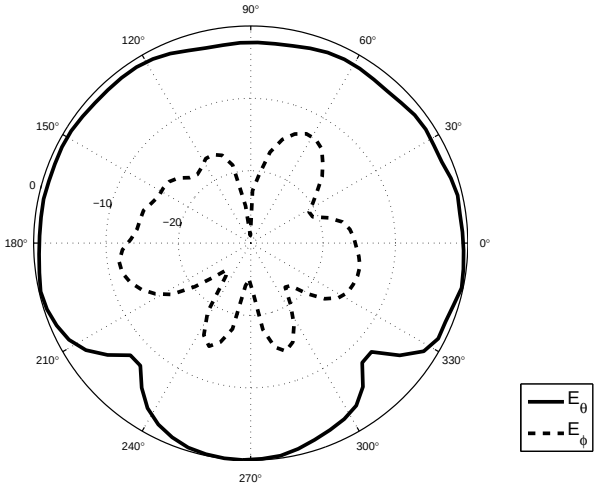

Figure 4.36: H-plane radiation pattern for a single low-profile folded monopole fed with a microstrip line.

4.9 Coupling Assessment Between Low-Profile Folded Monopoles

Throughout the study of the proposed low-profile folded monopoles, it has been discovered that one of their major advantages, as compared to conventional monopoles, is that they exhibit reduced mutual coupling when operating in close proximity to each other. This feature might be extremely useful for many applications. For this reason, in this section the coupling between two $\lambda/12$ low-profile folded monopoles is assessed as a function of the distance between them, and compared to the coupling between the conventional $\lambda/4$ monopoles. The assessment is performed through both full-wave and

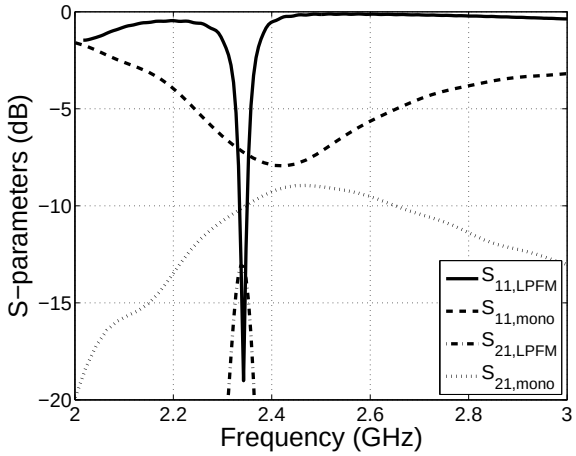

Figure 4.37: Return loss and coupling coefficient between two $\lambda/4$ monopoles and two low-profile folded monopoles (LPFM), respectively, being 0.2λ apart.

semi-analytical methods.

4.9.1 Full-wave Analysis

The most accurate assessment of the coupling between any pair of antennas can be performed through full-wave simulations. In this section, the results of the full-wave analysis of two-element arrays of conventional monopoles and the proposed low-profile monopoles are reported.

Inter-element spacing : 0.2λ

In the first case, the inter-element distance is assumed to be $d = 25mm$ or, approximately, $d = 0.2\lambda$. In this case, the return loss and the coupling coefficient between the $\lambda/4$ monopoles and the proposed low-profile monopoles are shown in Fig. 4.37. According to this figure, the maximum coupling level for the low-profile folded monopole is of the order of $S_{21} = -13.5\,dB$, while for the conventional monopoles the corresponding coupling level is approximately $3.5\,dB$ larger.

Inter-element spacing : 0.15λ

In the second case, the inter-element distance is assumed to be $d = 19\,mm$ or, approximately, $d = 0.15\lambda$. In this case, the return loss and the coupling coefficient between

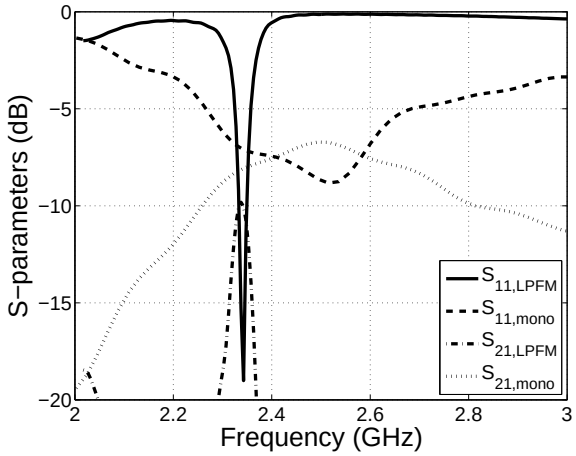

Figure 4.38: Return loss and coupling coefficient between two $\lambda/4$ monopoles and two low-profile folded monopoles (LPFM), respectively, being 0.15λ apart.

the $\lambda/4$ monopoles and the proposed low-profile monopoles are shown in Fig. 4.38. According to this figure, the maximum coupling level for the low-profile folded monopole is of the order of $S_{21} = -10\,dB$, while for the conventional monopoles the corresponding coupling level is approximately $3.0\,dB$ larger. In this case, the coupling between the conventional monopoles is that high that the monopoles are also detuned.

All the results for the full-wave coupling assessment between pairs of $\lambda/4$ monopoles and the proposed low-profile folded monopoles (LPFM) for different inter-element distances are summarized in Table 4.3.

A/A	$\lambda/4$ Monopole	Proposed LPFM
$d = 0.2\lambda$	$S_{21} = -9.0\,dB$	$S_{21} = -13.0\,dB$
$d = 0.15\lambda$	$S_{21} = -6.5\,dB$	$S_{21} = -10.0\,dB$

Table 4.3: Coupling coefficients between pairs of $\lambda/4$ monopoles and the proposed low-profile folded monopoles (LPFM) for different inter-element distances.

4.9.2 Analytical Approach

For the rigorous modeling of the coupling between a pair of monopoles, the EMF method, as presented in [120], for the calculation of the mutual impedance supported between two side-by-side dipoles could be employed. Nevertheless, some initial comparative quantita-

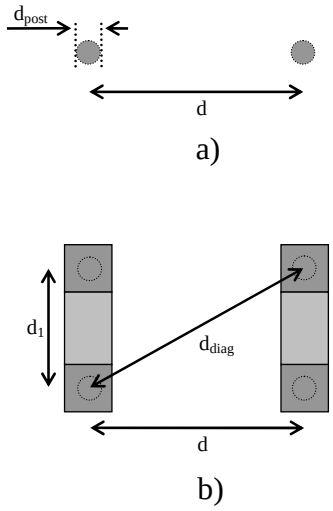

Figure 4.39: Configurations for the calculation of the mutual inductances supported between a pair of a) $\lambda/4$ monopoles and b) the proposed low-profile folded monopoles.

tive results can be faster obtained by the assumption that the major coupling mechanism between the $\lambda/4$ monopoles or the proposed the low-profile folded monopoles is the mutual inductance supported between the radiating vertical wires of the antennas. The mutual inductance at the operating frequencies of the examined antennas can be approximated using the electrostatic analysis of [106]. According to this analysis the mutual inductance between two wires of length h, being at a distance d apart, is given by equation (4.9).

$$M\left(h,d\right)=0.2\cdot h\cdot\left[\ell n\left(\frac{h}{d}+\sqrt{1+\frac{h^2}{d^2}}\right)-\sqrt{1+\frac{d^2}{h^2}}+\frac{d}{h}\right]\quad[nH]\tag{4.9}$$

Equation (4.4) can be employed directly for the estimation of the mutual inductance supported between two $\lambda/4$ monopoles in the configuration of Fig. 4.39(a). For the calculation of the mutual inductance in the case of the proposed low-profile folded monopoles the total mutual inductance of each of the two vertical posts of the first element with both posts of the second element should be considered. Therefore, using the notation of Fig. 4.39(b), the total mutual inductance of the proposed folded monopoles is given by equation (4.10), where h is the profile of the folded monopoles, d is the distance between them and $d_{diag}=\sqrt{d^2+d_1^2}$.

$$M_{LPFM}=2\left(M\left(h,d\right)+M\left(h,d_{diag}\right)\right)\quad[nH]\tag{4.10}$$

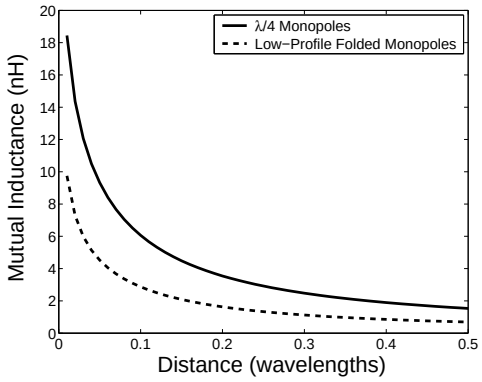

Figure 4.40: Mutual inductance supported between two $\lambda/4$ monopoles and two low-profile folded monopoles as a function of the distance between them.

The total mutual inductance supported between two $\lambda/4$ monopoles and two low-profile folded monopoles, calculated using equations (4.9) and (4.10), respectively, as a function of the distance between them is depicted in Fig. 4.40. By observing these results, it is concluded that the total mutual inductance supported between the $\lambda/4$ monopoles is approximately double than that supported by the low-profile folded monopoles for any possible distance between them. This conclusion is in agreement with the conclusion of the full-wave analysis, that suggested that the coupling coefficient for the proposed antennas are approximately $3\,dB$ below that of the conventional monopoles.

Chapter 5

Sub-wavelength Antenna Arrays

In this chapter, three different classes of compact (sub-wavelength) antenna arrays are designed and investigated. In all of the three cases, emphasis has be given on the enhancement of the array performance by means of reducing the electromagnetic coupling between the individual radiators. The first of these arrays is a two-element phased array with inter-element separation of the order of 0.2λ. The low-profile folded monopoles proposed in chapter 4 are employed in order to prevent the array performance degradation caused by the coupling between the array elements. The second investigated class of sub-wavelength arrays is the superdirective endfire arrays formed by low-profile folded monopoles. The reduced electromagnetic coupling between these antennas allows for the design of such arrays without the use of complicated decoupling networks or other tuning elements. Three superdirective arrays are designed and compared in terms of their achieved directivities and the delivered radiation efficiencies. Finally, a novel approach for the decoupling of conventional planar inverted-F antennas (PIFAs) built on a common compact ground plane is presented. The proposed approach could be used for the implementation of diversity gain schemes in handheld devices.

5.1 Introduction

The use of sub-wavelength antenna arrays in modern communication systems is becoming more and more frequent. This trend is imposed by the need for miniaturization of mobile terminals and the implementation of advanced communication techniques that exploit multiple antenna terminals for more efficient spectral usage (e.g. MIMO, beamforming, diversity schemes etc). The major difficulty in the design of such sub-wavelength antenna

arrays is the electromagnetic coupling between the individual radiators that results in the change of the antennas' input impedance (increase of the corresponding return loss) and also the increase of their mutual impedance (increased correlation between the received signals by different antennas).

In order to overcome these difficulties, two major strategies have be proposed in the literature. The first of them relies on the use of decoupling feeding networks that compensate for any perturbation of the input impedance of each radiator due to its mutual impedances with its adjacent radiators [121], [122],[123], [124]. The major disadvantages of this approach are that for the efficient design of the decoupling networks the mutual impedances of the array elements should be known a priori (a condition that can not be always satisfied) and that imperfections in the operation of the decoupling networks (*e.g.* ohmic losses) degrade the performance of the designed arrays.

The second approach for the reduction of the coupling between radiators participating in arrays is the use of insulating structures between the radiating elements [72], [125], [126]. This approach became quite popular with the advent of electromagnetic bandgap (EBG) and other metamaterial structures that can act as electromagnetic insulators between the radiating elements. The major disadvantage of this approach is that the employed insulating structures are being placed in the near-field of the radiating elements, affecting the radiating properties of the antennas and dissipating power. Besides, given that the insulating structures are usually periodic structures, they occupy certain volume/area and therefore their use in ultra compact arrays encounters practical restrictions.

In this chapter, it is shown that sub-wavelength arrays could be designed and effectively operate without the use of decoupling networks or insulating structures, provided that self-resonant radiating elements exhibiting ultra low coupling between them are being employed. The low-profile folded monopoles of chapter 4 meet all these requirements and, hence, in this chapter are employed for the design of sub-wavelength arrays. Specifically, first, a two-element sub-wavelength phased array, composed of two low-profile folded monopoles and designed to scan its beam at 60^o off broadside, is built and compared with the corresponding sub-wavelength array that is composed of $\lambda/4$ monopoles. In turn, the theory for the design of superdirective endfire arrays, that considers uncoupled array elements, along with the proposed low-profile folded monopoles, are effectively employed for the synthesis of sub-wavelength superdirective endfire arrays. Finally, for applications that require the use of arrays of conventional antennas, such as PIFAs, built

within small volumes, a simplified metamaterial-inspired approach is proposed for the decoupling of such antenna elements.

5.2 Sub-wavelength Phased Arrays

In this section of the chapter a sub-wavelength two-element phased array comprising of low-profile folded monopoles is built and its performance is compared to a two-element phased array composed of conventional $\lambda/4$ monopoles. The purpose of this study is to examine the potential advantages of sub-wavelength arrays composed of low-coupling radiating elements as compared to their conventional counterparts.

The design procedure starts with the assumption of the design parameters of the phased array. First, the targeted operating frequency of the sub-wavelength phased array is set to be $2.45\,GHz$. For the design of the considered sub-wavelength phased array, microstrip technology will be employed. In this framework, both the low-profile folded monopoles and the feeding network will be microstrip-based. This will enable the simplification of the fabrication procedure, reduce the fabrication cost (fully-printed feeding network and radiating elements) and will also allow the direct deployment of the array (passive, single-port-fed antenna).

The fully-printed, microstrip-based feeding network that will be employed for the design of the sub-wavelength phased array is depicted in Fig. 5.1. It is composed of a quadrature hybrid that equally splits the power of a single microstrip feeding port and provides two signals of equal amplitude being -90^o out-of-phase. Then, a transmission line segment of electrical length -215^o connected in series with the out-of-phase port secures a 55^o phase difference between the two output ports at $2.45\,GHz$. The physical distance between these ports is $d = 22.0mm$. Given that this feeding network was already available when the sub-wavelength phased arrays were investigated, it was decided for the built phased array to be fed with a phase progression of $a = 55^o$ and the array elements to be at a distance $d = 22.0\,mm$. At $2.45\,GHz$, this physical length corresponds to an electrical length of $\beta d = 0.36\pi$. The normalized array factor of the two-element array is then given by equation (5.1), where $\phi = \pm 90^o$ along the axis of the array, and $\phi = 0^o$ in the broadside direction.

$$|AF\,(\phi)| = \left| cos\left(\frac{\beta d sin\phi + a}{2}\right)\right| \tag{5.1}$$

Equation (5.1) assumes its maximum when $\left|cos\left(\frac{\beta dsin\phi+a}{2}\right)\right| = 1$, or equivalently when $\beta dsin\phi + a = 0$. For a phase progression $a = 55^o$, an ideal two-element array similar with the one under investigation is expected to scan its beam at 58^o off broadside.

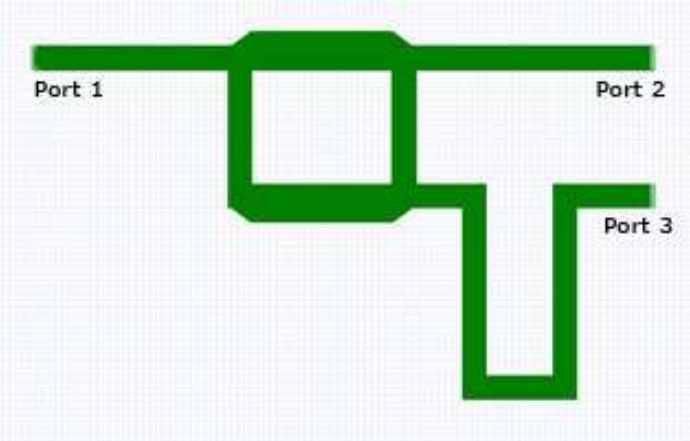

Figure 5.1: Microstrip-based feeding network employed for the synthesis of the two-element sub-wavelength phased array.

The feeding network of Fig. 5.1 was built on $1.15\,mm$ thick $TACONIC\,TLY-5A$ dielectric substrate ($\epsilon_r = 2.2$). The simulated (ANSOFT Designer) $S-$parameters of the feeding network are shown in Fig. 5.2 and Fig. 5.3 (magnitude and phase, respectively). These results validate that the quadrature hybrid is designed to operate in the $2.45\,GHz$ band. Specifically, at $2.45\,GHz$ $|S_{11}| < -20\,dB$, $|S_{21}| \approx |S_{31}| \approx -3\,dB$ and also $\angle S_{31} - \angle S_{21} \approx 55^o$.

The feeding network of Fig. 5.1 is employed to feed two different two-element antenna arrays. In the first array, the radiating elements are low-profile folded monopoles, identical with those presented in section 4.8. Their profile is considered to be $h = 10.3\,mm$ ($\lambda/12$). In the second array, the radiating elements are conventional $\lambda/4$ monopoles. Both types of monopoles are directly attached at the open ends of the feeding networks. A photograph of the fabricated array with the low-profile folded monopoles is depicted in Fig. 5.4.

In the following text, the two phased arrays are compared in terms of their measured performance. Specifically, in Fig. 5.5 the return losses of the two arrays are shown. As expected, the return loss of the conventional monopoles are much more broadband than the return loss of the low-profile folded monopoles array. Nevertheless, both arrays can be considered to be matched at $2.45\,GHz$ ($|S_{11} < -10\,dB|$).

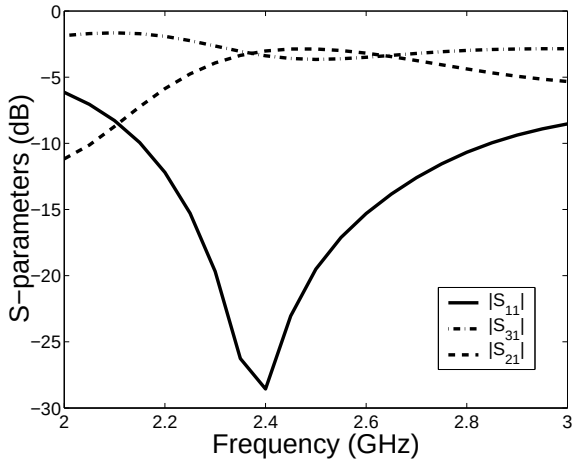

Figure 5.2: $S-$parameters (magnitude) of the feeding network of Fig. 5.1.

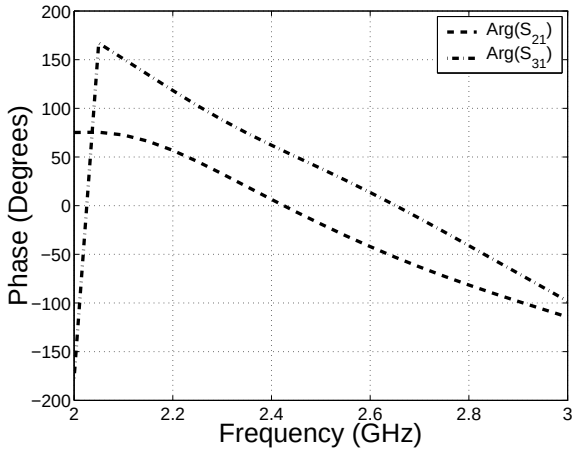

Figure 5.3: $S-$parameters (phase) of the feeding network of Fig. 5.1.

In Fig. 5.6 the normalized patterns of the two arrays under investigation are plotted. The range of the patterns extends from -90^o to $+90^o$. These results show that the radiation pattern of the low-profile monopole array achieves its maximum closer to the theoretically calculated scanning angle of $\varphi_o = 58^o$. Specifically, the low-profile monopole array scans its beam at 55^o while the conventional monopole array scans its beam at 50^o. It is noted that the angular resolution during the radiation pattern measurements is 5^o. One potential physical explanation for the divergence between the measured and the theoretically calculated scanning angles could be the coupling between the radiating elements of the array, that affects the feeding phase of each of the elements of the array.

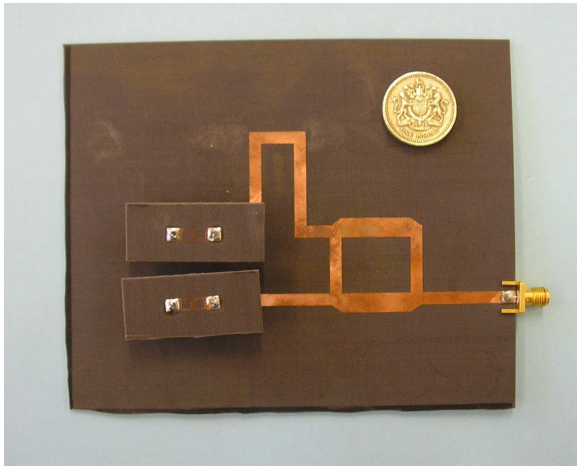

Figure 5.4: Photograph of the fabricated prototype of the investigated sub-wavelength phased array of low-profile folded monopoles.

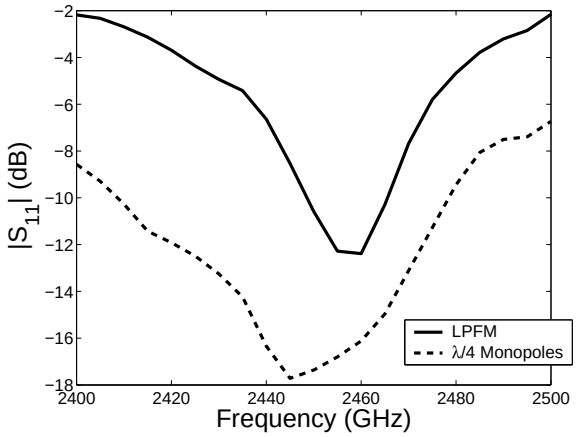

Figure 5.5: Measured return losses (S_{11}) of the two sub-wavelength arrays.

In that case, given that the coupling between the low-profile folded monopoles has been shown to be weaker than that between conventional monopoles, the performance of the low-profile array is less affected by the coupling and the error in its scanning angle becomes smaller. Finally, the measured results show that the delivered radiation efficiency of the low-profile array (this efficiency was measured to be 45%) is almost equal with that of the conventional array (the radiation efficiency for the conventional array was measured to be 48%). Even though this result is slightly counterintuitive, given that the low-profile monopoles are significantly less efficient than conventional monopoles, this result was validated through multiple measurements.

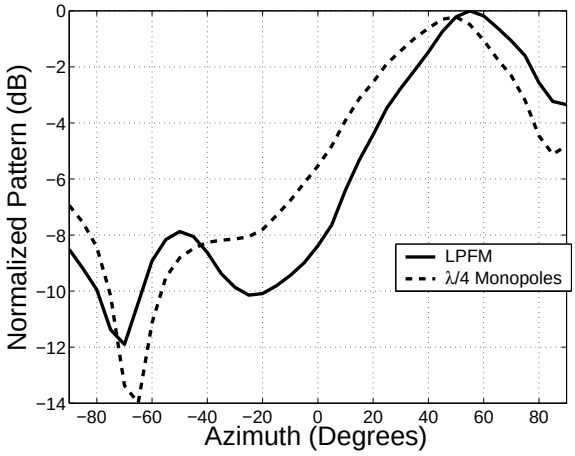

Figure 5.6: $H-$plane patterns of the two compared sub-wavelength arrays.

5.3 Sub-wavelength Superdirective Endfire Arrays

5.3.1 General

Superdirective arrays have attracted for years the interest of antenna engineers both from theoretical (conceptual) and practical point of view [127], [128], [129]. In principle, the design of superdirective antennas relies on the synthesis of optimized current distributions on a given physical area that enables this area to deliver high effective aperture efficiencies. In linear arrays, it corresponds to the synthesis of $N-$element arrays that would be excited with such currents that would enable the array to deliver array gains higher than N.

For endfire arrays composed of N isotropic and uncoupled radiators, it has been shown that, as element spacing goes to zero, the upper limit for the delivered directivity is given by equation (5.2) [4]. The maximum directivity can be delivered only if the elements of the arrays are properly excited. Nevertheless, in practice, the theoretical upper limit of the endfire directivity has never been achieved as the superdirective arrays are extremely sensitive to any deviations between the theoretical and the experimental excitation signals and the coupling between the radiating elements [127].

$$D = \sum_{n=0}^{N-1} (2n+1) = N^2 \tag{5.2}$$

Out of all the types of superdirective antennas, the design of electrically small superdirective arrays is potentially the most demanding and attractive. One of the most

challenging tasks in the design of a superdirective electrically small array is the design of its feeding network. Such a feeding network usually performs two majors tasks. First, it is responsible for the matching of the electrically small radiating elements that, in most cases, are not self-resonant. Secondly, it decouples the radiating elements that, being in close proximity, exhibit high mutual impedances and properly sets the relative magnitude and phase of the excitation signals at the port of each antenna of the array. The complexity of these networks and the imperfections associated with their operation (i.e. ohmic losses) are usually the reasons for not experimentally demonstrating the maximum directivity of equation (5.2).

With the use of metamaterial structures some of the issues currently handled by the feeding network could be possibly addressed in a different way, simplifying the design of the feeding network and improving its performance. For example, in [72], the use of a metamaterial insulator was proposed for the decoupling of the array elements. In the present work, the self-resonant low-profile folded monopoles presented in chapter 4, that exhibit reduced mutual coupling, are employed for the design of two-element endfire superdirective arrays. Given the features of the employed radiators (self-resonant, low-coupling), the feeding network can be simplified and perform a single function; that of properly setting the excitation currents of the array elements. As a result, this feeding network becomes simple to design, low-cost and easy to fabricate.

5.3.2 Feeding Network

As it has been already mentioned, in this approach, self-resonant, low-coupling radiating elements are employed for the design of two-element superdirective endfire arrays. As a result, the required feeding network implements a single function, that of setting the proper excitation currents at the inputs of the two radiating elements. Based on the analysis of [4], for two-element arrays, endfire superdirective patterns are obtained when the two radiators are fed with currents equal in magnitude and a relative phase-shift equal with that of Fig. 5.7. As Fig. 5.7 suggests, the phase-shift between the two elements is dependent on the distance between them. Therefore different separation between the radiators would require different phase-shifts to deliver superdirective patterns.

The results of Fig. 5.7 show that the required phase-shift between the excitation currents of the two radiating elements of the considered superdirective antennas are of the order of $140^o - 180^o$. Therefore, the required feeding network has been chosen to be

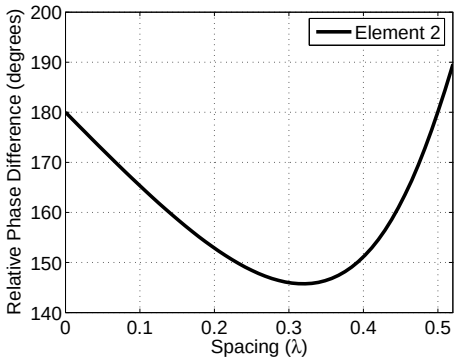

Figure 5.7: Relative excitation phase, according to the analysis of [4], for the design of two-element superdirective arrays.

implemented through a 180^o microstrip-based ring hybrid. Specifically, the differential ports of the hybrid are employed together with transmission line segments of proper length connected in series to them to synthesise the required pairs of phase-shift and distance according to Fig. 5.7. The ring-based feeding network is depicted in Fig. 5.8. The single feeding port of the antenna arrays is considered the port 1 of the ring of Fig. 5.8. The incoming signal is split into two equal in magnitude and 180^o out of phase output signals. The length of the transmission line segments attached to the output ports of the hybrid are properly adjusted so that the distance d between the physical ports 2 and 4 of the feeding network corresponds to the phase required for the synthesis of the two-element endfire superdirective array (according to the results of Fig. 5.7).

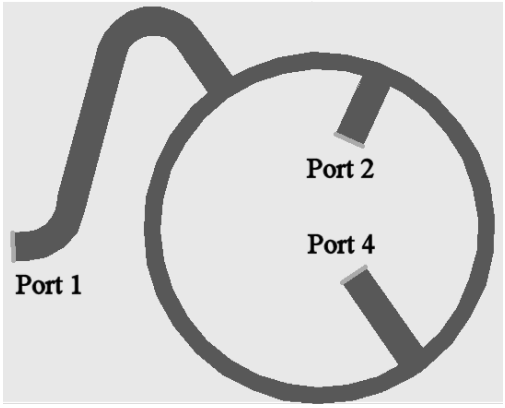

Figure 5.8: Top view schematic of the modified ring hybrid used as feeding network for the proposed superdirective endfire two-element array designs.

The feeding network of Fig. 5.8 is built on a $TACONIC \quad TLY - 5A$ dielectric

substrate of dielectric constant $\epsilon_r = 2.2$ and is designed for operation in the $2.45\,GHz$ band. The $S-$parameters of this feeding network, optimized to feed a superdirective endfire array with element separation of 0.2λ, are shown in Fig. 5.9.

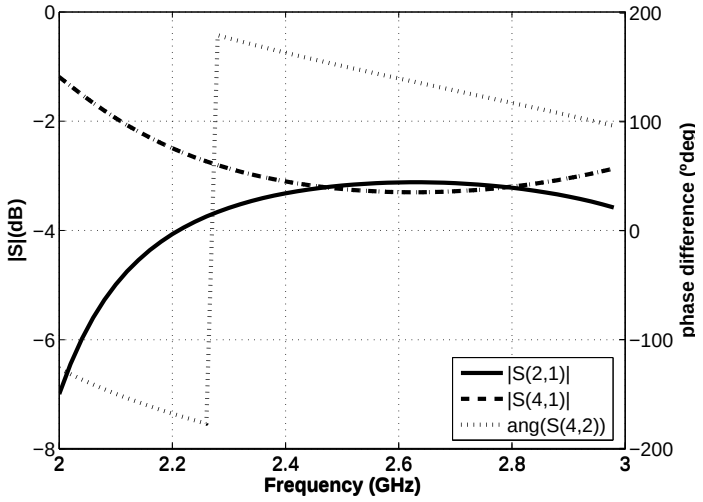

Figure 5.9: Insertion loss and phase difference between the two output ports of the modified hybrid of Fig. 5.8.

5.3.3 Driven Superdirective Arrays

In the following text, the measurement results of two different designs of superdirective enfdire arrays driven by the feeding network of Fig. 5.8 are presented. A representative schematic of the fabricated and measured driven superdirective arrays is shown in Fig. 5.10.

In the first of the fabricated prototypes, the separation between the radiating elements is considered to be 0.2λ. The employed feeding network and its $S-$parameters are those presented in the previous section. In the second fabricated prototype, the separation between the radiating elements is decreased to 0.15λ. For this design the transmission line segments attached to the outputs of the ring have been adjusted according to the requirements suggested by Fig. 5.7. It is noted that for both these designs the height of the employed low-profile monopoles is $h = 10.3\,mm$ $(\lambda/12)$

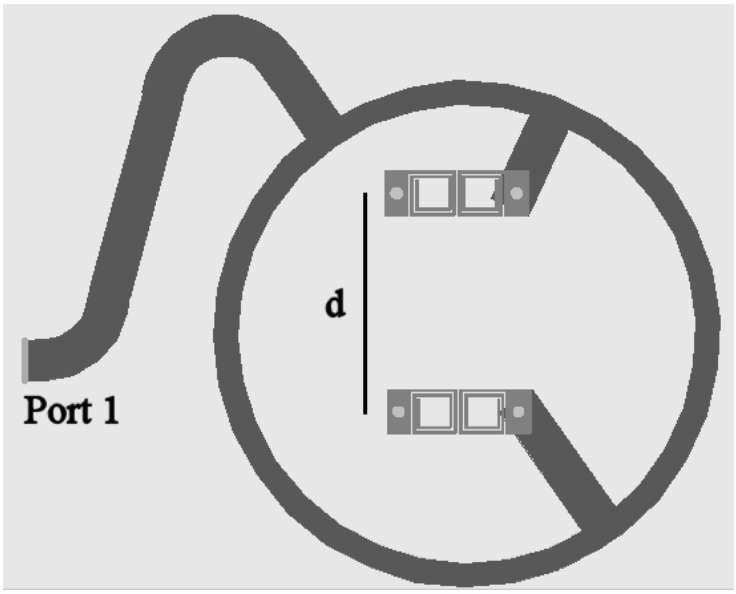

Figure 5.10: A schematic representation of the proposed superdirective arrays.

0.2λ Array

The first fabricated prototype is the 0.2λ array. A photograph of this prototype is shown in Fig. 5.11.

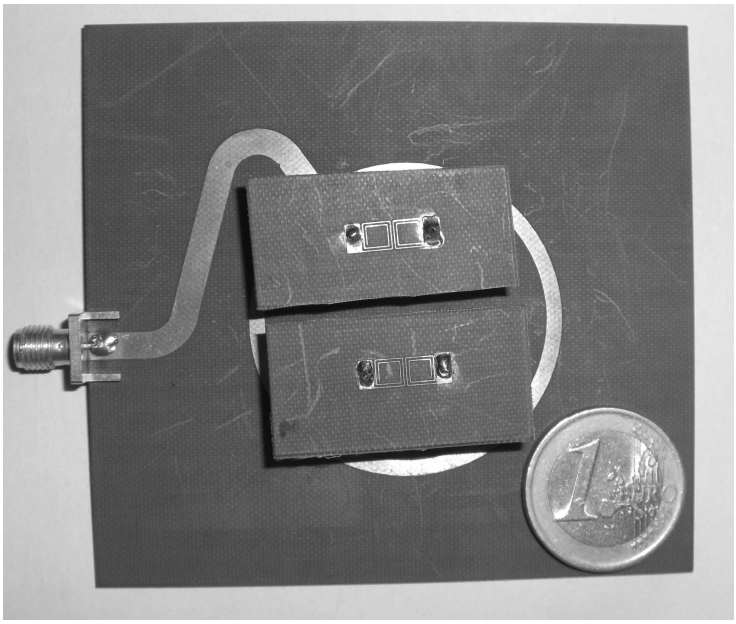

Figure 5.11: Photograph of the fabricated two-element superdirective endfire array.

The measured and simulated return loss of the prototype of Fig. 5.11 is depicted in

Fig. 5.12. These results show that the designed array is matched at the target frequency of 2.45 GHz. The second deep that appears at the return loss curve at approximately 2.1 GHz, and is more profound for the simulated results, corresponds to the transmission line resonance of the employed low-profile folded monopoles.

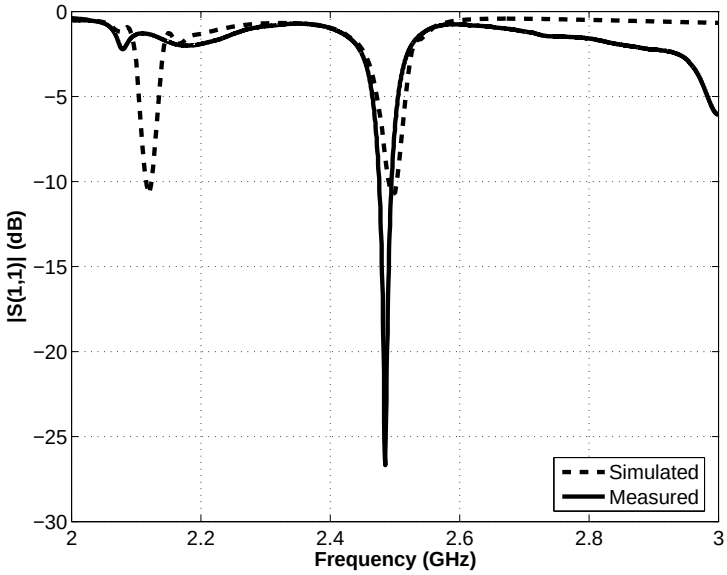

Figure 5.12: Return loss for the 0.2λ superdirective endfire array.

To experimentally show the highly directive properties of the fabricated prototype, the radiation patterns of the array were measured and compared to that of a single microstrip-fed low-profile folded monopole. As was expected, the directive properties of the synthesised arrays appear in the H-plane. The measured H-plane of the 0.2λ prototype, measured at 2.45 GHz, together with that of the single low-profile monopole, are depicted in Fig. 5.13.

These results suggest that the synthesised array exhibits a much more directive pattern than the single element. Specifically, the directivity of the array in the endfire direction was measured to be 5.7 dBi, while the directivity of the single low-profile folded monopole in the same direction had been measured to be 3.17 dBi.

0.15λ Array

The 5.7 dBi of the 0.2λ array do not prove the superdirective properties of the designed array, given that the two-element array exhibits less than 3 dB improvement in the directivity as compared to the single element. A second attempt to implement a superdirective,

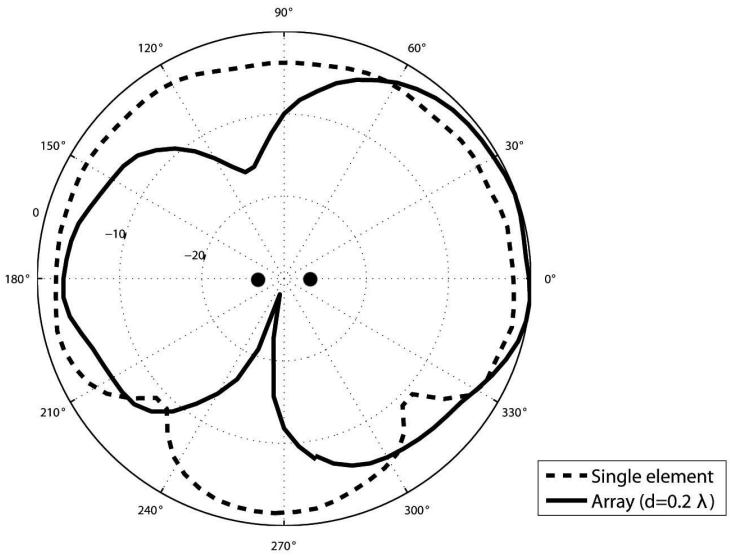

Figure 5.13: $H-$plane radiation pattern for the 0.2λ array prototype compared with that of a single low-profile monopole. The orientation of the 2-element array with respect to the measured pattern has been noted with the two dots in the middle of the plot (each dot represents each element of the array).

two-element array is presented in this section. In this effort, the separation between the antenna elements is considered to be 0.15λ at $2.45\,GHz$. For the implementation of this design the feeding network of Fig. 5.8 has been properly adjusted to implement the phase requirement suggested by the results of Fig. 5.7. Other than that, all the parameters of this array are identical with that of the 0.15λ array.

The simulated and measured return loss of the 0.15λ array is depicted in Fig. 5.14. These results validate that the antenna arrays is matched at the target frequency of $2.45\,GHz$

The measured H-plane pattern of the 0.15λ array, compared with that of the single element, is shown in Fig. 5.15. These results suggest that the H-plane pattern of the 0.15λ array is more directive than that of the 0.2λ array. Specifically, the directivity of the 0.15λ array at the endfire direction was measured to be $6.9\,dBi$, as compared to $3.16\,dBi$ of the single element and $5.7\,dBi$ of 0.2λ array. This proves that a superdirective sub-wavelength array design has been achieved.

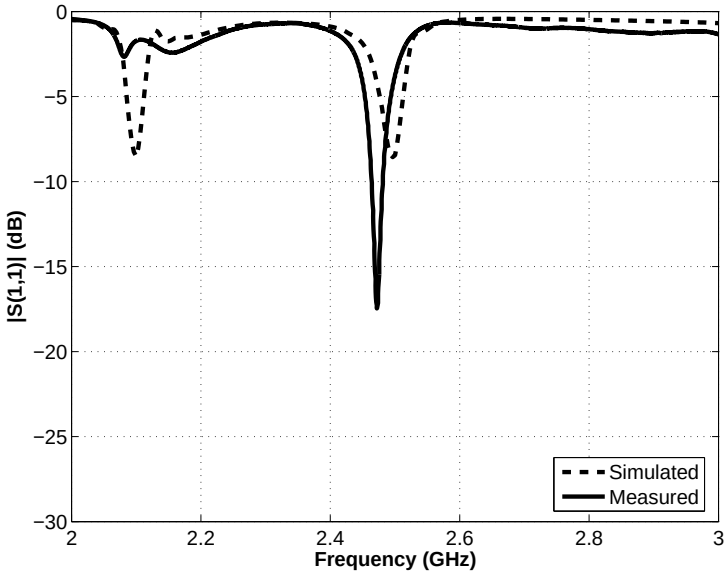

Figure 5.14: Return loss for the 0.15λ superdirective enfdire array.

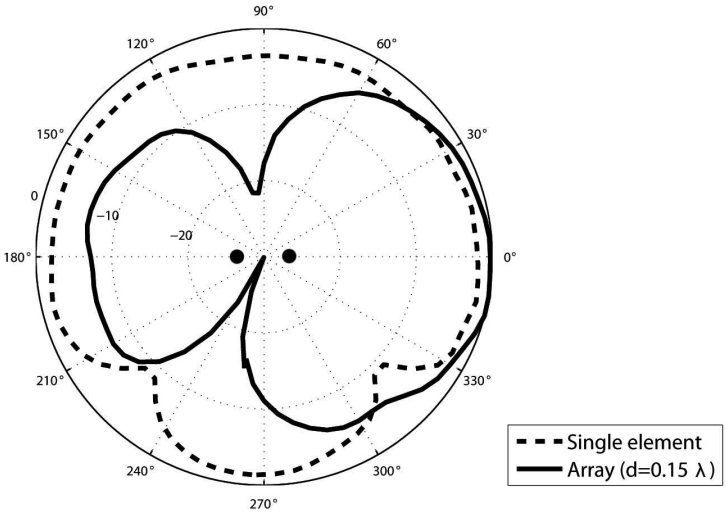

Figure 5.15: $H-$plane radiation patterns for the 0.15λ array prototype and the single monopole. The orientation of the 2-element array with respect to the measured pattern has been noted with the two dots in the middle of the plot (each dot represents each element of the array).

5.3.4 0.1λ Parasitic Array

Considering the fabrication and testing of further smaller superdirective arrays, practical difficulties on the implementation of the feeding network were encountered. Therefore, for the design of further smaller superdirective endfire arrays alternative approaches were

searched.

As Fig. 5.7 suggests, for inter-element separations smaller than 0.15λ and as $d \rightarrow 0$ the phase-shift between the feeding currents of the two elements moves linearly to 180^o. This observation, together with the fact that for such small separations between the low-profile monopoles the electromagnetic coupling is not insignificant, lead to the conclusion that two-element superdirective endfire arrays could be designed with the one of the elements being directly-fed and the other being parasitically-fed, as also suggested in [130]. Similarly with the Yagi-Uda antennas, the excited current on the parasitically-fed element is expected to be approximately equal in magnitude and roughly 180^o out of phase, as compared with the current of the directly-fed element, implementing in that way the requirement imposed by Fig. 5.7

Based on these arguments, a parasitic two-element array, with element separation equal to 0.1λ was built and its electromagnetic properties were measured. For the fabrication of this array, a ground plane of identical dimensions with those of the driven arrays was employed. The driven element was fed using a 50 Ω microstrip-line, while both posts of the parasitic element were shorted to the common ground plane. Given that a microstrip-fed low-profile folded monopole is slightly electrically smaller than an identical shorted folded monopole, in the proposed two-element array the parasitic element behaves as the reflector of a conventional two-element Yagi-Uda antenna.

The measured and simulated return loss of the parasitic array is depicted in Fig. 5.16 and its $H-$plane is depicted in Fig. 5.17.

The measured directivity of the parasitic array in the endfire direction was measured to be 7.6 dBi.

5.3.5 Comparison

All the presented antenna designs exhibited enhanced directivities as compared to the single low-profile monopole. Specifically, it has been shown that the achieved directivity is increasing as the distance between the antenna elements is decreasing, as also suggested by the theory for the design of superdirective arrays. Nevertheless, a more inclusive characterization and comparison of the three different designs showed that the increment of the directive properties of the arrays is accompanied by a decrease in their radiation efficiencies. Specifically, the use of the Directivity/Gain comparison method for the estimation of the efficiency of each of the designs provided the results presented in Table

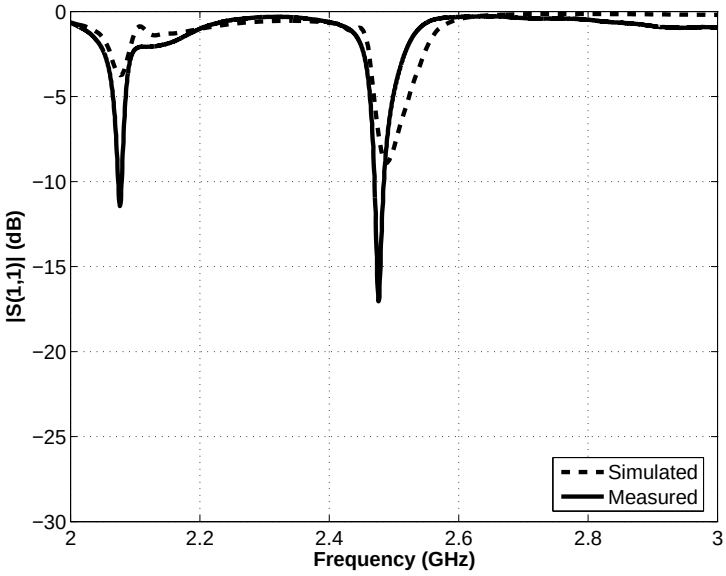

Figure 5.16: Return loss for the 0.1λ parasitic array.

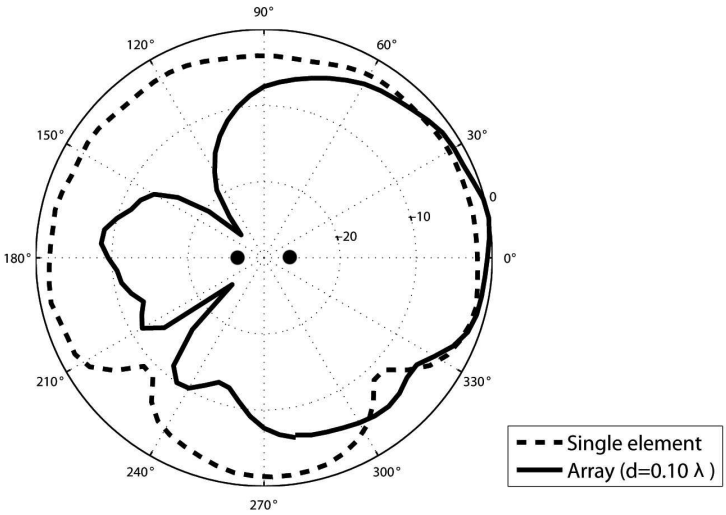

Figure 5.17: $H-$plane radiation patterns for the 0.10λ array prototype and the single monopole. The orientation of the 2-element array with respect to the measured pattern has been noted with the two dots in the middle of the plot (each dot represents each element of the array).

5.1. These results show that the most directive array design (parasitic array) achieves an average efficiency of only 24%, while the directivity of the least directive array (0.2λ) was measured to be 40%, which is very close with the efficiency of the single element (43%). This trent is attributed to the fact that decrease of the inter-element separation leads to

antenna designs with higher current densities. Given that the single element is inherently lossy, the higher current densities lead to higher losses on the antenna structure and hense reduced radiation efficiencies.

At this point, it should be pointed out that there is always an error associated with the measurement of antenna radiating efficiencies and gains. This error is dependent on the performance/accuracy of the employed measurement setup. For the measurement setup (fully automated anechoic chamber) employed for the characterization of the superdirective antennas of this section, it has been estimated that the absolutely maximum uncertainty that is introduced in the radiation efficiency measurements due to the associated measurement errors is approximately 6 percentage units on the reported efficiency values. In other words, a maximum deviation of ± 3 percentage units may be expected for any reported efficiency value. This rough empirical estimation has been extracted through multiple measurements of the same antenna in the chamber and through the comparison of the efficiency values of the same antenna measured using different measurement techniques (*i.e.* Wheeler Cap measurement results compared with the anechoic chamber measurement results for the same antenna). Nevertheless, given that all the superdirective antennas reported in this section were measured using the same measurement setup, it is expected that a uniform error would have been applied to all of them and, therefore, it is believed that the accuracy of the comparative reported results is even better.

Antenna Description	Directivity (dBi)	Efficiency (%)	Gain (dBi)
Single element	3.16	43	-0.5
Driven 0.2λ array	5.7	40	1.7
Driven 0.15λ array	6.9	30	1.6
Parasitic 0.10λ array	7.6	24	1.4

Table 5.1: Comparative study of the three antenna designs with enhanced directivities.

5.4 Decoupling PIFAs on Handhelds

In the previous sections of this chapter, antenna elements that exhibit reduced mutual electromagnetic coupling were employed for the synthesis of sub-wavelength arrays. In this section of the chapter, a novel approach for reducing the electromagnetic coupling

between conventional planar inverted-F antennas (PIFAs), built on a common ground plane and forming sub-wavelength antenna arrays on handheld devices, is presented.

The use of multiple-element antenna arrays, implementing either diversity gain or spatial multiplexing schemes, has been extensively proposed for the enhancement of the spectral efficiency of wireless communication systems. In mobile communication systems such antenna arrays are already being employed at the base stations. Nevertheless, the implementation and the performance of these schemes at mobile terminals are influenced by the spatial fading correlation [131] and the electromagnetic coupling between the densely packed array elements [132], [133]. The latter factor is addressed in this section and a novel approach for the suppression of the electromagnetic coupling between PIFA elements, built on the same handheld device, is proposed.

PIFAs have been proved the most popular antenna solution for compact handheld devices (cellular mobile terminals, PDAs, etc). Nevertheless, in such applications the coupling between the antenna elements is significantly high, due to the fact that all the antenna elements are usually built on the same ground plane and the high degree of integration, while none of the conventional approaches for coupling reduction (decoupling networks, metamaterial insulating structures) is of great applicability (the first would increase the cost and reduce the efficiency of handheld devices, while the second could not be employed due to size and volume restrictions). Therefore, an alternative technique, inspired by the design of metamaterial resonators, for the coupling reduction in such application is presented in the following text.

The proposed technique is based on the insertion of two coupled quarter-wavelength slits on the ground plane between the antennas. By optimizing the distance between the coupled slits, a magnetic resonance can be established within the operating bandwidth of the PIFAs. This resonance inserts a transmission zero in the coupling path between the closely spaced PIFAs, enabling the reduction of the coupling between them to very low levels without significantly disturbing their operating bandwidth.

For the demonstration of the proposed decoupling scheme, let us consider a two-element PIFA array built on a $100\,mm\,x\,40\,mm$ large, $1.55\,mm$ thick, grounded $FR-4$ dielectric substrate ($\epsilon_r = 4.5$). The layout of each of the employed single-band PIFA elements, designed to operate from $1.7\,GHz$ to $2.0\,GHz$, and the original two-element array configuration are depicted in Fig. 5.18(a) and Fig. 5.18(b), respectively. At the considered frequency band, the two PIFAs are approximately half-wavelength apart and, therefore, the spatial fading correlation shall not impose major limitations. Nevertheless,

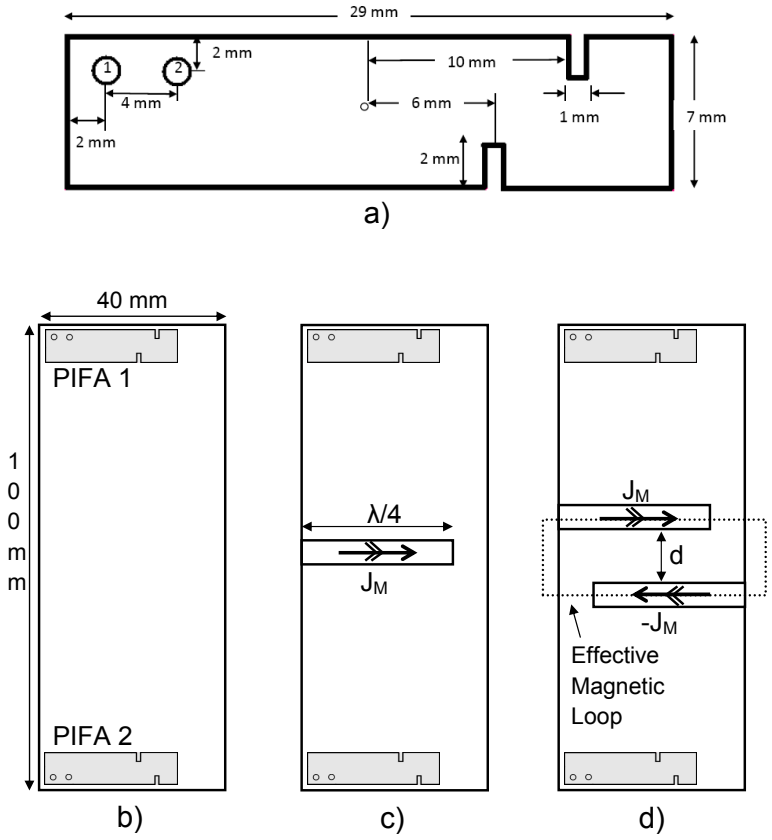

Figure 5.18: Layout of the a) single PIFA element, b) two-element array on handheld (no slits on the ground plane), c) coupling reduction scheme by inserting a single slit (notch) on the ground plane, d) coupling reduction scheme by inserting two coupled slits at a distance d from each other.

the electromagnetic coupling between the two array elements, that is attributed mostly to the currents on the common ground plane, was found to be relatively high. Specifically, the structure was simulated using CST Microwave Studio (CST MWS) and the maximum coupling between the antennas was found to be $S_{21} = -9dB$ (Fig. 5.19, original design).

A well-known practice in reducing the coupling between antenna elements built on a common ground plane is the introduction of resonant defects on the ground plane between the antennas [134], [135]. Such an approach is shown in Fig. 5.18(c), where a slit (represented also as a magnetic current J_M) has been inserted at the edge of the ground plane. By properly setting the length of the slit to be $29\,mm$ (approximately a quarter-wavelength at the middle of the operating bandwidth), the slit resonates acting as a notch and trapping some of the power that was to be transmitted between the two radiating elements. In fact, for the configuration of Fig. 5.18(c) it was found that the insertion of such a slit reduces the coupling between the antennas by approximately $4.5\,dB$ (in this case $S_{21} = -13.5\,dB$, as shown in Fig. 5.19). The coupling between the two antennas can be further reduced by inserting a second slit of the same length at a distance d from the first slit, as in Fig. 5.18(d). In the general case, the second notch introduces another 4.5 dB reduction of the coupling between the antennas (for the configuration of Fig. 5.18(d), with an arbitrarily chosen value for d, $S_{21} = -18dB$). Nevertheless, even in that case the coupling between the PIFAs, being approximately half-wavelength apart, remains above -20 dB.

In the proposed approach, it is suggested that a configuration similar with that of Fig. 5.18(d) can be employed to achieve coupling coefficient values significantly below $-20dB$, provided that the distance between the two slits is properly chosen. Careful examination of the electromagnetic fields in the configuration of Fig. 5.18(d) suggests that the two slits are coupled. Hence, by optimizing the distance between them, they can be made to resonate forming an effective magnetic loop. By this means, a transmission zero is introduced in the coupling path between the two radiating elements, reducing further the electromagnetic coupling between them. Full-wave optimization of the distance between the slits, carried out using CST MWS, showed that the value of d that makes the coupled slits to resonate at $1.85\,GHz$ (middle frequency of the operating band) is $d = 11\,mm$. In order to show that the distance between the slits can be set so as for the coupled pair of slits to behave as a magnetic loop, the currents on the ground plane and the electric field normal to it are depicted in Fig. 5.20. These results validate that the currents on the slits simultaneously achieve their maximum values (being in phase), resulting in a common,

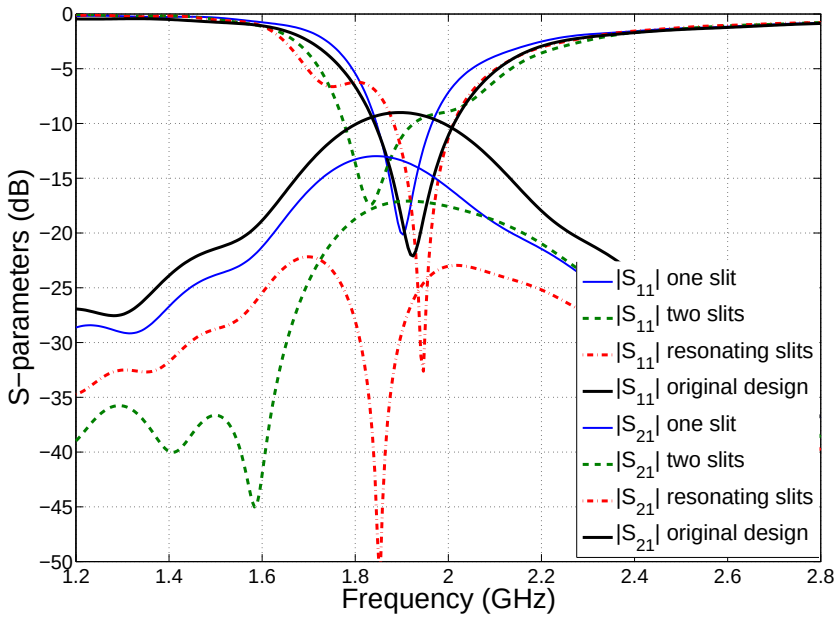

Figure 5.19: Simulated (using CST MWS) $S-$parameters of the two-element array in the cases that no slits (original design), one slit, two slits and two resonating coupled slits have been inserted on the common ground plane.

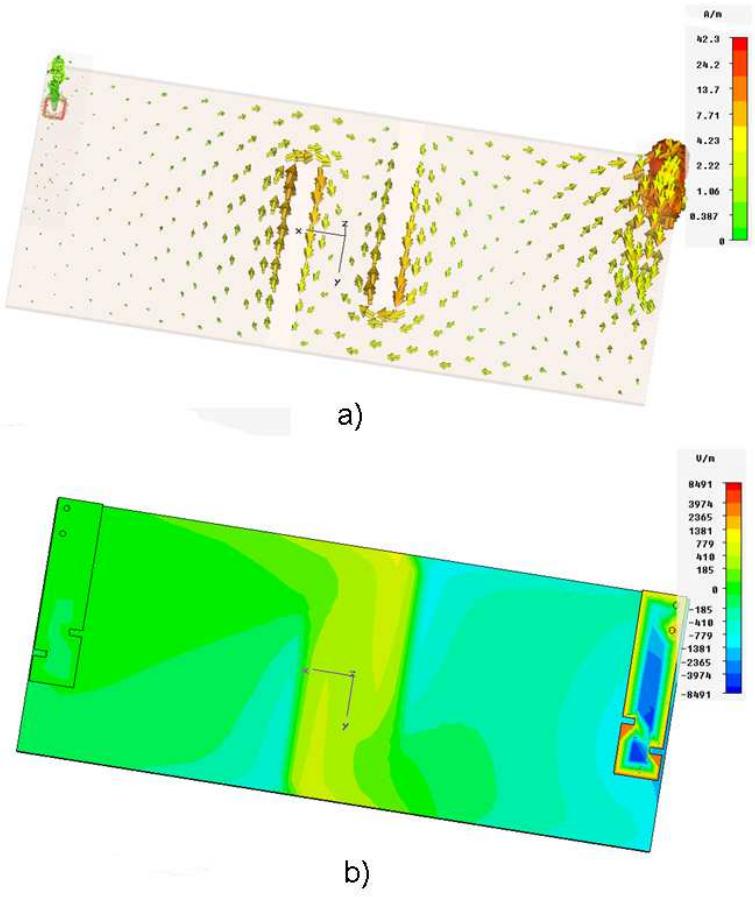

Figure 5.20: Ground plane currents and normal electric field for the resonating effective magnetic loop.

maximized vertical electric field component in the area between the two coupled slits.

For the value of d that the two slits behave as a resonating magnetic loop, the coupling between the two antennas is also plotted in Fig. 5.19. This result suggests that for the resonating coupled slits, the coupling between the PIFAs, at $1.85\,GHz$, drops below $-50\,dB$ (transmission zero), while it remains below $-23\,dB$ for the whole bandwidth of interest. At this bandwidth both PIFAs remain matched ($S_{11} < -6dB$ and $S_{22} < -6dB$), even though their input impedances are slightly altered.

It is noted that the resonating coupled slits are expected to radiate. Therefore, the radiation patterns of the proposed decoupled antenna array have been studied and have been found to be slightly different than those of the array without the slits. In fact, the patterns of the proposed structure is slightly more omni-directional (maximum directivity of $3.5\,dBi$ compared to $4.5\,dBi$) which is well suited for handset applications. This is

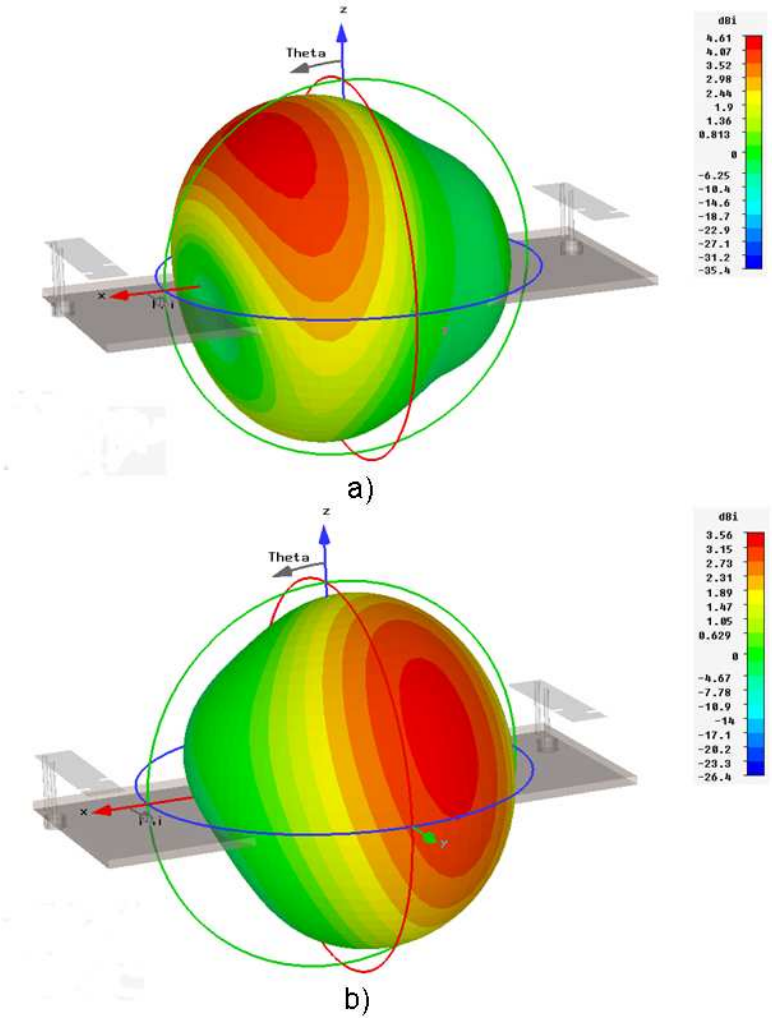

Figure 5.21: Radiation patterns comparison between the conventional and the decoupled PIFA arrays at 1.85 GHz.

shown in Fig. 5.21, where the radiation patterns for the two compared cases have been plotted. Also, regarding the radiation efficiency of the decoupled array elements, it has been found that the proposed scheme for the reduction of coupling decreases the efficiency of each of the radiating elements by approximately 4% (due to the strong currents on the ground plane).

In order to experimentally validate the proposed technique for coupling reduction between PIFAs built on the same ground plane, two antenna prototypes (the original array and the one with the resonating coupled slits) have been fabricated and measured. The measured $S-$parameters in the two cases are depicted in Fig. 5.22. These results

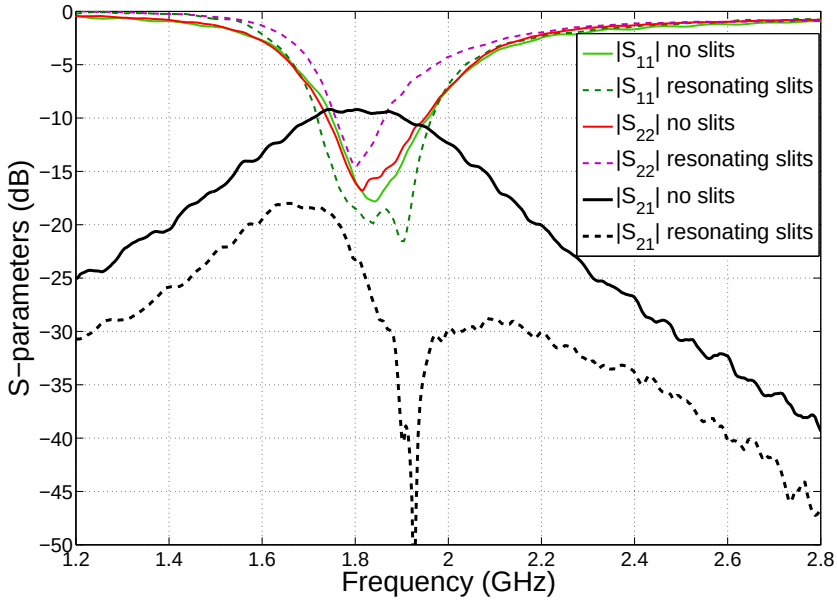

Figure 5.22: Measured $S-$parameters for the configurations of Fig. 5.18(b) and Fig. 5.18(d), when $d = 11\,mm$. Due to fabrication imperfections, the resonance of the coupled slits is achieved at $1.92\,GHz$.

suggest that the measured maximum coupling in the original array is of the order of $S_{21} = -9dB$ and that the insertion of the resonating coupled slits adds a transmission zero in the coupling coefficient between the antennas. Nevertheless, in the measured data, this transmission zero occurs at $1.92\,GHz$, instead of the design frequency ($1.85\,GHz$), due to fabrication imperfections (mostly to the length of the slits). As a result, the coupling coefficient becomes slightly larger than $-20dB$ at the lower edge of the operating bandwidth and a slightly decreased operating bandwidth for the second PIFA is observed. However, at the resonance of the coupled slits ($1.92\,GHz$) both antennas are matched ($S_{11} < -6dB$ and $S_{22} < -6dB$) and the coupling drops below $-50\,dB$, as suggested by the simulations. Furthermore, the measured coupling coefficient between the antennas in the proposed design is significantly reduced, as compared to the original design, for the whole operating bandwidth of the PIFAs.

Chapter 6

Periodic FDTD Analysis of Leaky-Wave Antennas

This chapter presents the development of an efficient and accurate periodic FDTD-based computational tool for the analysis of leaky-wave structures and its application to the design and optimization of novel, flat-plate, metamaterial-based, high-gain leaky-wave antennas. Specifically, in the first part of the chapter, a post-processing methodology that allows the periodic FDTD tool of [93] to solve periodic leaky-wave structures employing half of the computational resources that were originally required is derived and validated. In turn, employing this improved methodology, a novel, computationally demanding, periodic leaky-wave antenna is modeled and its radiation properties are optimized. Finally, a semi-analytical model that allows for the fast calculation of the radiation patterns of finite-size, 2-D leaky-wave structures, given the complex propagation constants of the supported leaky-modes, is developed.

6.1 Introduction

Leaky-wave structures have been for decades a particularly challenging research field due to their several applications in antenna technology and the richness of electromagnetic phenomena associated with them. During the recent years, the interest for leaky-wave structures has been renewed mostly because of the development of metamaterials and their potential applicability for the design of novel in leaky-wave antennas (LWAs). Towards this direction, two main classes of novel leaky-wave structures have been proposed in the literature. The first of them involves LWAs that are formed from NRI metamateri-

als. These structures have been shown to support both backward and forward fast-waves and, therefore, they are capable of continuously steering their main radiating lobe with frequency, theoretically from backward to forward endfire [83],[84],[136],[137]. The second class of the recently proposed metamaterial-based LWAs includes structures that make use of High-Impedance Surfaces (HISs) or Artificial Magnetic Conductors (AMCs) together with Partial Reflective Surfaces (PRSs) for the formation for sub-wavelength cavity type LWAs [65],[67]. These LWAs are low-profile, low-cost, highly directive, broadside radiators. Both these novel classes of LWAs involve periodic structures.

For the analysis of leaky-wave structures, the estimation of the complex propagation constant $\gamma = \beta - j\alpha$ of the supported fast-waves is of first priority. The phase constant β defines the scanning angle of the leaky-wave beam according to equation (6.1), while the attenuation constant α effectively defines the beamwidth of this beam and correlates the total size of the radiating structure with the total radiating efficiency of the LWA according to equation (6.2). For the analytical calculation of the complex propagation constants of leaky-waves and the efficient and rigorous modeling of LWAs, during the years, several analytical techniques have been proposed. Nowadays, though, the development of numerical methodologies that would allow for the efficient modeling of any kind of LWAs is strongly favored. On this front, the most challenging issue to be resolved is the usually large physical and electrical size of actual LWAs or segmentations of them that would electromagnetically behave as their original versions.

Novel numerical approaches for the numerically efficient analysis of LWAs and applications of those are discussed in this chapter.

$$\theta_m \cong sin^{-1}(\frac{\beta}{k_o}) \tag{6.1}$$

$$\Delta\theta \cong \frac{1}{\frac{L}{\lambda_o}cos\theta_m} \approx \frac{\frac{\alpha}{k_o}}{0.183cos\theta_m} \tag{6.2}$$

6.2 Periodic FDTD Analysis of LWA

6.2.1 Background

Towards the direction of creating a technique for the efficient numerical modeling of periodic leaky-wave structures, the periodic FDTD analysis of [92] was proposed (the major aspects of this technique were presented in chapter 2). In that approach, the unit

cell of a periodic leaky-wave structure is modeled within a FDTD computational domain that is terminated with periodic boundary conditions, implemented through the sine-cosine technique [103]. As it was shown in [92], when exciting the computational domain with a broadband source and enforcing, through the periodic boundary conditions, a phase-shift between the planes of periodicity (corresponding to a real phase constant β), this type of modeling is able of rigorously solving for all the bounded (slow) and radiating (fast) waves supported by the structure under consideration. The output of this type of computational analysis is time-domain waveforms similar with those of Fig. 6.1 and Fig. 6.2. Specifically, Fig. 6.1 corresponds to a bounded slow-wave, since the amplitude of the supported resonance remains constant with time. On the contrary, Fig. 6.2 corresponds to a radiating fast-wave, since the decaying amplitude of the supported resonance suggests some kind of power loss or power leakage from the structure.

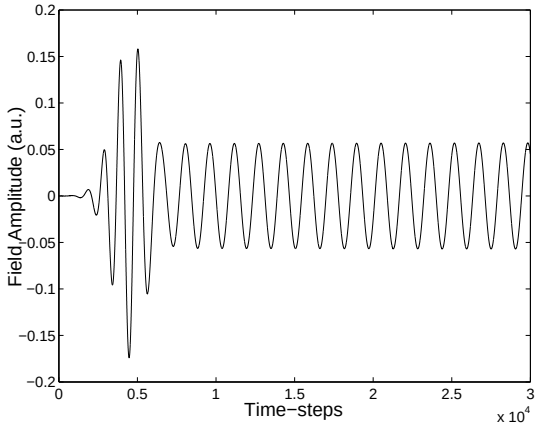

Figure 6.1: Time-domain waveform extracted from the simulation of a non-radiating structure using the periodic FDTD technique presented in chapter 2.

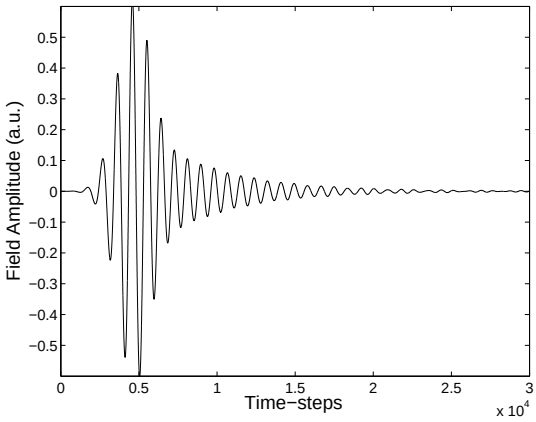

Figure 6.2: Time-domain waveform extracted from the simulation of a leaky-wave structure using the periodic FDTD technique presented in chapter 2.

The calculation of the parameters of the supported modes (e.g. dispersion relation, attenuation constant) relies on the post-processing of the time-domain waveforms such as those of Fig. 6.1 and Fig. 6.2. The calculation of the dispersion diagram can be directly performed by the spectral analysis of the time-domain data, using either Fourier transform or more sophisticated techniques such as Matrix Pencil [138], [139], [140]. On the other hand, for the calculation of the attenuation constant of leaky-waves, more sophis-

ticated electromagnetic arguments were employed in [92]. According to the approach of [92], the complex propagation constant of the leaky-modes can be calculated by treating radiating structures as lossy. In this approach, the complex propagation constant γ is given by equation (6.3). This equation involves two different time-domain samples of the fields $w(t, z_i)$ and $w(t, z_j)$, sampled at two different points z_i and z_j which are usually one spatial period apart. Therefore for the calculation of equation 6.3, the periodic FDTD analysis of two unit cells is required (as shown in Fig. 6.3).

$$\gamma(\omega) = j\frac{1}{z_j - z_i}\log\frac{\mathcal{F}\left[w(t, z_i)\right]}{\mathcal{F}\left[w(t, z_j)\right]}, \tag{6.3}$$

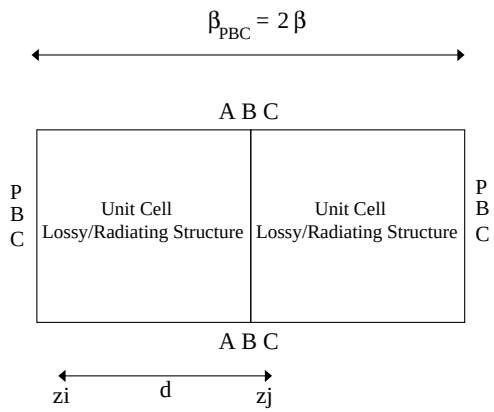

Figure 6.3: Generic representation of the periodic FDTD computational domain required for the implementation of equation (6.3).

Treating leaky-wave structures as lossy and calculating the complex propagation constant using equation (6.3) has been proved to work satisfying rigorously and efficiently. Nevertheless there is a significant weak point associated with this technique; two spatially separated field samples, being usually one spatial period apart, are required for the calculation of equation (6.3). This usually requires the simulation of two identical unit cells of the structure under consideration, leading to the increase of the computational resources and the computational time required for the inclusive characterization of a single structure. Furthermore, it is because of this feature that the proposed technique can be applied only to propagating (traveling) waves with relatively small attenuation constant, and not to quickly attenuated traveling waves or even evanescent waves. Although the latter restriction usually does not apply to the analysis of leaky-waves, it does prevent the use of the proposed technique for the analysis of periodic structures employed as EBGs and the calculation of the attenuation constants of modes within stop-bands.

6.2.2 An Improved Methodology

In order to further reduce the computational resources required for the analysis of leaky-wave structures and allow the use of the periodic FDTD tool for the calculation of large attenuation constant values, an improved methodology is developed and proposed in this section. The novel features of the improved methodology are related mostly with the post-processing of the time-domain data obtained from the periodic FDTD simulation of the single unit cell of a periodic structure.

For the presentation of the improved methodology, let us assume a complex leaky-wave $U(z,t)$ propagating along the $z-$axis. This wave can be written as in equation (6.4)

$$U(z,t) = U_o e^{-j\gamma z} e^{j\omega_r t} \tag{6.4}$$

where $\gamma = \beta - j\alpha$ stands for the complex propagation constant and ω_r is the real frequency of the propagating wave. Substituting γ in equation (6.4), the leaky-wave can be rewritten as

$$U(z,t) = U_o e^{-j(\beta - j\alpha)z} e^{j\omega_r t} \tag{6.5}$$

or, equivalently,

$$U(z,t) = U_o e^{-j\beta z} e^{j\left(\omega_r + j\frac{\alpha z}{t}\right)t} \tag{6.6}$$

In equation (6.6), the leaky-wave has been represented in terms of a real propagation constant β and an effective complex frequency $\omega = \omega_r + j\frac{\alpha z}{t}$. This effective complex frequency defines the characteristics of the decaying time-domain waveform of Fig. 6.2 and, therefore, can be estimated from the spectral analysis of a single waveform such as that of Fig. 6.2. As a result, it can be suggested that the attenuation constant α of the complex propagation constant can be linked directly to the imaginary part of the complex frequency extracted from the spectral analysis of the decaying time-domain waveforms.

According to equation (6.6), the imaginary part of the effective complex frequency of the leaky-wave, that can be calculated through the spectral analysis of the time-domain waveform, is $\omega_i = \frac{\alpha z}{t}$. Given that in a homogeneous and stationary (i.e. non time-varying) medium the phase velocity is defined as $|u_{ph}| = \left|\frac{dz}{dt}\right| \approx \left|\frac{z}{t}\right|$, and also $|u_{ph}| = \left|\frac{\omega_r}{\beta}\right|$, the ratio $\frac{z}{t}$ can be approximated as $\frac{z}{t} \approx \frac{\omega_r}{\beta}$. Hence, the imaginary part of the effective complex frequency of the leaky-wave ω_i can be rewritten as

$$\omega_i = \frac{\alpha \omega_r}{\beta}. \tag{6.7}$$

Equation (6.7) can be employed for the extraction of the following expression for the attenuation constant of the leaky-wave under consideration

$$\alpha = \frac{\omega_i}{\omega_r}\beta. \tag{6.8}$$

Equation (6.8) relates the attenuation constant α of a leaky-wave with the propagation constant of the same leaky-wave β and the real and imaginary parts of its corresponding effective complex frequency. Given that all the aforementioned quantities can be calculated by the periodic FDTD analysis of a single unit cell of a leaky-wave structure and the post-processing of a single time-domain waveform, equation (6.8) can be employed for the estimation of the attenuation constant α from the periodic FDTD analysis of a single unit cell. This constitutes a major computational improvement of the developed technique and also provides the possibility of its applicability to the analysis of periodic structures supporting rapidly attenuated waves. Specifically, regarding the computational benefits of the proposed algorithm, it is expected to reduce the computational memory requirements by a factor of two, the total calculations during the solution of a 3-D electromagnetic problem by a factor of two, as well, and the total execution time of a single simulation by a factor of four.

6.2.3 Validation of the Improved Methodology

For the validation of the improved methodology, two periodic leaky-wave structures are analysed using both the two-unit-cells and the single-unit-cell approaches and the results are compared. The two leaky-wave structures that are being analysed are the metal-strip-loaded dielectric rod LWA [141], [142], [143], [144] and the partially-reflective-surface (PRS) half-wavelength LWA of [5].

Metal-strip-loaded dielectric rod LWA

The first leaky-wave antenna that is analysed for the validation of the proposed methodology is the well-known metal strip loaded dielectric rod leaky-wave antenna. This leaky-wave antenna is fabricated by periodically loading a simple dielectric rod with metallic strips. These periodic perturbations allow the structure to support fast-waves that result in leaky-wave radiation. The unit cell of the simulated structure is depicted in Fig. 6.4.

For the purposes of this study, a metal-strip-loaded dielectric rod leaky-wave antenna designed to operate around $80\,GHz$ is simulated. The physical length d of the unit cell,

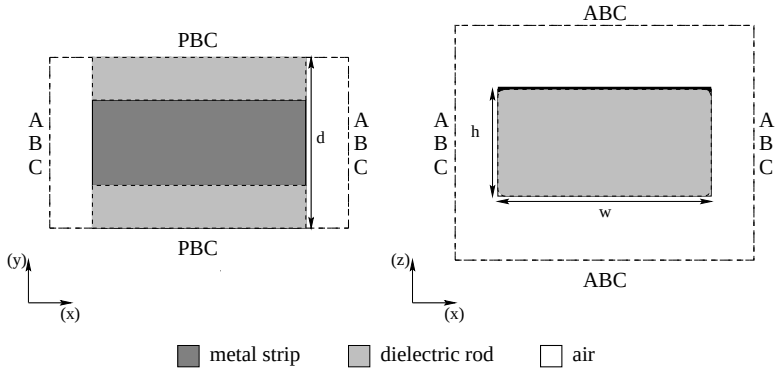

Figure 6.4: Unit cell of the metal-strip-loaded dielectric rod LWA, as modeled through the periodic FDTD analysis.

i.e. the spatial periodicity of the structure, is $d = 2.5\,mm$. The width and the height of the dielectric rod is $w = 3\,mm$ and $h = 1.5747\,mm$, respectively, and the dielectric constant of the rod is $\epsilon_r = 2.33$. The width of the metal strips are $0.5d$, while they are modeled as perfect conductors. For the needs of this analysis, a computational domain of $N_x \times N_y \times N_z = 20 \times 40 \times 33$ Yee's cells is used. This computational domain includes the dielectric rod surrounded with air: as far as the $z-$direction is concerned, 15 cells of air are assumed below and above the structure, to make sure that the absorbing boundary conditions do not affect the radiation of the structure, while in the x-direction two cells of air are assumed at the sides of the structure. The computational domain is excited with a Gabor pulse (sinusoidally modulated Gaussian pulse) of a bandwidth of $10\,GHz$ around the operating frequency. This pulse excites an electric field which is polarized parallel to the metal strips and has a spatial profile of the form $F(x,z) = sin(\frac{\pi x}{w})sin(\frac{\pi z}{h})$, which corresponds to the TE_{11} mode.

The results of the dispersion analysis (complex propagation constant calculation) of the unit cell of Fig. 6.4 employing the two-unit-cells approach (lossy medium approach) and the improved methodology (complex frequency exploitation) are shown in Fig. 6.5. These results suggest that the α values obtained by treating the leaky-wave structure as a lossy structure are in good agreement with those obtained using equation (6.8) and the extracted complex frequency values. As a result, the proposed improved methodology can be considered valid.

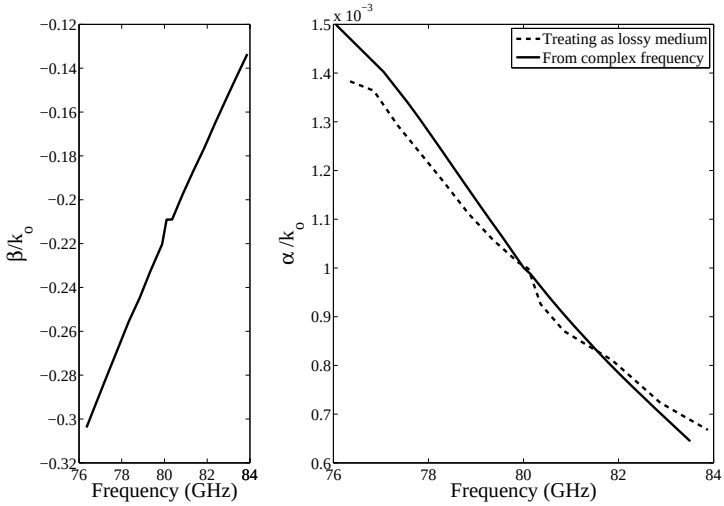

Figure 6.5: Complex propagation constant calculation for the leaky-mode supported by the antenna of Fig. 6.4 calculated using both equation (6.3) and the improved methodology.

Partially-reflective-surface (PRS) half-wavelength LWA

To further validate the proposed methodology, a second leaky-wave structure is analysed using both the improved methodology and the lossy medium approach. The second considered leaky-wave structure is the dipole-based PRS half-wavelength LWA. This structure, that has been analysed in [5] using the lossy medium approach, is composed of a ground plane and a dipole-based PRS being half wavelength above the ground plane. Between these two surfaces leaky-modes can be supported (these leaky-waves are perturbations of the standard parallel-plate modes) allowing for the structure to radiate. The schematic representation of this structure is shown in Fig. 6.6(a). Referring to Fig. 6.6(a), the parameters of the leaky-wave structure that was analysed in [5], using the lossy medium approach, are $l_1 = 14.5\,mm$, $l_2 = 13.5\,mm$, $w_1 = 1\,mm$, $w_2 = 0.5\,mm$ and $h = 10.7\,mm$. This structure supports a perturbed (leaky) TE_1 parallel-plate mode that is developed slightly beyond $14\,GHz$.The computational domain that has been employed in this work for the analysis of the unit cell of that structure, also schematically shown in Fig. 6.6(b), is $N_x \times N_y \times N_z = 8 \times 116 \times 40$ Yee's cells, while 15 cells have been considered in the parallel-plate cavity. For the excitation of the perturbed TE_1 mode, propagating along $x-$axis (short unit cell dimension), a $y-$oriented current source has been used. The spectrum of this source extended from $6\,GHz$ to $20\,GHz$ (Gabor pulse).

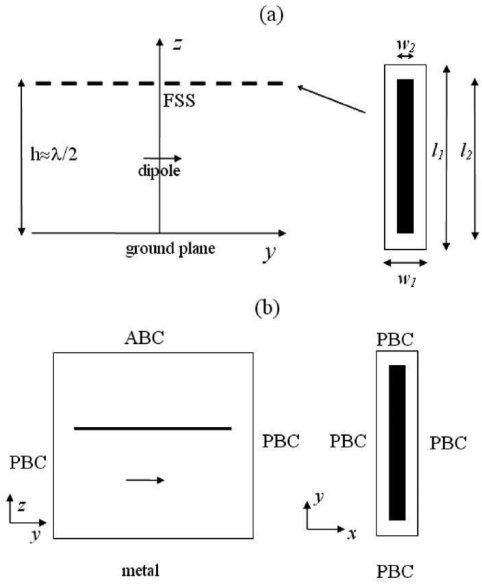

Figure 6.6: a) Schematic representation of the dipole-based partially-reflective-surface (PRS) half-wavelength leaky-wave structure of [5]. b) Computational domain used for the periodic FDTD analysis of the unit cell of the structure of a).

The results of the dispersion analysis for the considered $x-$axis propagating, perturbed TE_1 leaky-wave are depicted in Fig. 6.7. In that plot the extracted attenuation constant values estimated using the complex frequencies that correspond to the extracted time-domain waveforms are compared with the results reported in [5], where the lossy medium approach has been employed. These results are in good agreement, validating the proposed improved methodology that allows for the analysis of the same structure using approximately half the computational resources (computational time and memory).

6.2.4 Large *alpha* Values Assessment

The major disadvantage of the calculation of complex propagation constants using a periodic FDTD analysis together with the lossy medium approach [92] is the failure of the methodology to solve for large values of the attenuation constant α. This is due to the large and fast spatial decay of the propagating signal and the fact that two spatial samples, being one spatial period apart, are required for the calculation of the complex propagation constant. Nevertheless, experimentation has shown that this disadvantage remains unimportant for the analysis of any leaky-wave structure, given that in leaky-wave structures the attenuation constant assumes relatively small values (α/k_o assumes

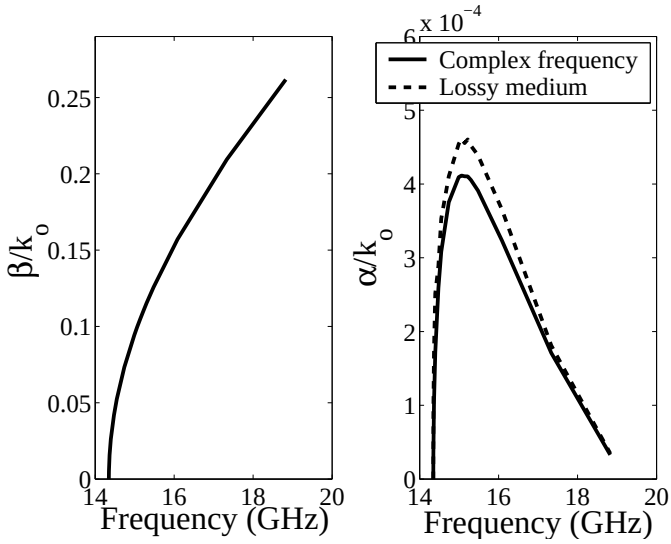

Figure 6.7: Complex propagation constant values of the perturbed, $x-$axis propagating TE_1 mode, calculated using the lossy medium approach [5] and the proposed improved methodology.

values in the range of $10^{-5}-10^{-3}$ in order for the resulting LWA to achieve high directivity through the maximization of its effective radiating aperture). On the other hand, this disadvantage becomes dominant when periodic structures are solved for evanescent modes (e.g. in cases in which periodic structures are designed to be used as EBGs). This suggestion had been also mentioned in [92], where the the proposed methodology had failed to calculate the dispersion diagram of the unbalanced LC loaded transmission line metamaterial within the formulated stopbands.

Given the fact that the improved methodology employs only one spatial sample of the field, it is expected to exhibit an enhanced performance as far as the calculation of large α values are concerned. In the following text, it is attempted to quantify this expectation and quantitatively compare the two approaches by means of a numerical experiment. For this purpose, an 1-D wave of the form of equation (6.9) is assumed.

$$A\left(x,t\right)=A_o e^{-j((\beta-j\alpha)(x-x_o)-\omega_r(t-t_o))} \tag{6.9}$$

As shown above, this wave can be rewritten as

$$A\left(x,t\right)=A_o e^{-j\left(\beta(x-x_o)-\left(\omega_r+j\frac{\alpha\omega_r}{\beta}\right)(t-t_o)\right)} \tag{6.10}$$

This wave is considered to be a leaky-wave (i.e. $\beta<k_o$ and $\alpha>0$) of radial frequency $\omega=\omega_r$, emanating from point $x=x_o$ at the time moment $t=t_o$. The attenuation

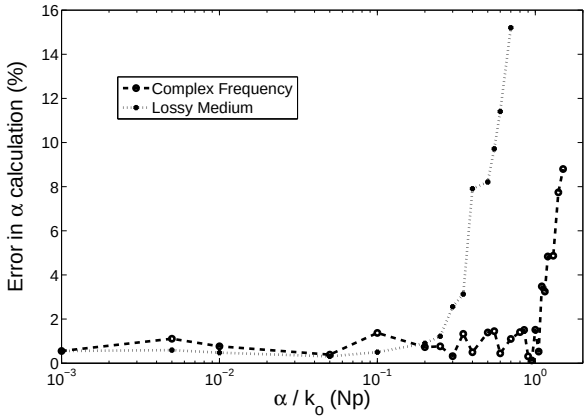

Figure 6.8: Error in α calculation using the lossy medium approach the improved methodology as a function of the magnitude of α.

constant α is considered to be arbitrary large, while its exact value is being preset. To make this ideal wave to resemble more a real-world wave, white Gaussian noise is added to it so as its SNR level to be $40\,dB$. This 1-D wave is sampled at points $x = x_1$ and $x = x_2$, where $x_1 - x_o = 0.1\lambda$ and $x_2 - x_1 = 0.2\lambda$ (the first sampling point $x = x_1$ is considered to be very close to the source $x = x_o$, while the second sampling point $x = x_2$ is considered to be $\lambda/5$ away from the first point, distance that could in many cases correspond to the periodicity of a periodic EBG structure). Then, the two samples are employed together with the lossy medium approach for the estimation of the preset attenuation constant value while only the first sample is employed together with the improved methodology for the estimation of the same attenuation constant value. The error between the calculated values and the preset value of α is then estimated and the same experiment is repeated for several growing α values. The results of this numerical experiment are reported in Fig. 6.8. These results suggest that for small values of the attenuation constant α both methods can effectively estimate it with an average error of 1 %. This error must be attributed to the numerical errors involved in the implementation of the two methods. Nevertheless, the error in the calculation of α when using the traditional lossy medium approach starts increasing for values of α that are greater than $0.11k_o$. On the other hand, the error remains bounded when the improved methodology is employed for values of α as large as k_o. Therefore, it is reasonable to suggest that the proposed improved methodology may be used for the estimation of attenuation constant values that are 10 times larger that those that can be estimated using the lossy medium approach.

6.3 Periodic FDTD Analysis of Sub-wavelength Resonant Cavity Type 2-D LWA

In this section, the periodic FDTD technique of [92] together with the proposed improved methodology for the post-processing of the time-domain data and the calculation of the complex propagation constants of leaky-modes are employed for the analysis of a novel leaky-wave structure, namely, the sub-wavelength resonant cavity type 2-D LWA. The underlying operating concept for this class of antennas is similar with any partially-reflective-surface cavity-type LWA, such the one analysed in the previous section; the power leakage accompanying a perturbed parallel plate mode, supported between a ground plane and a partially-reflective-surface, is exploited for the design of highly-directive antennas. Nevertheless, the structures under consideration are of sub-wavelength heights (instead of being of height $\lambda/2$, at which the first mode of a parallel plate waveguide is supported). This is achieved with the use of artificial magnetic conductors (AMCs) (or high impedance surfaces (HISs)) for ground planes instead of conventional electric conductors. By properly setting the properties of the employed artificial ground plane (the reflective coefficient of the AMCs or the impedance of the HISs), the first cavity resonance between the PRS and the artificial ground plane is supported for separations (cavity heights) much smaller than half-wavelength.

A schematic representation of the investigated sub-wavelength resonant cavity type 2-D LWA is depicted in Fig. 6.9. Specifically, in Fig. 6.9(a), where the side view of the antenna is depicted, it can be seen that the antenna is mainly composed of a PRS, printed on a free standing dielectric substrate, and a magnetic ground plane (MGP), printed on a grounded dielectric substrate. These two surfaces, brought close to each other (at distance $h < \lambda/2$), form a resonant cavity. As already mentioned, the resonant height h is defined mostly by the properties of the MGP. In the following text, cavities of different heights, PRSs and MGPs will be investigated. In Fig. 6.9(b) the top view of the PRS is depicted. For the investigated antenna designs the PRS is composed of square aperture patches (of length L_{prs}) arranged in 2-D periodic configurations (of spatial period D_{prs}) and printed on low loss dielectric substrates. This substrate is considered to be outside the cavity (just above the cavity) to minimize the dielectric losses of the antenna. Finally, the top view of the of the employed MGP is shown in Fig. 6.9(c). The MGP is composed of square patches (of length L_{mgp}) arranged in a 2-D periodic

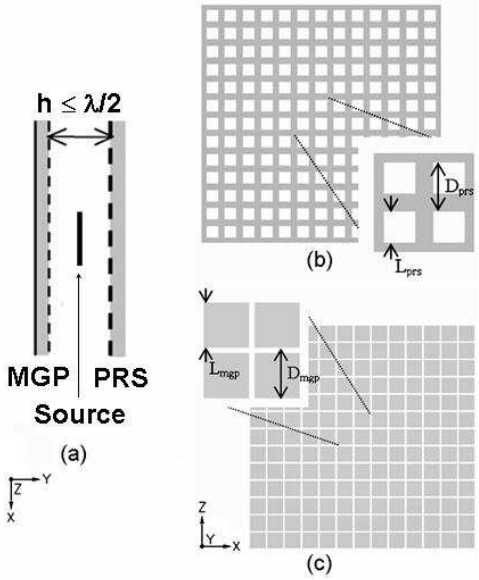

Figure 6.9: Schematic representation of the investigated sub-wavelength resonant cavity type 2-D leaky-wave antennas. a) Cross-section of the investigated antennas, b)top-view of the employed PRS and c) top-view of the employed MGP.

configuration (of spatial period D_{mgp}) and is printed on a grounded dielectric substrate. Due to the strong fields that are supported in this substrate, the employed dielectric substrate should be of minimal dielectric losses. The aforementioned dimensions of the PRS and the MGP determine the electromagnetic properties of these two surfaces and the LWA thereof. Specifically the dimensions related to the PRS define its reflection coefficient and therefore the power leakage rate of the LWA. Those related to the MGP define its reflection phase and by adjusting them different resonant cavity heights can be achieved.

The purpose of the periodic FDTD analysis for this class of antennas is the investigation of the impact of the cavity height to the complex propagation constants of the supported leaky-modes, and, therefore, the optimization of the delivered directivity by an antenna of a given physical aperture with respect to its cavity height. For this purpose, several resonant cavity antennas of different cavity heights (and, therefore, of different MGP parameters) are analysed and the supported complex propagation constants are compared. A list of all the antenna structures that have been investigated is reported in Table 6.3. It is pointed out that all these structures have been designed for operation at about $3.7\,GHz$. In all of them, the periodicity of both the PRS and the MGP

are $D_{prs} = D_{mgp} = 22\,mm$ ($D_{prs}, D_{mgp} \approx 0.27\lambda$), while the employed dielectric substrates parameters in all of them are $\epsilon_{r,prs} = 2.46$, $h_{sub,prs} = 3.198\,mm$, $\epsilon_{r,mgp} = 2.56$, $h_{sub,prs} = 3.152\,mm$.

$Structure\ ID$	$CavityHeight\,(mm)$	$L_{mgp}\,(mm)$	$\angle L_{mgp}\,(degrees)$
$\lambda/2$	38.89	-	-
$\lambda/3$	26.6	18.25	75.45
$\lambda/3.9$	20.9	19.03	15.67
$\lambda/4.9$	16.5	19.50	-33.43
$\lambda/6.1$	13.2	19.80	-62.05
$\lambda/7.0$	11.6	19.95	-74.33
$\lambda/12.7$	6.4	20.50	-107.92
$\lambda/19.8$	4.1	20.80	-120.67

Table 6.1: Cavity heights and MGP parameters of the investigated antenna structures.

Fig. 6.10 shows the cross-section of the computational domain that is used for the periodic FDTD analysis of the sub-wavelength resonant cavity type 2-D LWAs. As already suggested, this computational domain is comprised from a single unit cell of the antenna and is terminated with PBCs at the planes of periodicity. A polarized line current source along $x-$axis is employed to excite simultaneously TE modes along the $z-$axis and TM modes along the $x-$axis. It is pointed out that, given that different discretization (meshing) schemes were employed for each of the structures of Table 6.3, very dense meshes, that would minimize the numerical error in each of them, were employed. The need for extremely dense meshes was also imposed by the strong electric fields supported within the resonating cavity and especially within the substrate of the MGP. Due to all these reasons, the computational domain of Fig. 6.10 was composed of large numbers of Yee's cells (of the order of several millions). Therefore, the improved methodology that allows for the calculation of the complex propagation constants using a single spatial time-domain sample enabled and significantly accelerated the implementation of this study.

The computational domain of Fig. 6.10 is initially employed for the analysis of four of the antenna structures that are described in Table 6.3, namely the $\lambda/2$, the $\lambda/4.9$, the $\lambda/12.7$ and the $\lambda/19.8$. All these designs incorporate a PRS having a reflection coefficient of 0.962 (*i.e.*, $L_{prs} = 14.\,mm$). The results of the analysis of these four structures

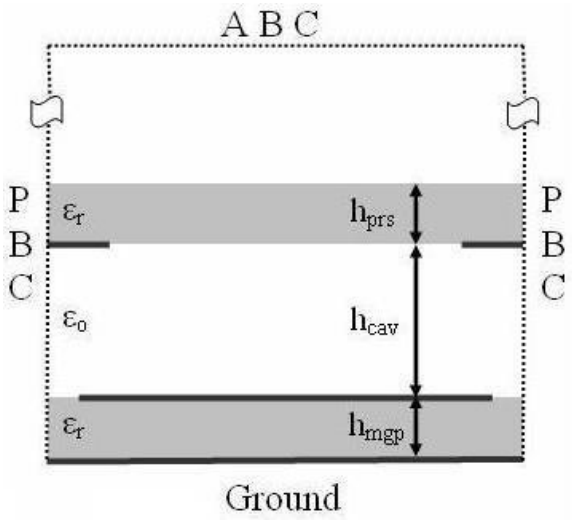

Figure 6.10: Side view of the computational domain employed for the periodic FDTD analysis of the sub-wavelength resonant cavity type 2-D LWAs.

are depicted in Fig. 6.11 and Fig. 6.12. Specifically, Fig. 6.11 shows the section of the dispersion diagram that corresponds to TE leaky-modes which only propagate along the $z-$axis and are characterized by small phase constants (*i.e.*, $\beta d \leq 15^o$). The reason for the latter restriction is that this analysis is focused on broadside radiators, and broadside radiation occurs when $|\alpha| \leq |\beta|$. All of the four antennas support fast-waves at approximately $3.7\,GHz$. It has to be pointed out that all the modes depicted in Fig. 6.11 are deep in the radiating region of the dispersion diagram, given the relatively large periodicity of the antennas under investigation.

Based on simple inspection of the slope of the dispersion curves of Fig. 6.11, it is concluded that the investigated antenna becomes more narrowband as the cavity height is reduced. Therefore, the $\lambda/19.8$ resonant cavity antenna is the most narrowband of the four structures considered, while the $\lambda/2$ antenna is the most broadband.

Fig. 6.12 depicts the attenuation constants associated with the fast-waves shown in Fig. 6.11. Inspection of these results suggests that the attenuation constants do not vary monotonically with the change of the cavity height. Instead, they decrease as the cavity height is reduced from to $\lambda/9$ to $\lambda/4.9$. When the cavity height is reduced below $\lambda/4.9$ the attenuation constants begin to increase again. This observation, motivated us to extend our study to consider additional cavity heights, and further antenna designs were investigated (i.e. all the antennas of Table 6.3, in conjunction with three different

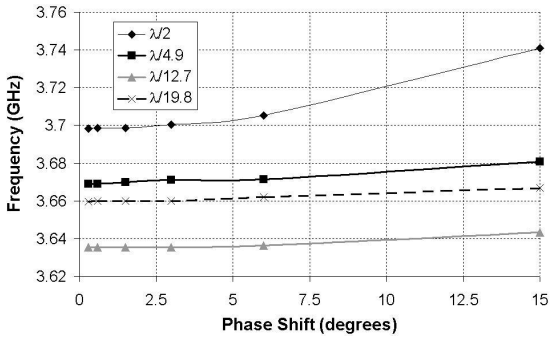

Figure 6.11: Phase constant of the supported TE leaky-modes.

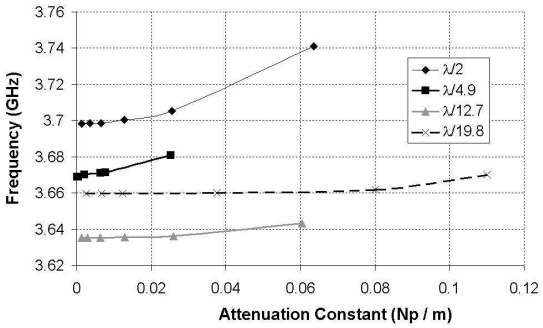

Figure 6.12: Attenuation constants of the leaky-modes shown in Fig. 6.11.

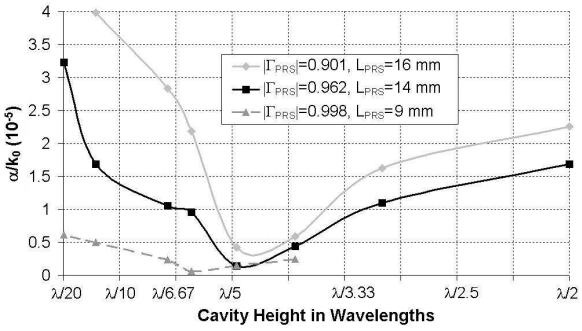

Figure 6.13: Normalized attenuation constant as a function of cavity height for three different PRSs.

PRSs). The results of this study are presented in Fig. 6.13. Upon inspection of this graph it is possible to precisely point out the cavity height which yields the smallest attenuation constant. This height is of the order of $\lambda/4.9$. There is however a trend for this optimum point to move towards lower cavity heights as the PRS reflectivity is increased. It is expected, therefore, that for the first two PRS designs (those with reflectivity $|\Gamma_{PRS}| = 0.901$ and $|\Gamma_{PRS}| = 0.962$) this cavity height will deliver the maximum value of directivity. For a PRS reflectivity of 0.998 the optimum point occurs for a cavity height of approximately $\lambda/6$.

All the aforementioned conclusions were validated through full-wave simulations of antenna structures of finite lateral dimensions and were employed for the fabrication of antenna prototypes with optimized (maximized) delivered directivities. Several of these results have been presented in [6].

6.4 Radiation Pattern Calculation of Finite-size LWAs Using Periodic FDTD Simulations

6.4.1 General

Up to this point, the periodic FDTD technique together with the proposed improved methodology for the post-processing of time-domain waveforms were presented and employed for the calculation of the complex propagation constants of the leaky-modes supported by sub-wavelength resonant cavity type 2-D LWAs. Although the values of the complex propagation constants of the leaky-modes provide several indirect information about the radiating properties of the considered structures, they can not provide directly their radiation patterns. For this reason, the development of a semi-analytical formulation for the estimation of the expected radiation patterns of periodic, finite-size, sub-wavelength resonant cavity type 2-D LWA, composed of sub-wavelength unit cells, given the complex propagation constants of the supported modes is presented in this section.

Under the effective aperture condition, any infinitely long [1] periodic LWA, composed of unit cells of sub-wavelength dimensions, can be treated as a phased array [145], [146]. In that case, each cell of the antenna is assumed to be an omnidirectional point radiator fed with a current of the form $I_n = I_o e^{-n\alpha d} e^{-jn\beta d}$, where $\gamma = \beta - j\alpha$ is the complex propagation constant of the supported leaky-wave. That current value would correspond to the magnitude of a traveling leaky-wave at the location of this unit cell. Therefore, the total radiation pattern of the array is identical with the array factor of the equivalent phased array (equation (6.11)) and is given by equation (6.12).

$$AF = \sum_{n=0}^{N-1} I_n e^{jnk_o dcos\theta} \tag{6.11}$$

$$AF = \sum_{n=0}^{N-1} e^{-n\alpha d} e^{jn(k_o dcos\theta - \beta d)} \tag{6.12}$$

[1] A LWA can be assumed to be infinitely long when it is long enough to radiate all the power that is fed to it.

6.4.2 Electromagnetic Behavior of Finite-size LWA

The attenuation constant of the supported leaky-waves α usually assumes extremely small values and, therefore, in order for most of the power fed into the antennas to be radiated, leaky-wave structures should be large in size (several wavelengths). In many practical cases, this is not possible due to space/volume restrictions. Such is the case for the sub-wavelength resonant cavity type 2-D LWA of the previous section; for an attenuation constant of $\alpha = 0.01$, in order for the 90% of the fed power to be radiated the structure should be approximately $4.5\,m$ long. This is not possible for an antenna operating at $3.7\,GHz$ and being designed for use in commercial communications. Nevertheless, the aforementioned antennas have been prototyped in reasonable lateral sizes (i.e. $29\,cm$, 13 unit cells) and have been measured to deliver high gains corresponding to aperture efficiencies of the order of 50% or more [6], [5]. Therefore, the question to be answered is how such high aperture efficiencies are achieved by antennas of finite and compact lateral size.

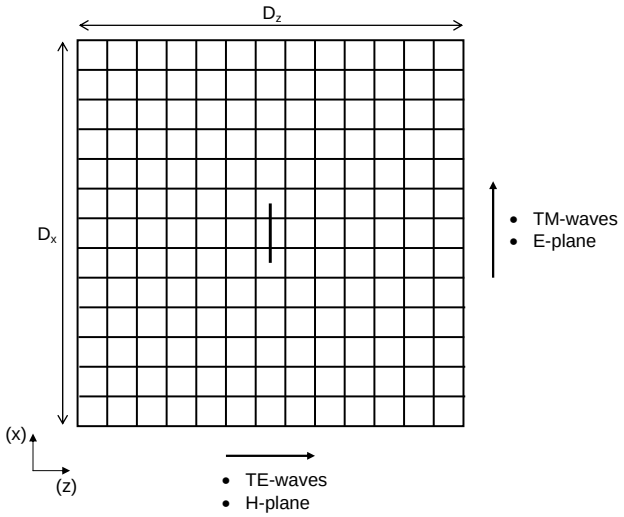

Figure 6.14: Top view of a finite size resonant cavity type 2-D LWA. If the structure is excited with an $x-$axis oriented current source, a TE wave will be supported along $z-$axis and a TM wave along $x-$axis. The TE wave will correspond the $yz-$plane to the H-plane of the antenna and the TM wave would create an E-plane in the xy-plane.

In order to answer this question, let us use the resonant cavity type 2-D LWA as a driving example and consider the leaky-modes supported in these structures. In Fig. 6.14 the top view of a square, periodic resonant cavity type 2-D LWA with finite dimensions

D_z and D_x is depicted. If this structure is excited with an $x-$oriented line source, the fundamental established modes will be a TE wave along $z-$axis and a TM wave along $x-$axis. These waves are in principle perturbations of the TE and TM modes supported by parallel plate waveguides (PPW) [5]. Therefore the impedance of these two modes can be approximated by the impedances of the unperturbed modes

$$Z_{TM,perturbed} \approx Z_{TM,PPW} = \frac{\beta(\omega)}{\omega\epsilon} \tag{6.13}$$

$$Z_{TE,perturbed} \approx Z_{TE,PPW} = \frac{\omega\mu}{\beta(\omega)} \tag{6.14}$$

where $\beta(\omega) = \sqrt{\omega^2\epsilon\mu - (n\pi/h)}$ is the dispersion relation of the unperturbed modes and ϵ, μ the parameters of the materials filling the cavity. When the perturbed TE and TM waves are excited with small phase velocities $\beta_{TM,perturbed} \longrightarrow 0$ and $\beta_{TE,perturbed} \longrightarrow 0$ (very close to the cut-off frequency of the mode), equations (6.13) and (6.14) suggest that $Z_{TM,perturbed} \longrightarrow 0$ and $Z_{TE,perturbed} \longrightarrow \infty$. In that case, the TM leaky-waves supported by the open resonant cavity type 2-D leaky-wave structure will propagate through a very small impedance and the corresponding TE leaky-waves through a very high impedance. This is depicted in Fig. 6.15 and Fig. 6.16 where the analytical dispersion relations and the corresponding impedances of the TE_1 and TM_1 modes supported by a $\lambda/2$ parallel plate waveguide with a cut-off frequency at $3.7\,GHz$ have been plotted.

Going back to the motivating example of the resonant cavity type 2-D LWA of Fig. 6.14, when the perturbed TM waves, that propagate along the $x-$axis through a low impedance, and the perturbed TE waves, that propagate along the $z-$axis through a high impedance, reach the edges of the finite-size structure, they face free space and a medium impedance of $120\pi\,\Omega$. Because their characteristic impedances are much different than the free space impedance, both waves will be reflected back in the structure and will start traveling towards the opposite directions. If we ignore any diffraction effects that might appear when the traveling waves reach the edges of the structure, the reflection coefficients for both the TM and TE waves at the edges of the structure are presented in Fig. 6.17. These results suggest that the TM waves are reflected with a positive coefficient R_{TM} that assumes the maximum value of unity at cut-off (when $Z_{TM,perturbed} \longrightarrow 0$) and decays away from cut-off. On the other hand, the TE waves are reflected with a negative coefficient R_{TE} that again assumes the maximum magnitude of unity at cut-off (when $Z_{TE,perturbed} \longrightarrow \infty$) and decays away from cut-off. In other words, the open edges of the finite size structure act as shorts (electric walls) for the impinging TE waves and as

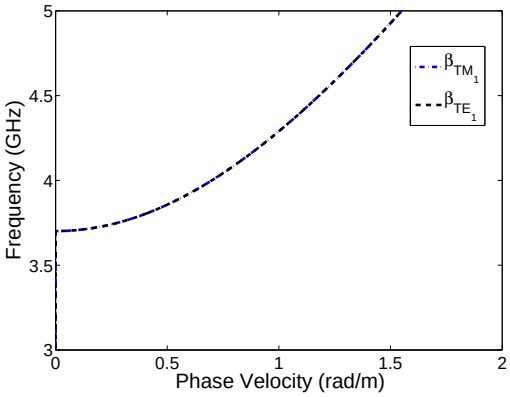

Figure 6.15: Dispersion relations of the TE_1 and TM_1 modes supported by a $\lambda/2$ parallel plate waveguide with a cut-off frequency at $3.7\,GHz$

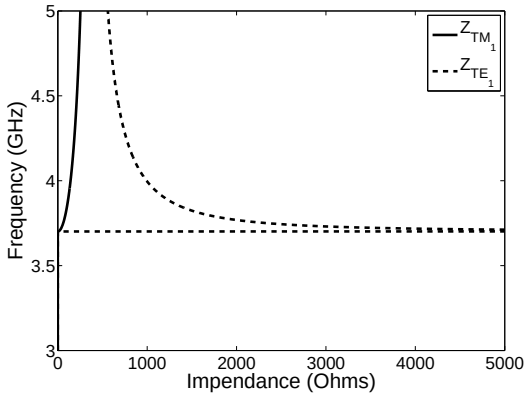

Figure 6.16: Impedances of the TE_1 and TM_1 modes supported by a $\lambda/2$ parallel plate waveguide with a cut-off frequency at $3.7\,GHz$.

opens (magnetic walls) for the TM waves.

Based on this analysis, it is concluded that in a finite size resonant cavity type 2-D leaky-wave structure, such as that of Fig. 6.14, traveling waves are bouncing back and forth, being reflected whenever they impinge on an open edge. Between any two consecutive reflections they remain leaky, radiating power towards $y-$axis. Therefore, in configurations like that of Fig. 6.14, traveling leaky-waves form after multiple reflections a standing field distribution in the structure, and, hence, the radiating properties of the structure (i.e. aperture efficiency, radiation patterns) should be attributed more to that standing field distribution than to a single conventional, traveling leaky-wave.

6.4.3 Array Factor of Finite-size LWA

Proposed Model

Given the analysis of the previous section it becomes clear that equation (6.12) can not be employed, under the effective aperture approach, for the calculation of the radiation patterns of finite size LWAs, when the complex propagation constants of the supported modes are known. This is because equation (6.12) considers conventional traveling leaky-waves and, hence, excitation currents for the point radiators of the form

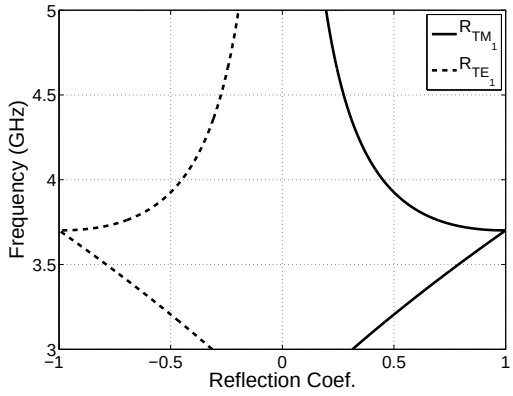

Figure 6.17: Reflection coefficients for the TE and TM wave impinging at the open ends of a finite size waveguide structure (with a cut-off frequency at $3.7GHz$), when diffraction effects are not considered.

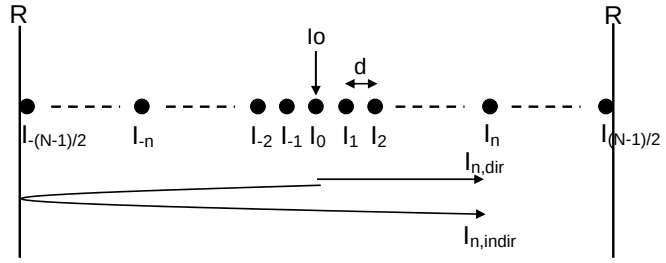

Figure 6.18: Array representation of a cross section of a finite size LWA along any of its principal planes.

$I_n = I_o e^{-n\alpha d} e^{-jn\beta d}$. On the contrary, it is suggested hereby, that the generic array factor equation (6.11) could be used for the calculation of the radiation patterns of finite-size LWAs, at least at the principal radiation planes of the antenna, provided that the correct current coefficients I_n that correspond to each of the unit cells along these planes are calculated in accordance with the analysis of the previous section. That calculation of the current coefficients is attempted in the following text.

For this purpose, let us consider an 1-D array of N point radiators (N is considered to be an odd number) terminated at both edges with reflective surfaces of reflection coefficient R, as shown in Fig. 6.18. These point radiators correspond to the sub-wavelength unit cells of the finite-size LWA under investigation, R corresponds to the reflection coefficient facing the traveling leaky-waves when reaching the edges of the structure, while

the entire array can be representative of any principal planes cross sections of the LWA. Assuming that the array is externally fed at its middle element with a current I_o (feeding point of the LWA), traveling leaky-waves will be excited towards both directions of the array, with respect to the middle element (left and right). Each of these two waves will be consecutively reflected whenever it reaches any edge of the array and eventually a standing field distribution will be created. For the estimation of the equivalent excitation currents of the array elements, it is considered that the total current of the $n^{th}-$radiator I_n is consisted of two components; the first is derived from the wave the directly arrives at this unit cell from the feeding point of the array and the multiple reflections of that wave, and the second is derived from that wave that originally traveled towards the opposite direction and indirectly reached that unit cell after a single reflection at the opposite edge, and the multiple reflections of that wave. This is also shown in Fig. 6.18, and can be expressed as

$$I_n = I_{n,dir} + I_{n,indir} \tag{6.15}$$

The component $I_{n,dir}$ of equation (6.15) can be expressed in terms of the array parameters and the complex propagation constant of the examined leaky-waves as

$$I_{n,dir} = I_n^+ + I_n^+ \left(\Phi^+ R \Phi^+\right) + I_n^+ \left(\Phi^+ R \Phi^+\right)\left(\Phi^- R \Phi^-\right) + I_n^+ \left(\Phi^+ R \Phi^+\right)\left(\Phi^- R \Phi^-\right)\left(\Phi^+ R \Phi^+\right) + ... \tag{6.16}$$

where I_n^+ is given by equation (6.17) and corresponds to the wave that directly reaches the n^{th} unit cell from the feeding point, the second term of equation (6.16) corresponds to the first reflection of I_n^+ to the closest reflection surface, the third term of equation (6.16) corresponds to the second reflection of I_n^+ to the opposite reflection surface etc. The coefficient Φ^+ is the transmission coefficient (phasor) of a wave traveling from the n^{th} element to the nearest reflecting surface and is given by equation (6.18), and Φ^- is the transmission coefficient of a wave traveling from the n^{th} element to the other (opposite) reflecting surface and is given by equation (6.19)

$$I_n^+ = I_o e^{-jn(\beta - j\alpha)d} \tag{6.17}$$

$$\Phi_n^+ = e^{-j\left(\frac{N-1}{2} - n\right)(\beta - j\alpha)d} \tag{6.18}$$

$$\Phi_n^- = e^{-j\left(\frac{N-1}{2} + n\right)(\beta - j\alpha)d} \tag{6.19}$$

Similarly, the contribution of the indirect component involved in equation (6.15) can

be written as

$$I_{n,indir} = I_n^- + I_n^- \left(\Phi^+ R \Phi^+\right) + I_n^- \left(\Phi^+ R \Phi^+\right)\left(\Phi^- R \Phi^-\right) + I_n^- \left(\Phi^+ R \Phi^+\right)\left(\Phi^- R \Phi^-\right)\left(\Phi^+ R \Phi^+\right) + ... \tag{6.20}$$

where I_n^- corresponds to the indirect wave that reaches the n^{th} radiatos and is given by equation (6.21).

$$I_n^- = I_o e^{-j\left(\frac{N-1}{2}\right)(\beta - j\alpha)d} \Phi_n^- \tag{6.21}$$

Combining equation (6.15) with equations (6.16) and (6.20), the total current on the n^{th} element of the array can be written as

$$I_n = \sum_{m=0}^{\infty} \left(I_n^+ + I_n^-\right) \left[\Phi_n^+ R \Phi_n^+\right]^m \left[\Phi_n^- R \Phi_n^-\right]^m + \sum_{m=1}^{\infty} \left(I_n^+ + I_n^-\right) \left[\Phi_n^+ R \Phi_n^+\right]^m \left[\Phi_n^- R \Phi_n^-\right]^{(m-1)} \tag{6.22}$$

Equation (6.22) can be then used together with the conventional generic array factor equation (6.11) for the calculation of the principal planes radiation patterns of finite size LWAs.

Validation - Discussion

For the validation of the proposed model, the principal radiation patterns of a sub-wavelength finite size resonant cavity type 2-D LWA are calculated, using the proposed model together with the FDTD results reported in section 6.3, and are compared with the corresponding radiation patterns, obtained through the simulation of the entire finite-size structure using a commercial full-wave EM solver (CST Microstripes), that have been reported in [6].

The antenna under consideration is a $\lambda/4.9$ resonant cavity type 2-D LWA composed of 13 unit cells, identical with that of Fig. 6.10, along both principal planes (the antenna is composed of 13^2 unit cells in total). The reflection coefficient of the employed PRS has been considered to be $\Gamma_{PRS} = 0.962$, while the periodicity of the structure is $d = 22\,mm$ in both principal planes. This unit cell has been analysed in section 6.3 and the supported complex propagation constants derived by its periodic FDTD analysis have been presented in Fig. 6.11 and Fig. 6.12.

Using the proposed model (with $R_{E-plane} = 1$ and $R_{H-plane} = -1$), the aforementioned parameters and the results of the periodic FDTD analysis of the unit cell, the calculated E- and H-plane radiation patterns are presented in Fig. 6.19.

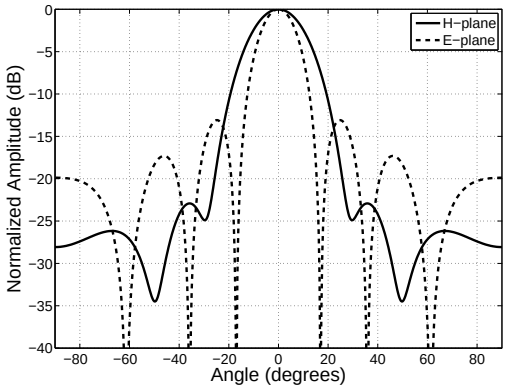

Figure 6.19: E- and H-plane radiation patterns of a $\lambda/4.9$ resonant cavity type 2-D leaky-wave antenna composed of 13 unit cells, calculated using the proposed model.

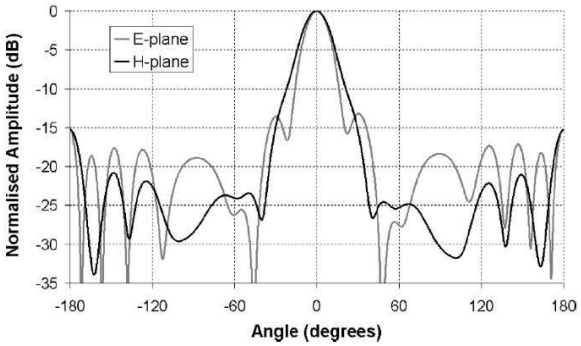

Figure 6.20: E- and H-plane radiation patterns of a $\lambda/4.9$ resonant cavity type 2-D leaky-wave antenna composed of 13 unit cells, calculated using the a full-wave simulation of the entire finite size structure (obtained from [6]).

In Fig. 6.20 the radiation patterns of the same structure, calculated using CST Microstripes and originally reported in [6], are depicted. Comparing the radiation patterns of Fig. 6.19 and Fig. 6.20 good agreement can be observed. The E-plane radiation pattern calculated using the proposed model achieves the same number of nulls and at roughly the same angles with that calculated through the full-wave simulation. The sidelobe level and the endfire radiation in both patterns are of the same order of magnitude (roughly $-13\,dB$ and $-19\,dB$, respectively), while similar directivity values can be extracted from both patterns. Good agreement is also observed for the H-plane patterns. In that case, both the full-wave and the array factor patterns exhibit two nulls left and right of the broadside direction, both patterns exhibit a sidelobe level of the order of $-23\,dB$ and endfire directivity of the order of $-28\,dB$, and both patterns suggest that the H-plane pattern of the investigated antenna is less directive than its E-plane pattern.

Nevertheless, between the two sets of patterns there are also some disagreements, mostly related with the exact position and the depth of the nulls. This disagreement is attributed to the fact that no diffraction effects have been considered in the proposed model for the calculation of the radiation patterns. In fact, diffraction is expected to affect the total radiation patterns of the finite-size antenna in two different ways. First, due to the diffraction of waves at the open edges, the reflection coefficient encountered by the traveling leaky-waves when reaching the edges of the structure would deviate form the ideal values of $R_{E-plane} = 1$ and $R_{H-plane} = -1$ that were considered in the proposed model. This deviation concerns both the magnitude of the reflection coefficients (they are expected to be less than the unity) and also its phase (due to the diffraction, the reflection coefficients are expected to possess some small imaginary part). Secondly, the diffracted power at the edges of the finite-size structure is also radiated in the free space and is part of the total radiation patterns that are calculated with the full-wave simulation of the finite structure. Therefore, the patterns of Fig. 6.20 also include the contributions of the diffracted fields, while those of Fig. 6.19 were derived by considering only radiated from the array fields.

Conclusively, even though the proposed model is inherently an approximate one, it could be used to some extend for the fast and analytical calculation of the radiation patterns of finite-size LWAs. For the calculation of these patterns, only the complex propagation constants of the supported leaky-waves, that can be extracted using the proposed single-cell periodic FDTD methodology, are required. The benefit of using this model may be huge as the full-wave simulation of the entire finite-size LWA may require

several hours of computational time and significantly large computational resources.

Chapter 7

Conclusions

7.1 Review

In this thesis, the analysis, design and modeling of novel metamaterial and metamaterial-inspired microwave structures and antenna applications were presented. Motivated by the challenge of enhancing the penetration of metamaterial-related applications into commercial products, novel, low cost, easily deployable metamaterial structures were proposed. Such metamaterial structures were employed for the design of easily fabricated antenna elements and arrays of those. Also, a periodic, full-wave, FDTD-based tool was developed, optimized and linked to novel post-processing algorithms that enabled the computationally efficient, rigorous and inclusive characterization of high-gain, metamaterial-based, flat-plate antennas.

In chapter 2, all the theoretical aspects that were employed throughout the thesis were presented. Specifically, all the possible approaches for the synthesis of metamaterial structures were briefly described and modeled through the equivalent circuit analysis of resonators either interacting with impinging plane waves or forming arrays of tightly coupled unit cells. It was shown that the latter approach, that has been much less investigated in the literature, can be employed for the synthesis of any of the well-known metamaterial properties and applications, depending on the magnitude and the nature of the coupling between the resonators. Also, in the same chapter, all the theoretical background of the in-house periodic FDTD-based computational tool, that has been extensively employed and furthered developed in this thesis, was briefly presented.

In chapter 3, the theory for the design of metamaterial structures employing tightly coupled resonators was employed together with compact resonators printed on grounded

dielectric substrates for the synthesis of microstrip-based artificial transmission lines and applications of those. Specifically, the double-spiral resonator (DSR) was identified as a proper modular element for the design of such lines, was extensively analysed and all its unique properties were identified. In turn, such resonators were employed for the design of DSR-based artificial lines supporting backward waves over a measured fractional bandwidth of 13%. Such lines were used for the synthesis of broadband series-fed microstrip patch arrays, exhibiting reduced sidelobe levels and beam-scanning capabilities.

In chapter 4, tightly coupled resonators were employed in non-grounded configurations for the synthesis of compact, phase-shifting lines that were used for the design of low-profile folded monopoles. In the proposed approach, two low-profile, vertical, radiating posts were connected through an artificial, non-radiating, phase-shifting line that was used to enforce the resonance condition of conventional folded monopoles. Therefore, the resulting radiators were self-resonant while they exploited the four-fold increase of the radiation resistance of folded monopoles to exhibit decent radiation resistances even though being of low profile. Such monopoles were explicitly modeled and analysed, radiators of different profiles were investigated while the impact of the ground plane against which they were fed was also studied. Both coaxially and microstrip-fed monopoles were considered while it was shown that pairs of such monopoles exhibit reduced electromagnetic coupling as compared to the coupling between conventional quarter-wavelength monopoles.

The self-resonant, low-profile, low-coupling monopoles of chapter 4 were employed in chapter 5 for the design of two classes of sub-wavelength antenna arrays. The first of them was a two-element phased array in which the array element separation was approximately $\lambda/5$. Even that small inter-element separation the measured performance of the array was close to the theoretically expected, in contrast to the performance of the corresponding array of conventional monopoles. The second class of sub-wavelength arrays that were investigated were two-element superdirective endfire arrays. In that case, the inherent properties of the employed low-profile folded monopoles enabled the simplification of the required feeding network and the fabrication of single-port microstrip-based arrays. The directivity and the gain delivered by such arrays were rigorously measured to validate both their superdirective properties and the fundamental limitations associated with their operation. In the same chapter, a metamaterial-inspired decoupling mechanism was proposed for the coupling reduction between conventional planar inverted-F antennas participating in compact arrays built on a common ground plane (handheld devices).

According to this scheme, a resonating pair of slits (effective magnetic loop) was added in the coupling path between the two coupled antennas to insert a transmission-zero.

The last chapter of the thesis was dedicated to the numerically efficient modeling of periodic leaky-wave structures with emphasis to metamaterial-based high-gain leaky-wave antennas. The periodic in-house FDTD-based tool of [92] was linked with novel post-processing algorithms that enabled the reduction of the computational resources required for the analysis of periodic leaky-wave structures. The numerically improved methodology was employed for the analysis of novel sub-wavelength resonant cavity type 2-D leaky-wave antennas and the optimization of their directivity with respect to their profile. Finally, post-processing algorithms that allowed the approximate calculation of radiation patterns of electrically large, finite-size, 2-D leaky-wave antennas through the periodic FDTD analysis of their unit cell were developed.

7.2 Future Work

The objective of this thesis was to propose novel, low-cost, easily fabricated metamaterial structures that could be easily deployed within commercial microwave applications. For this purpose, the least investigated class of metamaterial structures, those formed by arrays of tightly coupled resonators, was employed. The outcomes of this research endeavor include several interesting metamaterial structures that could be deployed in several commercial applications given that they address many of the requirements of modern telecommunication systems such as size/volume reduction, low fabrication cost and compatibility with standard microwave technologies. For this reason, it is believed that this research endeavor could potentially inspire future research activity targeting at the development and validation of more metamaterial-based microwave applications. In the following text, some of the directions of future research related with the context of this thesis are briefly presented.

First, on the front of the synthesis of metamaterial structures using tightly coupled resonators, it would be interesting if the coupling requirements for the synthesis of different metamaterial properties could be married with traditional filter synthesis theory [32]. The results of this study should comment on which of the metamaterial properties could be achieved under the restrictions imposed by the filter synthesis theory on the sign of the coupling coefficients. Then, these metamaterial properties could be synthesised over an exact and predefined bandwidth.

On the front of the design of microstrip-based artificial lines, the use of different resonators for the synthesis of such lines may be worth investigating. Even though the double-spiral resonator investigated in this thesis exhibits several comparative advantages (small footprint, discrete inductive components) it does not provide a direct means of reconfiguring its electromagnetic properties (e.g. through a tuning discrete component such a varactor or a PIN diode). This is mostly due to the fact that it does not possess a discrete capacitive gap on which a tuning discrete element could be fit. Therefore, future research on reconfigurable resonators and how they could be employed for the synthesis of artificial lines could lead to the design of novel reconfigurable metamaterial structures.

Regarding the proposed low-profile folded monopoles, future research work may involve the implementation of these monopoles in planar form, using both single layer and multilayer PCB technology. Some initial investigations carried out showed that such implementations are definitely possible. In their planar form, such antennas could be also considered for applications that require integrated, fully-printed, electrically small radiators. Also, in their planar form, such monopoles could be designed in dually-polarized configurations. Another promising feature of the proposed low-profile folded monopoles is that their radiating mechanism is to a certain degree decorrelated to their reactive components. Therefore, the self-resonance of such monopoles can be tunned only by tunning the properties of the embedded matching network (phase-shifting line). As a result, it is reasonable to expect that reconfigurable folded monopoles could be easily designed if reconfigurable coupled resonators were employed as embedded phase-shifting lines. Also, regarding the arrays of low-profile folded monopoles, given the comparative advantages of such monopoles when forming compact arrays (reduced mutual coupling, robust input impedance), it would be interesting to test such compact arrays within an experimental MIMO setup in order to experimentally assess the capacity gain obtained by employing such sub-wavelength arrays.

Finally, on the front of the periodic modeling of electrical large, metamaterial-based, high-gain antennas, it is strongly believed that most of the identifying antenna parameters of such radiators can be rigorously obtained by the full-wave periodic analysis of a single unit-cell and the post-processing of the extracted data. Therefore, more post-processing algorithms, similar with those presented in this thesis, should be developed and employed together with the periodic analysis to achieve the computationally efficient analysis of these antennas. For example, such post-processing algorithms may be developed for the calculation of the impedance characteristics of an antenna, its effective aperture and its

radiation efficiency. For the improvement of the accuracy of all these algorithm the effect of the diffraction at the edges of the finite-size antenna should be also modeled and taken into account.

Appendix A

Analysis Of Coupled Lines

Any pair of microstrip lines that are located close to each other can be assumed to be coupled. In this case, the electrical characteristics of these lines, for TEM type of propagation, can be completely determined in terms of the phase velocity supported by each line and the effective capacitances between them.

In the following, two different extreme types of excitations for the coupled lines are examined. The first type refers to the case in which the currents on the coupled strips are equal in magnitude and in the same direction. This type of coupled line is shown in Figure A.1 and is referred in the literature as even-mode excited lines. In this case, a hypothetical magnetic wall can be assumed between the two lines, no displacement currents and no effective capacitance are supported between the lines, and, consequently, the propagation on each line is defined by the characteristics of each line.

The second type of excitation is the odd-mode excitation, in which the currents on the lines are of the same magnitude but are flowing in opposite directions. This case is depicted in Figure A.2.

Under an odd-mode excitation, a hypothetic electric wall can be assumed between the lines and the coupling between the lines can be modeled through a capacitance between the strips. This capacitance can be expressed in terms of the parallel combination of a capacitance that represents the fringing fields within the dielectric substrate just below the strips ($C_{gd}/2$ in Figure A.2) with the capacitance that represents the fringing fields in the air just above them $C_{ga}/2$ in Figure A.2). Each one of these two capacitances are expressed as a series combination of two capacitors (C_{gd} and C_{ga}, respectively), while the mutual poles of these capacitors are grounded, due the created electric wall. Therefore, all the capacitances of Figure A.2 are grounded.

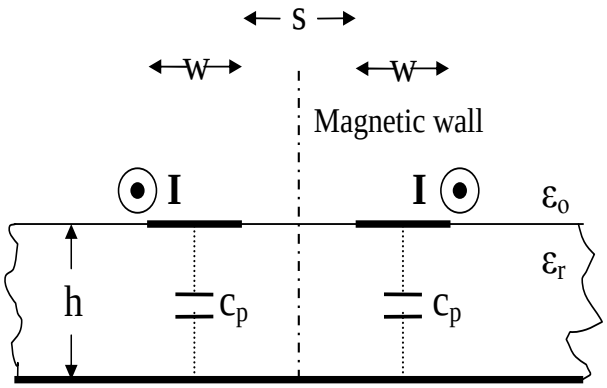

Figure A.1: Microstrip lines coupled under an even-mode excitation. In that case a magnetic wall can be assumed between the lines and, therefore, no capacitance is supported between them.

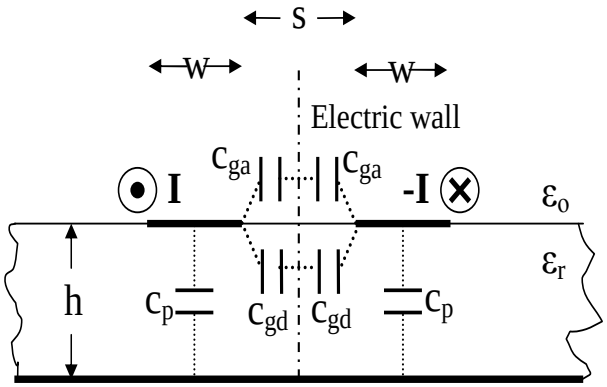

Figure A.2: Microstrip lines coupled under an odd-mode excitation. In that case an electric wall can be assumed between the lines and, therefore, a fringing field capacitance is supported between them.

To conclude the analysis of the coupled lines under an odd-mode excitation, the values of the aforementioned capacitances should be estimated. For this purpose, in this study, the semi-empirical formulas of [147] are employed.

According to the analysis of [147], the fringing fields capacitances for the air is given by the equation

$$C_{ga} = \epsilon_o \frac{K(k')}{K(k)} \tag{A.1}$$

where,

$$k = \frac{s/h}{s/h + 2w/h} \tag{A.2}$$

and

$$k' = \sqrt{1 - k^2}. \tag{A.3}$$

Then, the ratio of the elliptic function of equation A.1 depends on the value of k. Specifically,

$$\frac{K(k')}{K(k)} = \frac{1}{\pi} \ell n \left(2 \frac{1 + \sqrt{k'}}{1 - \sqrt{k'}} \right), \quad if \quad 0 \leq k^2 \leq 0.5 \tag{A.4}$$

and

$$\frac{K(k')}{K(k)} = \frac{\pi}{\ell n \left\{ 2 \left(1 + \sqrt{k} \right) / \left(1 - \sqrt{k} \right) \right\}}, \quad if \quad 0.5 \leq k^2 \leq 1 \tag{A.5}$$

Finally, the fringing field capacitances on the dielectric are given by equation A.6

$$C_{gd} = \frac{\epsilon_o \epsilon_r}{\pi} \ell n \left\{ coth \left(\frac{\pi}{4} \frac{s}{h} \right) \right\} + 0.65 C_f \left(\frac{0.02}{s/h} \sqrt{\epsilon_r} + 1 - \epsilon_r^{-2} \right) \tag{A.6}$$

where

$$C_f = \frac{\sqrt{\epsilon_{eff}}}{2 c Z_0} - \frac{C_p}{2} \tag{A.7}$$

and

$$C_p = \epsilon_o \epsilon_r \frac{w}{h}. \tag{A.8}$$

Bibliography

[1] A. Taflove and S. C. Hagness, *Computational Electrodynamics: The Finite-Difference Time-Domain Method*, 2nd ed. Boston: Artech House, 2000.

[2] A. Grbic and G.V Eleftheriades, "Periodic analysis of a 2-D negative refractive index transmission line structure," *IEEE Microwave Wireless Compon. Lett.*, vol. 51, no. 10, pp. 2604–2611, Oct. 2003.

[3] J.B. Pendry, A.J. Holden, A.J. Robbins, and W.J. Stewart, "Magnetism from conductors and enhanced nonlinear phenomena," *IEEE Trans. Microwave Theory Tech.*, vol. 47, no. 11, pp. 2075–2084, Nov. 1999.

[4] A.I. Uzkov, "An approach to the problem of optimun directive antennae design," *Comptes Rendus Academ. Sci. USSR*, vol. 53, pp. 35–38, 1946.

[5] P. Kosmas, A.P. Feresidis, and G. Goussetis, "Periodic FDTD analysis of a 2-D leaky-wave planar antenna based on dipole frequency selective surfaces. ," *IEEE Trans. Antennas Propagat.*, vol. 55, no. 6, pp. 2006–2012, Jul. 2007.

[6] J.R. Kelly, T. Kokkinos, and A.P. Feresidis, "Analysis and design of sub-wavelength resonant cavity type 2-D leaky-wave antennas ," *IEEE Trans. Antennas Propagat.*, vol. 56, no. 9, pp. 2817–2825, Sept. 2008.

[7] V.G. Veselago, "The electrodynamics of substances with simultaneously negative values of ϵ and μ ," *Soviet Physics Uspekhi*, vol. 10, no. 4, pp. 509–514, Jan-Feb 1968.

[8] R. Collin, *Foundations For Microwave Engineering*, 2nd ed. Toronto, ON: McGraw-Hill Inc., 1992.

[9] W. Rotman, "Plasma simulation by artificial dielectrics and parallel-plate media," *IRE Trans. on Ant. and Propag.*, vol. 10, no. 1, pp. 82–95, Jan. 1962.

[10] J.D. Joannopoulos, S.G. Johnson, J.N. Winn, and R.D. Meade, *Photonic Crystals: Molding the Flow of Light*, 2nd ed. New Jersey: Princeton University Press., 2008.

[11] J. B. Pendry, "Calculating photonic band structure," *J. Phys. : Condens. Matter*, vol. 9, Feb. 1996.

[12] E. Yablonovitch, "Photonic Crystals: Semiconductors of Light ," *Scientific American*, pp. 47–55, Dec. 2001.

[13] M.M. Sigalas, C.T. Chan, K.M. Ho, and C.M. Soukoulis, "Metallic photonic bandgap materials," *Phys. Rev. B*, vol. 52, no. 16, pp. 11 744–11 752, Oct. 1995.

[14] A.S. Barlevy, D. Sievenpiper, and Y. Rahmat-Samii, "Photonic bandgap (PBG) structures of multiple metallic periodic screens: efficient electromagnetic characterization," in *Proc. IEEE Antennas and Propagation International Symposium (AP-S)*, vol. 2, Jun. 1998, pp. 1216–1219.

[15] D. Sievenpiper and E. Yablonovitch, "Eliminating surface currents with metallodielectric photonic crystals," in *Proc. IEEE International Microwave Symposium (MTT-S)*, vol. 2, Jun. 1998, pp. 663–666.

[16] B.A. Munk, *Frequency Selective Surfaces: Theory and Design*, 1st ed. New York: John Wiley and Sons, Ltd., 2000.

[17] J.C. Vardaxoglou, *Frequency Selective Surfaces: Analysis and Design* , 1st ed. Research Studies Press Ltd, 1997.

[18] P.-S. Kildal, "Artificially soft and hard surfaces in electromagnetics," *IEEE Trans. Antennas Propagat.*, vol. 38, no. 10, pp. 1537–1544, Oct. 1990.

[19] F. Mariotte, S.A. Tretyakov, and B. Sauviac, "Modeling effective properties of chiral composites," *IEEE Antennas Propagat. Mag.*, vol. 38, no. 2, pp. 22 – 32, Apr. 1996.

[20] N. Engheta, D.L. Jaggard, and M.W. Kowarz, "Electromagnetic waves in Faraday chiral media," *IEEE Trans. Antennas Propagat.*, vol. 40, no. 4, pp. 367 – 374, Apr. 1992.

[21] F. Mariotte and N. Engheta, "Reflection and transmission of guided electromagnetic waves at an air-chiral interface and at a chiral slab in a parallel-plate waveguide," *IEEE Trans. Microwave Theory Tech.*, vol. 41, no. 11, pp. 1895–1906, Nov. 1993.

[22] J.B. Pendry, A.J. Holden, W.J. Stewart, and I. Youngs, "Extremely Low Frequency Plasmons in Metallic Mesostructures," *Phys. Rev. Lett.*, vol. 76, p. 47734776, Jun. 1996.

[23] D.R. Smith, W.J. Padilla, D.C. Vier, S.C. Nemat-Nasser, and S. Schultz, "Composite Medium with Simultaneously Negative Permeability and Permittivity," *Phys. Rev. Lett.*, vol. 84, no. 18, pp. 4184–4187, May 2000.

[24] R.A. Shelby, D.R. Smith, and S. Schultz, "Experimental verification of a negative index of refraction," *Science Magazine*, vol. 292, pp. 77–79, Apr. 2001.

[25] R.W. Ziolkowski and F. Auzanneau, "Artificial molecule realization of a magnetic wall," *J. Appl. Phys*, vol. 82, no. 7, pp. 3192 – 3194, Oct. 1997.

[26] ——, "Passive artificial molecule realizations of dielectric materials," *J. Appl. Phys*, vol. 82, no. 7, pp. 3195 – 3198, Oct. 1997.

[27] D. Sievenpiper, Z. Lijun, R.F.J. Broas, N.G. Alexopolous, and E. Yablonovitch, "High-impedance electromagnetic surfaces with a forbidden frequency band," *IEEE Trans. Microwave Theory Tech.*, vol. 47, no. 11, pp. 2059–2074, Nov. 1999.

[28] G.V. Eleftheriades, A.K Iyer, and P.C Kremer, "Planar negative refractive index media using periodically L-C loaded transmission lines," *IEEE Trans. Microwave Theory Tech.*, vol. 50, no. 12, pp. 1494–1504, Dec. 2002.

[29] G.V. Eleftheriades and K.G. Balmain, *Negative-Refraction Metamaterials; Fundamental Principles and Applications.* Hoboken, NJ: John Wiley and Sons, Inc., 2005.

[30] A. Lai, T. Itoh, and C. Caloz, "Composite right/left-handed transmission line metamaterials," *IEEE Microwave Magazine*, vol. 5, no. 3, pp. 34–50, Sept. 2004.

[31] S. Ramo, J.R. Whinnery, and T. Van Duzer, *Fields and Waves in Communication Electronics*, 3rd ed. New York, NY: John Wiley and Sons, Inc., 1994.

[32] J.S. Hong and M.J. Lancaster, *Microstrip filters for RF microwave applications*, 2nd ed. West Sussex, UK: John Wiley and Sons, Ltd., 2001.

[33] A.K. Iyer and G.V. Eleftheriades, "Negative refractive index metamaterials supporting 2-D waves," in *Proc. IEEE Intl. Symp. on Microwave Theory and Tech.*, vol. 2, Seattle, WA, July 2002, pp. 1067–1070.

[34] S.M. Rudolph and A. Grbic, "Volumetric negative refractive index medium exhibiting broadband negative permeability," *J. Appl. Phys.*, vol. 102, p. 013904 013906, Jul. 2007.

[35] A.K Iyer and G.V. Eleftheriades, "A three-dimensional isotropic transmission-line metamaterial topology for free-space excitation," *J. Appl. Phys.*, vol. 92, no. 26, pp. 261 106 – 261 108, Jun. 2008.

[36] J.M. Williams, "Some Problems with Negative Refraction," *Phys. Rev. Lett.*, vol. 87, no. 24, p. 249703, Dec 2001.

[37] G.W.'t Hooft, "Comment on 'Negative Refraction Makes a Perfect Lens'," *Phys. Rev. Lett.*, vol. 87, no. 24, p. 249701, Dec 2001.

[38] N. Garcia and M. Nieto-Vesperinas, "Left-Handed Materials Do Not Make a Perfect Lens," *Phys. Rev. Lett.*, vol. 88, no. 20, pp. 207 403–207 407, May 2002.

[39] ——, "Is there experimental verification of a negative index of refraction yet?" *Opt. Lett.*, vol. 27, no. 11, pp. 885–887, Jun. 2002.

[40] B.E. Spielman, S. Amari, C. Caloz, G.V. Eleftheriades, T. Itoh, D.R. Jackson, R. Levy, J.D. Rhodes, and R.V. Snyder, "Metamaterials: A Rich Opportunity for Discovery or an Overhyped Gravy Train," *IEEE Microwave Magaz.*, vol. 10, no. 3, pp. 8–42, May 2009.

[41] B.A. Munk, *Metamaterials: Critique and Alternatives*. Hoboken, NJ: John Wiley and Sons, Inc., 2009.

[42] J. B. Pendry, "Negative refraction makes a perfect lens," *Phys. Rev. Lett.*, vol. 85, no. 18, pp. 3966–3969, Oct. 2000.

[43] A. Grbic and G.V. Eleftheriades, "Overcoming the Diffraction Limit with a Planar Left-Handed Transmission-Line Lens," *Phys. Rev. Lett.*, vol. 92, no. 11, pp. 117 403–117 406, Mar. 2004.

[44] A.K Iyer and G.V. Eleftheriades, "A Multilayer Negative-Refractive-Index Transmission-Line (NRI-TL) Metamaterial Free-Space Lens at X-Band," *IEEE Trans. Antennas Propagat.*, vol. 55, no. 10, pp. 2746 – 2753, Oct. 2007.

[45] ——, " Free-Space Imaging Beyond the Diffraction Limit Using a Veselago-Pendry Transmission-Line Metamaterial Superlens," *IEEE Trans. Antennas Propagat.*, vol. 57, no. 6, pp. 1720–1727, Jun. 2009.

[46] S.M. Rudolph and A. Grbic, "Super-resolution focusing using volumetric, broadband NRI media," *IEEE Trans. Antennas Propagat.*, vol. 56, no. 9, p. 2963 2969, Sept. 2008.

[47] J.B. Pendry, D. Schurig, and D.R. Smith, "Controlling Electromagnetic Fields," *Science*, vol. 312, no. 5781, pp. 1780 – 1782, Jun. 2006.

[48] A. Alu and N. Engheta, "Achieving transparency with plasmonic and metamaterial coatings," *Phys. Rev. E*, vol. 72, no. 1, pp. 016 623 – 016 628, Jul. 2006.

[49] D. Schurig, J. J. Mock, J. Justice, S. A. Cummer, J. B. Pendry, A. F. Starr, and D.R. Smith, "Metamaterial Electromagnetic Cloak at Microwave Frequencies," *Science*, vol. 314, no. 5801, pp. 977 – 980, Nov. 2006.

[50] M. Silveirinha and N. Engheta, "Tunneling of Electromagnetic Energy through Subwavelength Channels and Bends using epsilon-Near-Zero Materials," *Phys. Rev. Lett.*, vol. 97, no. 15, pp. 157 403 – 157 406, Oct. 2006.

[51] B. Edwards, A. Alu, M.E. Young, M. Silveirinha, and N. Engheta, "Experimental Verification of Epsilon-Near-Zero Metamaterial Coupling and Energy Squeezing Using a MicrowaveWaveguide," *Phys. Rev. Lett.*, vol. 100, no. 3, pp. 033 903 – 033 906, Jan. 2008.

[52] J.D. Baena, R. Marques, F. Medina, and J. Martel, "Artificial magnetic metamaterial design by using spiral resonators," *Phys. Rev. B*, vol. 69, no. 1, pp. 014 402–1 – 014 402–5, 2004.

[53] H. Mosallaei and K. Sarabandi, "Magneto-dielectrics in electromagnetics: concept and applications," *IEEE Trans. Antennas Propagat.*, vol. 52, no. 6, pp. 1558 – 1567, Jun. 2004.

[54] L.J. Chu, "Physical limitations of omni-directional antennas," *J. Appl. Phys.*, vol. 9, pp. 1163–1175, Dec. 1948.

[55] H.A. Wheeler, "Fundamental limitations of small antennas," *Proc. IRE*, pp. 1479 – 1484, Dec. 1947.

[56] R. C. Hansen, "Fundamental limitations in antennas," *Proceedings of the IEEE*, vol. 69, no. 2, pp. 170–182, Feb. 1981.

[57] A.D. Yaghjian and S.R. Best, "Impedance, bandwidth and Q of antennas," *IEEE Trans. Antennas Propagat.*, vol. 53, no. 4, p. 12981324, Apr. 2005.

[58] J.S. McLean, "A re-examination of the fundamental limits on the radiation Q of electrically small antennas," *IEEE Trans. Antennas Propagat.*, vol. 44, no. 5, p. 672676, May 1996.

[59] R. C. Hansen and M. Burke, "Antenna with magneto-dielectrics," *Microwave Opt. Technol. Lett.*, vol. 26, no. 2, p. 7578, 2000.

[60] P.M.T. Ikonen, S.I. Maslovski, C.R. Simovski, and S.A. Tretyakov, "On artificial magnetodielectric loading for improving the impedance bandwidth properties of microstrip antennas," *IEEE Trans. Antennas Propagat.*, vol. 54, no. 6, pp. 1654–1662, Jun. 2006.

[61] P.M.T. Ikonen, K.N. Rozanov, A. V. Osipov, P. Alitalo, and S.A. Tretyakov, "Magnetodielectric substrates in antenna miniaturization: potential and limitations," *IEEE Trans. Antennas Propagat.*, vol. 54, no. 11B, pp. 3391 – 3399, Nov. 2006.

[62] K. Buell, H. Mosallaei, and K. Sarabandi, "A substrate for small patch antennas providing tunable miniaturization factors," *IEEE Trans. Microwave Theory Tech.*, vol. 54, no. 1, pp. 135–146, Jan. 2006.

[63] D. Psychoudakis, S. Koulouridis, and J.L. Volakis, "Magneto-dielectric antenna designs using material and metallic genetic algorithm optimization," in *Proc. IEEE Antennas and Propagation Symposium*, Jul. 2006, pp. 4505 – 4508.

[64] G. Goussetis, A. P. Feresidis, and J. C. Vardaxoglou, "Tailoring the AMC and EBG Characteristics of Periodic Metallic Arrays Printed on Grounded Dielectric Substrate," *IEEE Trans. Antennas Propagat.*, vol. 54, no. 1, pp. 82–89, Jan. 2006.

[65] A. P. Feresidis, G. Goussetis, S. Wang, and J. C. Vardaxoglou, "Artificial magnetic conductor surfaces and their application to low profile high-gain planar antennas," *IEEE Trans. Antennas Propagat.*, vol. 53, no. 1, pp. 209–215, Jan. 2005.

[66] A. P. Feresidis and J. C. Vardaxoglou, "High gain planar antenna using optimised partially reflective surfaces," *IEE Proc. Microw., Antennas and Propag.*, vol. 148, no. 6, pp. 345–350, Dec. 2001.

[67] S. Wang, A.P. Feresidis, G. Goussetis, and J.C. Vardaxoglou, "High-Gain Subwavelength Resonant Cavity Antennas Based on Metamaterial Ground Planes," *IEE Proc. Microw., Antennas and Propag.*, vol. 153, no. 1, pp. 1–6, Feb. 2006.

[68] G. K. Palikaras, A.P. Feresidis, and J.C. Vardaxoglou, "Cylindrical electromagnetic band gap structures for directive base station antennas," *IEEE Antennas Wireless Propagat. Lett.*, vol. 3, no. 6, pp. 87–89, 2004.

[69] E. Saenz, K. Guven, E. Ozbay, I. Ederra, and R. Gonzalo, "Enhanced directed emission from metamaterial based radiation source," *Appl. Phys. Lett.*, vol. 92, pp. 204 103–204 106, 2008.

[70] E. Saenz, R. Gonzalo, I. Ederra, J. C. Vardaxoglou, and P. de Maagt, "Resonant meta-surface superstrate for single and multi-frequency dipole antenna arrays," *IEEE Trans. Antennas Propagat.*, vol. 56, no. 4, pp. 951–960, Apr. 2008.

[71] E. Saenz, I. Ederra, P. Ikonen, S. Tretyakov, and R. Gonzalo, "Power transmission enhancement by means of planar meta-surfaces," *J. Optics A: Pure and Applied Optic*, vol. 9, p. S308S314, 2007.

[72] K. Buell, H. Mosallaei, and K. Sarabandi, "Metamaterial insulator enabled superdirective array," *IEEE Trans. Antennas Propagat.*, vol. 55, no. 4, pp. 1074 – 1085, Apr. 2007.

[73] M.A. Antoniades and G.V. Eleftheriades, "Compact linear lead/lag metamaterial phase shifters for broadband applications," *IEEE Antennas Wireless Propagat. Lett.*, vol. 2, no. 1, pp. 103–106, 2003.

[74] ——, "A Broadband Wilkinson Balun Using Microstrip Metamaterial Lines," *IEEE Antennas Wireless Propagat. Lett.*, vol. 4, pp. 209–212, 2005.

[75] R. Islam, F. Elek, and G.V. Eleftheriades, "Coupled-line metamaterial coupler having co-directional phase but contra-directional power flow," *Electronics Letters*, vol. 40, no. 5, pp. 315–317, Mar. 2004.

[76] H. Okabe, C. Caloz, and T. Itoh, "A compact enhanced-bandwidth hybrid ring using an artificial lumped-element left-handed transmission-line section," *IEEE Trans. Microwave Theory Tech.*, vol. 52, no. 3, pp. 798–804, Mar. 2004.

[77] C. Caloz, A. Sanada, and T. Itoh, "A novel composite right-/left-handed coupled-line directional coupler with arbitrary coupling level and broad bandwidth," *IEEE Trans. Microwave Theory Tech.*, vol. 52, no. 3, pp. 980–992, Mar. 2004.

[78] J.K.H. Wong, K.G. Balmain, and G.V. Eleftheriades, "A diplexer based on the spatial filtering property of planar anisotropic transmission-line metamaterials," in *Proc. IEEE International Workshop on Antenna Technology Small Antennas and Novel Metamaterials*, Mar. 2006, pp. 241–244.

[79] O.F. Siddiqui and G.V. Eleftheriades, "Spatial-filtering microwave devices using metallic anisotropic grids over ground," in *Proc. 36th European Microwave Conference*, Sept. 2006.

[80] J. Bonache, I. Gil, J. Garcia-Garcia, and F. Martin, "Novel microstrip bandpass filters based on complementary split-ring resonators," *IEEE Trans. Microwave Theory Tech.*, vol. 54, no. 1, pp. 265–271, Jan. 2006.

[81] J. Garcia-Garcia, J. Bonache, I. Gil, F. Martin, M.dC. Velazquez-Ahumada, and J. Martel, "Miniaturized microstrip and CPW filters using coupled metamaterial resonators," *IEEE Trans. Microwave Theory Tech.*, vol. 54, no. 6, pp. 2628–2635, Jun. 2006.

[82] N. Engheta, "An idea for thin subwavelength cavity resonators using metamaterials with negative permittivity and permeability," *IEEE Antennas Wireless Propagat. Lett.*, vol. 1, no. 1, pp. 10–13, 2002.

[83] L. Liu, C. Caloz, and T. Itoh, "Dominant mode leaky-wave antenna with backfire-to-endfire scanning capability," *IEE Electronics Letters*, vol. 38, pp. 1414–1416, Nov. 2002.

[84] S. Lim, C. Caloz, and T. Itoh, "Metamaterial-based electronically controlled transmission- line structure as a novel leaky-wave antenna with tunable radiation angle and beamwidth," *IEEE Trans. Microwave Theory Tech.*, vol. 52, pp. 2678–2690, Dec. 2004.

[85] A.K Iyer and G.V. Eleftheriades, "Leaky-wave radiation from planar negative-refractive-index transmission-line metamaterials," in *Proc. IEEE Antennas and Propagation Symposium*, vol. 2, Jun. 2004, pp. 1411–1414.

[86] H. Iizuka and P.S. Hall, "Left-handed dipole antennas and their implementations," *IEEE Trans. Antennas Propagat.*, vol. 55, no. 5, p. 1246 1253, May 2007.

[87] A.L. Borja, P.S. Hall, L. Qing, and H. Iizuka, "Omnidirectional loop antenna with left-handed loading," *IEEE Antennas Wireless Propagat. Lett.*, vol. 6, p. 495 498, 2007.

[88] A. Erentok and R.W. Ziolkowski, "Metamaterial-inspired efficient electrically small antennas," *IEEE Trans. Antennas Propagat.*, vol. 56, no. 3, pp. 691–707, Mar. 2008.

[89] R.W. Ziolkowski and A. Erentok, "Metamaterial-based efficient electrically small antennas," *IEEE Trans. Antennas Propagat.*, vol. 54, no. 7, p. 2113 2130, Jul. 2006.

[90] A. Grbic, L. Jiang, and R. Merlin, "Near-Field Plates: Subdiffraction focusing with patterned surfaces," *Science*, vol. 320, no. 5874, pp. 511–513, Apr. 2008.

[91] A. Grbic and R. Merlin, "Near-field focusing plates and their design," *IEEE Trans. Antennas Propagat.*, vol. 56, no. 10, pp. 3159–3165, Oct. 2008.

[92] T. Kokkinos, C.D. Sarris, and G.V. Eleftheriades, "Periodic FDTD analysis of leaky-wave structures and applications-to the analysis of negative-refractive-index leaky-wave antennas ," *IEEE Trans. Microwave Theory Tech.*, vol. 54, no. 4, pp. 1619–1630, Apr. 2006.

[93] T. Kokkinos, "Periodic Finite-Difference Time-Domain Analysis of Negative-Refractive-Index Metamaterials." Master's thesis, University of Toronto, Toronto, ON, 2005.

[94] O.F. Siddiqui, M. Mojahedi, and G.V. Eleftheriades, "Periodically loaded transmission line with effective negative refractive index and negative group velocity," *IEEE Trans. Antennas Propagat.*, vol. 51, pp. 2619–2625, Oct. 2003.

[95] T. Kokkinos, C.D. Sarris, and G.V. Eleftheriades, "Periodic finite-difference time-domain analysis of loaded transmission-line negative-refractive-index metamaterials ," *IEEE Trans. Microwave Theory Tech.*, vol. 53, no. 4, pp. 1488–1495, Apr. 2005.

[96] A. Grbic and G.V. Eleftheriades, "Periodic analysis of a 2-D negative refractive index transmission line structure," *IEEE Trans. Antennas Propagat.*, vol. 51, pp. 2604–2611, Oct. 2003.

[97] D.M. Pozar, *Microwave engineering*, 2nd ed. Toronto, Ontario: John Wiley and Sons, Inc., 1998.

[98] G.V. Eleftheriades, "Analysis of bandwidth and loss in negative-refractive-index transmission-line (NRITL) media using coupled resonators," *IEEE Microwave Wireless Compon. Lett.*, vol. 17, no. 6, pp. 412 – 414, Jun. 2007.

[99] E. Shamonina, V.A. Kalinin, K.H. Ringhofer, and L. Solymar, "Magnetoinductive waves in one, two, and three dimensions," *J. Appl. Phys.*, vol. 92, no. 10, pp. 6252–6261, 2002.

[100] E. Shamonina and L. Solymar, "Magneto-inductive waves supported by metamaterial elements: components for a one-dimensional waveguide," *J. Phys. D: Appl. Phys.*, vol. 37, pp. 362–367, Jan. 2004.

[101] K. S. Yee, "Numerical solution of initial boundary value problem involving maxwell's equation in isotropic media," *IEEE Trans. Antennas Propagat.*, vol. 14, pp. 302–307, May 1966.

[102] G. Floquet, "Sur les quations Diffrentielles Linaires Coefficients Priodiques," *Annales de l'Ecole Normale Suprieur*, vol. 12, pp. 47–89, 1883.

[103] P. Harms, R. Mittra, and W. Ko, "Implementation of the periodic boundary condition in the finite-difference time-domain algorithm for FSS structures," *IEEE Trans. Antennas Propagat.*, vol. 42, pp. 1317–1324, Sep. 1994.

[104] L. Brillouin,, *Wave Propagation in Periodic Structures: Electric Filters and Crystal Lattices*, 1st ed. New York,: McGraw-Hill, 1946.

[105] M. Boroditsky, "Modification of spontaneous emission in photonic crystals," Ph.D. dissertation, University of California, Los Angeles, CA, 1999.

[106] F.W. Grover, *Inductance calculations: working formulas and tables*, 2nd ed. New York City, NY: Dover Publications, Inc., 1973.

[107] S.S. Mohan, M.d.M Hershenson, S.P. Boyd, and T.H. Lee, "Simple accurate expressions for planar spiral inductances," *IEEE J. Solid-State Circuits*, vol. 34, no. 10, pp. 1419–1424, Oct. 1999.

[108] F. Bilotti, A. Toscano, and L. Vegni, "Design of spiral and multiple split-ring resonators for the realization of miniaturized metamaterial samples," *IEEE Trans. Antennas Propagat.*, vol. 55, no. 8, pp. 2258–2267, Aug. 2002.

[109] M.d.M Hershenson, S.S. Mohan, S.P. Boyd, and T.H. Lee, "Optimization of inductor circuits via geometric programming," in *Proc. 36th Design Automation Conference*, New Orleans, LA, Jun. 1999, pp. 994 – 998.

[110] G.V. Eleftheriades, O. Siddiqui, and A.K. Iyer, "Transmission line models for negative refractive index media and associated implementations without excess resonators," *IEEE Microwave Wireless Compon. Lett.*, vol. 13, no. 2, pp. 51–53, Feb. 2003.

[111] P. Wang, M.A. Antoniades, and G.V. Eleftheriades, "An investigation of printed Franklin antennas at X-band using artificial (Metamaterial) phase-shifting lines," *IEEE Trans. Antennas Propagat.*, vol. 56, no. 10, pp. 3118–3128, Oct. 2008.

[112] W.L. Stutzman and G.A. Thiele, *Antenna theory and design*, 2nd ed. John Wiley and Sons, Inc., 1998.

[113] S.R. Best, "The performance properties of electrically small resonant multiple-arm folded wire antennas ," *IEEE Antennas Propagat. Mag.*, vol. 47, no. 4, pp. 13–27, Aug. 2005.

[114] F. Qureshi, M.A. Antoniades, and G.V. Eleftheriades, "A compact and low-profile metamaterial ring antenna with vertical polarization," *IEEE Antennas Wireless Propagat. Lett.*, vol. 4, no. 1, pp. 333 – 336, 2005.

[115] M.A. Antoniades and G.V. Eleftheriades, "Applications of negative-refractive-index transmission-line (NRI-TL) metamaterials in planar antennas and their feed networks," in *Proc. 2nd European Conference on Antennas and Propagation (EuCAP 2007)*, Edinburgh, UK, Nov. 2007.

[116] G.V. Eleftheriades and M.A. Antoniades, "Antenna applications of negative-refractive-index transmission-line (NRI-TL) metamaterials," in *Modern Antenna Handbook edited by C.A. Balanis*, John Wiley and Sons, Inc., pp. 713-718 2008.

[117] M.A. Antoniades and G.V. Eleftheriades, "A folded-monopole model for electrically small NRI-TL metamaterial antennas," *IEEE Antennas Wireless Propagat. Lett.*, vol. 7, pp. 425 – 428, 2008.

[118] H.A. Wheeler, "The radiansphere around a small antenna," *Proc. IRE*, vol. 47, no. 8, pp. 1325 – 1331, Aug. 1959.

[119] S.R. Best, "Low Q Electrically Small Linear and Elliptical Polarized Spherical Dipole Antennas," *IEEE Trans. Antennas Propagat.*, vol. 53, no. 3, p. 10451053, Mar. 2005.

[120] C.A. Balanis, *Antenna theory: analysis and design*, 3rd ed. New York: Wiley, 2005.

[121] J.C. Coetzee and Y. Yu, "Port decoupling for small arrays by means of an eigenmode feed network," *IEEE Trans. Antennas Propagat.*, vol. 56, no. 6, pp. 1587 – 1593, Jun. 2008.

[122] C. Volmer, J. Weber, R. Stephan, K. Blau, and M.A. Hein, "An eigen-analysis of compact antenna arrays and its application to port decoupling," *IEEE Trans. Antennas Propagat.*, vol. 56, no. 2, pp. 360 – 370, Feb. 2008.

[123] J. Weber, C. Volmer, K. Blau, R. Stephan, and M.A. Hein, "Miniaturized antenna arrays using decoupling networks with realistic elements," *IEEE Trans. Microwave Theory Tech.*, vol. 54, no. 6, pp. 2733 – 2740, Jun. 2006.

[124] J. Weber, C. Volmer, R. Stephan, and M.A. Hein, "Eigenmode decoupling of miniaturized diversity antennas using compact quasi-lumped networks," in *Proc. IEEE Loughborough Antennas and Propagation Conference(LAPC)*, Mar. 2008, pp. 89 – 92.

[125] I.S. Nefedov, S.A. Tretyakov, J. Saily, L. Xu, and T. Mynttinen, "Application of wire media layers for coupling reduction in antenna arrays and microwave devices," in *Proc. IEEE Loughborough Antennas and Propagation Conference(LAPC)*, Apr. 2007, pp. 39 – 44.

[126] P.J. Ferrer, J.M. Gonzalez-Arbesu, and J. Romeu, "Bidirectional metamaterial separator for compact antenna systems," in *Proc. IEEE Antennas and Propagation Symposium*, Jun. 2007, pp. 1893 – 1896.

[127] E.H. Newman and M.R. Schrote, "A wide-band electrically small superdirective array," *IEEE Trans. Antennas Propagat.*, vol. 30, no. 6, pp. 1172 – 1176, Nov. 1982.

[128] E.E. Altshuler, T.H. O'Donnell, A.D. Yaghjian, and S.R. Best, "A monopole superdirective array," *IEEE Trans. Antennas Propagat.*, vol. 53, no. 8, pp. 2653 – 2661, Aug. 2005.

[129] S.R. Best, E.E. Altshuler, A.D. Yaghjian, J.M. McGinthy, and T.H. O'Donnell, "An impedance-matched 2-element superdirective array," *IEEE Antennas Wireless Propagat. Lett.*, vol. 7, pp. 302 – 305, 2008.

[130] T.H. O'Donnell and A.D. Yaghjian, "Electrically small superdirective arrays using parasitic elements," in *Proc. IEEE Antennas and Propagation Symposium*, Jul. 2006.

[131] D.-S. Shiu, G.J. Foschini, M.J. Gans, and J.M. Kahn, "Fading correlation and its effect on the capacity of multi-element antenna systems," *IEEE Trans. Communications*, vol. 48, no. 3, p. 502 513, Mar. 2000.

[132] P.N. Fletcher, M. Dean, and A.R. Rix, "Mutual coupling in multi-element array antennas and its influence on MIMO channel capacity," *Electronics Letters*, vol. 39, no. 4, p. 342 344, Feb. 2003.

[133] S. Lu, H.T. Hui, and M. Bialkowski, "Optimizing MIMO channel capacities under the influence of antenna mutual coupling," *IEEE Antennas Wireless Propagat. Lett.*, vol. 7, p. 287 290, 2008.

[134] D.-Y. Chiu, C.-H. Cheng, R.D. Murch, and C.R. Rowell, "Reduction of mutual coupling between closely packed antenna elements," *IEEE Trans. Antennas Propagat.*, vol. 55, no. 6B, pp. 1732–1738, Jun. 2007.

[135] I. Kim, C.w. Jung, Y. Kim, and Y.e. Kim, "Low-profile wideband MIMO antenna with suppressing mutual coupling between two antennas," *Microw. Optical Techn. Letters*, vol. 50, no. 5, pp. 1336–1339, May 2008.

[136] A.K Iyer and G.V. Eleftheriades, "Leaky-wave radiation from a two-dimensional NRI TL metamaterials," in *Proc. URSI International Symposium on EM Theory*, vol. 2, May 2004, pp. 891–893.

[137] D. Sievenpiper, "Forward and Backward Leaky Wave Radiation With Large Effective Aperture From an Electronically Tunable Textured Surface," *IEEE Trans. Antennas Propagat.*, vol. 53, pp. 236–247, Jan. 2005.

[138] R.S. Adve, T.K. Sarkar, O.M.C.Pereira-Filho, and S.M. Rao, "Extrapolation of Time-Domain Responses from Three-Dimensional Conducting Objects Utilizing the Matrix Pencil Technique," *IEEE Trans. Antennas Propagat.*, vol. 45, pp. 147–156, Jan. 1997.

[139] T.K. Sarkar and O. Pereira, "Using Matrix Pencil Method to Estimate the Parameters of a Sum of Complex Exponentials," *IEEE Trans. Antennas Propagat.*, vol. 45, pp. 48–55, Feb. 1995.

[140] Y. Hua and T.K. Sarkar, "Matrix Pencil Method for Estimating Parameters of Exponentially Damped/Undamped Sinuoids in Noise," *IEEE Trans. Acoustics, Speech and Signal Processing*, vol. 38, pp. 814–824, May 1990.

[141] K.L. Klohn, R.E. Horn, H. Jacobs, and E. Freibergs, "Silicon waveguide frequency scanning linear array antenna," *IEEE Trans. Microwave Theory Tech.*, vol. 26, p. 764773, Oct. 1978.

[142] R. E. Horn, H. Jacobs, E. Freibergs, and K. L. Klohn, "Electronic modulated beam-steerable silicon-waveguide array antenna," *IEEE Trans. Microwave Theory Tech.*, vol. 28, p. 647653, Jun. 1980.

[143] S. Kobayashi, R. Lampe, R. Mittra, and S. Ray, "Dielectric rod leakywave antennas for millimeter-wave applications," *IEEE Trans. Antennas Propagat.*, vol. 29, p. 822824, Sept. 1981.

[144] M. Chen, B. Houshmand, and T. Itoh, "FDTD Analysis of a Metal-Strip-Loaded Dielectric Leaky-Wave Antenna," *IEEE Trans. Microwave Theory Tech.*, vol. 45, pp. 1294–1301, Aug. 1997.

[145] C. Caloz and T. Itoh, "Array factor approach of leaky-wave antennas and application to 1-D/2-D composite right/left-handed (CRLH) structures," *IEEE Microwave Wireless Compon. Lett.*, vol. 14, pp. 274–276, Jun. 2004.

[146] A. Grbic and G.V. Eleftheriades, "Leaky CPW-based slot antenna arrays for millimeter-wave applications," *IEEE Trans. Antennas Propagat.*, vol. 50, pp. 1494–1504, Nov. 2002.

[147] T. Edwards, *Foundation for microstrip circuit design*, 2nd ed. West Sussex, UK: John Wiley and Sons, Ltd., 1992.